

## INFORMATION TO USERS

This manuscript has been reproduced from the microfilm master. UMI films the text directly from the original or copy submitted. Thus, some thesis and dissertation copies are in typewriter face, while others may be from any type of computer printer.

**The quality of this reproduction is dependent upon the quality of the copy submitted.** Broken or indistinct print, colored or poor quality illustrations and photographs, print bleedthrough, substandard margins, and improper alignment can adversely affect reproduction.

In the unlikely event that the author did not send UMI a complete manuscript and there are missing pages, these will be noted. Also, if unauthorized copyright material had to be removed, a note will indicate the deletion.

Oversize materials (e.g., maps, drawings, charts) are reproduced by sectioning the original, beginning at the upper left-hand corner and continuing from left to right in equal sections with small overlaps. Each original is also photographed in one exposure and is included in reduced form at the back of the book.

Photographs included in the original manuscript have been reproduced xerographically in this copy. Higher quality 6" x 9" black and white photographic prints are available for any photographs or illustrations appearing in this copy for an additional charge. Contact UMI directly to order.

# UMI

A Bell & Howell Information Company  
300 North Zeeb Road, Ann Arbor MI 48106-1346 USA  
313/761-4700 800/521-0600



UNIVERSITY OF OKLAHOMA

GRADUATE COLLEGE

**AN EXPERIMENTAL AND NUMERICAL STUDY OF GAS  
JET DIFFUSION FLAMES ENVELOPED BY  
A CASCADE OF VENTURIS**

A Dissertation

SUBMITTED TO THE GRADUATE FACULTY

in partial fulfillment of the requirements for the

degree of

Doctor of Philosophy

By

ALA RAFAT QUBBAJ

Norman, Oklahoma

1998

---

**UMI Number: 9914419**

---

**UMI Microform 9914419**  
**Copyright 1999, by UMI Company. All rights reserved.**

**This microform edition is protected against unauthorized  
copying under Title 17, United States Code.**

---

**UMI**  
**300 North Zeeb Road**  
**Ann Arbor, MI 48103**

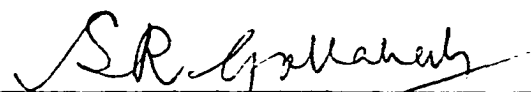
©Copyright by ALA RAFAT QUBBAJ 1998  
All Rights Reserved.

---

**AN EXPERIMENTAL AND NUMERICAL STUDY OF GAS  
JET DIFFUSION FLAMES ENVELOPED BY  
A CASCADE OF VENTURIS**

**A Dissertation APPROVED FOR  
THE SCHOOL OF AEROSPACE AND MECHANICAL  
ENGINEERING**

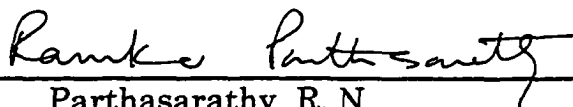
BY



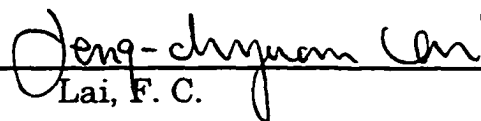
Gollahalli, S. R. (Chairman)



Rasmussen, M. L.



Parthasarathy, R. N.



Lai, F. C.



Lobban, L.

## ACKNOWLEDGMENTS

*I begin with the name of Allah, the most beneficent and the most merciful*

First of all, I wish to express my deep gratitude and thanks to my advisor Dr. S. R. Gollahalli, Lesch Centennial Professor of Mechanical Engineering, for his supervision, encouragement and guidance during this work and throughout my whole Ph.D. program. Working with Prof. Gollahalli has been extremely exciting, beneficial and fruitful. I perceive Dr. Gollahalli as my perfect role model not only in the teaching and research professions but also in my life. I am also grateful to Dr. M. L. Rasmussen, Dr. F.C. Lai, Dr. R. N. Parthasarathy and Dr. L. Lobban for being my teachers during my course work and for serving on my advisory committee.

Also, I would like to thank my colleagues Benjamin Baird and Sien Goh, in the combustion laboratory, for their assistance. Special thanks go to my friend and colleague Ahsan Choudhuri for his generous help. Thanks are also due to my friend Zahid Hossain and to my roommate Mostafa El-Shahed for their encouragement.

I have reserved my last and best acknowledgments and gratitude to my family: my beloved parents Al-Haj Ra'fat Al-Qubbaj and Al-Hajah Intesar Jardaneh, my brothers Abdel Raouf and Mohammad, my sisters Nasreen and Nida', all for their love, prayers, encouragement and sacrifices. Because of their help, after the gracious kindness of Allah, I am able to achieve my academic goals.

*This dissertation is dedicated to  
my Dad, my Mom, my brothers and sisters  
with love and appreciation*

# TABLE OF CONTENTS

<b>CONTENTS</b>	<b>PAGE NO.</b>
<b>ACKNOWLEDGMENTS</b>	iv
<b>TABLE OF CONTENTS</b>	vi
<b>LIST OF TABLES</b>	x
<b>LIST OF FIGURES</b>	xi
<b>LIST OF PHOTOGRAGHS</b>	xix
<b>LIST OF APPENDICES</b>	xx
<b>NOMENCLATURE</b>	xxi
<b>ABSTRACT</b>	xxv
<b>CHAPTER 1: INTRODUCTION</b>	1
<b>CHAPTER 2: BACKGROUND AND LITERATURE</b>	6
2.1: Diffusion Gas Flames	7
2.2: Gas Jet Ejectors and Venturis	8
2.3: Carbon Monoxide Formation and Oxidation	9
2.4: Nitric Oxide Formation	10
2.5: Soot Formation and Destruction	12
2.6: Spectroscopic Techniques	13
2.6.1: Laser Induced Fluorescence	15
2.6.2: Spectroscopic Data for Flame species	17
2.7: Control of Combustion-Generated Nitrogen Oxides	18

2.8: Motivation and Scope of the Present Study	20
<b>CHAPTER 3: EXPERIMENTAL METHODS</b>	<b>21</b>
3.1: Laboratory Combustion Chamber	21
3.2: Venturi Shape and Material	22
3.3: Instrumentation	22
3.3.1: Flame Photography	23
3.3.2: Exhaust Emission Measurements	23
3.3.3: Flame Temperature Measurements	24
3.3.4: Soot Concentration Measurements	24
3.3.5: Air Entrainment Measurements	25
3.3.6: Flame Radiation Measurements	25
3.3.7: Laser Diagnostic System	26
3.3.7.1: Laser Excitation Source and Frequency Tuning	26
3.3.7.2: Focusing and Collection Optics	28
3.3.7.3: Fluorescence Detection and Timing	29
<b>CHAPTER 4: EXPERIMENTAL RESULTS AND DISCUSSIONS</b>	<b>48</b>
4.1: Visible Flame Appearance	48
4.2: Exhaust Temperature	49
4.3: Exhaust Carbon Dioxide Concentration	51
4.4: Exhaust Oxygen Concentration	52

<b>4.5:</b>	<b>Emission Indices</b>	<b>53</b>
<b>4.6:</b>	<b>Optimal Conditions</b>	<b>55</b>
<b>4.7:</b>	<b>Flame Temperature Profiles (Thermal Structure)</b>	<b>56</b>
<b>4.8:</b>	<b>Carbon Dioxide Concentration Profiles</b>	<b>57</b>
<b>4.9:</b>	<b>Oxygen Concentration Profiles</b>	<b>58</b>
<b>4.10:</b>	<b>Carbon Monoxide Concentration Profiles</b>	<b>59</b>
<b>4.11:</b>	<b>Nitric Oxide Concentration Profiles</b>	<b>60</b>
<b>4.12:</b>	<b>Volumetric Soot Concentration Profiles (w)</b>	<b>61</b>
<b>4.13:</b>	<b>Air Entrainment</b>	<b>62</b>
<b>4.14:</b>	<b>Radiant Fraction of Heat Release (F)</b>	<b>64</b>
<b>4.15:</b>	<b>OH Radical Relative Concentration Profiles</b>	<b>65</b>
<b>4.16:</b>	<b>CH Radical Relative Concentration Profiles</b>	<b>70</b>
<b>4.17:</b>	<b>CN Radical Relative Concentration Profiles</b>	<b>73</b>
<b>CHAPTER 5:</b>	<b>NUMERICAL ANALYSIS</b>	<b>108</b>
<b>5.1:</b>	<b>Physical Model</b>	<b>108</b>
<b>5.2:</b>	<b>Numerical Model</b>	<b>109</b>
	<b>5.2.1: Governing Equations</b>	<b>110</b>
	<b>5.2.2: Solution Methodology and Algorithm</b>	<b>112</b>
	<b>5.2.3: Reaction Model</b>	<b>114</b>
	<b>5.2.4: Assumptions and Boundary Conditions</b>	<b>116</b>
<b>5.3:</b>	<b>Carbon Monoxide and Nitric Oxide Post Processing</b>	<b>117</b>

<b>5.3.1: Carbon Monoxide Post Processing</b>	117
<b>5.3.2: Nitric Oxide Post Processing</b>	118
<b>5.4: Results and Discussion</b>	119
<b>5.4.1: Flame Temperature Profiles</b>	119
<b>5.4.2: Carbon Dioxide Concentration Profiles</b>	122
<b>5.4.3: Oxygen Concentration Profiles</b>	124
<b>5.4.4: Carbon Monoxide Concentration Profiles</b>	126
<b>5.4.5: Nitric Oxide Concentration Profiles</b>	129
<b>5.4.6: Hydroxyl Radical Concentration Profiles</b>	132
<b>5.4.7: Equivalence Ratio Profiles</b>	136
<b>5.4.8: Axial and Radial Velocity Profiles</b>	137
<b>CHAPTER 6: CONCLUSIONS AND RECOMMENDATIONS</b>	209
<b>6.1: Conclusions</b>	209
<b>6.2: Recommendations</b>	212
<b>REFERENCES</b>	213
<b>APPENDICES</b>	222

## LIST OF TABLES

<b>TABLE</b>		<b>PAGE NO.</b>
<b>2.1:</b>	Spectroscopic Data for Species of Interest	18
<b>3.1a:</b>	Conventional Instrument Specifications	31
<b>3.1b:</b>	Laser Diagnostic System Instrument Specifications	32
<b>3.2:</b>	Nominal Operating Conditions	34
<b>3.3:</b>	Laser Operating Wavelengths	35
<b>3.4:</b>	Estimated Uncertainties	35
<b>5.1:</b>	Conditions Used in the Computations	144
<b>5.2:</b>	Extended Zeldovich Reaction Rate Constants	144

# LIST OF FIGURES

## Chapter 2

Page (8, 16)

---

- Fig. 2.1** Thrust augmenting ejector
- Fig. 2.2** Possible modes of energy transfer from an excited state

## Chapter 3

Page (36-43)

---

- Fig. 3.1** Combustion chamber and fuel supply train
- Fig. 3.2** Venturi shape and dimensions
- Fig. 3.3** Venturi-cascading
- Fig. 3.4** Instrumentation for emission index measurement
- Fig. 3.5** Instrumentation for temperature measurement
- Fig. 3.6** Instrumentation of soot concentration measurement
- Fig. 3.7** Instrumentation of flame radiation measurement
- Fig. 3.8** Schematic of LIF instrumentation

## Chapter 4

Page (76-107)

---

- Fig. 4.1a** Photograph of the baseline gas jet flame at  $Re=5100$
- Fig. 4.1b** Photograph of the cascaded gas jet flame at  $Re=5100$
- Fig. 4.2** Effect of venturi diameter, spacing and  $Re$  on combustion product temperature
- Fig. 4.3** Effect of venturi diameter, spacing and  $Re$  on  $CO_2$  molar concentration in combustion products

- Fig. 4.4** Effect of venturi diameter, spacing and Re on O<sub>2</sub> molar concentration in combustion products
- Fig. 4.5** Effect of venturi diameter, spacing and Re on CO emission index
- Fig. 4.6** Effect of venturi diameter, spacing and Re on NO emission index
- Fig. 4.7a** Radial temperature profiles for the baseline and cascaded flames in the near-burner region ( $x/d=20$ ) at Re=5100
- Fig. 4.7b** Radial temperature profiles for the baseline and cascaded flames in the mid-flame region ( $x/d=100$ ) at Re=5100
- Fig. 4.7c** Radial temperature profiles for the baseline and cascaded flames in the far-burner region ( $x/d=180$ ) at Re=5100
- Fig. 4.8a** Radial concentration profiles of CO<sub>2</sub> for the baseline and cascaded flames in the near-burner region ( $x/d=20$ ) at Re=5100
- Fig. 4.8b** Radial concentration profiles of CO<sub>2</sub> for the baseline and cascaded flames in the mid-flame region ( $x/d=100$ ) at Re=5100
- Fig. 4.8c** Radial concentration profiles of CO<sub>2</sub> for the baseline and cascaded flames in the far-burner region ( $x/d=180$ ) at Re=5100
- Fig. 4.9a** Radial concentration profiles of O<sub>2</sub> for the baseline and cascaded flames in the near-burner region ( $x/d=20$ ) at Re=5100
- Fig. 4.9b** Radial concentration profiles of O<sub>2</sub> for the baseline and cascaded flames in the mid-flame region ( $x/d=100$ ) at Re=5100
- Fig. 4.9c** Radial concentration profiles of O<sub>2</sub> for the baseline and cascaded flames in the far-burner region ( $x/d=180$ ) at Re=5100
- Fig. 4.10a** Radial concentration profiles of CO for the baseline and cascaded flames in the near-burner region ( $x/d=20$ ) at Re=5100
- Fig. 4.10b** Radial concentration profiles of CO for the baseline and cascaded flames in the mid-flame region ( $x/d=100$ ) at Re=5100
- Fig. 4.10c** Radial concentration profiles of CO for the baseline and cascaded flames in the far-burner region ( $x/d=180$ ) at Re=5100
- Fig. 4.11a** Radial concentration profiles of NO for the baseline and cascaded flames in the near-burner region ( $x/d=20$ ) at Re=5100

- Fig. 4.11b** Radial concentration profiles of NO for the baseline and cascaded flames in the mid-flame region ( $x/d=100$ ) at  $Re=5100$
- Fig. 4.11c** Radial concentration profiles of NO for the baseline and cascaded flames in the far-burner region ( $x/d=180$ ) at  $Re=5100$
- Fig. 4.12a** Axial volumetric soot concentration profiles for the baseline and cascaded flames at  $Re=3500$
- Fig. 4.12b** Axial volumetric soot concentration profiles for the baseline and cascaded flames at  $Re=5100$
- Fig. 4.12c** Axial volumetric soot concentration profiles for the baseline and cascaded flames at  $Re=6500$
- Fig. 4.13** Secondary air entrainment ratio in the baseline and cascaded cold jets at different axial conditions for  $Re=5100$
- Fig. 4.14** Radiant fraction for the baseline and cascaded flames at three  $Re$  numbers
- Fig. 4.15** Relative LIF OH signal (concentration) profiles at  $x/d=20$  for the baseline and cascaded flames at  $Re=5100$
- Fig. 4.16** Relative LIF OH signal (concentration) profiles at  $x/d=100$  for the baseline and cascaded flames at  $Re=5100$
- Fig. 4.17** Relative LIF CH signal (concentration) profiles at  $x/d=20$  for the baseline and cascaded flames at  $Re=5100$
- Fig. 4.18** Relative LIF CH signal (concentration) profiles at  $x/d=100$  for the baseline and cascaded flames at  $Re=5100$
- Fig. 4.19** Relative LIF CN signal (concentration) profiles at  $x/d=20$  for the baseline and cascaded flames at  $Re=5100$

## **Chapter 5**

**Page (145-208)**

- Fig. 5.1a** Geometry and boundary conditions
- Fig. 5.1b** Non-uniform grid used for flow computations

- Fig 5.1c** Locations of velocity computations with respect to the venturis
- Fig 5.1d** Locations of velocity computations for venturi number 3
- Fig. 5.2** 2-D discretization of convection and diffusion terms
- Fig. 5.3a** Solution flowchart for SIMPLIC algorithm
- Fig. 5.3b** Solution procedure for a single dependent variable
- Fig. 5.4a** Radial temperature profiles for the baseline and cascaded flames in the near-burner region ( $x/d=20$ )
- Fig. 5.4b** Radial temperature profiles for the baseline and cascaded flames in the mid-flame region ( $x/d=100$ )
- Fig. 5.4c** Radial temperature profiles for the baseline and cascaded flames in the far-burner region ( $x/d=180$ )
- Fig. 5.5a** Radial concentration profiles of  $\text{CO}_2$  for the baseline and cascaded flames in the near-burner region ( $x/d=20$ )
- Fig. 5.5b** Radial concentration profiles of  $\text{CO}_2$  for the baseline and cascaded flames in the mid-flame region ( $x/d=100$ )
- Fig. 5.5c** Radial concentration profiles of  $\text{CO}_2$  for the baseline and cascaded flames in the far-burner region ( $x/d=180$ )
- Fig. 5.6a** Radial concentration profiles of  $\text{O}_2$  for the baseline and cascaded flames in the near-burner region ( $x/d=20$ )
- Fig. 5.6b** Radial concentration profiles of  $\text{O}_2$  for the baseline and cascaded flames in the mid-flame region ( $x/d=100$ )
- Fig. 5.6c** Radial concentration profiles of  $\text{O}_2$  for the baseline and cascaded flames in the far-burner region ( $x/d=180$ )
- Fig. 5.7a** Radial concentration profiles of  $\text{CO}$  for the baseline and cascaded flames in the near-burner region ( $x/d=20$ )
- Fig. 5.7b** Radial concentration profiles of  $\text{CO}$  for the baseline and cascaded flames in the mid-flame region ( $x/d=100$ )
- Fig. 5.7c** Radial concentration profiles of  $\text{CO}$  for the baseline and cascaded flames in the far-burner region ( $x/d=180$ )

- Fig. 5.8a** Radial concentration profiles of thermal-NO for the baseline and cascaded flames in the near-burner region ( $x/d=20$ )
- Fig. 5.8b** Radial concentration profiles of thermal-NO for the baseline and cascaded flames in the mid-flame region ( $x/d=100$ )
- Fig. 5.8c** Radial concentration profiles of thermal-NO for the baseline and cascaded flames in the far-burner region ( $x/d=180$ )
- Fig. 5.9a** Radial concentration profiles of OH radical for the baseline and cascaded flames in the near-burner region ( $x/d=20$ )
- Fig. 5.9b** Radial concentration profiles of OH radical for the baseline and cascaded flames in the mid-flame region ( $x/d=100$ )
- Fig. 5.9c** Radial concentration profiles of OH radical for the baseline and cascaded flames in the far-burner region ( $x/d=180$ )
- Fig. 5.10a** Radial profiles of equivalence ratio ( $\phi$ ) for the baseline and cascaded flames in the near-burner region ( $x/d=20$ )
- Fig. 5.10b** Radial profiles of equivalence ratio ( $\phi$ ) for the baseline and cascaded flames in the mid-flame region ( $x/d=100$ )
- Fig. 5.10c** Radial profiles of equivalence ratio ( $\phi$ ) for the baseline and cascaded flames in the far-burner region ( $x/d=180$ )
- Fig. 5.11a** Radial profiles of axial velocity ( $U$ ) for the baseline and cascaded flames in the near-burner region ( $x/d=20$ )
- Fig. 5.11b** Radial profiles of axial velocity ( $U$ ) for the baseline and cascaded flames in the mid-flame region ( $x/d=100$ )
- Fig. 5.11c** Radial profiles of axial velocity ( $U$ ) for the baseline and cascaded flames in the far-burner region ( $x/d=180$ )
- Fig. 5.12a** Radial profiles of radial velocity ( $V$ ) for the baseline and cascaded flames in the near-burner region ( $x/d=20$ )
- Fig. 5.12b** Radial profiles of radial velocity ( $V$ ) for the baseline and cascaded flames in the mid-flame region ( $x/d=100$ )

- Fig. 5.12c** Radial profiles of radial velocity (V) for the baseline and cascaded flames in the far-burner region ( $x/d=180$ )
- Fig. 5.13a** Radial profiles of axial velocity (U) for the baseline and cascaded flames at  $x/d=80$
- Fig. 5.13b** Radial profiles of axial velocity (U) for the baseline and cascaded flames at  $x/d=160$
- Fig. 5.13c** Radial profiles of axial velocity (U) for the baseline and cascaded flames at  $x/d=240$
- Fig. 5.14a** Radial profiles of radial velocity (V) for the baseline and cascaded flames at  $x/d=80$
- Fig. 5.14b** Radial profiles of radial velocity (V) for the baseline and cascaded flames at  $x/d=160$
- Fig. 5.14c** Radial profiles of radial velocity (V) for the baseline and cascaded flames at  $x/d=240$
- Fig. 5.15a** Radial profiles of axial velocity (U) for the baseline and cascaded flames at  $x/d=40$
- Fig. 5.15b** Radial profiles of axial velocity (U) for the baseline and cascaded flames at  $x/d=120$
- Fig. 5.15c** Radial profiles of axial velocity (U) for the baseline and cascaded flames at  $x/d=200$
- Fig. 5.16a** Radial profiles of radial velocity (V) for the baseline and cascaded flames at  $x/d=40$
- Fig. 5.16b** Radial profiles of radial velocity (V) for the baseline and cascaded flames at  $x/d=120$
- Fig. 5.16c** Radial profiles of radial velocity (V) for the baseline and cascaded flames at  $x/d=200$
- Fig. 5.17a, b** Total velocity vector field in the baseline and cascaded flames
- Fig. 5.18a** Radial profiles of axial velocity (U) for the baseline and cascaded flames at  $x/d=142.5$

- Fig. 5.18b** Radial profiles of axial velocity (U) for the baseline and cascaded flames at 2.5d above base of venturi 3
- Fig. 5.18c** Radial profiles of axial velocity (U) for the baseline and cascaded flames at 5d above base of venturi 3
- Fig. 5.18d** Radial profiles of axial velocity (U) for the baseline and cascaded flames at 8.75d above base of venturi 3
- Fig. 5.18e** Radial profiles of axial velocity (U) for the baseline and cascaded flames at 17.5d above base of venturi 3
- Fig. 5.18f** Radial profiles of axial velocity (U) for the baseline and cascaded flames at 26.25d above base of venturi 3
- Fig. 5.18g** Radial profiles of axial velocity (U) for the baseline and cascaded flames at 30d above base of venturi 3
- Fig. 5.18h** Radial profiles of axial velocity (U) for the baseline and cascaded flames at 35d above base of venturi 3
- Fig. 5.19a** Radial profiles of radial velocity (V) for the baseline and cascaded flames at  $x/d=142.5$
- Fig. 5.19b** Radial profiles of radial velocity (V) for the baseline and cascaded flames at 2.5d above base of venturi 3
- Fig. 5.19c** Radial profiles of radial velocity (V) for the baseline and cascaded flames at 5d above base of venturi 3
- Fig. 5.19d** Radial profiles of radial velocity (V) for the baseline and cascaded flames at 8.75d above base of venturi 3
- Fig. 5.19e** Radial profiles of radial velocity (V) for the baseline and cascaded flames at 17.5d above base of venturi 3
- Fig. 5.19f** Radial profiles of radial velocity (V) for the baseline and cascaded flames at 26.25d above base of venturi 3
- Fig. 5.19g** Radial profiles of radial velocity (V) for the baseline and cascaded flames at 30d above base of venturi 3
- Fig. 5.19h** Radial profiles of radial velocity (V) for the baseline and cascaded flames at 35d above base of venturi 3

**Fig. 5.20a, b** Total velocity vector field for venturi 3 in the baseline and cascaded flames

---

**Appendix 5**

**Page (233-235)**

**Fig. A5.1** Injection seeder and GCR host laser

**Fig. A5.2** MOPO optical layout

**Fig. A5.3** Typical tuning performance of MOPO-FDO

---

**Appendix 6**

**Page (236-241)**

**Fig. A6.1** Thrust augmenting ejector

**Fig. A6.2** Test configuration (Lund et al., 1986)

**Fig. A6.3** Comparison of surface pressure distribution (Lund et al., 1986)

**Fig. A6.4** Optimization parameters:  $X_n$ ,  $X_L$  and  $\theta$ ,  $L/2H=3.28$  (Lund et al., 1986)

**Fig. A6.5** Effect of primary nozzle position on thrust augmentation (Tavella et al., 1987)

**Fig. A6.6** Dual jet ejectors and the viscous-inviscid approach (Lund, 1991)

**Fig. A6.7** Ejector schematic (Miller et al., 1991)

---

**Appendix 7**

**Page (243-245)**

**Fig. A7.1** Static pressure drop along a single venturi positioned at three axial locations: 1, 2 and 3 (Fig. 5.1c) for a nitrogen cold jet at  $Re=5100$

**Fig. A7.2** Static pressure drop along venturi 1, 2, 3 and 4 in the cascade (Fig. 5.1c) for a nitrogen cold jet at  $Re=5100$

**Fig. A7.3** Static pressure drop along venturi 1, 2 and 3 in the cascade (Fig. 5.1c) for the propane flame at  $Re=3500$

## LIST OF PHOTOGRAGHS

<b>PHOTOGRAGH</b>		<b>PAGE NO.</b>
3.1:	The cascade in the combustion chamber and the analysis apparatus	44
3.2:	Side view of the laser diagnostic system (Nd-YAG and MOPO)	45
3.3:	Front view of the laser diagnostic system	46
3.4:	Top view of the laser diagnostic system	47
4.1a:	The baseline gas jet flame at $Re=5100$	76
4.1b:	The cascaded gas jet flame at $Re=5100$	77

## LIST OF APPENDICES

<b>APPENDIX</b>		<b>PAGE NO.</b>
1:	Energy Balance Equation for Thermocouple	223
2:	Derivation of Equations	225
3:	Sample Calculations	228
4:	Estimation of Uncertainties	231
5:	Details of the Laser System	233
6:	Gas Jet Ejectors: Principle and Applications	236
7:	Pressure Drop Through Venturis	242

## NOMENCLATURE

A	Pre-exponential factor
$A_{ij}$	Einstein coefficient for spontaneous emission from state $i$ to $j$ ( $i > j$ )
$d$	Burner-exit diameter
D	Venturi throat diameter, diffusion coefficient
DI	Venturi inlet diameter
E	Activation energy
EI	Emission index
$f$	Mixture fraction
F	Radiant fraction
FDE	Finite difference equation
Fr	Froude number
$h$	Enthalpy, convective heat transfer coefficient, Planck's constant
H	Venturi height
I	Laser beam intensity
K	Thermal conductivity
$k$	Reaction rate constant
LHV	Lower heating value of the fuel
$m$	Mass
M	Molecular weight
N	Population density of state $i$

n	Number of moles
NITER	Number of iterations
NV	No venturi (baseline case)
p	Static pressure
P	Laser pulse
q	Heat flux
Q	Heat rate
$Q_{ij}$	Quenching coefficient
r	Radial distance from burner axis
Re	Reynolds number
S	Source term
$S_x$	Sample standard deviation
t	Flame thickness
T	Temperature
U	Axial velocity component
$u_j$	$j^{\text{th}}$ component of velocity
V	Radial velocity component
w	Volumetric soot concentration
$W_{ij}$	Einstein coefficient; for absorption ( $i < j$ ), for stimulated emission ( $i > j$ )
X	Mole fraction
x	Vertical distance above burner exit
Y	Mass fraction

## **Greek Symbols**

$\nu$	Stoichiometric coefficient in the overall reaction
$\nu$	Frequency
$\Gamma$	Transport coefficient
$\alpha$	Absorptivity
$\rho$	Density
$\phi$	Dependent variable
$\varepsilon$	Emissivity
$\mu$	Fluid dynamic viscosity
$\sigma$	Steffan Boltzman constant
$\lambda$	Wavelength
$\tau_{ij}$	Viscous stress tensor
$\delta_{ij}$	Kronecker delta
$\xi_{ik}$	Mass fraction of the $i^{\text{th}}$ species in the $k^{\text{th}}$ mixture

## **Subscripts**

a	Additional
A	Air
atm	Atmospheric
B	Background
b	Thermocouple bead
e	Excited (upper) State

f	Fuel
g	Ground state, gas
i	Species i, state i, i <sup>th</sup> component
j	j <sup>th</sup> component
o	Reference value
u	Unreacted
w	Thermocouple wire

## ABSTRACT

A new technique to control carbon monoxide, nitric oxide, and soot emissions of a propane diffusion flame by modifying the air infusion rate into the flame was developed. The modification was achieved by installing a cascade of venturis around the burning gas jet, which, therefore, was given the appellation “venturi-cascading”. The basic idea behind this technique is controlling the stoichiometry of the flame through changing the flow dynamics and rates of mixing in the combustion zone with a set of venturis surrounding the flame. In this study, the effectiveness of the “venturi-cascading” technique was experimentally as well numerically investigated.

Propane jet diffusion flames at three burner-exit Reynolds numbers (3600, 5100 and 6500) corresponding to burner-rim-attached, undergoing transition from attached to lifted, and fully-lifted configurations were examined with several sets of venturis of different sizes and spacing arrangements. Temperature, and the concentrations of carbon dioxide, oxygen, carbon monoxide and nitric oxide in the exhaust products were measured before and after the modification, and optimal conditions to minimize pollutant emissions were obtained. The optimal value of venturi throat/burner-exit diameter ratio ( $D/d$ ) was  $32\pm 3$ , which corresponded to an approximate clearance of  $5\pm 2$  mm between the venturi throat and the burning jet width at the mid-flame height. The influence of venturi/burner diameter ratio was stronger than that of the spacing distribution. The highest effect of the venturi-cascade was observed on the flame in transition from attached to lifted configurations at a Reynolds number of 5100.

The *venturi-cascading* technique at its optimal conditions resulted in a decrease of 87% and 33% in CO and NO emission indices along with a 24% decrease in soot emission from a propane jet flame, compared to the baseline condition (same flame without venturis). The reduction of NO without increasing CO was the main attraction of this technique.

The temperature and composition measurements, at the optimal conditions, showed that, in the near-burner region, the venturi-cascaded flame had lower temperature and CO<sub>2</sub> concentration by an average of 5% and 7%, respectively, than the baseline flame. However, in the mid-flame and far-burner regions, it has higher temperature by 13% and 12%, and higher CO<sub>2</sub> concentration by 16% and 13%, in average values, respectively. An opposite trend was noticed for O<sub>2</sub> concentration; the cascaded flame has higher O<sub>2</sub> concentration in the near-burner region by 10%. however, it has lower O<sub>2</sub> concentrations by 8% and 10%, in average values, in the mid-flame and far-burner regions, respectively, than in the baseline case. The results also showed that, in the near-burner, mid-flame, and far-burner regions, the venturi-cascaded flame has lower CO concentrations by 8%, 12% and 15%, respectively, and lower NO concentrations by 16%, 5% and 3%, in average values, respectively, compared to the baseline case.

Laser Induced Fluorescence (LIF) measurements, in the near-burner region of the venturi-cascaded flame, indicated an average decrease of 18%, 24% and 12% in OH, CH and CN radical species, respectively, along with 11% drop in soot precursors (PAH), from their baseline values. However, in the mid-flame region, a 40% average increase in OH, from its baseline value, was observed. In this particular region, it was

hard to detect any CH or CN radicals. The results showed that the OH radical, in the downstream locations, was mostly affected by soot rather than by temperature. In addition, the prompt-NO mechanism appeared to play a significant role besides the conventional thermal-NO mechanism.

The thermal and composition fields of the baseline and venturi-cascaded flames were numerically simulated using CFD-ACE+, an advanced computational environment software package. The CO and NO concentrations were determined through CFD-POST, a post processing utility program for CFD-ACE+. The final simulated results were compared with the experimental data. Good agreement was found in the near-burner region. However, the agreement was poor in the downstream regions. The numerical results substantiate the conclusion, which was drawn in the experimental part of this study, that venturi-cascading is a feasible method for controlling the pollutant emissions of a burning gas jet, if used at appropriate conditions.

# CHAPTER I

## INTRODUCTION

Pollutant emissions in the atmosphere contribute to specific health hazards, photochemical smog, formation of acid rain precursors, destruction of the ozone layer in the stratosphere and global warming. Therefore, over the last two decades, increasingly stringent regulations reducing allowable emissions from combustion sources have been implemented. The main objective of these regulations was to restrict the emission of combustion pollutants such as carbon monoxide, nitrogen oxides and soot from both stationary and mobile combustors. As a consequence, coal in most of the power plants was replaced by cleaner (gaseous) fuels, and developing new control technologies to adapt with the new standards has become the focus of research in the field of combustion.

The Kyoto protocol of December 1998 has imposed stricter standards on allowable emissions; it targeted the gas emissions to be reduced in developed countries by a collective average of 5.2%, below the 1990/1995 baseline by the year 2008-2012. This imposes an additional challenge for combustion researchers to develop new effective techniques that control pollutant emissions from combustion sources, in order to meet the future standards.

In most of the practical combustors, diffusion flames have been employed for a long time; the reason is attributed to their advantages of the absence of flash back, controlled flammability, ease of burning, and heat release control. However, their

inherent tendency to produce soot and high radiation make them less desirable in some applications. Furthermore, the nature of diffusion flames in which fuel and oxidizer enter the reaction zone from opposite directions, results in the unavoidable existence of stoichiometric mixture contour and the consequent high temperature and thermal-NO zones.

The key for controlling the burning rate and NO production is to control the local air-fuel ratio so that the extent of stoichiometric regions is minimized. In premixed flames, this may be achieved by staging of fuel-air mixing, so that the residence time of the flame is most likely confined to fuel-rich or fuel-lean zones (Bowman, 1992).

In hydrocarbon diffusion flames, except in the near-burner region, the local air-fuel ratio depends upon the diffusion and air-entrainment rate into the burning jet, which can be also controlled either by changing the flow dynamics or manipulating the downstream flow characteristics of the gas jet. The applications of non-axisymmetric burner exit geometries (Gollahalli et al., 1992; Gutmark et al., 1991; Schadow et al., 1989) and swirl-flame burners (Tangirala et al., 1987; Chen and Driscoll, 1988) are examples of such a technique that showed significant improvements in the combustion and emission characteristics of gas burning jets.

The general objective of this study was to test the feasibility of a concept, similar to the applications mentioned earlier, in gas diffusion flames. In this technique the downstream flow characteristics are manipulated by employing the method of *venturi-cascading*, in which a set of venturis is arranged around the flame so that each venturi acts as an ejector that accelerates the air inflow into the combustion zone.

In general, better combustion and emission characteristics are achieved by selecting and designing the operating conditions such that the emission of pollutants is minimum and combustion efficiency is maximum. Furthermore, reliability, compatibility, flexibility, safety, material limitation and cost are all important factors that should be taken into account. However, in practical combustors, some tradeoff between those parameters has to be considered in the design process. Therefore, an extensive parametric study was performed to obtain the optimal performance of venturi-cascading.

As pointed out earlier, reducing combustion-generated emissions was the main goal of the present study. However, this problem can not be addressed properly unless the thermo-chemical processes involved are being well-identified and understood, and, therefore, this was set as the second-stage goal of this study. For this purpose, highly-accurate diagnostics were needed, to obtain an improved understanding of the combustion processes that involve many intermediate radicals and reaction steps.

Standard gas analysis equipment can measure stable species such as: CO, NO, O<sub>2</sub>, and CO<sub>2</sub>. However, these analyzers are subject to numerous errors due to the loss of kinetics and quenching in the sampling probes. Moreover, the analyzers are unable to detect transient or intermediate radicals in chemical reactions, which are necessary to develop a deeper understanding of the mechanisms involved.

Combustion intermediates and radicals are of great interest and importance. For instance, the hydroxyl radical (OH) is a major combustion intermediate which plays a vital role in the thermal NO formation mechanism (Bowman, 1992) that will be

explained later. Moreover, the OH distribution acts as a flame zone marker that provides a relative scale of temperature which helps in the design of the combustor (Hicks, 1995). The OH radical has also been implemented as a dominant oxidizer of soot particles in flames (Neoh, 1984). Another example is the amount of CH radical present in the flame is directly related to the production of nitric oxide by the prompt NO mechanism. This NO, produced at temperatures lower than those for thermal NO (Bowman, 1992), is formed through a series of reactions that begin by CH reacting with  $N_2$  (as will be explained in chapter 2). The CN radical is another important radical in NO<sub>x</sub> and soot formations (Turns, 1996). All the above mentioned radicals are very sensitive to the local flow field conditions and reside spatially within a narrow region at a concentration typically below 100 ppm. Information about these radicals, which is very important in combustion chemistry, is inaccessible through conventional sampling techniques and gas analyzers.

Laser induced fluorescence spectroscopy (LIF) possesses the capability to detect flame radicals and pollutant species at ppm or even sub-ppm level. It is a sensitive, selective, non-intrusive spectroscopic diagnostic technique, and consequently has been receiving considerable attention. This technique was used to detect the aforementioned radicals.

In addition, the venturi-cascading technique, studied experimentally in the first part of this research, was numerically modeled and analyzed. The numerical computations were conducted using the *CFDRC-ACE+* (advanced computational environment) software package, version 5.0, 1998. Temperatures, equivalence ratios, velocities and the concentrations of CO<sub>2</sub>, O<sub>2</sub>, CO, NO and OH were numerically

computed. The concentrations of CO and NO were determined using CFD-POST, a post processing utility program for CFD-ACE+. The details and results of the numerical modeling are presented in chapter 5.

The body of this dissertation consists mainly of six chapters. Chapter one is an introduction. The necessary background and literature are discussed in chapter two. A description of the apparatus and experimental methods is outlined in chapter three. Chapter four contains the experimental results and discussions. Chapter five presents the numerical modeling and analysis, and finally, chapter six contains the overall conclusions and recommendations.

## CHAPTER II

### BACKGROUND AND LITERATURE

A literature survey was performed to know what has been accomplished and what is currently in progress in the field of combustion relevant to the topic of this project. Regarding venturi-cascading, because the concept was originally and recently implemented in the combustion laboratory at the University of Oklahoma, to the best of our knowledge there was no information except a preliminary study reported by Gollahalli and Wright (1996). That study provided only highlights of this technique.

Since this study is an attempt to control the combustion pollutants from gas jet diffusion flames by a cascade of venturis, it is instructive to go over the definition of diffusion flames, followed by the principle of operation of venturis in the cascade, and the formation mechanisms of the primary pollutants (CO, NO and soot) and their control technologies. This helps in gaining a better understanding of the problem of interest.

In addition, a general review of the spectroscopic techniques and their applications in combustion is presented. This is followed by a detailed review of Laser Induced Fluorescence (LIF), the technique of interest in the present study.

## 2.1 Diffusion Gas Flames

According to Kanury (1992), diffusion (non-premixed) flames are those in which the chemical reaction rate is very high compared to the rate of mixing and molecular diffusion. The fuel and oxidizer are originally unmixed. Sometimes, partially mixed flames may behave as diffusion flames if the mixture falls outside its flammability.

An ideal diffusion flame consists of an infinitesimally thin exothermic reaction zone which separates the fuel stream from the oxidant stream; that is, in ideal diffusion flames the fuel and oxidant are separated by an interface. They diffuse towards the reaction zone due to the composition gradients which are strongly governed by the flow and mixing dynamics.

Reynolds number is a parameter that distinguishes laminar and turbulent flames; the critical Reynolds number for a propane jet flame lies between 8800 and 11000 (Kanury, 1992), whereas Froude number characterizes whether the flame is momentum- or buoyancy-controlled, since it physically represents the ratio of the initial jet momentum flow to the buoyant force experienced by the flame (Turns, 1996).

## 2.2 Gas Jet Ejectors and Venturis

Gas jet ejectors have important applications in aerospace engineering. The application of thrust augmenting ejectors can be found in vertical and short takeoff / landing of aircrafts, where there is a need for a large source of powered lift. Another application of gas ejectors, is the mixer-ejector concept developed by Presz et al. (1988), which was effective in reducing the noise from aircraft engines.

A thrust augmenting ejector consists of one or more high momentum primary jets that are issued into the confines of an aerodynamic shroud (Fig. 2.1). As the jet evolves, it entrains some of the ambient fluid contained within the ejector, thereby inducing a secondary stream to flow in through the ejector inlet. As the secondary flow is accelerated around the leading edges of the ejector shroud, it lowers the surface pressure in these regions. The resulting leading edge suction creates aerodynamic forces that have a large component in the direction of the primary nozzle throat. These forces augment the force produced by the primary jet.

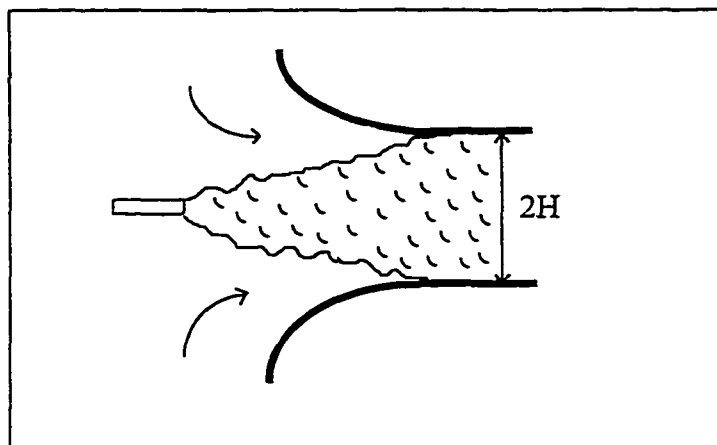


**Fig. 2.1: Thrust augmenting ejector**

The idea of using a cascade of venturis around the flame basically was deduced from the above mentioned application. The cascade of venturis was installed around the gas jet flame in such a way that each venturi acts as an ejector that accelerates the secondary air flow into the combustion zone.

As has been mentioned earlier, to the best of our knowledge, no literature was found regarding venturi-cascading around a flame except a preliminary study reported by Gollahalli and Wright (1996). On the other hand, a considerable amount of literature was found concerning the applications and performance of jet ejectors, some of which that pertains to this study are summarized in appendix 6.

### **2.3 Carbon Monoxide Formation and Oxidation**

Carbon monoxide is inevitably formed as an intermediate product of hydrocarbon oxidation. When a substantial concentration of CO is found in the exhaust gases of a combustion system, the cause usually is a localized fuel rich area. Excess CO levels can also be caused by inadequate burning rates in the primary combustion zones combined with quenching of post-flame products downstream of the flame (Gupta and Lilley, 1985).

Oxidation of CO is extremely important to the oxidation of hydrocarbons. Hydrocarbon combustion can simply be characterized as a two-step process: the first step involves the conversion of the fuel to carbon monoxide and radicals, with the second step being the final oxidation of carbon monoxide to carbon dioxide and formation of water.

It is well known that CO is slow to oxidize unless there are some hydrogen containing species ( $H_2O$ ,  $H_2$ ) present. This is because the CO oxidation step involving the hydroxyl radical is much faster than the steps involving  $O_2$  and O. Assuming water as the primary hydrogen containing species, the following four steps describe the oxidation of CO (Glassman, 1987):



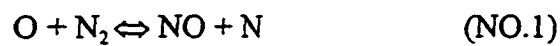
The reaction CO.1 is slow and doesn't contribute significantly to the formation of  $CO_2$ , but rather serves as an initiator for the chain sequence. The actual CO oxidation step (CO.3) is also a chain-propagating step, producing H atoms that will react with  $O_2$  to form OH and O (CO.4). The radicals, in turn, feed back into the oxidation step (CO.3) and the first chain-branching step (CO.2). Therefore, reaction CO.3 is the key reaction in the overall scheme.

## 2.4 Nitric Oxide Formation

Nitric oxide is an important minor species in combustion because of its contribution to air pollution; it is ultimately oxidized in the atmosphere to form

nitrogen dioxide which is the reason for the production of acid rain and photochemical smog. In the combustion of fuels that contain no nitrogen, nitric oxide is formed by three chemical mechanisms or routes that involve nitrogen from the air (Bowman, 1992): the **Thermal-Zeldovich mechanism**, the **Fenimore or Prompt mechanism**, and the **N<sub>2</sub>O-intermediate mechanism**.

**Thermal-Zeldovich mechanism** dominates in high temperature combustion over a fairly wide range of equivalence ratios and consists of the two chain reactions:

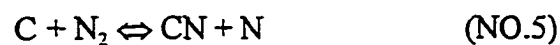


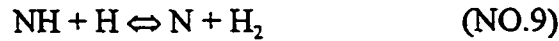
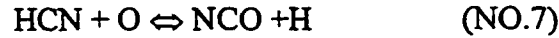
which can be extended by adding the reaction



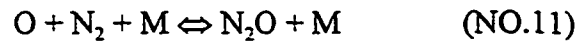
The activation energy for NO.1 is relatively large (319050 kJ/kmol) thus this reaction is very strongly temperature dependent. As a rule of thumb, the thermal mechanism is usually unimportant at temperatures below 1800 K (Turns, 1996).

**The Fenimore mechanism** is particularly important in fuel-rich combustion, sometimes accounting for greater than 50% of the total NO formation (Bowman, 1992). The general scheme of this mechanism is that hydrocarbon radicals react with molecular nitrogen to form amines or cyano compounds which are converted to intermediate compounds that form NO. The Fenimore mechanism can be written as (Turns, 1996):





**N<sub>2</sub>O-intermediate mechanism** is important in very lean low temperature combustion, it consists of the following three steps (Bowman, 1992):



## 2.5 Soot Formation and Destruction

The formation and destruction of soot are important features of diffusion hydrocarbon flames. The incandescent soot within the flame is the primary source of flame luminosity which contributes significantly to radiant heat losses from the flame. Although the chemistry and physics of soot formation is complex, many studies concerning soot formation in laminar flames were reported in the literature (Axelbaum et al., 1990; Glassman, 1988).

Turns (1996) has summarized that soot is usually formed over a range of temperatures between 1300 K to 1600 K via a four-step sequence:

1. Formation of precursor species: polycyclic aromatic hydrocarbons (PAH) are thought to be important intermediates between the original fuel

molecule and what can be considered as a primary soot particle. The exact mechanisms involved and the identity of these precursor are still a subject of research.

2. Particle inception: which involves the formation of small particles of a critical size (3000-10000 atomic mass units) from growth by chemical means and coagulation. It is in this step that large molecules are transferred to, or become identified as, particles.
3. Surface growth and particle agglomeration: this is experienced as the primary soot particles continue to be exposed to the bath of species from the pyrolyzing fuel as they travel through the flame.
4. Particle oxidation: this is the last stage in which the soot particles pass through an oxidizing region of the flame.

## **2.6 Spectroscopic Techniques**

Spectroscopic techniques are excellent tools for thermodynamic measurements. Typically, they do not require a direct contact with the tested medium and are therefore considered non-intrusive. This is a significant advantage over measurements that require physical probes, particularly when the environment at the point of measurement is of high temperature and undergoing chemical reaction like the flames.

Spectroscopic techniques can be classified into two groups (Laufer,1996): passive techniques, which depend on the spontaneous emission of the tested object, and active

techniques which require an excitation of the tested object to induce detectable emission. An example of the first group is analyzing the radiation emitted by an object which can lead to determination of its temperature without any physical contact. On the other hand, in active techniques the tested medium is excited by an external source. The thermodynamic properties are then determined from the analysis of the absorbed, scattered or emitted radiation. Techniques such as laser-induced fluorescence (LIF), planar laser-induced fluorescence (PLIF), Raman and Raleigh scattering are active techniques. These techniques are more selective than the passive ones. Moreover, the use of an external light source allows the stroboscopic excitation along with synchronized recording; this helps in avoiding interference of other competing phenomena such as background radiation.

Active spectroscopic techniques can be further divided into resonant and nonresonant techniques. In resonance techniques, the excitation source is tuned (in wavelength) to coincide with a selected transition of the tested medium. These include LIF, PLIF and resonantly-enhanced Raman techniques. On the other hand, in active nonresonant techniques such as Raman and Raleigh scattering, the excitation source does not match any transition of the tested species. However, resonant techniques (in general) yield a much stronger signal than do nonresonant techniques.

The use of active spectroscopic techniques for thermodynamic diagnostics requires bright, coherent and monochromatic light, which can be obtained only by lasers. Other desirable properties of the light source such as tunability, accurate control of excitation, and its timing require expensive and highly-developed lasers.

### 2.6.1 Laser-Induced Fluorescence (LIF)

Laser-Induced Fluorescence is one of the developing techniques. As its name implies, LIF requires an excitation of the tested species by a light source (typically a laser) that is resonant with a selected transition. It can be viewed as a derivative of the absorption spectroscopy. The objective of the LIF measurement is to determine the population density of selected quantum states from which some or all of the thermodynamic properties of the tested medium can be deduced. In LIF, a narrow-band laser is tuned to excite one or more transitions in the tested atom or molecule. Using a spectrally narrow bandwidth, individual rotational transitions that originate from certain vibrational and electronic levels can be selectively excited. In the absence of competing energy loss mechanisms, the population of the excited state, and hence the emitted fluorescence, are proportional to the population of the ground state.

Figure 2.2 describes the energy levels that participate in a typical LIF experiment. A narrow-band laser beam is tuned until its photon energy  $h\nu_{ge}$  matches the energy difference between the ground state  $g$  and the excited (upper) state  $e$ .

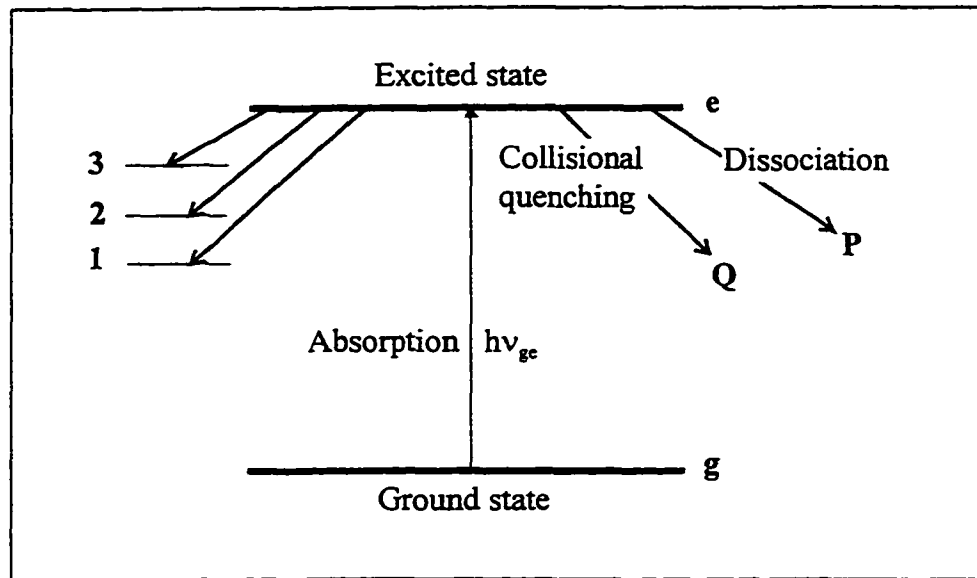


**Fig. 2.2: Possible modes of energy transfer from an excited state**

If single-photon transitions between these states are allowed, a part of the ground state population is excited. Once in the upper state, the excited species may relax spontaneously to any one of the lower states (1,2 or 3) while emitting a photon. Alternatively, it may give up its energy by dissociation (ionization), stimulated emission or collisional quenching. The latter includes collisions with other molecules and atoms.

To describe the exact response of an atom or molecule to the laser excitation, the set of rate equations for each quantum state needs to be examined. The rate equations describe the balance of sources and sinks for each quantum state. For an atom or molecule individual quantum state  $i$ , the rate of change of concentration of this state is given by the rate equation (Daily, 1997):

$$\frac{dN_i}{dt} = \sum_{j=i, W_{ji} \neq 0} (W_{ji} N_j - W_{ij} N_i) + \sum_{j>i} A_{ji} N_j - \sum_{j<i} A_{ij} N_i + \sum (Q_{ji} N_j - Q_{ij} N_i) \dots\dots\dots(2.1)$$

+ Chemical Source Terms – Chemical Sink Terms – Pr edissociation

Where:

$N_i$  : Population density of state  $i$

$W_{ij}$  : Einstein coefficient for absorption, if  $i < j$

Einstein coefficient for stimulated (induced) emission, if  $i > j$

$A_{ij}$  : Einstein coefficient for spontaneous emission from state  $i$  to  $j$ ,  $i > j$

$Q_{ij}$  : Quenching coefficient

The first two terms represent radiative excitation and de-excitation. The next terms account for spontaneous emission; these are followed by collisional excitation and de-excitation. The final terms are for chemical reaction and predissociation.

### 2.6.2 Spectroscopic Data for Flame Species

To perform an LIF measurement on a given molecule, several basic criteria should be satisfied:

1. The molecule must have a known emission spectrum.
2. The molecule must have an absorption wavelength which is accessible to a tunable laser source.
3. The rate of radiative decay of the excited state must be known; this is due to the fact that the fluorescence power is proportional to this rate.
4. If other molecules are present, which is the case in flames, it is necessary to correct the measured fluorescence power for quenching (the increase in the

excited state loss rate due to collisions involving the excited state and other molecules).

The necessary spectroscopic data to perform LIF for some of the diatomic flame species of interest have been obtained from literature and listed in Table 3.1.

**TABLE 2.1**  
**Spectroscopic Data for Species of Interest**

Species	Transition	Wavelength (nm)	Transition	Wavelength (nm)	Reference
OH	$A^2\Sigma^+ \leftarrow X^2\Pi$ $P_1(9), (0,0)$	286	$A^2\Sigma^+ \leftarrow X^2\Pi$ $(1,1)$	314	Smyth et al.(1990)
CH	$A^2\Delta \leftarrow X^2\Pi$ $R(7), (0,0)$	427.4	$A^2\Delta \leftarrow X^2\Pi$ $(0,0)$	431	Norton et al. (1991)
CN	$B^2\Sigma \leftarrow X^2\Sigma$ $R(34), (0,0)$	388.3	$B^2\Sigma \leftarrow X^2\Sigma$ $(1,1)$	385	Eckbreth (1996)

## 2.7 Control of Combustion-Generated Nitrogen Oxides

The nitrogen oxides NO and NO<sub>2</sub> are usually grouped together as NO<sub>x</sub>, of which, NO is the major contributor in most combustion devices. Several studies are found in literature to reduce NO<sub>x</sub> from combustion systems, and different control technologies to control NO<sub>x</sub> have been developed.

In fuels that contain no nitrogen such as hydrocarbons, the control techniques are based on reducing the temperature of the combustion gases; since NO (Thermal) formation rate is a strong function of temperature. Flue Gas Recirculation (FGR), water injection, and after burning are all techniques that are employed (Bowman,

1992; Gupta, 1985). However, in most of the cases, the reduction of NO results in an increase in CO due to the quenching of the oxidation reactions.

The most effective methods for reducing NO<sub>x</sub> emissions from stationary combustors, including steam boilers, gas turbines and diesel engines, are the selective catalytic and non-catalytic reduction techniques (SCR and SNCR); in which the maximum NO removal efficiency exceeds 90% (Bowman, 1992). These involve injection of a nitrogen-containing additive into the combustion products in order to convert NO to N<sub>2</sub>; the additives used are ammonia, urea or cyanuric acid. Temperature is a critical variable, and operation with a relatively narrow range of temperatures is required, thereby leading to difficulty in some applications.

Combustion modifications to manipulate the flow dynamics of the flame and to control the stoichiometry of the combustion zone were the focus of research in the last decade. The application of non-axisymmetric burner-exit geometries (Kamal and Gollahalli, 1993; Papanikolau and Wierzba, 1996; Papanikolau et al., 1997), introducing swirl into the combustion chamber (Tangirala et al., 1987; Chen and Driscoll, 1988) and staging of fuel-air mixing in premixed flames (Turns, 1996) have resulted in only a moderate NO<sub>x</sub> reduction compared to SCR, SNCR and FGR methods. However, their reliability, flexibility, safety, and cost make them more attractive and desirable.

## 2.8 Motivation and Scope of the Present Study

Motivated by the aforementioned statement, the general objective of the present project was to develop new strategies to control pollution characteristics of diffusion flames. A new technique, venturi-cascading of gas jet diffusion flames, to reduce pollutant emissions and possibly improve the combustion efficiency of gas burners, was the focus of this study.

The project was conducted in two phases. The first phase objectives of the present study were to test the feasibility of venturi-cascading, investigate the effects of venturi diameter, spacing configuration and Reynolds number on combustion characteristics and pollutant emissions of a propane jet flame, and to obtain the optimal performance conditions. At the optimal configuration, further studies were conducted to determine the flame thermal structure, composition, soot concentration, air-entrainment and radiation characteristics. Throughout the phase 1, only conventional measurements and techniques were applied.

The second phase objectives were to conduct further detailed studies in order to understand the thermo-chemical processes involved. In this phase, both laser diagnostics and computer simulations were employed. Laser induced fluorescence (LIF) was used to detect the key radicals present in the flame (OH, CH and CN). On the other hand, CFD-ACE+ software package was utilized to numerically model venturi-cascading and its influence on the combustion characteristics of gas jet diffusion flames. The results of the second phase were essential to interpret the observations and results of the first phase.

# **CHAPTER III**

## **EXPERIMENTAL METHODS**

This Chapter provides a brief description of the apparatus, instrumentation and methodology that were used in the present study. In general, all the experiments were performed in a laboratory-scale combustion chamber with various sampling, analyzing and measuring instruments shown in Figs. (3.1-3.7). The laser diagnostics experiments (LIF) are outlined in Fig. 3.8, and more details are given in appendix 5. All instruments, along with their models, manufacturers and technical specifications are provided in Tables 3.1a and 3.1b. The nominal operating conditions, laser system operating wavelengths and estimated uncertainties in the measurements (at 95% confidence interval) are given in Tables 3.2, 3.3 and 3.4, respectively.

### **3.1 Laboratory Combustion Chamber**

Experiments were conducted in a steel combustion chamber of 76 cm x 76 cm cross-section and 163 cm height. The chamber was provided with air-cooled Pyrex windows of dimensions of 20 cm x 20 cm x 145 cm on all four side-walls (Fig. 3.1). A circular opening covered with three layers of fine-mesh screens in the base plate allowed the insertion of a vertically mounted fuel burner. This opening also allowed uniform natural convection of air into the chamber. The top of the chamber was connected to the atmosphere through an exhaust duct. Commercial propane (95%  $C_3H_8$ , 3%  $C_4H_{10}$  and the rest  $C_3$ -hydrocarbons) was used as the fuel. The fuel burner

was a stainless-steel circular tube of 2 mm internal diameter. The tube was longer than 150 hydraulic diameters to ensure a fully developed flow at the exit. The ambient pressure of the laboratory was maintained slightly above the atmospheric pressure to insure a positive draft inside the combustion chamber.

The LIF experiments were conducted in the same combustion chamber described before. However, some modifications were made in the test rig to adapt with those diagnostic techniques. The burner was mounted on a two-dimensional traversing mechanism to obtain measurements at different axial locations in the flame without moving the excitation or detection systems. Besides, one of the rectangular glass windows was replaced with a slotted metal sheet for introducing the laser beam or sheet.

### **3.2 Venturis shape and material**

The venturis were made of aluminum-flashing stock and painted with a high-resistance high-temperature cement (Fig. 3.2) to produce a smooth finish. In the present study, four sets of venturis with different sizes were used; each set consisted of four identical venturis to form a cascade in which the venturis were arranged in various spacing configurations (Table 3.2) as shown in Fig. 3.3.

### **3.3 Instrumentation**

Intrusive and non-intrusive techniques were employed to diagnose the effect of venturi-cascading on gas jet diffusion flames. The baseline and cascaded flames were

examined using both conventional and specialized-sophisticated instruments. The former included; calibrated flowmeters, thermocouples, data acquisition system, radiometer, power meter and various emission analyzers. Those are summarized along with their model, manufacturer, and technical specifications in Table 3.1a. The other group of instruments encompasses sophisticated and state-of-the-art equipment such as; Nd-YAG pulsed laser, optical parametric oscillator (OPO), gated integrator/boxcar averager, photomultiplier tube, preamplifier and many other accessories. These, all together, were arranged to form the laser diagnostic system of the combustion laboratory, which was utilized in the LIF experiments. The laser diagnostic system equipment and specifications are listed in Table 3.1b. The following subsections describe the various experimental arrangements and methods.

### **3.3.1 Flame Photography**

Direct color photography with a 35 mm Kodacolor 100 ASA film (exposure time of 1 second) was used to record the appearance of the flame in the venturi-cascaded and baseline conditions.

### **3.3.2 Exhaust Emission Measurements**

For measuring exhaust emissions, a quartz flue gas collector was mounted over the visible flame and was axially aligned with the burner (Fig. 3.4). It was found that the variations in combustion product composition and temperature across the outlet of the flue collector were within the experimental uncertainty limits, and hence, the

data at the central point were considered as averaged values. Gas samples were withdrawn from the combustion products through an uncooled quartz probe of tip diameter 1mm and were treated to remove particulates and moisture with a series of filters and an ice-chilled moisture trap. The samples were analyzed for the concentrations of CO<sub>2</sub> and CO with nondispersive infrared (NDIR) analyzers (Rosemount analytical model 880A), for O<sub>2</sub> with a polarographic (Miniox-II) analyzer, and for NO with a chemiluminescence (Thermoenvironmental Inc. model 42H) analyzer. Flue gas temperatures were measured using a Chromel-Alumel (*Type K*) grounded-junction type thermocouple.

### **3.3.3 Flame Temperature Measurement**

For measuring thermal flame structure, a Platinum-Platinum 13% Rhodium (*Type R*) L-shaped thermocouple (bead diameter 280 μm) was used. The thermocouple was mounted on a computer- controlled, stepper-motor-driven two-dimensional traversing mechanism (Fig. 3.5). The measurements were sampled at a rate of 1kHz and averaged over 10 seconds using a high speed data acquisition system (Strawberry Tree Inc.) and a PC based data acquisition software (Quicklog).

### **3.3.4 Soot Concentration Measurements**

For measuring, volumetric soot concentration ( $w$ ), a non-intrusive method proposed by Yagi and Iino (1960) was used. The attenuation of a 0.95 mW He-Ne laser beam (Spectra Physics) was measured with a pyro-electric laser power meter

and a narrow-band pass laser filter (Fig. 3.6), from which the volumetric soot concentration was calculated.

### **3.3.5 Air Entrainment Measurements**

To measure the changes in air-entrainment due to the venturi-cascade, cold jet experiments were performed. For safety reasons, an equivalent amount of nitrogen, instead of propane, was sent through the burner at the same exit Reynolds number. An uncooled sampling probe with an internal diameter of 0.5 mm, mounted on a two-dimensional traversing mechanism was used to draw gas samples which were analyzed for O<sub>2</sub> concentration. The entire radial plane was traversed and the average air-entrainment was calculated as explained in section 4.9. Since it was not possible to directly observe the edges of the cold jet, the radial traversing was continued until the environmental concentration value of oxygen was detected.

### **3.3.6 Flame Radiation Measurements**

Flame radiation was measured with a highly sensitive radiometer (Pyroheliometer type Hy-Cal Model) of absorptivity 0.96 mounted on a tripod stand such that its view angle covered the whole length of the flame (Fig. 3.7). The output voltage of the radiometer was recorded using a digital multimeter (Micronta model 22-167) and converted into radiant intensity via a calibration chart. The results were also corrected for the background radiation from the chamber walls.

### **3.3.7 Laser Diagnostic System (LIF)**

Figure 3.8 illustrates the general layout of the LIF experiments. The LIF setup consists mainly of the laser excitation system in conjunction with the focusing and detection systems. The laser beam was focused into the flame and the fluorescence was detected via a photomultiplier tube (PMT).

#### **3.3.7.1 Laser Excitation Source and Frequency Tuning**

The light source that was used in LIF experiments was a solid state pulsed Nd:YAG (Neodymium-doped Yttrium Aluminum Garnet) laser (GCR 200, Quanta Ray, Spectra Physics Inc.), operating at a standard pulse repetition rate of 10 Hz. The Nd:YAG rod was optically pumped by a flash lamp whose output matches principal absorption bands in the red and near infrared. A pulse of laser at 1064 nm (fundamental wavelength) was emitted each time the flash lamp fires. The result was a train of pulses with long duration (~200ms) and low peak power, in what was called 'the long pulse mode', which allowed a safer alignment and set-up. However, an electro-optic Q-switch option was used to shorten the pulse to less than 10 ns and raise its peak power.

This short pulse with high power (Q-switch mode) was the key for the usefulness of the pulsed Nd:Yag laser. Its high peak power permitted wavelength conversion through several nonlinear processes (e.g. frequency doubling or mixing). Moreover, the short pulse provided excellent temporal resolution of fast phenomena such as rapid chemical reactions or high-speed motion.

An injection seeding system (Model 6350, Spectra Physics Inc.) was built inside the GCR Nd:YAG laser (see Fig. A5.1 for details). It was a single frequency Nd:YVO<sub>4</sub> laser source that produced a CW 1064 nm laser (same wavelength as the Nd-YAG) in order to seed the GCR host laser. This seeding process was necessary not only to reduce the Q-switch build-up but also to produce a single longitudinal mode with smooth temporal profile and narrow line width ( $\sim 0.003 \text{ cm}^{-1}$ ) of the output laser pulses.

The 1064 nm fundamental output from the GCR was converted to other wavelengths by the Harmonic Generator (HG) at the output of the GCR, which provided an efficient non-linear wavelength conversion of the 1064 nm using negative-uniaxial nonlinear crystals (KD\*P) to produce first, second and third harmonics of wavelengths 532 nm, 355 nm and 266nm respectively. The (KD\*P) crystals were very sensitive to any temperature changes, and hence a temperature controller was used to stabilize the temperature of the HG crystals to maintain a stable output.

To obtain a continuous tuning of the laser wavelength, a pulsed Optical Parametric Oscillator (MOPO-730, Quanta Ray, Spectra Physics) was pumped by the second harmonic (355 nm, 587 mJ/pulse) output of the GCR. It employed type I phase matched Beta Barium Borate (BBO) as the nonlinear gain medium. The BBO is a negative uniaxial crystal with intrinsic birefringence properties that were used to achieve critical phase matching. The MOPO-730 was a coupled dual oscillator system (see Fig. A5.2 for optical layout). In this scheme, a high energy Power Oscillator was injection seeded with a narrow linewidth output from a Master Oscillator. This

enabled the coupled oscillator system to produce narrow bandwidth, high energy, tunable coherent radiation. The acronym MOPO (Master Oscillator/ Power Oscillator) was derived from this design concept.

Tuning the MOPO output was obtained by rotating the BBO crystal with respect to the optical axis of the resonator (angle tuning). The BBO crystals for the Master and Power Oscillators were mounted on the opposite end of a rotary shaft. The output from the MOPO consisted of two waveforms; the signal and the idler, the tuning range of the signal was from 440 nm to 690 nm, while that of the idler was from 735 nm to 1800 nm. Generation of a tunable ultra-violet wave from 220 to 440 nm was achieved by frequency doubling of either the signal or the idler waves through the Frequency-Doubler Option (FDO) located at the output end of MOPO. Frequency tuning and power monitoring were accomplished with an automated microprocessor-based control electronic accessed from the front panel of the electronic controller. Figure A5.3 illustrates the available tuning ranges of the MOPO-FDO system.

### **3.3.7.2 Focusing and Collection Optics**

In LIF, the laser beam was turned 90° via a turning mirror, then focused into the test sample (flame) using a fused-silica best-form laser focusing lens. Measurements were performed for a single point defined by the intersection of the laser beam and the collection optics (see Fig. 3.8).

The fluorescence was collected at 90° by a dual lens collimator consisting of two fused silica plano convex lenses, the collected light or fluorescence then passed

through a filter to select the detection spectral window (based on the species of interest) and finally it reached the detector which was a photomultiplier tube (PMT).

### **3.3.7.3 Fluorescence Detection and Timing**

In LIF experiments, a photomultiplier tube with 0.25 mm aperture (End-on PMT, Model 77345, Oriel Corporation) was used to detect the fluorescence signal after passing through the filter (Fig. 3.8). The output signal from the PMT was amplified using a fast preamplifier (Model SR 445, Stanford Research Systems Inc.) before passing to the Gated Integrator/Boxcar Averager (Model SRS 250, Stanford Research Systems Inc.). The Gate Generator was triggered externally by the Q-switch synchronization from the GCR, which could provide an adjustable delay from few nanoseconds to 100 milliseconds. It integrated the input signal during the gate, and the output from the integrator was then normalized by the gate width to provide a voltage which was proportional to the average of the input signal during the sampling gate. This signal was further amplified according to the front panel sensitivity setting before being sampled by a low droop sample and hold amplifier, and outputting via a front panel BNC connector. The output voltage was acquired using a data acquisition software (WorkBench PC software, Strawberry Tree Inc.) in conjunction with a laboratory computer. During the experiment, a portion of the pump laser beam was deviated by a beam splitter to a power meter to monitor the pulse to pulse energy. This was used to normalize the measurements and consequently account for any pulse to pulse energy variation.

Owing to the short duration ( $\approx 10\text{ns}$ ) of laser pulse application to the flame, the LIF signal was present only briefly and synchronously with the laser pulse. Therefore, for the increased rejection of any background signal or noise, the detection was gated and synchronized electronically with the laser pulse; this was achieved using a Fast-Gated Boxcar Integrator (SRS 250, Stanford Research systems) triggered externally by the Q-switch synchronization from the GCR. In addition, a dual channel oscilloscope triggered by the Gate Integrator was used to position the gate accurately over the portion of the signal for which the laser was on. This ensured that the Gate Integrator was open only while the S/N ratio was favorable i.e. only during the 10 ns pulse.

**TABLE 3.1a****Conventional Instrument Specifications**

<b>EQUIPMENT</b>	<b>MODEL / MANUFACTURER</b>	<b>SPECIFICATIONS</b>
Chemiluminescence NO Analyzer	42H Thermo Environment Model	Range: 0-5000 ppm
NDIR CO <sub>2</sub> Analyzer	880A Rosemount Analyzer Model	Range: 0-30%
NDIR CO Analyzer	880A Rosemount Analyzer Model	Range: 0-2%
	Model 702D OFC Infrared Instruments	Range: 0-10 <sup>6</sup> ppm
Polarographic O <sub>2</sub> Analyzer	Miniox III Catalytic Research Model	Range: 0-22%
Thermocouple Type R Type C	Omega Engineering Inc.	Range: 350-1800 K
	Omega Engineering Inc.	Range: 500 -2340 K
He-Ne Laser	Model 155 Spectra Physics	Range: 0-95 mw
Pyroelectric Laser Power Meter	Coherent Model Field Master	Range: 0-30 mw
Radiometer	Pyroheliometer Hy-Cal	
35 mm Camera	Nikon 8088 / Miranda	
Rotameter	N044-40G Cole Parmer Co.	1115-23 121 ml/min (air)
	1/4-33-G-5 Amtek, inc.	2-80 cu.ft/hr (air)
Data-Acquisition Hardware	WorkMate™ Strawberry Tree Inc.	
Data Acquisition Software	Quicklog PC Strawberry Tree Inc.	
2 Computers	P5-200 P5-75 GATEWAY 2000	200 MHz, 32 MB RAM 75 MHz, 16 MB RAM

**TABLE 3.1b**

**Laser Diagnostic System Instrument Specifications**

<b>EQUIPMENT</b>	<b>MODEL / MANUFACTURER</b>	<b>SPECIFICATIONS</b>
Pulsed Nd: YAG Laser	GCR-250-10 Spectra Physics	Repetition Rate: 10Hz Wavelengths: 1064, 532, 355 <sup>1</sup> , 266 nm Line Width: <0.003 cm <sup>-1</sup> Pulse Width: 6-7 ns (for the 355 output)
Optical Parametric Oscillator (OPO)	MOPO-730 Spectra Physics	Tuning Range: 440-690 (Signal) 735-1800 (Idler) Line Width: <0.2 cm <sup>-1</sup> Pulse Width: 4-5 ns
Frequency Doubler Option <sup>2</sup>	FDO-970 Spectra Physics	Tuning Range: 220-440 (UV region)
Gated Integrator and Boxcar Averager	SR 250, SR 280 Stanford Research Systems	Gate Width: 2 ns-15 μs Delay: 1 ns-100ms Sensitivity: 1 V/V-1 V/5mV
Photomultiplier Tube and Housing	77345, 77265 Oriental Instruments	Wavelength Range: 185-650 nm Supply Voltage: 1000 V Photocathode Size: 25 mm Diameter
Photomultiplier Power Supply	70705 Oriental Instruments	Voltage Range: -200 to -2000 V Current Load: 2 mA
Fast Preamplifier	SR 445 Stanford Research Systems	Bandwidth: Dc to 300 MHz Maximum Gain: 125
Pulsed Laser High Power/Energy Meter (Display and Detector Head)	NOVA, 30 (150)A - HE-SH Ophir Optronics Ltd.	Thermopile High-Damage Threshold Absorber, Aperture: 18 mm Diam. Wavelength: 0.19-20 μm Power Range: 50 mW-150 W Energy Range: 100 mJ-200J Maximum Power Density: 20 KW/cm <sup>2</sup>
Digital Storage Oscilloscope	2210 Tektronix	Analog Bandwidth: DC to 50 MHz Digital Bandwidth: DC to 10 MHz
He-Ne Laser <sup>3</sup>	105-1 spectra Physics	Wavelength: 632.8 nm Power: 0.95 mW
CW Laser Power Meter	407A Spectra Physics	Wavelength Range: 250 nm-11 μm Power Range: <5 mW to 20 W Maximum Power Density: 20 KW/ cm <sup>2</sup>

<sup>1</sup> The current wavelength in use to Pump the MOPO

<sup>2</sup> Incorporated inside the MOPO to access the UV regime

<sup>3</sup> For alignment purposes

**TABLE 3.1b (continue)**

**Laser Diagnostic System Instrument Specifications**

<b>EQUIPMENT</b>	<b>MODEL / MANUFACTURER</b>	<b>SPECIFICATIONS</b>
2 Pentium Laboratory Computers for Data Acquisition	P5-200, P5-75 GATEWAY 2000	200 MHz, 75 MHz 32 MB RAM, 16 MB RAM
Quicklog /WorkBench PC Software	Strawberry Tree Inc.	For LIF Signal Acquisition, Control and processing
<b>In addition, the following accessories are incorporated in the system:</b> <ul style="list-style-type: none"><li>• Glass Cut-off and band-pass Filters</li><li>• Turning Mirrors</li><li>• Beam Splitters</li><li>• Plano-Convex Lenses</li><li>• He-Ne Mirrors</li><li>• Right-angle Prisms</li><li>• Polarizers</li><li>• beam Dumps</li><li>• Infrared Sensors</li><li>• Beam Apertures</li><li>• Iris diaphragm</li><li>• different Mountings and Holders for the aforementioned optics and accessories</li></ul>		

**TABLE 3.2**  
**Nominal Operating Conditions**

Fuel	Propane (95%+)
Jet diameter	2 mm
Jet exit Reynolds number	3600, 5100, 6500
Jet exit Froude number	3200, 6300, 10400
Flame type	rim attached, transition, fully-lifted
Venturi throat diameter	40, 55, 70, 85 mm
Venturi height	same
Venturi inlet diameter	80,110,140,170 mm
Spacing distribution* (x/d venturi location)	Equ. (0, 80, 160, 240) Incr. (0, 40, 120, 240) Dec. (0, 120, 200, 240)
Axial Locations	near-burner (x/d=20) mid-flame (x/d=100) far-burner (x/d=180)
Ambient Temperature	295 K
Ambient Pressure	100 kPa

\* Equ. Equal spacing  
Incr. Increasing spacing  
Dec. Decreasing spacing

**TABLE 3.3**  
**Laser Operating Wavelengths**

Species	Excitation (nm)	Detection (nm)
OH	286	314
CH	427.4	431
CN	388.3	385

**TABLE 3.4**  
**Estimated Uncertainties**

Measurements	% of Mean Value
Temperature	2.8
Concentration of CO <sub>2</sub>	7.1
Emission index of NO	8.4
Emission index of CO	9.2
Concentration of O <sub>2</sub>	4
Volumetric soot concentration	6.2
Radiant fraction	2.3
Air entrainment	3.2
OH	2.6
CH	1.5
CN	2.5

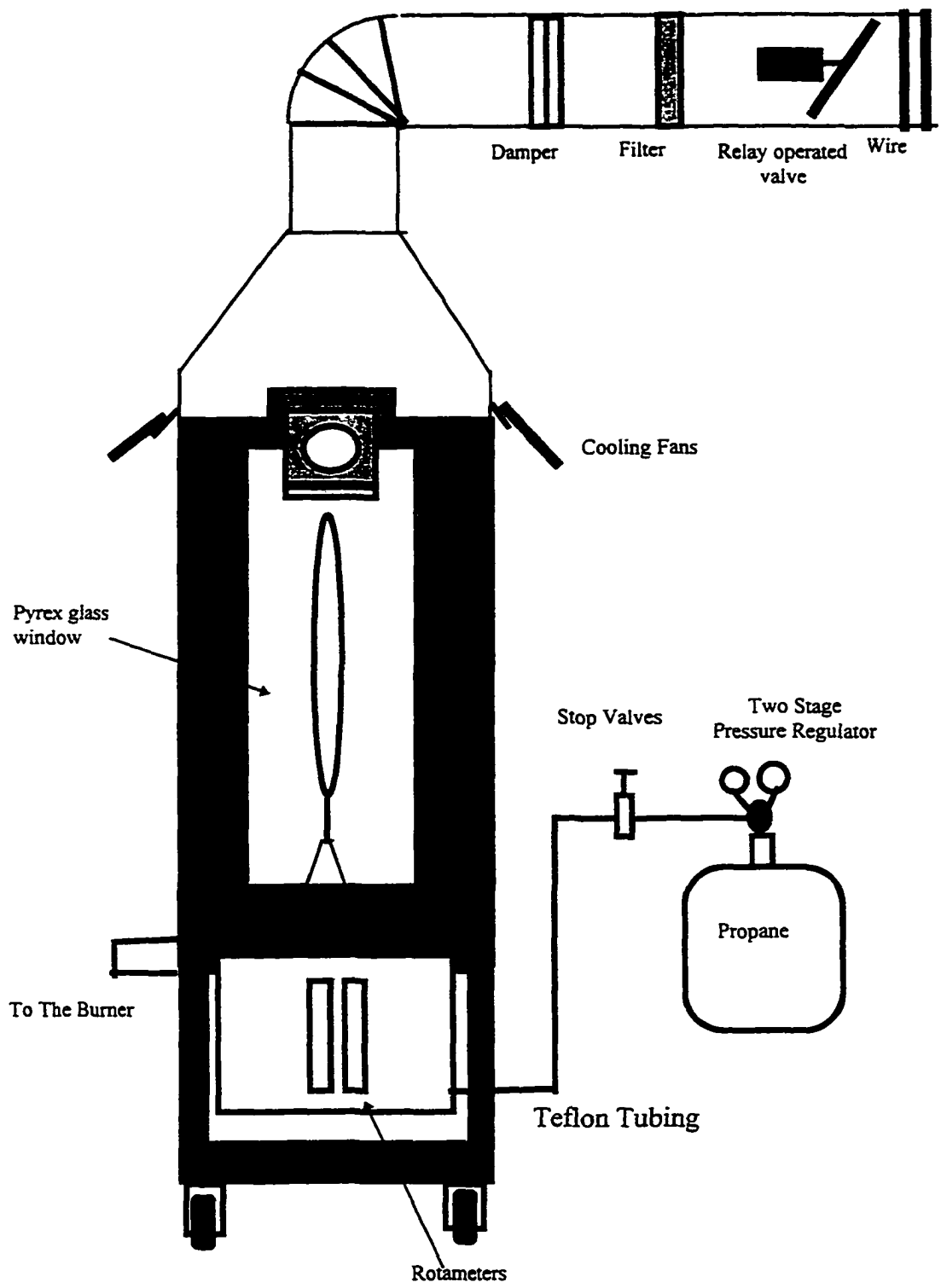


**Fig. 3.1: Combustion chamber and fuel supply train**

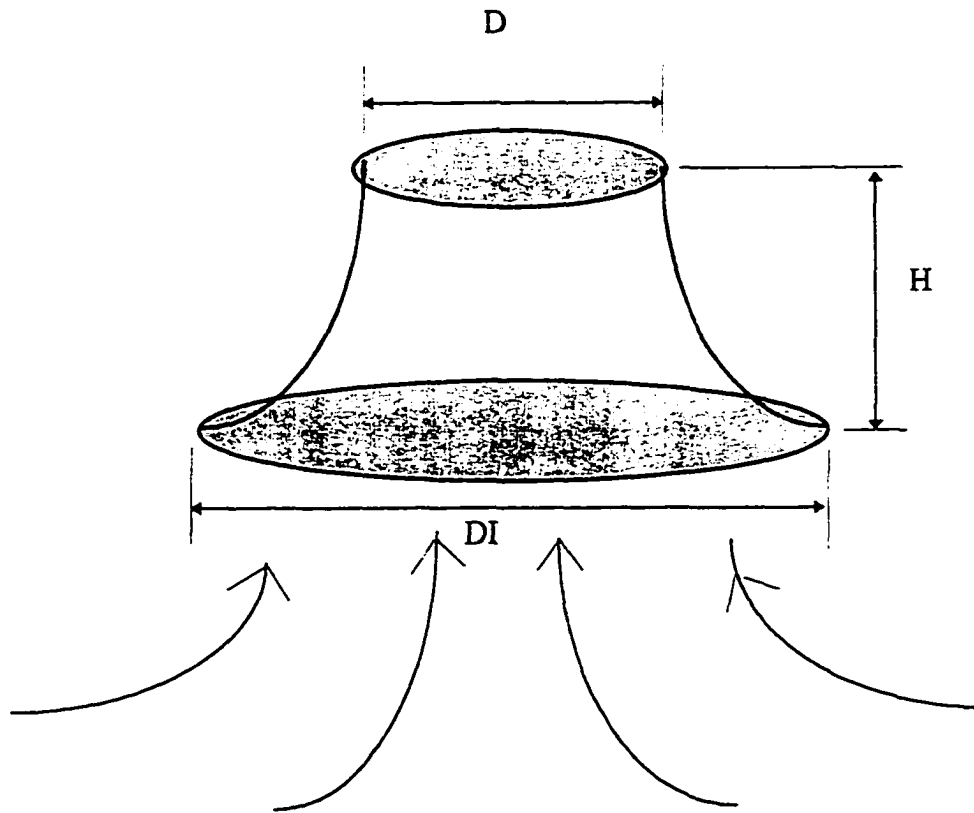


**Fig. 3.2: Venturi shape and dimensions**

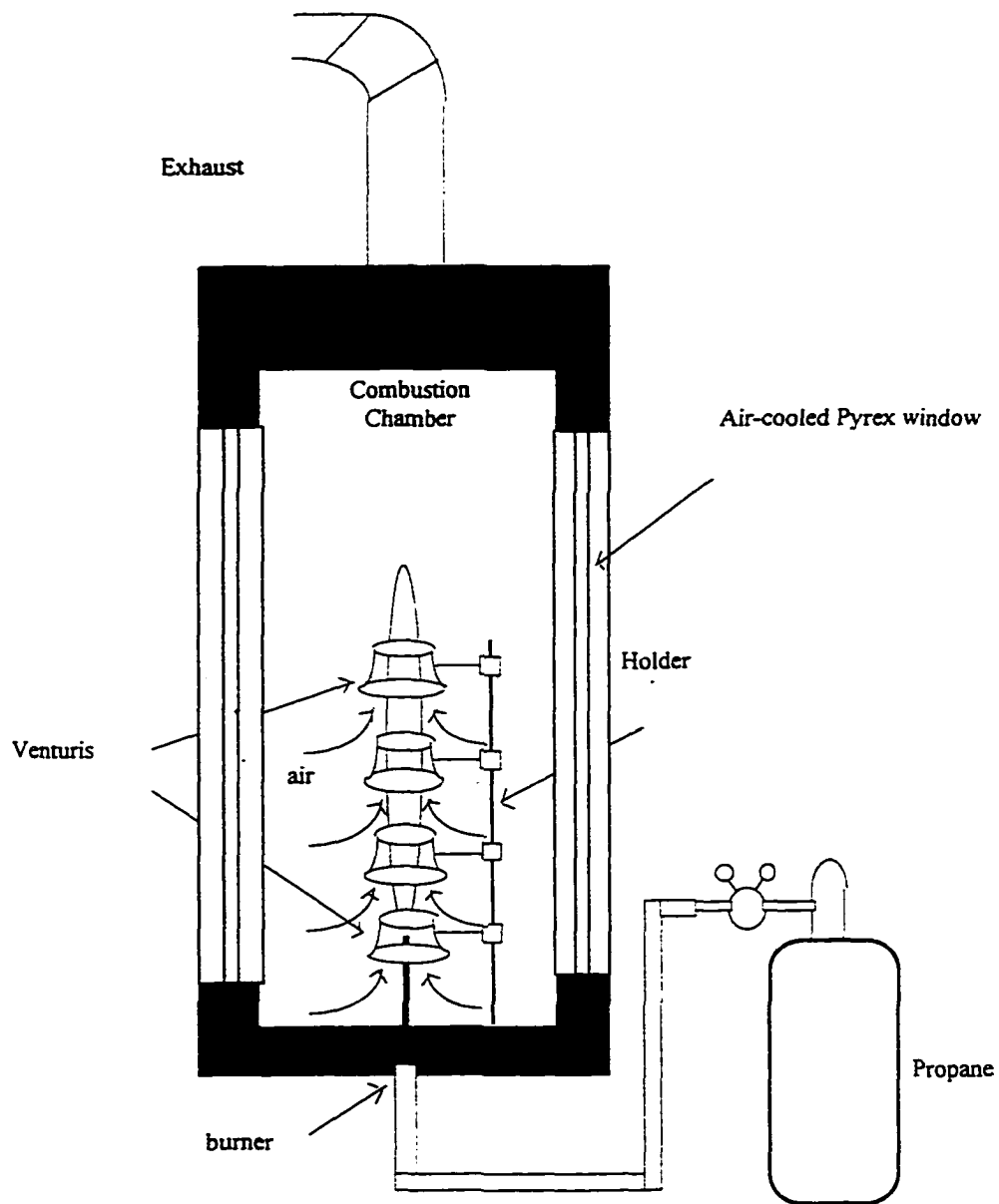


**Fig. 3.3: Venturi-cascading**

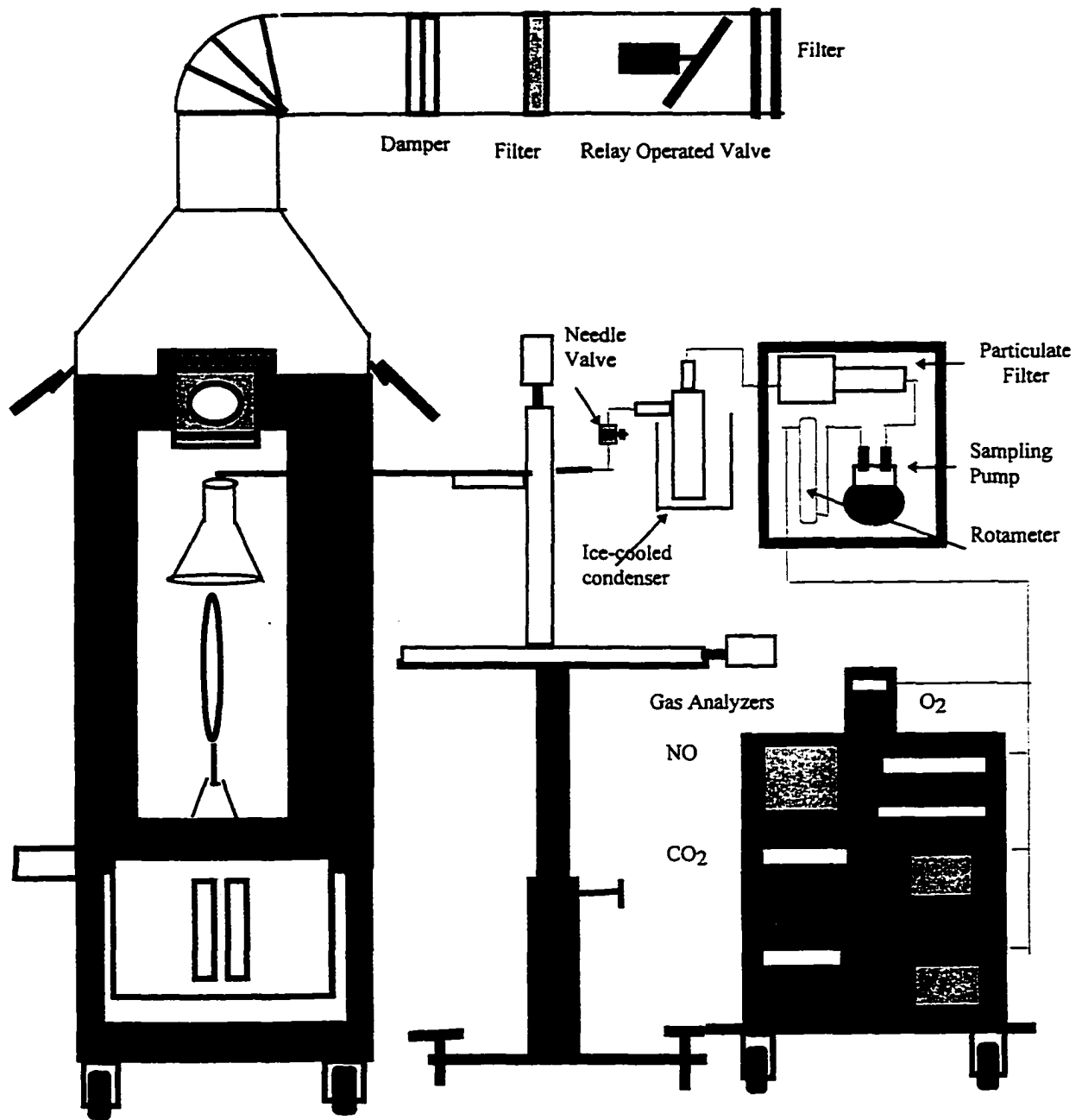


**Fig. 3.4: Instrumentation for emission index measurement**

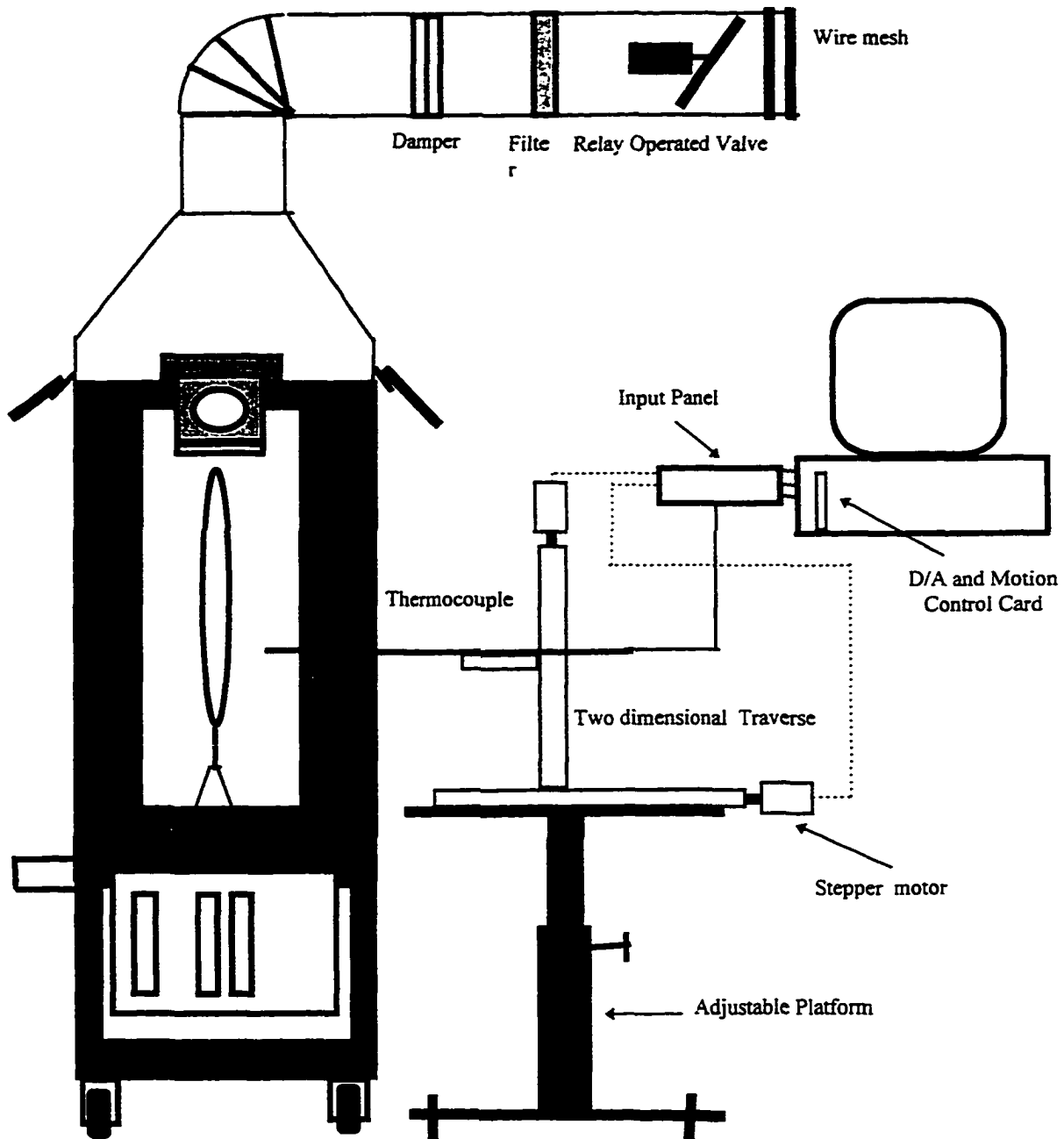


**Fig. 3.5: Instrumentation for temperature measurement**

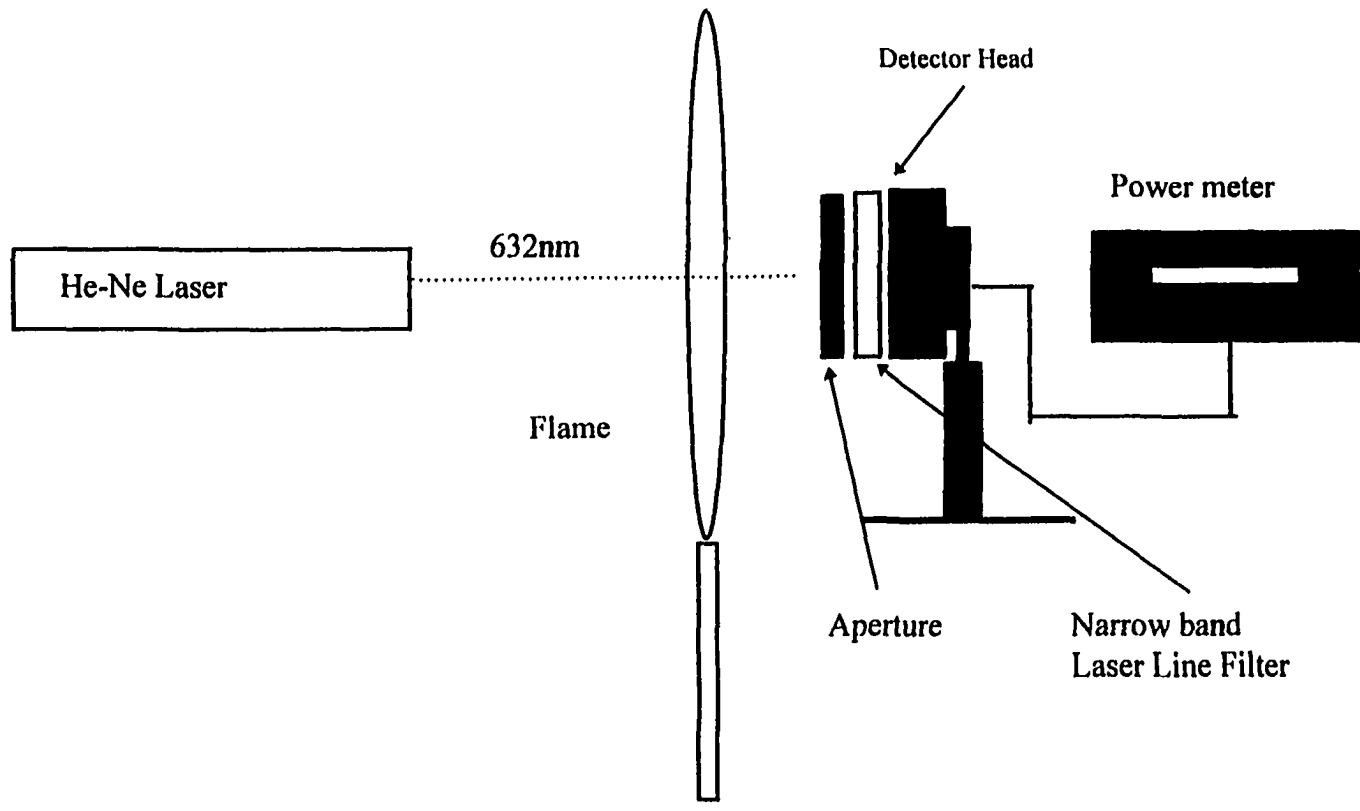


**Fig. 3.6: Instrumentation for soot concentration measurement**

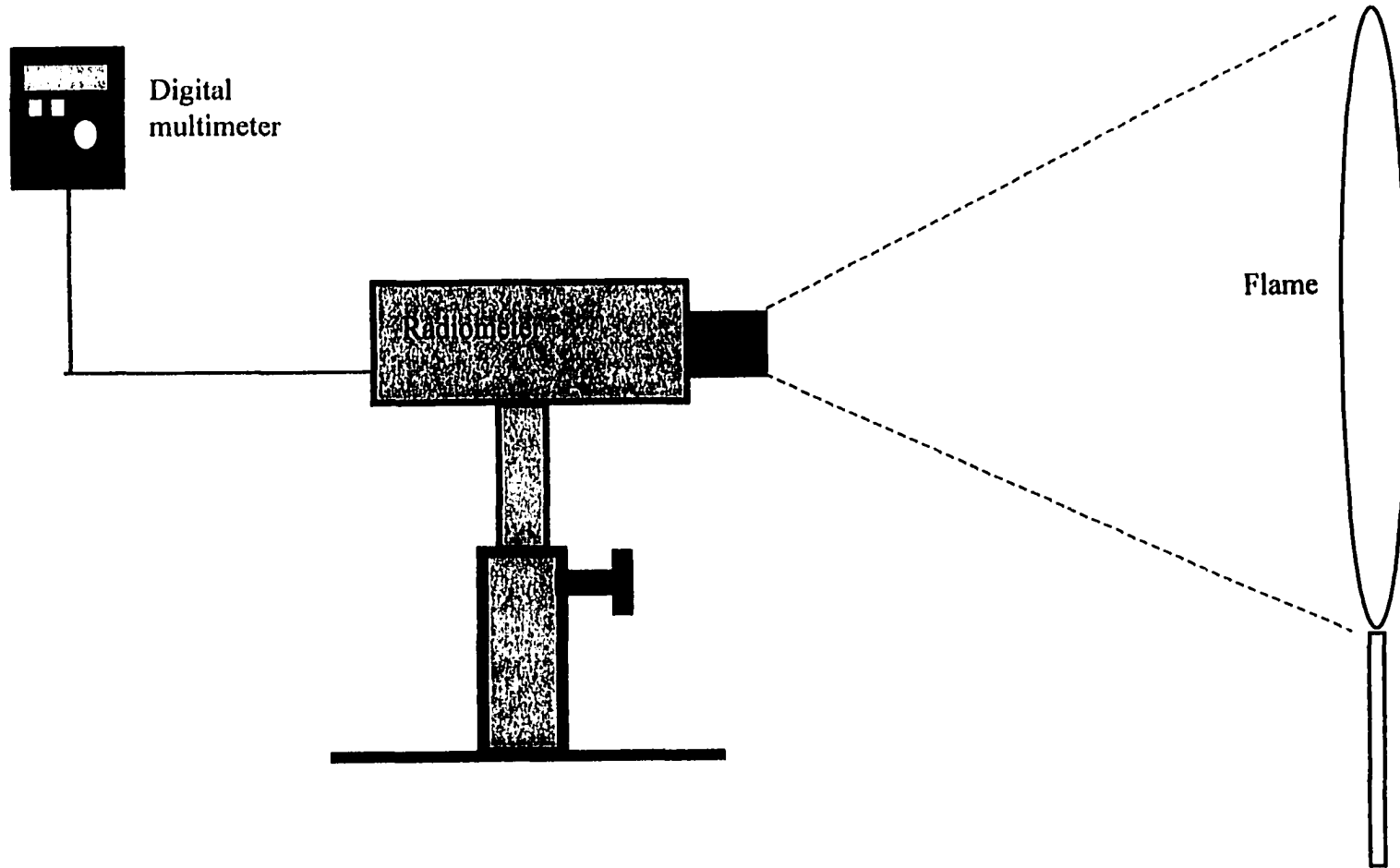


**Fig. 3.7: Instrumentation for flame radiation measurement**

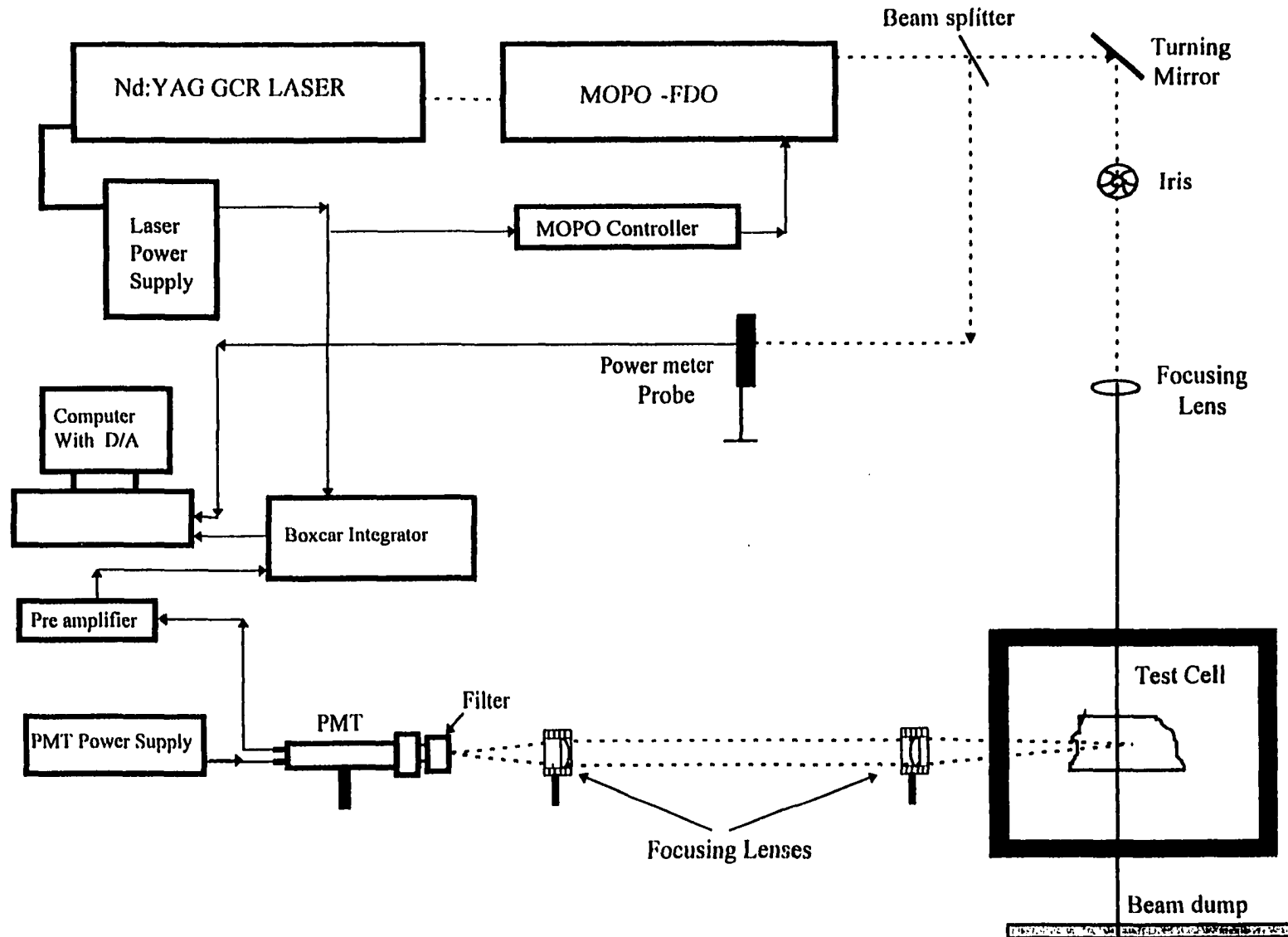
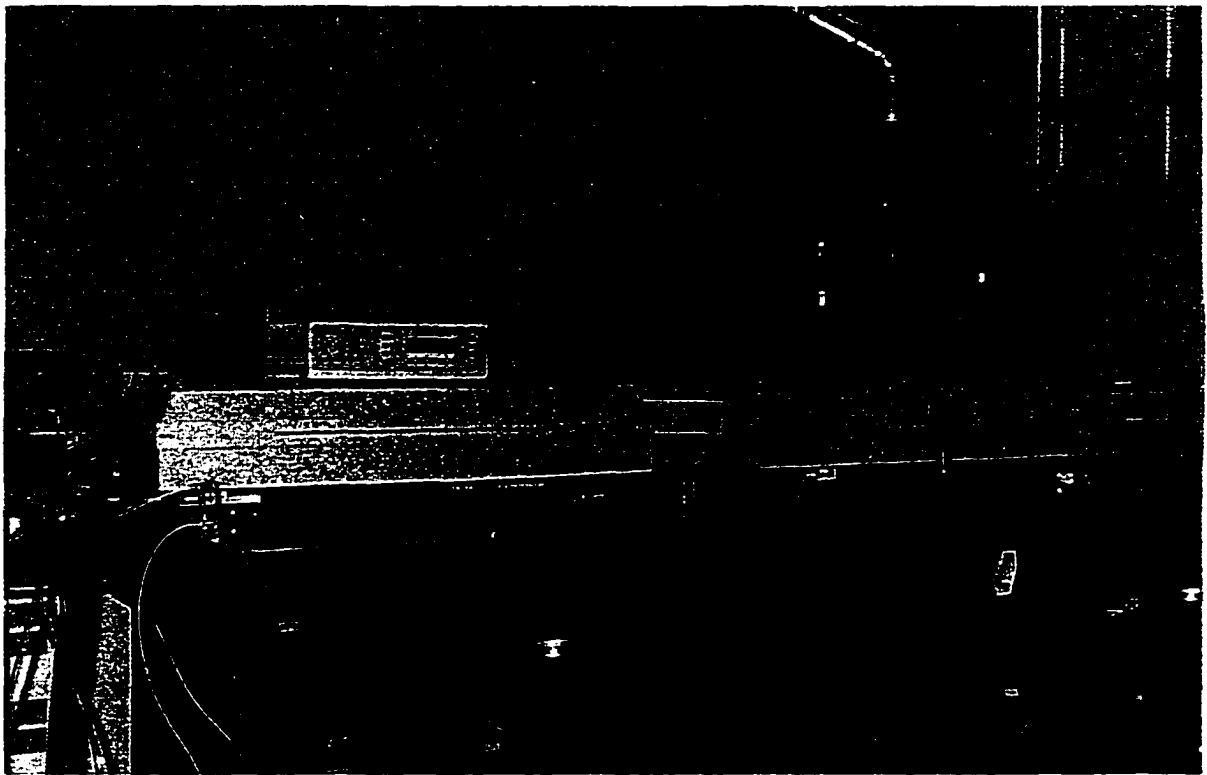


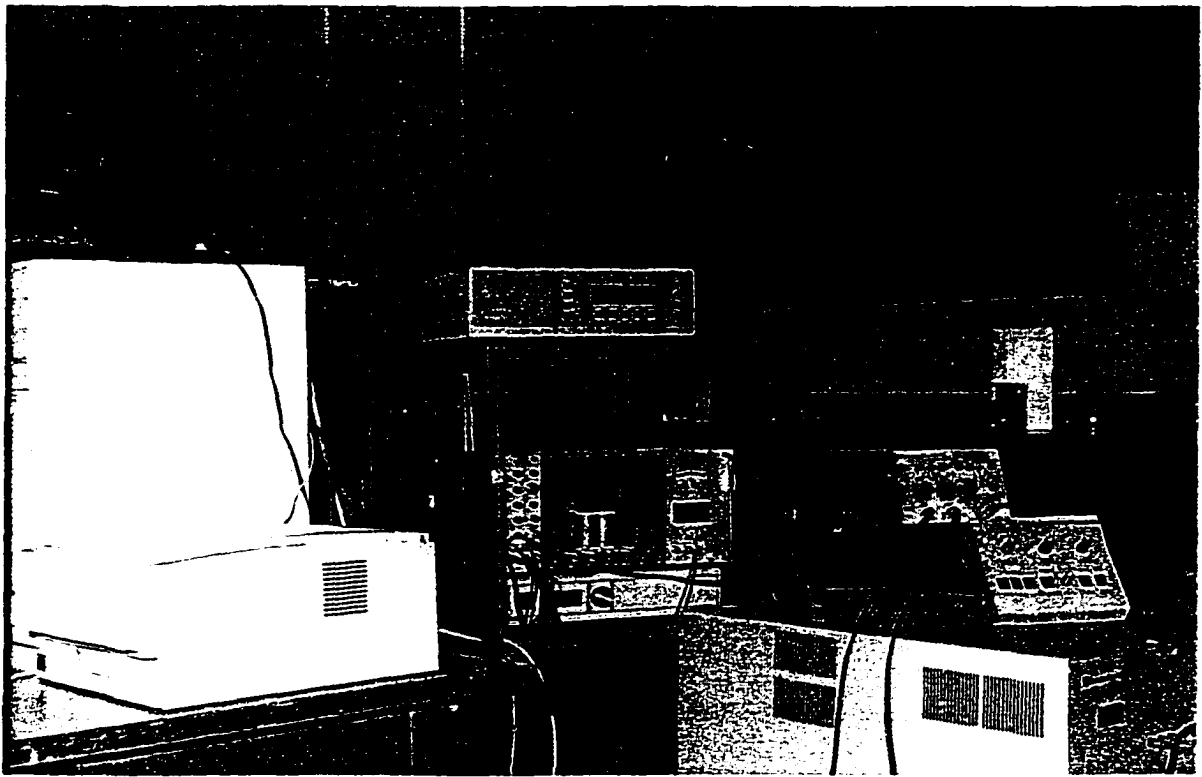
**Fig. 3.8: Schematic of LIF instrumentation**



**Photograph 3.1: The cascade in the combustion chamber and the analysis apparatus**



**Photograph 3.2: Side view of the laser diagnostic system  
(Nd-YAG and MOPO)**



**Photograph 3.3: Front view of the laser diagnostic system**



**Photograph 3.4: Top view of the laser diagnostic system**

## CHAPTER IV

### EXPERIMENTAL RESULTS AND DISCUSSIONS

In this chapter, the experimental results are presented and discussed. The results obtained were for both the cascaded and baseline cases at different operating conditions as given in Table 3.2. Feasibility and optimal conditions were established from the first few experiments based on exhaust measurements. At those optimal conditions, more experiments were conducted to investigate the effects of venturi-cascading on flame thermal structure, composition, volumetric soot concentration, air entrainment, and radiant fraction of heat release. The last part of the experimental study dealt with minor species measurements by laser induced fluorescence (LIF), which was performed to understand the details of thermo-chemical processes involved.

#### 4.1 Visible Flame Appearance

Flame photographs (exposure time of 1 second) on color print films with and without venturis are shown in Figs. 4.1 (a, b). Without venturis (baseline condition) at the near-burner region of the flame, the luminosity is weak, a characteristic of a soot-free region. However, at higher levels above the burner, considerable quantities of soot exist and the flame exhibits a yellow-orange appearance. With cascading, the following changes are generally observed compared to the baseline conditions:

(i) visible flame length increases; (ii) luminosity decreases; (iii) flow stabilizes so that the flame appears steadier.

The increase in the flame length can be attributed to the reduction in the net shear forces acting on the jet edges. This reduction occurs due to the reduced difference in velocities between the jet and the surroundings due to the co-flow air stream induced by the venturis, thereby leading to a higher axial velocity and the consequent increase in flame length. Since the flame was positioned in the center of the cascade, the induced co-flow stream tends to reduce azimuthal instabilities and to even out the shear forces on the flame periphery so that the flame appears steadier than in the baseline case. The decrease in luminosity is attributed to the less sooty flame obtained due to the higher entrainment of air, an effect of the venturis.

## 4.2 Exhaust Temperature

The exhaust temperature, measured at the end of the collector cone, for different venturi diameters, spacing configurations, and burner-exit Reynolds numbers (corresponding to attached, transitional, and fully-lifted flames) is shown in Fig. 4.2. On the same plot, the corresponding measurements for the baseline case (no venturi) are given and assigned the symbol ( $NV$ ).

The following can be observed from Fig. 4.2: (i) with venturis, regardless of their diameter, spacing and burner-exit Reynolds number, the combustion product temperature is higher than the baseline value; (ii) for given values of venturi diameter and spacing, the transitional and fully-lifted flames have higher temperatures than the

attached flame; (iii) for given values of spacing and burner-exit Reynolds number, the product temperature increases with increasing venturi diameter up to an optimal value, beyond which, the temperature levels off and even begins to decrease. That optimal diameter, however, varies between  $D/d=27.5$  and  $D/d=35$  depending upon the spacing configuration and Reynolds number used; (iv) The effect of spacing increases with increasing venturi diameter, but, with a large increase in diameter, it follows the law of diminishing returns; (v) The equal-spacing configuration shows the highest temperatures over most of the conditions used; (vi) the maximum percent increase in temperature from the baseline case was: 41% for the attached flame (at  $D/d=27.5$ ), 53% for the transition flame (at  $D/d=35$ ) and 49% for the fully-lifted flame (at  $D/d=35$ ).

The higher combustion exhaust product temperature obtained in the case of venturi-cascading may seem surprising because of the increased excess-air expected from venturis and the consequent decrease of the adiabatic flame temperature. However, the baseline propane ( $C_3H_8$ ) flame is highly luminous and sooty, and by the effect of venturis; the flame becomes less sooty. Hence, the increase in oxidation rate and the decrease in radiant heat losses overshadow the excess-air dilution effect; as a result, the combustion product temperature increases (Turns et al., 1993). Moreover, the venturis provide a radiation shielding around the flame, which also contributes to the temperature increase.

The increase in temperature with increasing burner-exit Reynolds number may be attributed to the higher energy input rate to the burner, and higher oxidation rates due

to the formation of some amount of premixed reaction zone in the lifted region of the flame.

The initial increase in temperature, accompanying the increase in venturi throat diameter, can be accounted for by the higher entrainment of air into the flame zone and the corresponding increase in the oxidation rates. However, this increase levels off for large venturi diameters. The most likely reason is that at large venturi diameters, the clearance between the burning jet and the venturi becomes so large that it reduces the static pressure drop through the venturi and the consequent air infusion into the flame; and hence, the effect of venturi diminishes.

The effect of venturi spacing configuration is closely related to the effect of venturi diameter. When the effect of venturi diameter is dominant, the effect of spacing becomes significant; however, once the diameter effect diminishes (at large diameters), any influence of spacing configuration vanishes (within the measurement uncertainty limits). The concept underlying the spacing variation is to introduce more oxidizer into certain regions of the burning jet than into other regions. The results demonstrate that equal space distribution, and hence air infusion, over the flame length results in the highest product temperature.

### **4.3 Exhaust Carbon Dioxide Concentration**

The CO<sub>2</sub> molar concentration in the exhaust was measured, for the same conditions at which the exhaust temperature was measured, and these results are shown in Fig. 4.3. Since CO<sub>2</sub> is a major final product of combustion, the trends in its

concentration variation are similar to those that have been observed for temperature, except for  $D/d=20$ . For that diameter, although temperature increases significantly,  $\text{CO}_2$  increases at a lower rate or even decreases. This may be explained by the fact that a small venturi diameter blocks the air inflow into the burning jet, and consequently nullifies the benefits of cascading. However, the combustion product temperature still increases due to other effects (example: radiation shielding by venturis).

The maximum increase in  $\text{CO}_2$  molar concentration is observed for the flame in transition from attached to fully-lifted configuration at  $D/d=35$ . Considering  $\text{CO}_2$  concentration as a measure of combustion efficiency, the largest effect of venturis is observed for the flame in the transition from attached to lifted configuration, while the least influence is noticed for the fully-lifted flame. The latter observation may be attributed to the higher turbulence level present in the fully-lifted flame, and consequently the air inflow and mixing rates are already so high that the effect of venturi-cascade is masked.

#### **4.4 Exhaust Oxygen Concentration**

The effects of venturi diameter, spacing distribution, and burner-exit Reynolds number on  $\text{O}_2$  molar concentration in the combustion exhaust products are presented in Fig. 4.4. These results are in good agreement with the aforesaid discussions. With venturis, a significant decrease in  $\text{O}_2$  molar concentration is observed in the exhaust products. It is another indication of the superior combustion efficiency that the

cascaded flame produces over the baseline case. The effects of venturi diameter and spacing configuration on O<sub>2</sub> molar concentration are the inverse of those observed earlier for temperature and CO<sub>2</sub>

#### 4.5 Emission Indices

The Emission Index (EI) of species, defined as the mass of the species emitted per unit mass of the fuel burned, was calculated following Gollahalli (1994) and Turns (1996):

$$EI_i = \left( \frac{X_i}{X_{CO} + X_{CO_2}} \right) \left( \frac{n M_i}{M_F} \right) \dots\dots\dots (4.1)$$

where n is the number of carbon atoms in a mole of fuel; X<sub>i</sub> is the measured mole fraction of the species 'i', X<sub>CO<sub>2</sub></sub> is the measured mole fraction of CO<sub>2</sub>, X<sub>CO</sub> is the measured mole fraction of CO, M<sub>i</sub> is the molecular weight of the species 'i' and M<sub>f</sub> is the molecular weight of the fuel. This equation was further simplified by assuming complete combustion of the fuel, i.e. X<sub>CO</sub>=0, which is reasonable for the purpose of the present study. The emission index is particularly useful because it unambiguously expresses the amount of pollutant formed per unit mass of the fuel input, independent of any dilution of the product stream or efficiency of the combustion process.

Figures 4.5 and 4.6 show the CO and NO emission indices for different venturi diameters, spacing configurations and burner-exit Reynolds numbers. From these the following observations can be made: (i) except for the venturi with D/d=20, the cascade of venturis decreases both CO and NO emission indices markedly; (ii) for large venturis, the CO and NO emission indices level off and even begin to increase;

(iii) among the three flame configurations used, the attached flame has the highest CO EI, but the lowest NO EI. However, the opposite trend is observed for the fully-lifted flame; (iv) The maximum percent decrease in CO EI, from the baseline case, is 75%, 87% and 83% for the attached, transition and fully-lifted flames respectively, while the corresponding NO EI decrease is 27%, 33% and 22%; (v) the optimal (minimum) CO EI value is observed for the venturi with  $D/d=35$ . However, the optimal NO EI value is noticed for  $D/d$  between 27.5 and 35; (vi) The equal spacing arrangement shows the lowest CO EI except for venturi diameter  $D/d=20$ . However, for the optimal CO EI venturi diameter ( $D/d=35$ ), the influence of spacing distribution is negligible (within uncertainty limits); (vii) the effect of spacing configuration on NO EI is stronger than that on CO EI. However, for the optimal NO EI venturi diameters, the influence of spacing distribution is a function of venturi diameter and burner-exit Reynolds number.

The decrease in CO EI by the effect of venturi-cascading can be attributed to the following reasons: (i) The higher entrainment of air which results in better oxidation of pyrolysis fragments of fuel and precursors of soot; (ii) Since the fuel-rich zones are the main source of CO, the effect of venturis in increasing the rates of mixing with air makes the fuel-lean zones more dominant over the rich-ones; (iii) The decrease in radiation losses due to shielding by venturis leads to a decrease of quenching and consequent higher rates of oxidation of CO.

The decrease in NO EI observed in the venturi-cascaded flame does not follow the trends of temperature; this can be due to the mutually compensating effects of higher temperatures on the one hand and higher oxidation rates of hydrocarbon pyrolysis

fragments and radicals on the other (see sections 4.15-4.17). Furthermore, since the flame temperature is less than or equal to 1800 K (as shown in the flame thermal structure measurements), the prompt-NO (*Fenimore mechanism*) becomes more dominant than the thermal-NO (*Zeldovich mechanism*) (Turns, 1996). Hence, the additional infusion of air, by the effect of venturis, enhances the oxidation rates of CN and CH type radicals (the key radicals in the Fenimore chain reaction) (see sections 4.16 and 4.17) and consequently compensates for the increase in thermal-NO.

The reasons for the decrease in CO and NO emission indices with the increase in venturi diameter, except for  $D/d=20$ , and their leveling off observed for large venturis, were similar to those explained in the CO<sub>2</sub> and temperature discussions in sections 4.2 and 4.3. The highest decrease in CO and NO emission indices is noticed for the flame in transition from attached to lifted condition as pointed out earlier.

## 4.6 Optimal Conditions

Up to this point, all the measurements and results that have been discussed pertain to the combustion exhaust products, which represent the net effect and the overall picture of the combustion process. These results lead to the following optimal conditions for propane flames with the 2 mm burner.

<i>Venturi diameter</i>	<i>D/d=35</i>
<i>Spacing configuration</i>	<i>Equal interval</i>
<i>Flame condition</i>	<i>Transition from attached to lifted</i>

Once these conditions were identified, further experiments were performed to understand the flame thermal and composition structure characteristics.

#### **4.7 Flame Temperature Profiles (Thermal Structure)**

Figure 4.7 shows the radial temperature profiles, measured at three axial locations (near-burner, mid-flame and far-burner) for the partially lifted (transition) flame with and without venturi cascades. In both cases, the near-burner profile has sharp off-axis peaks. The mid-flame and far-burner profiles are flatter, but the off-axis peaks are still recognizable.

The peak temperatures, for the baseline case, in the near-burner, mid-flame and far-burner regions are 1766 K, 1511 K and 1384 K, respectively. However, the corresponding values in the venturi-cascaded flame are 1692 K, 1630 K and 1475 K.

A comparison of these temperature profiles reveals that, compared to the baseline (no venturi) case, the venturi-cascaded flame has lower temperatures in the near-burner region, but, it has higher temperatures in both mid-flame and far-burner regions. This observation may be explained as follows: in the near burner region, stoichiometric homogenous gas phase reactions are usually dominant; the infusion of additional air into the venturi-cascaded flame can lead to leaning and consequently lower temperatures. On the other hand, in the mid-flame and far-burner regions, the kinetics-controlled heterogeneous soot oxidation is the primary mechanism of combustion (Gollahalli et al., 1980). These relatively slow kinetics-controlled processes are enhanced in the venturi-cascaded flame by the larger availability of

oxygen, provided by the effect of venturis, thereby leading to higher rates of burning of soot. Therefore, the higher heat release rates and lower heat losses due to lower concentration of soot formed upstream and radiation shielding by venturis results in higher temperatures in the mid-flame and far-burner regions compared to the baseline case. In other words, the dilution effect of larger amount of air entrained into the venturi-cascaded flame is overshadowed by the enhancement of soot combustion in the mid-flame and far-burner regions.

Furthermore, and specially in the far-burner region, the venturi-cascaded flame shows a flatter temperature profile. It is a strong indication of better mixing due to the venturis which help entraining more air to the unburned reactants in the flame core.

#### **4.8 Carbon Dioxide Concentration Profiles**

Figures 4.8 (a, b, c) present the radial concentration profiles of CO<sub>2</sub> for the baseline and cascaded flames in the near-burner, mid-flame and far-burner axial locations, respectively, the same conditions pertaining to the earlier temperature profiles. CO<sub>2</sub> profiles follow the trends of the earlier temperature profiles. The off-axis peaks are prominent in the near-burner region. However, the profiles get flatter in the downstream regions. The average CO<sub>2</sub> concentration in the cascaded flame drops by 7% from its baseline value. On the other hand, it increases by 16% and 13% in the mid-flame and far-burner regions, respectively. The corresponding changes in temperature are; 5% decrease in the near-burner location, 13% and 12% increase in

the mid-flame and far-burner locations. Therefore, the influence of cascading on  $\text{CO}_2$  is almost similar to that on temperature, and consequently the same explanations hold. This is quite expected, since  $\text{CO}_2$  is a major combustion product which strongly depends on temperature.

#### 4.9 Oxygen Concentration Profiles

Figures 4.9 (a, b, c) show the radial molar concentration profiles of  $\text{O}_2$  for the baseline and cascaded flames in the near-burner, mid-flame and far-burner locations, respectively. In the near-burner region,  $\text{O}_2$  is zero at the central axis and increases gradually in the outward direction. The cascaded flame has higher  $\text{O}_2$  concentrations and rate of increase in the radial direction, compared to the baseline case. It is an indication of more air infusion into the jet (Ho and Gutmark, 1987).

In the mid-flame and far-burner regions, some  $\text{O}_2$  exists at the central axis of the flame, i.e.,  $\text{O}_2$  starts penetrating into the flame core as a result of greater mixing in the downstream regions. This argument is further augmented by the presence of some  $\text{CO}_2$  and  $\text{CO}$  in the flame core (central axis), as can be seen from their concentration profiles (Figs. 4.8 and 4.10).

In the near burner region,  $\text{O}_2$  molar concentration in the cascaded flame is higher by an average of 10 % from its baseline value. However, opposite results are observed in the mid-flame and far-burner regions;  $\text{O}_2$  concentration decreases by an average of 8 % and 10 %, respectively, with the presence of the cascade. The effect of cascading

on  $O_2$  is opposite to that observed earlier on  $CO_2$ , as expected by the mass conservation in chemical reactions.

In general, a higher  $O_2$  concentration is a result of an excess air in the combustion process. Therefore, the greater quantities of  $O_2$  observed with the presence of the cascade, in the near-burner region, should be the outcome of higher mixing rates with air (as supported by the numerical analysis in chapter 5) and the consequent leaning process provided by the effect of venturis. However, this dilution effect is overshadowed in the mid-flame and far-burner regions as has been explained earlier.

#### **4.10 Carbon Monoxide Concentration Profiles**

Figures 4.10 (a, b, c) show the radial concentration profiles of carbon monoxide for the baseline and cascaded flames in near-burner, mid-flame and far-burner regions, respectively. The off-axis hump structure is obvious in the near-burner region, however, the profiles become flatter in the downstream regions. Peak CO values occur close to  $r/d$  of 2, 3 and 4 in the near-burner, mid-flame and far-burner locations, respectively. These peaks do not coincide with the temperature peaks observed earlier. On the other hand, CO peaks are located inward of temperature peaks; closer to the flame core. This is reasonable, since CO usually forms in the fuel-rich side of the flame as an intermediate product of combustion due to the fuel pyrolysis.

The peak CO concentration in the cascade flame drops by 8 %, 12 % and 15 % in the near-burner, mid-flame and far-burner locations, respectively, from its baseline

values. The corresponding drop in arithmetic average of CO concentration is 5%, 11% and 10%. The decrease of CO in the cascaded flame can be attributed to the a larger dilution of the fuel-rich zones, higher oxidation rates and lower quenching rates by the effect of cascading.

#### 4.11 Nitric Oxide Concentration Profiles

Figures 4.11 (a, b, c) provide the radial concentration profiles of NO for the baseline and cascaded flames in the near-burner, mid-flame and far-burner regions, respectively. The hump structure with off-axis peak is noticeable in the near-burner region. However, the profiles become flatter in the downstream regions. Peak NO concentrations occur at  $r/d$  of 2.5, 3 and 4 in the near-burner, mid-flame and far-burner axial locations, respectively, for both baseline and cascaded flames. Those peaks, particularly in the mid-flame and far-burner regions, are located inward of the earlier peak temperatures; i.e., in the fuel-rich side of the flame.

The NO concentration in the cascaded flame decreases by 16 %, 5% and 3 % in the average value (13 %, 8 %, and 7% in the peak value), in the near-burner, mid-flame and far-burner regions, respectively, from its baseline values. The corresponding changes in the average value of temperature are; 5% decrease in the near-burner location, 13% and 12% increase in the mid-flame and far-burner locations. In other words, the NO reduction in the downstream regions does not keep pace with the temperature trends. The same result was brought about earlier along with the emission index measurements in section 4.6, and some initial speculations

and interpretations have been made there. These will be explained clearly through the results of both the LIF measurements of minor species, later in the current chapter, and the numerical model of NO-production in chapter 5.

#### **4.12 Volumetric Soot Concentration Profiles (w)**

The axial profiles of volumetric soot concentrations (w) in the venturi-cascaded and baseline cases for three values of burner-exit Reynolds number (Table 3.2) are presented in Figs. 4.12 (a, b, c). The general trend of these profiles shows that soot concentration is almost zero in the near-burner region where the formation of polycyclic aromatic hydrocarbons (PAH) and soot nucleation begins; then it readily builds up and attains a peak value somewhere in the mid-flame or early far-burner region as a result of particle inception and growth in the pyrolyzing fuel regions; and finally soot concentration falls in the far-burner region where it starts oxidizing.

In these profiles, the venturi-cascaded flame shows a decrease in peak soot concentration of 18.5%, 20.5% and 19% from the baseline values for the attached, transition, and fully-lifted flames, respectively. However, the corresponding decrease in the average soot concentration is 17%, 24% and 21% for the same cases.

The lower soot concentrations observed in the venturi-cascaded flame is in conformity with the expected influence of venturis in entraining more air into the burning jet. This has two effects: (i) it dilutes the fuel rich pyrolysis zones of the flame and consequently increases the time for soot particle inception to occur, thereby, leading to less residence time for soot growth (Axelbaum and Law, 1990);

(ii) higher entrainment of air prompts higher oxidation rates in mid-flame and far-burner regions. However, the axial profiles reveal a remarkable decrease of soot concentration in the mid-flame and far-burner regions; this points out clearly, the domination of the second effect.

For higher values of burner-exit Reynolds number, in the baseline (no venturi) case, higher soot concentrations are observed and the burn out rate of soot in far-burner region decreases; this may be due to the fact that air entrainment does not keep pace with the increase of fuel rate. Further, the reduced residence time at higher Reynolds numbers does not provide enough time for soot to be completely oxidized before being passed into the exhaust gas. Therefore, the effect of venturis becomes more crucial in this case, since it not only provides more air to keep pace with higher fuel flow rate (carbon input), but also elongates the flame and consequently allows more time for soot to get oxidized.

As a precaution, in this study, equal fuel input rates were maintained to the venturi-cascaded and non-cascaded flames, ensuring that the changes can be attributed only to the venturis effect.

#### **4.13 Air Entrainment**

To investigate the effects of venturi-cascading on the spread rate of the jet and the fuel-air mixing capabilities, air entrainment into the jet was measured. For safety reasons, nitrogen cold jet with corrected velocity (to account for the difference in

viscosity and density) was used instead of propane, while maintaining the same burner-exit Reynolds number.

First, the radial profiles of oxygen molar concentration at different axial venturi locations, with the corresponding baseline (no-venturi) values were obtained. From which, the weighted area average oxygen concentration ( $\bar{x}_{O_2}$ ) was determined and converted into air entrainment with the following equation:

$$\text{Air entrainment ratio} = \frac{n_A}{n_f} = \frac{4.76\bar{x}_{O_2}}{1-4.76\bar{x}_{O_2}} \dots\dots\dots(4.2)$$

Where  $n_A$  is the molar rate of secondary air,  $n_f$  is the molar rate of the fuel and  $\bar{x}_{O_2}$  is the average mole fraction of  $O_2$

The air entrainment at different venturi axial locations, for  $Re=5100$ , and compared to its value in the baseline case, is shown in Fig. 4.13. At  $x/d=260$ , where the fourth (last) venturi was installed, the air entrainment ratio ( $n_A/n_f$ ) increases from 27.5 in the baseline flame to 37.5 in the cascaded one, which represents an increase of 36% in the secondary air entrainment by the effect of venturis. Since this increase was measured at the last venturi, it represents the cumulative contribution of all the four venturis installed around the burning jet. The measurements at the intermediate locations show that the first venturi contributes by 8%, the second by 12%, the third by 11% and the fourth (last) by 5%. Hence, the higher contribution in air entrainment comes by the venturis located at  $x/d=100$  and  $x/d=180$  (intermediate area), while the lowest contribution comes from the venturi located at  $x/d=260$  (end of the flame).

#### 4.14 Radiant Fraction of Heat Release (F)

The radiant fraction (or radiative heat release factor) was calculated by the following equation:

$$F(\%) = \frac{Q_{\text{rad}}}{Q_{\text{total}}} \times 100 \dots\dots\dots (4.3)$$

Where,  $Q_{\text{rad}}$  is the radiant heat transfer rate from the flame to the surrounding, and  $Q_{\text{total}}$  is the total heat input rate based on the fuel flow rate and the heating value of the fuel.

The radiant fraction,  $F(\%)$ , at three burner-exit Reynolds numbers (3600, 5100 and 6500) corresponding to three types of flames (Table 3.2), is shown in Fig. 4.14 for both the venturi-cascaded and baseline cases. It is seen that cascading the flame decreases the radiant fraction by 17%, 10% and 15% of the baseline value, for the attached, transition and fully-lifted flames, respectively. This can be a result of the combined or net effects of higher temperature and length observed in the venturi-cascaded flame on the one hand, and lower soot concentrations and radiation blockage by venturis on the other.

The effect of burner-exit Reynolds number on the radiant fraction was such that as the former increases the latter decreases. This may be accounted for by the higher heat input rate into the burner and lower time available for radiant energy to be lost from the flame at higher Reynolds numbers.

#### 4.15 OH Radical Relative Concentration Profiles

For OH relative LIF signal measurements, the excitation of the  $P_1(9)$  rotational line in the (1,0) vibrational band of the  $A^2\Sigma^+ \leftarrow X^2\Pi_i$  electronic system near the frequency doubled (286 nm) laser wavelength was employed, and the fluorescence signal was detected in the (1,1) vibrational band near 314 nm (Smyth et al., 1990; Norton et al., 1993). Two filters; an ultra violet transmitting glass filter (UG5) and a colorless sharp cut-off glass filter (WG305), were used in conjunction with the photomultiplier tube to keep the detected signal near 314 nm. The signal gain was set to 20. The laser energy was kept around  $50 \mu\text{J}/\text{P}$  to be in the linear regime and avoid saturation which occurs at higher laser energies and may lead to the expansion of the focal volume and the consequent spatial broadening of the measured profiles (Smyth et al., 1990).

Figures 4.15 (a, b, c) show the relative LIF signal (concentration) radial profiles in the near-burner region at  $x/d=20$  for both the baseline and cascaded flames at  $Re=5100$ . Figure 4.15(a) shows the on-resonance (286 nm) relative signal profiles, which exhibit the combined contribution arising from OH fluorescence which peaks in the primary reaction zone (farthest from the centerline) and Polycyclic Aromatic Hydrocarbons (PAH) fluorescence which peaks in the fuel-rich region of the flame (closest to the centerline). In this near-burner region, no soot has formed yet, and those PAH species are thought to be the important intermediates between the original fuel molecule and what can be considered a primary soot particle (Glassman, 1988). With the laser wavelength being tuned off the resonance wavelength with respect to

OH rotational line by 0.03 nm (Puri et al., 1992), the signal due to OH fluorescence disappeared while that attributed to PAH fluorescence (which is broadband in nature) remained (Fig 4.15b). Therefore, the subtraction of the off-resonance profiles from the on-resonance profiles yielded the net OH fluorescence profiles (Fig. 4.15c). It should be noted that the small off-resonance wavelength shift (0.03 nm) has a negligible effect on the PAH broadband fluorescence signal for identical laser energies.

From Figs.4.15 (b, c), the following observations can be made: (i) PAH soot precursors starts to build up in the early fuel rich zone just after the flame sheet and attains a peak value somewhere in the far fuel-rich region at  $x/d=1$ , which corresponds to a temperature of about 1200 K; (ii) the OH relative concentration exhibits a sharp off-axis peak at  $x/d=3$ , which almost corresponds to the peak temperature of 1766 K, and sharply decreases towards the fuel-lean and fuel-rich regions. It almost follows the same trend as the radial temperature profile (Fig. 4.7a); (iii) the cascaded flame shows a decrease of 11% and 18% in average PAH and OH relative concentrations (17% and 11% in peak values) over the baseline flame, this corresponds to an the average decrease in temperature at this axial location of 5%; (iv) the radial positions of OH and PAH peak values remain unchanged for both the cascaded and baseline flames.

The peak PAH concentration in the fuel-rich side of the flame is expected, since those soot precursors should have found a suitable place to grow via chemical means in the fuel-pyrolyzing environment in the fuel-rich regions of the flame. These chemical mechanisms are still a subject of research (Turns, 1996). The reduced PAH

in the cascaded flame may be attributed to the higher rates of mixing with air and the consequent dilution of the previously mentioned fuel-rich pyrolysis zones.

The OH relative concentration profiles almost follow the temperature profiles obtained earlier, since this radical is very strongly temperature dependent, and particularly in this near-burner region, where stoichiometric homogenous gas phase reactions take place without any soot interference. Therefore, the decrease of OH in the cascaded flame is a direct result of the reduction in temperature that was explained earlier. The results indicate that the average OH concentration decreases at a rate approximately four times faster than temperature.

Figures 4.16 (a, b, c) present the relative LIF signal (concentration) profiles in the mid-flame region ( $x/d=100$ ) for the baseline and cascaded flames at  $Re=5100$ . The general trends of these profiles are similar to those in Figs 4.15, but the interference with the on-resonance signal is due to soot particles rather than PAH species. This is quite understandable since at this mid-flame axial location all PAH precursors are already converted to soot particles while being exposed to the pool of radical species from the pyrolyzing fuel as they travel through the flame (Turns, 1996). This argument is in conformity with the earlier soot concentration measurements (Fig. 4.12b) which indicated a dramatic increase in soot concentration up to 82% of its maximum value at this axial location ( $x/d=100$ ) for the baseline flame.

The following observation can be made from Figs. 4.16 (a, b, c): (i) The relative soot concentration for the baseline flame increases in the fuel-rich zone and reaches its maximum value at  $r/d=2$ , while that of the cascaded flame increases at a lower rate and reaches its maximum value at  $r/d=0$ ; (ii) The cascaded flame shows a decrease of

22% in average (28% in peak) soot concentration over the baseline flame; (iii) the cascaded flame has a higher OH concentration than the baseline flame by 40% in average value (38% in peak value); (iv) the off-axis peak OH relative concentration is shifted towards the fuel-rich region by 2 mm than in the baseline case.

The lower rate of soot increase in the fuel-rich zones of the cascaded flame, compared to the baseline case, is the resultant of many factors: higher rates of soot oxidation; lower PAH species formed earlier in the near-burner region; higher temperatures due to radiation blockage by venturis and higher OH concentrations; all together interact with each other in a complicated manner. The peak soot value of the cascaded flame (Fig. 4.16b) is not only less in magnitude but also closer to the centerline which is another indication of the better rates of mixing provided by the cascade of venturis.

The higher OH concentrations observed in the cascaded flame over the baseline flame is in conformity with the higher temperatures observed earlier in the cascaded flame (Fig. 4.7b), this is due to what can be called the “*thermal effect*” which includes radiation blockage by venturis and lower soot loading in the cascaded flame and was explained earlier in the temperature measurements. Another important factor that controls OH concentration in hydrocarbon diffusion flames, and particularly in the down-stream regions, is the reaction of OH with soot particles, the latter effect can be referred to as the “*chemical effect*”.

At this mid-flame location, 40% average increase in OH by the effect of the venturi-cascade corresponded to 24% average decrease in soot and 13% average increase in temperature. This reveals, with no doubt, the strong influence of soot

particles on OH radical in diffusion flames and particularly when fuels of high soot tendency, like propane, are in use.

The latter observation has a strong support from literature, since most of the recent studies in soot formation and oxidation has come to consider OH radical as the key oxidizer for soot particles (Puri et al.,1994; Smyth et al., 1994; Villasenor et al., 1992; Neoh et al., 1984). Therefore, OH concentrations were suppressed in the presence of soot and vice versa. Puri et al. (1994) reported in their study that OH concentration is reduced primarily due to reactions with soot rather than a consequence of lower temperatures measured for higher soot loading. They measured OH in the presence and absence of soot; the effect of lower temperatures on the OH concentrations was comparatively small, accounting for only 3% to 11% of the measured decrease in OH. In the same study, OH was found to be the dominant oxidizer of soot, with O<sub>2</sub> making only a small contribution. This latter conclusion was also supported with a recent study by Haudiquert et al. (1997).

The increase in OH radical and decrease in soot concentrations observed in the cascaded flame over the baseline case, have a direct influence on both CO and CO<sub>2</sub> emissions measured earlier; this is due to the fact that OH is the main oxidizer for both soot and CO, and hence, they compete continuously with each other for OH. Therefore, the lower soot and the abundance of OH in the cascaded flame will make the OH radical more available for CO oxidation ( $\text{CO} + \text{OH} \rightarrow \text{CO}_2 + \text{O}$ ) which will be enhanced remarkably due to lower competition with soot, thereby, leading to lower rates of CO and the consequent higher rates of CO<sub>2</sub>. This is in complete agreement

with our earlier CO and CO<sub>2</sub> emission measurements in which the cascaded flame had shown lower CO and higher CO<sub>2</sub> concentrations compared to the baseline one.

#### 4.16 CH Radical Relative Concentration Profiles

The LIF Relative CH Signal was obtained by exciting the R(7) rotational line in the (0,0) vibrational band of the  $A^2\Delta \leftarrow X^2\pi_i$  electronic transition at 427.4 nm. The signal was filtered through a dielectric filter (center wavelength = 436.95 nm, FWHM = 9.02 nm) before being captured by the photomultiplier tube, and the signal gain was set to 50. The laser energy was attenuated with a variable iris diaphragm and a beam splitter to around 50  $\mu\text{J/P}$  and focused to the point of measurement using a 1m focal length plano convex lens. The low energy laser beam is very important to avoid the photolytic production of CH which has been reported at energies higher or equal to 100  $\mu\text{J/P}$  (Norton et al., 1991). Furthermore, a dichroic sheet polarizer was placed in front of the photomultiplier tube and oriented to transmit horizontally polarized light, thereby, minimizing the Raleigh scattering from the flame gases. In all experiments, the laser frequency was tuned on and off the R(6) rotational transition in order to account for the interference from the PAH species.

Figures 4.17 (a, b, c) show the LIF relative signal at  $x/d=20$  in the near burner region at  $Re = 5100$  for the baseline and cascaded flames. The net CH relative signal was obtained by subtracting the off-resonance (PAH) signal (Fig. 4.17b) from the on-resonance (CH+PAH) signal (Fig. 4.17a). The following observations can be made from Fig. 4.17c: (i) the relative signals observed here are lower than that observed in

OH measurements (ii) the CH relative profiles have sharp off-axis peaks as have been observed for OH and temperature; (iii) the relative CH peak does not coincide with that of temperature and OH, the former occurs at  $x/d=2$ , whereas the latter have been observed at  $x/d=3$ ; (iv) The relative CH profile is narrower than that of OH; (v) the CH relative concentrations in the cascaded flame is 24% lower, in average value, (36% in peak value) than that in the baseline flame.

The weaker signals observed in the CH measurements compared to that of OH can be attributed to the original quantities of the two radicals of interest; CH does not exist in plenty as OH and as a result the signal of CH, which is generally proportional to the ground state population of that radical, is expected to be lower than that of OH. Another factor that can affect the fluorescence levels of the two radicals is their inherent molecular structure and the consequent different rates of radiative decay of the excited states (Einstein rate constants). However, OH and CH Einstein rate coefficients of the selected excited states ( $A_{ij}$ ) are within the same order of magnitude;  $1.4 \times 10^6 \text{ s}^{-1}$  and  $1.8 \times 10^6 \text{ s}^{-1}$ , respectively (Eckbreth, 1996). Therefore, the role of the latter factor seems to be negligible compared to the first factor.

The CH peaks do not coincide well with peak temperatures, as OH peaks do. On the other hand, CH peaks occur in the rich fuel region of the flame. Nevertheless, CH has been considered as an indicator of the instantaneous position of the reaction zone (Allen and Hanson, 1986). However, OH would seem to be a better marker of the primary reaction zone that follows a stoichiometric contour near  $\phi=1$ . The lower CH

relative concentrations observed in the cascaded flame over the baseline case, can be explained by the better mixing rates in the former

The latter result can be correlated to the NO and temperature measurements observed earlier in the cascaded flame, at that particular location; the 16% NO reduction from the baseline case corresponded to 24 % decrease in CH and 5% decrease temperature. Since the primary initiation reaction of the prompt-NO mechanism is that of the radical CH with the air nitrogen to produce HCN and nitrogen atoms, it can be concluded, that in this propane diffusion flame, the prompt-NO (Fenimore) mechanism; postulated by Fenimore in 1971 and extensively reviewed by Bowman in (1992), plays an important role besides the thermal-NO (Zeldovich) mechanism. The latter conclusion supports our earlier explanation of NO reduction in the cascaded flame.

The reduced CH levels in the cascaded flame, compared to the baseline case, may also be considered as another explanation for the reduction in soot that has been observed earlier. The CH radical has been implicated as a key factor in the inception stage of soot in hydrocarbon flames through the chemi-ionization reactions of ground state CH with atomic oxygen and of electronically excited CH ( $A^2\Delta$ ) with acetylene (Calcote, 1981).

Figures 4.18 (a, b, c) show the LIF relative signal at  $x/d=100$  at  $Re = 5100$  for the baseline and cascaded flames. At this mid-flame location, CH signal could not be identified clearly. The most probable reason is that at this mid-flame location, heterogeneous (soot) combustion starts playing the dominant role instead of the gas-

phase homogenous reactions. As a result, the temperature of the baseline flame drops by 14% (in average value) from the near-burner value. Therefore, it is quite understandable that all radical concentrations drop due to the increase in destruction rates and decrease in production rates of those radicals. Furthermore, due to the lower CH concentrations in the near-burner region, narrower radical profiles and smaller transition life time compared to the OH radical, CH is expected to last over a shorter distance from the burner-exit than OH does.

#### **4.17 CN Radical Relative Concentration Profiles**

For CN measurements, the excitation of the R(34) rotational line in the (0,0) vibrational band of the  $B^2\Sigma \leftarrow X^2\Sigma$  electronic system at 388.3 nm was used. The fluorescence signal was passed through an ultra violet interference filter (center wavelength =390 nm, FWHM =10.3 nm) before being detected by the photomultiplier tube, and the signal gain was set to 50. In the same arrangement, a dichroic sheet polarizer was placed in front of the photomultiplier tube to transmit horizontally polarized light, thus minimizing the Raleigh scattering which is expected to be significant in CN measurements due to the narrow wavelength band between the laser excitation and fluorescence detection.

Figures 4.19 (a, b, c) show the relative LIF signal for the baseline and cascaded flames at  $Re=5100$ . The off-resonance signal (Fig. 4.19b) was subtracted from the on-resonance signal (Fig. 4.19a) in order to get the net CN signal (Fig. 4.19c). From these figures, the following observations can be made: (i) PAH interference seems to

be negligible in CN measurements. However, the off-resonance profiles serve mainly as indicators of the background radiation; (ii) the CN relative concentration builds up and attains its maximum value at  $x/d=2$  in the fuel rich region of the flame and drops markedly at the stoichiometric contour ( $x/d=3$ ); (iii) the CN relative concentration in the cascaded flame decreases by 12% in average value (16% in peak value) from the baseline case.

The low PAH interference with the CN signal may be attributed to the high fluorescence power expected from CN radical; this power is proportional to the spontaneous emission Einstein coefficient of the selected transitions ( $A_{21}$ ), the latter coefficient for the transition used for CN is  $1.7 \times 10^7 \text{ sec}^{-1}$  (Eckbreth; 1996), which is greater than CH and OH Einstein coefficients by factors of 10 and 12 respectively. Therefore, the fluorescence signal is expected to be higher and as a result the interference from other intermediate species such as PAH becomes negligible.

The CN peak in the fuel rich side of the flame is also quite understandable, since most of the free radicals (except OH) form and build up in that fuel pyrolyzing region and are consumed at the stoichiometric contour. The destruction of CN relative concentration observed at the stoichiometric region, where OH exists in abundance, is due to the reaction of CN with the hydroxyl radical ( $\text{CN} + \text{OH} \rightarrow \text{NCO} + \text{H}$ ) (Smith et. al, 1986).

The decrease of CN in the cascaded flame over the baseline case is in good agreement with the corresponding decrease observed earlier in temperature, OH and

CH radicals; because the production rate of these radicals is an explicit function of temperature which in turn depends on the fuel-air mixing rates in the flame.

The decrease of CN in the cascaded flame can also support the NO reduction rates observed earlier. Since CN is one of the important radicals that take part in NO formation via the prompt-NO-Fenimore- mechanism (see chapter 2). Therefore, the lower CN concentrations in the cascaded flame can lead to lower NO levels assuming that prompt-NO is taking part in NO formation, which offers a strong evidence of support.

In the mid-flame location at  $x/d=100$ , CN signal was not detected. The reason, as explained earlier in CH measurements, is that this radical (and many others) forms and exists only over a short distance from the burner-exit. Beyond that point, the rates of radicals destruction exceed those of their formation as heterogeneous combustion starts taking over, thereby leading to the decrease in temperature and the consequent sharp drop in the concentration of these radicals.



**Fig. 4.1a: Photograph of the baseline gas jet flame at  $Re=5100$ .**



**Fig. 4.1b: Photograph of the cascaded gas jet flame at  $Re=5100$ .**

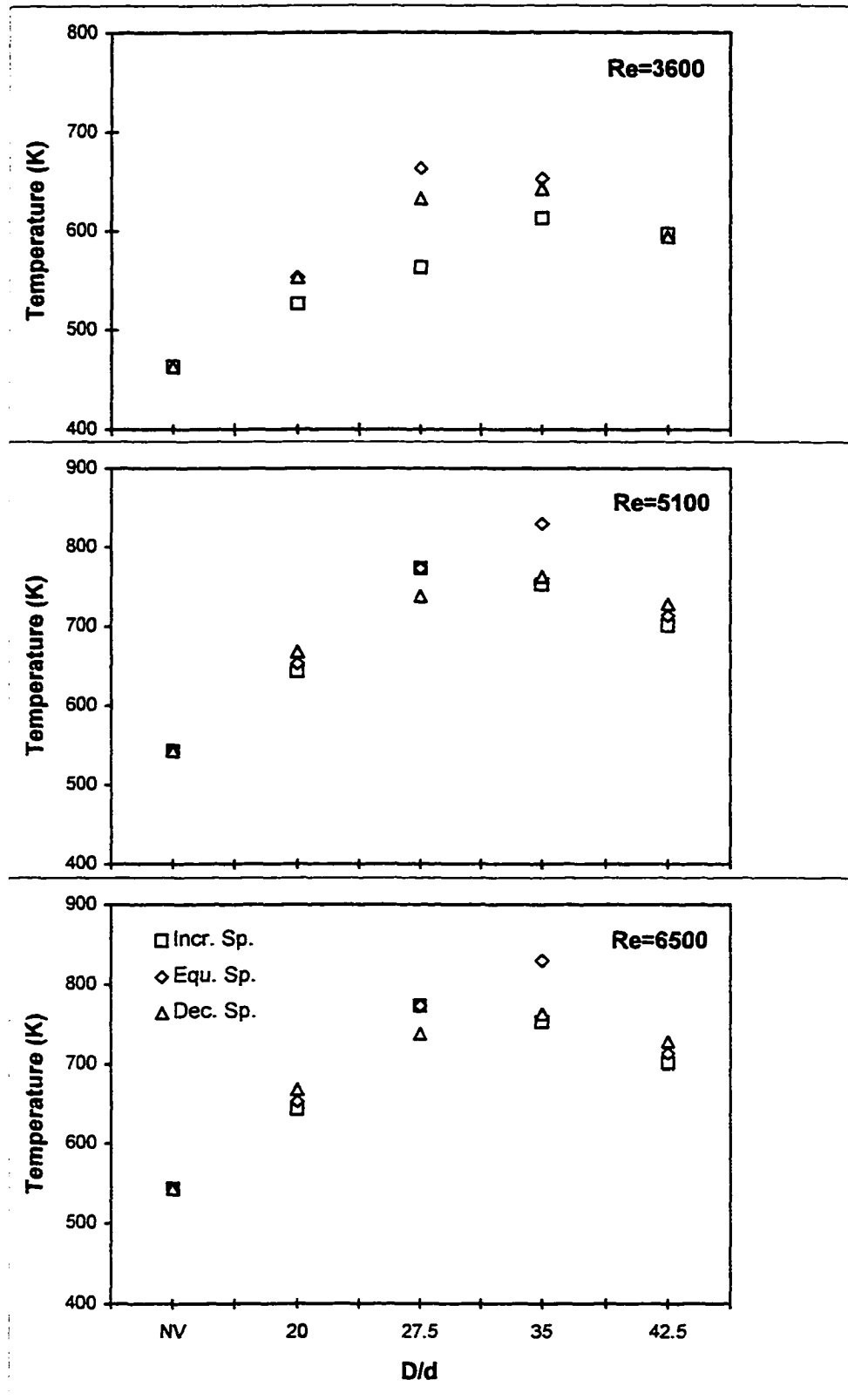
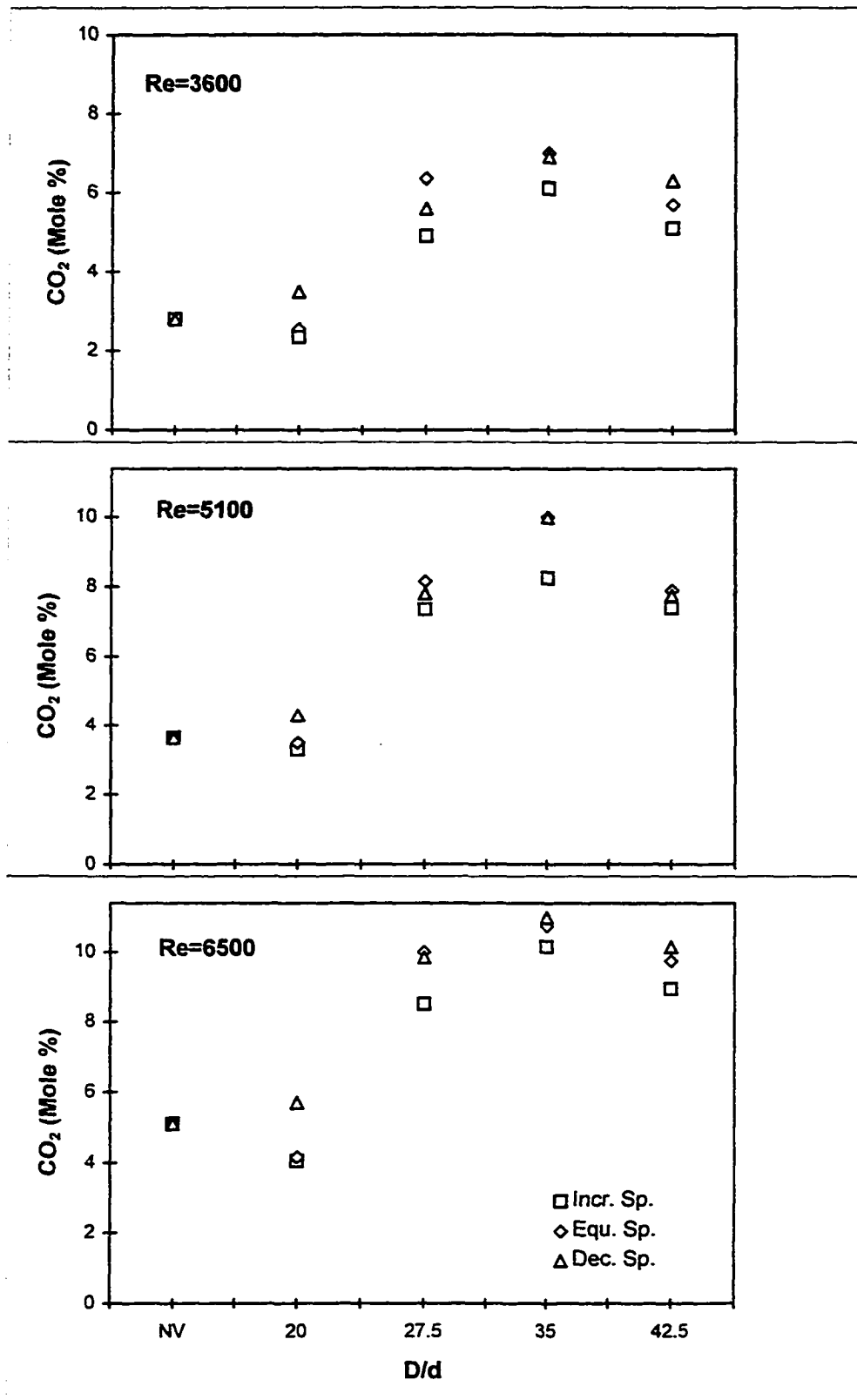
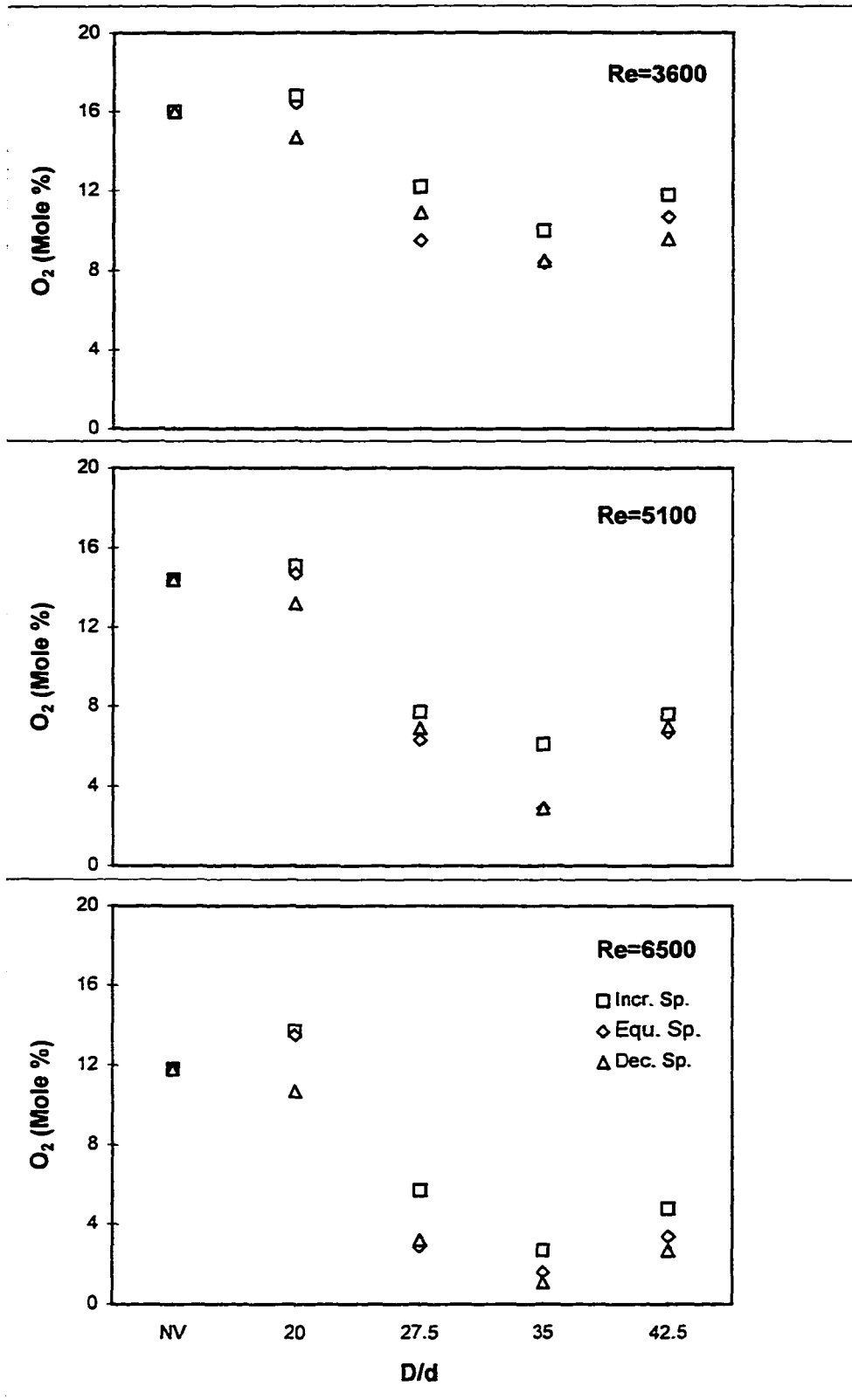


Fig. 4.2 Effect of venturi diameter, spacing and Re on combustion product temperature.



**Fig. 4.3 Effect of venturi diameter, spacing and Re on CO<sub>2</sub> molar concentration in combustion products.**



**Fig. 4.4 Effect of venturi diameter, spacing and Re on O<sub>2</sub> molar concentration in combustion products.**

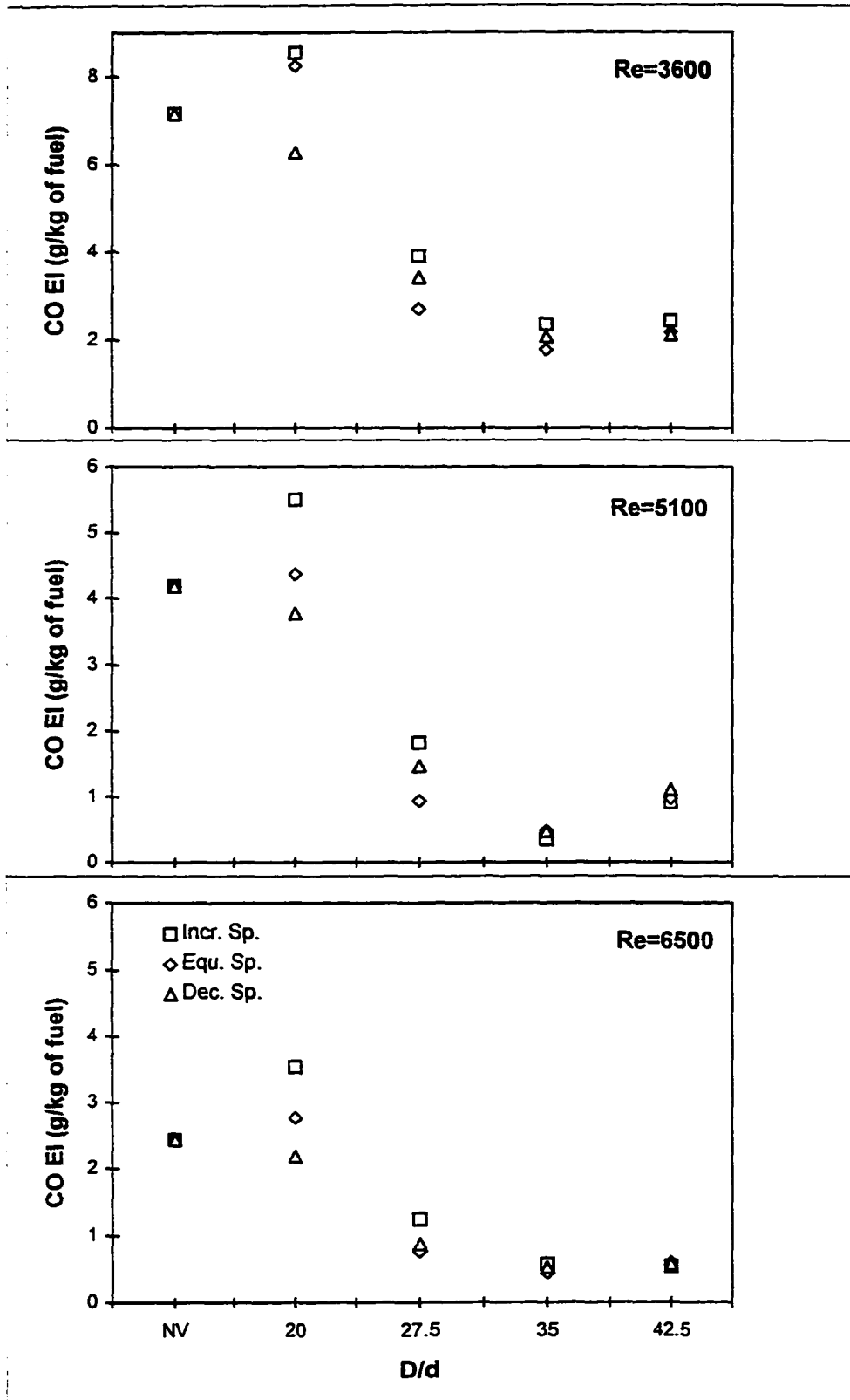


Fig. 4.5 Effect of venturi diameter, spacing and Re on CO emission index.

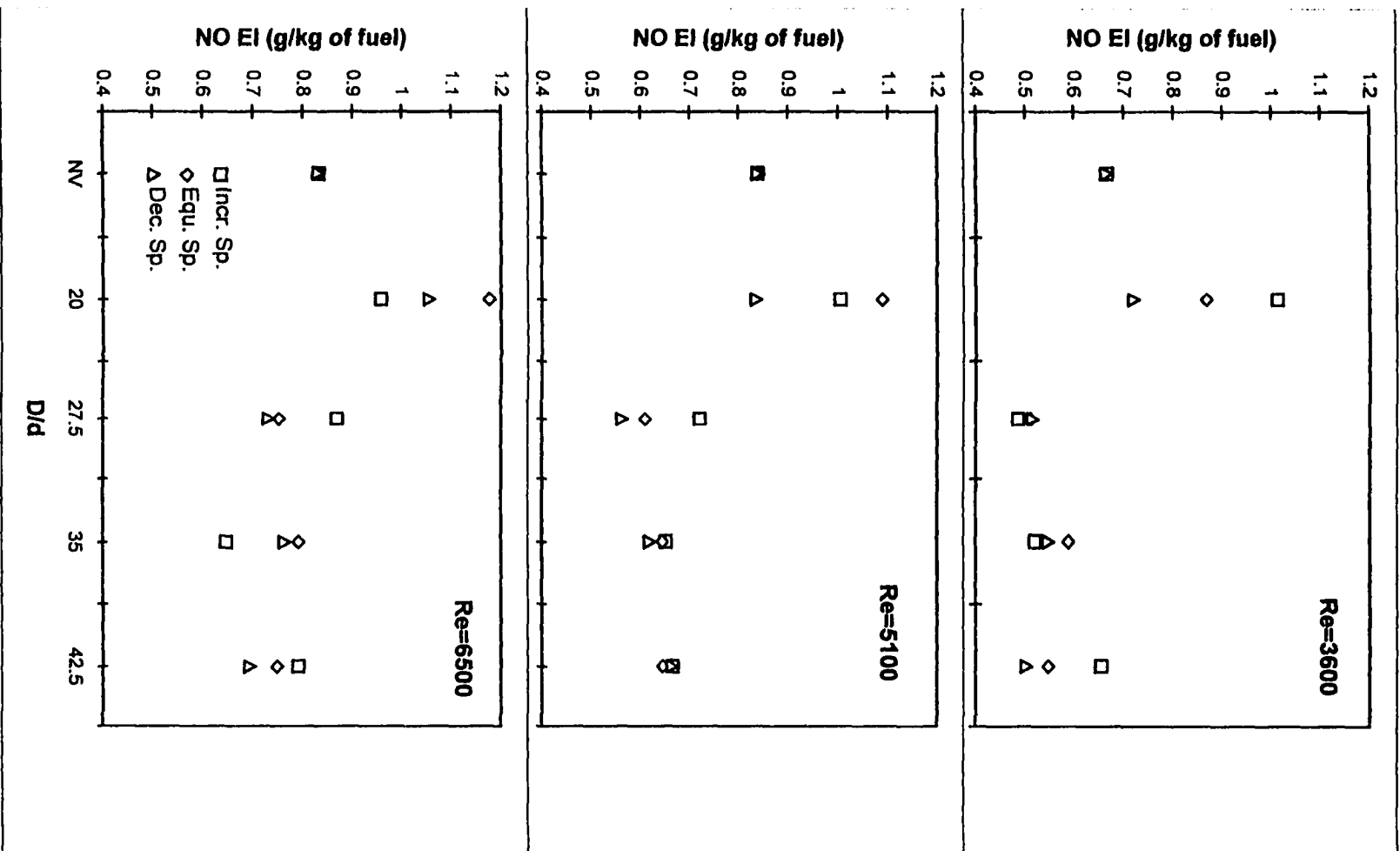
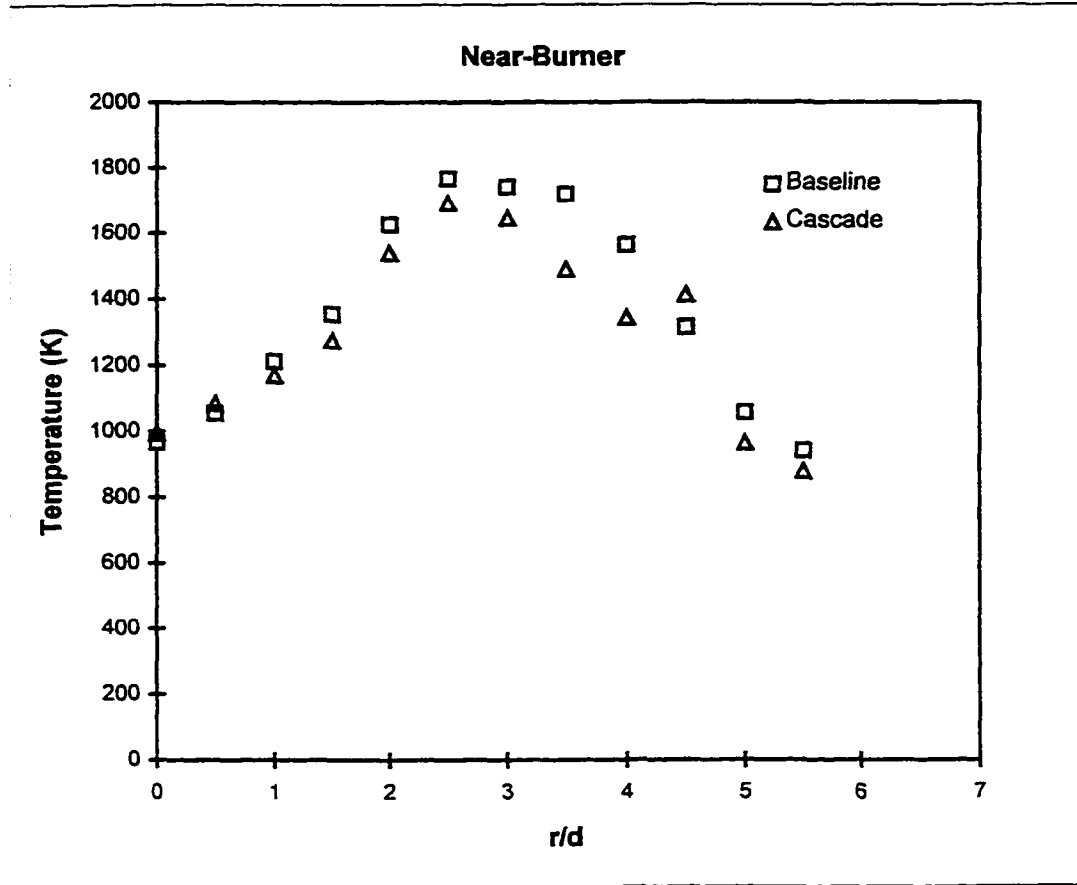
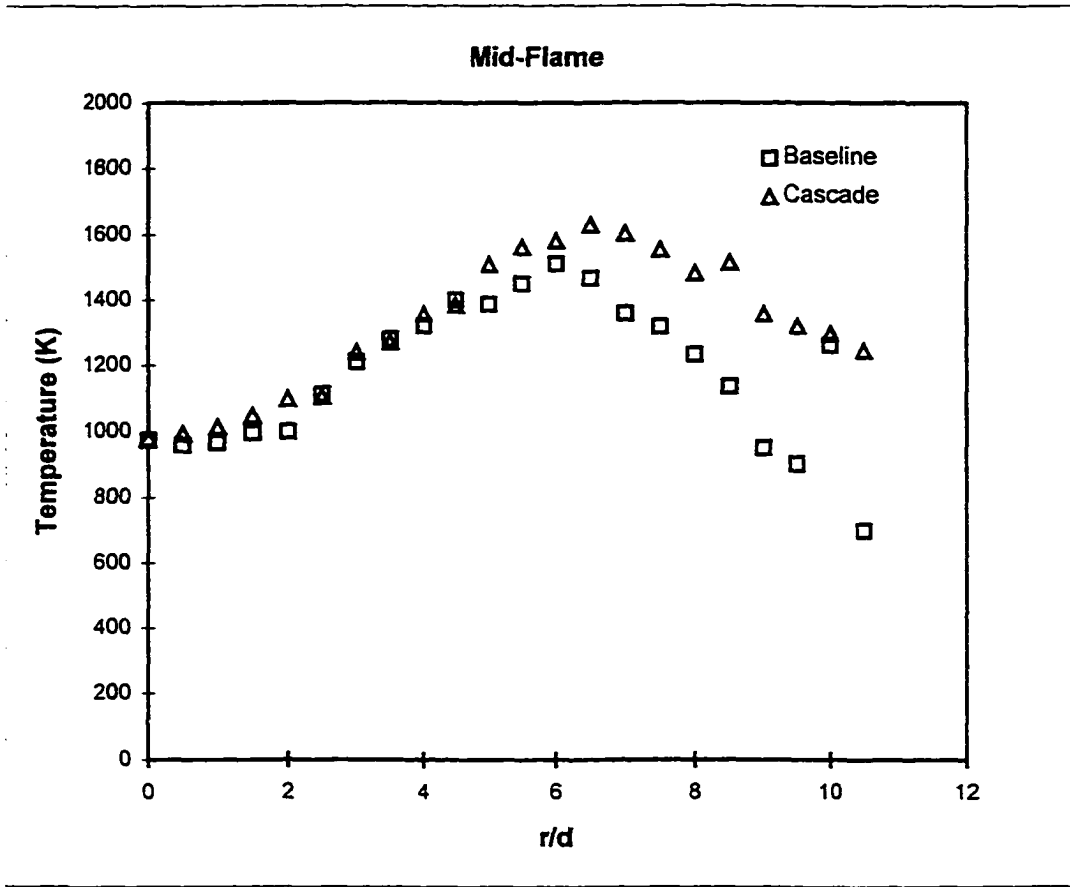


Fig. 4.6 Effect of venturi diameter, spacing and Re on NO emission index.



**Fig. 4.7a: Radial temperature profiles for the baseline and cascaded flames in the near-burner region ( $x/d=20$ ) at  $Re=5100$ .**



**Fig. 4.7b: Radial temperature profiles for the baseline and cascaded flames in the mid-flame region ( $x/d=100$ ) at  $Re=5100$ .**

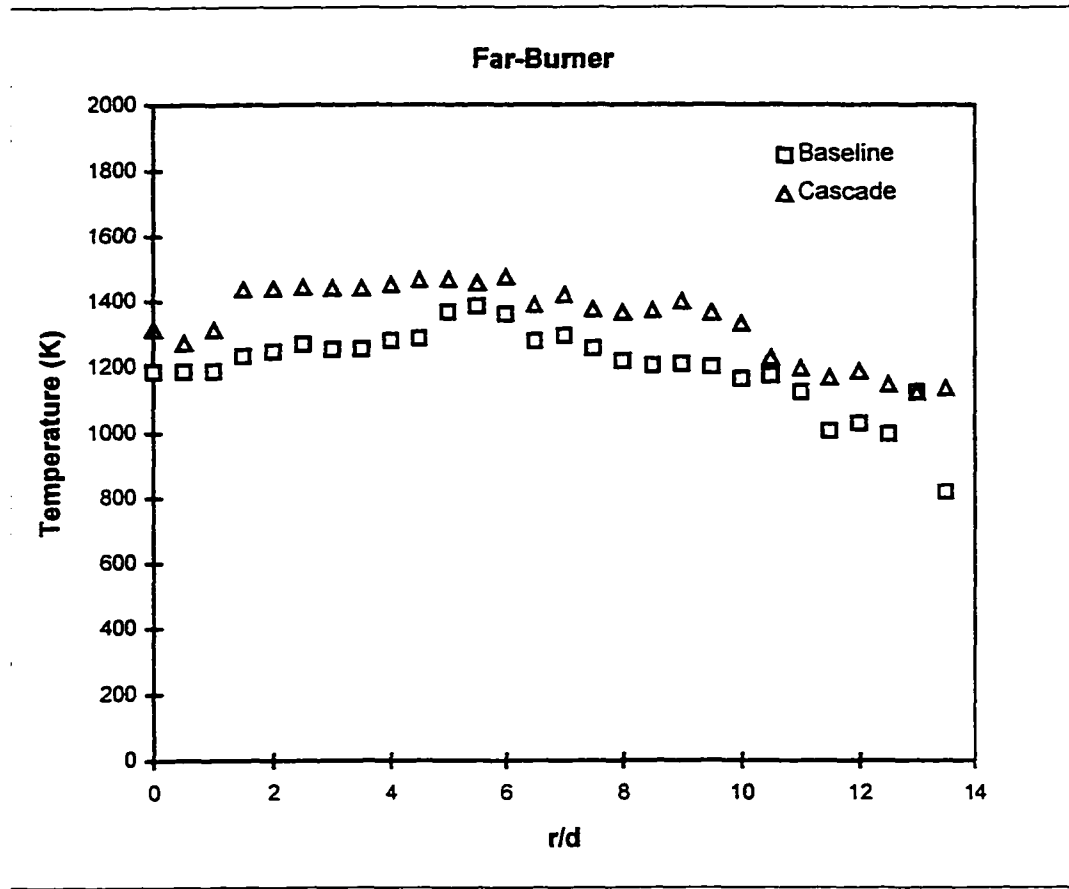


**Fig. 4.7c: Radial temperature profiles for the baseline and cascaded flames in the far-burner region ( $x/d=180$ ) at  $Re=5100$ .**

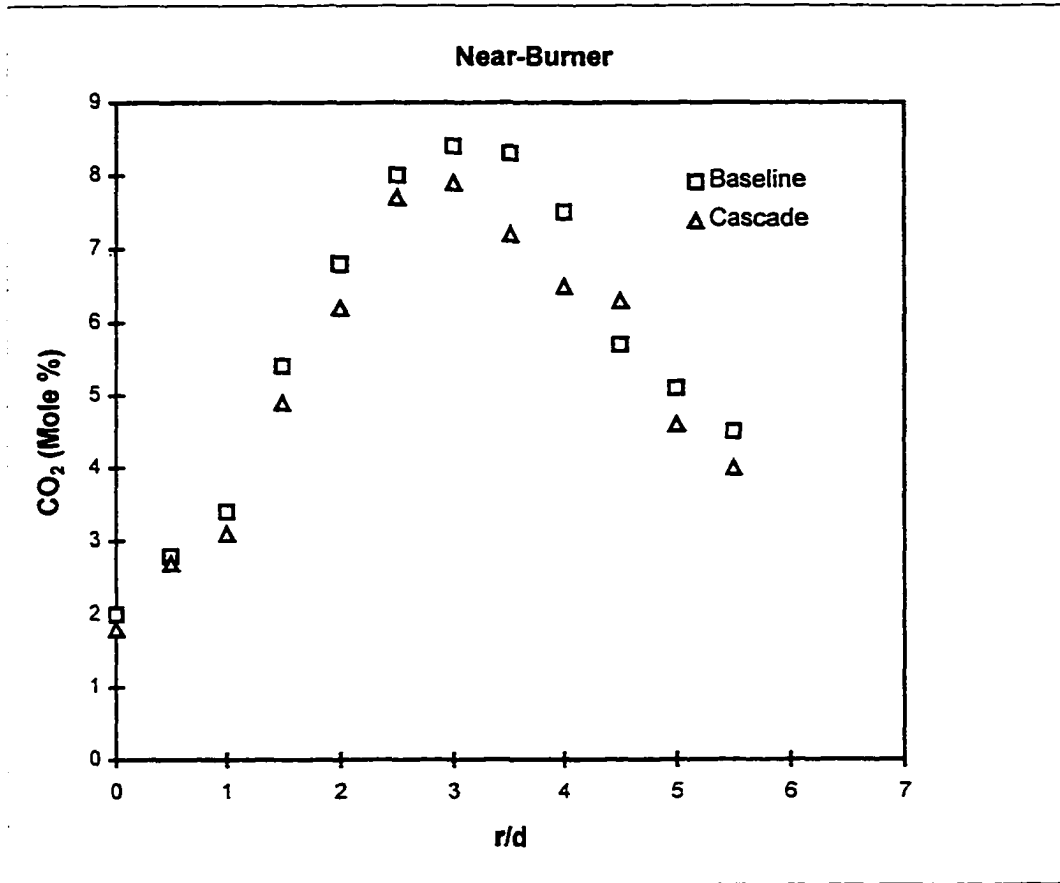


**Fig. 4.8a: Radial concentration profiles of CO<sub>2</sub> for the baseline and cascaded flames in the near-burner region ( $x/d=20$ ) at  $Re=5100$ .**

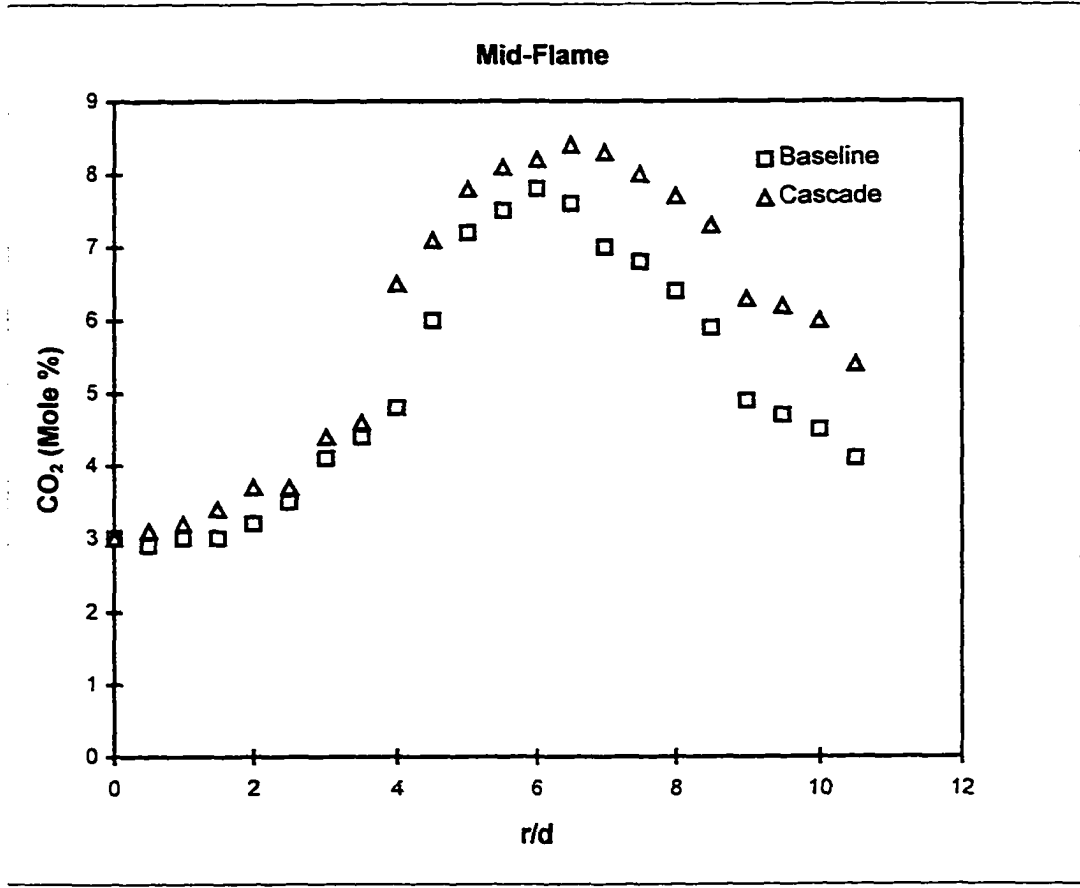


**Fig. 4.8b: Radial concentration profiles of CO<sub>2</sub> for the baseline and cascade flames in the mid-flame region ( $x/d=100$ ) at  $Re=5100$ .**

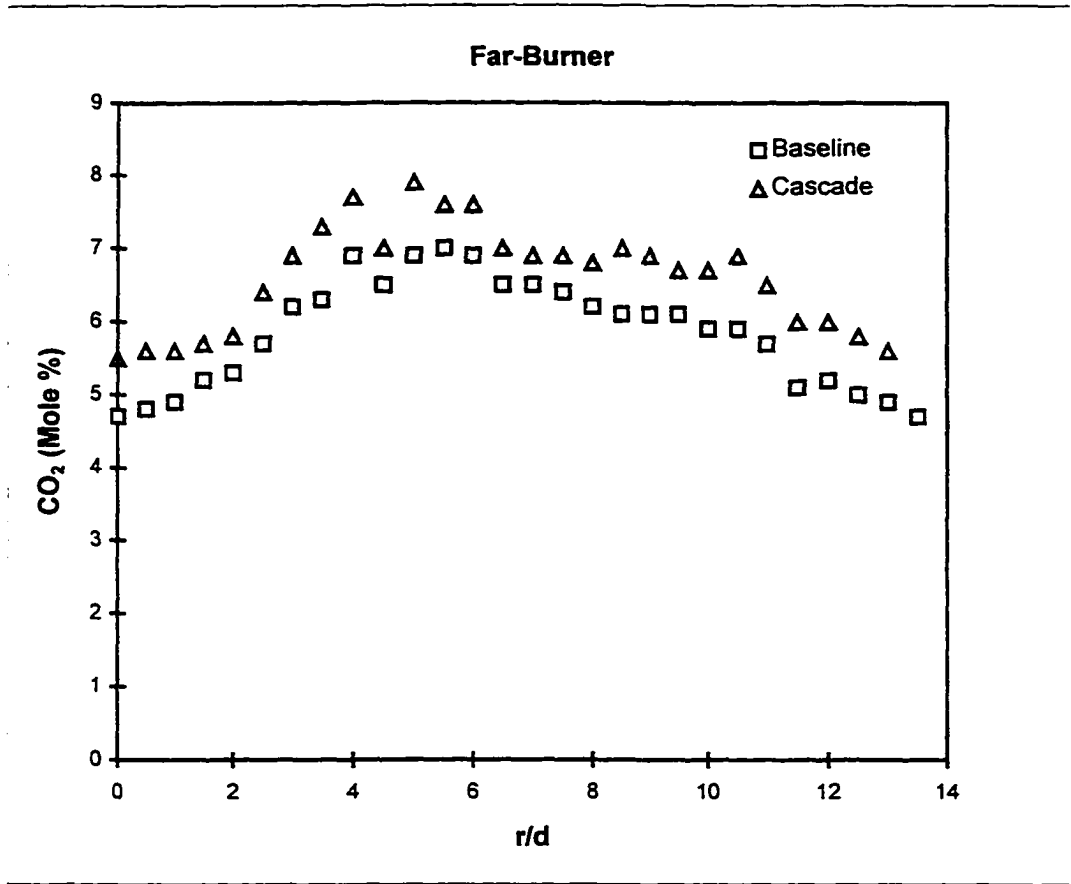


**Fig. 4.8c: Radial concentration profiles of CO<sub>2</sub> for the baseline and cascaded flames in the far-burner region (x/d=180) at Re=5100.**

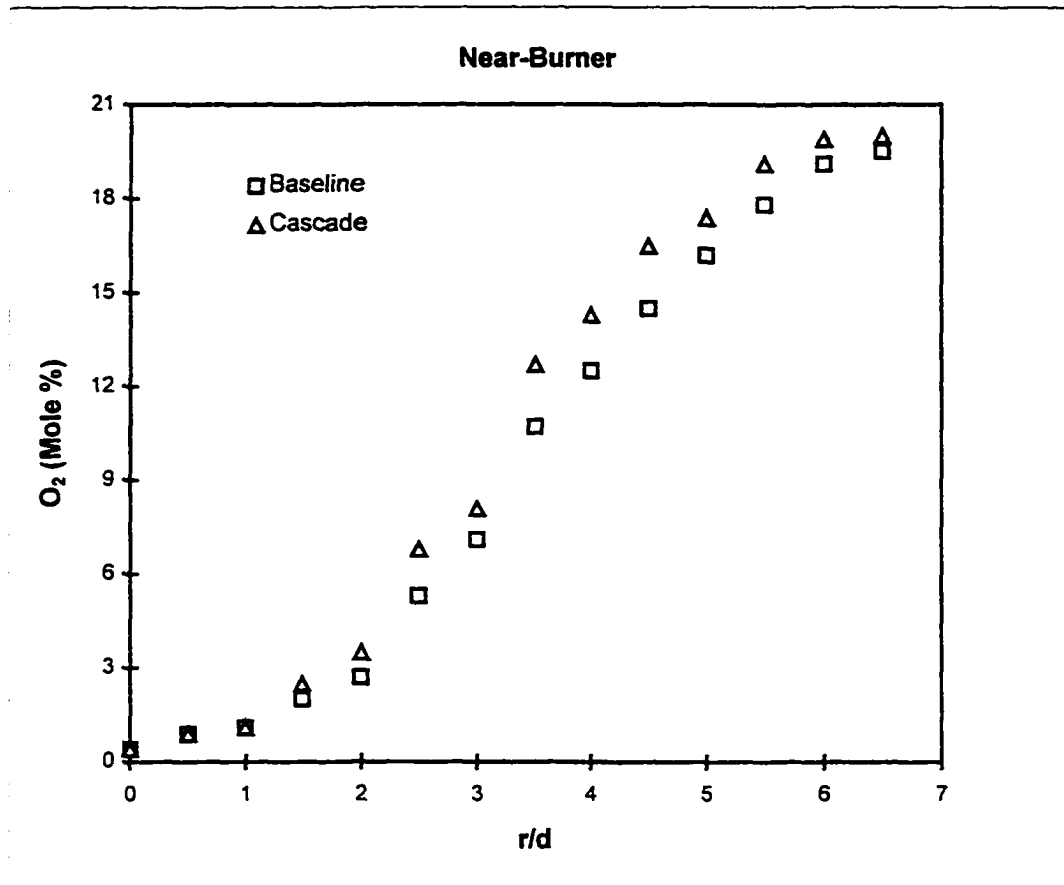


**Fig. 4.9a: Radial concentration profiles of O<sub>2</sub> for the baseline and cascaded flames in the near-burner region ( $x/d=20$ ) at  $Re=5100$ .**

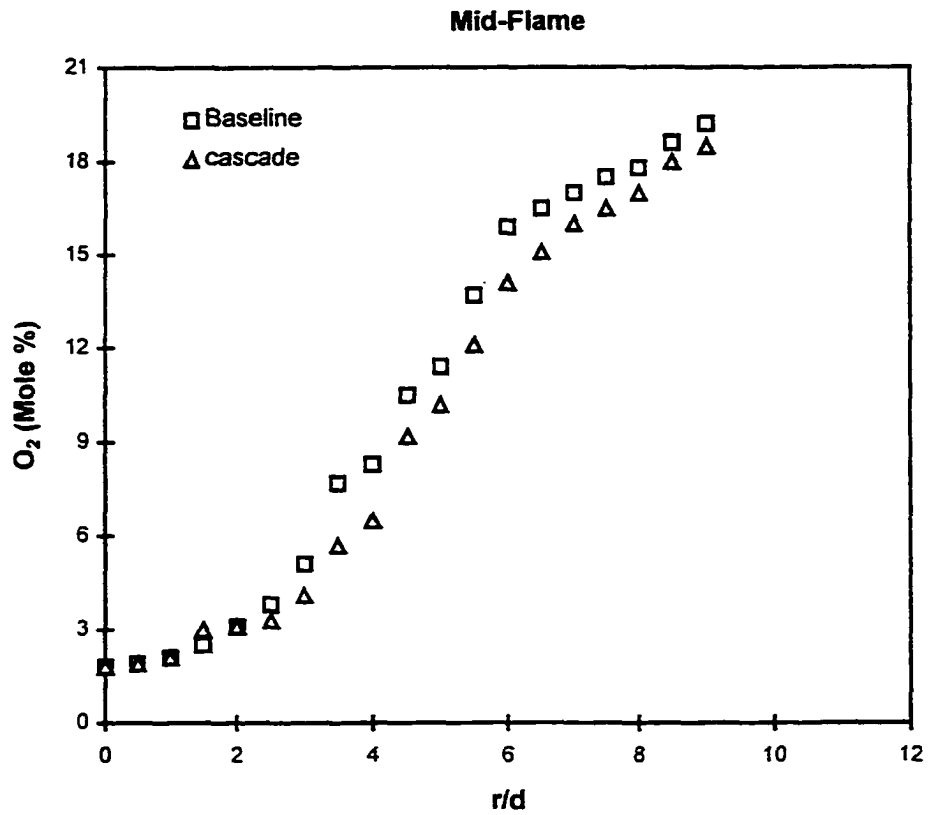


**Fig. 4.9b: Radial concentration profiles of O<sub>2</sub> for the baseline and cascaded flames in the mid-flame region ( $x/d=100$ ) at  $Re=5100$ .**

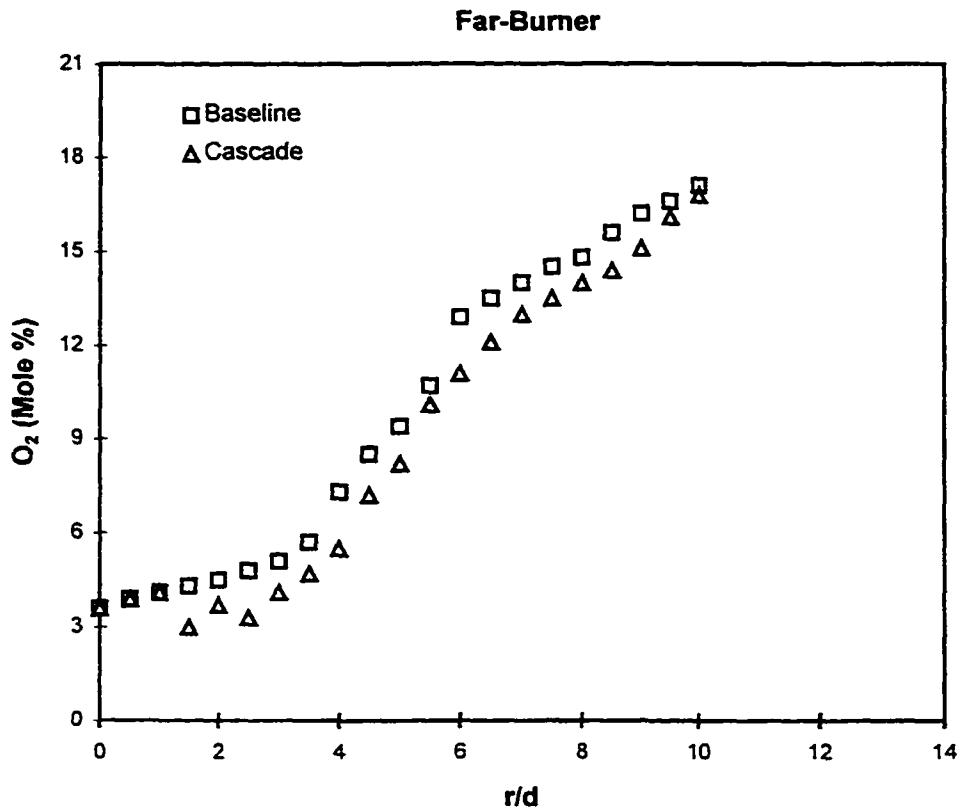


**Fig. 4.9c: Radial concentration profiles of O<sub>2</sub> for the baseline and cascaded flames in the far-burner region ( $x/d=180$ ) at  $Re=5100$ .**

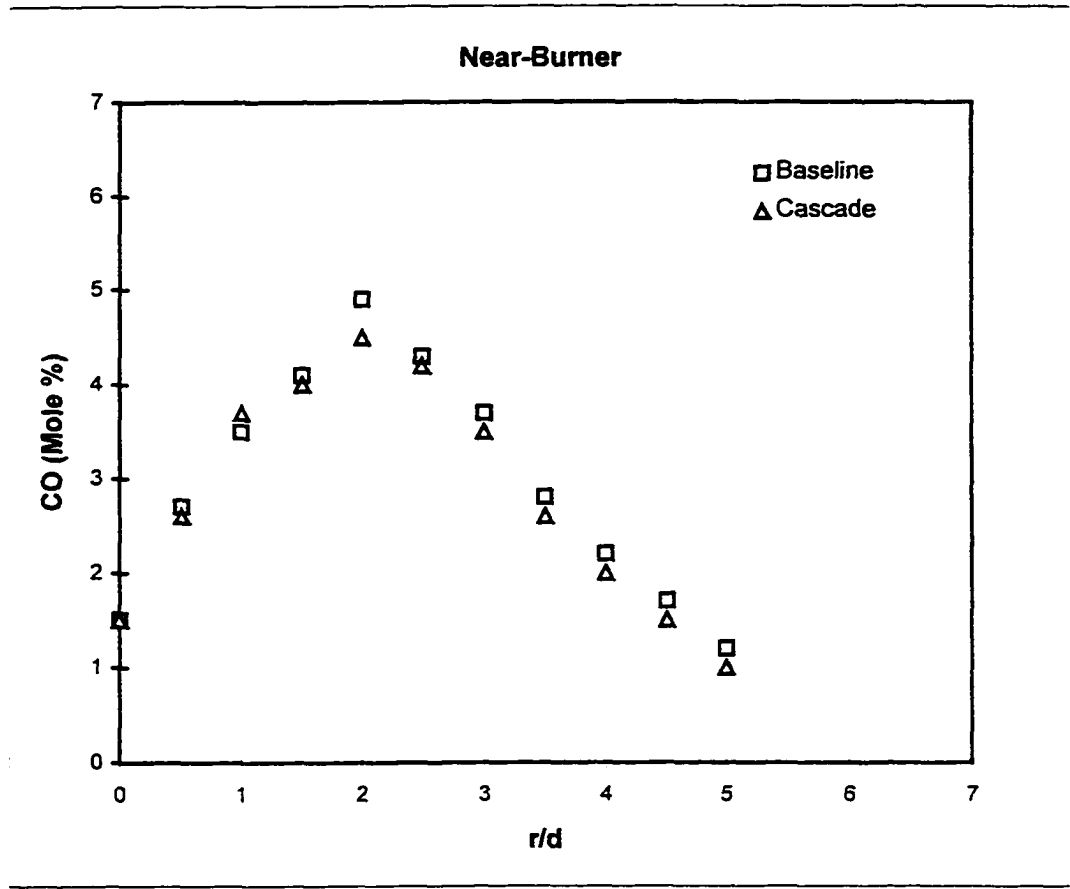


**Fig. 4.10a: Radial concentration profiles of CO for the baseline and cascaded flames in the near-burner region ( $x/d=20$ ) at  $Re=5100$ .**

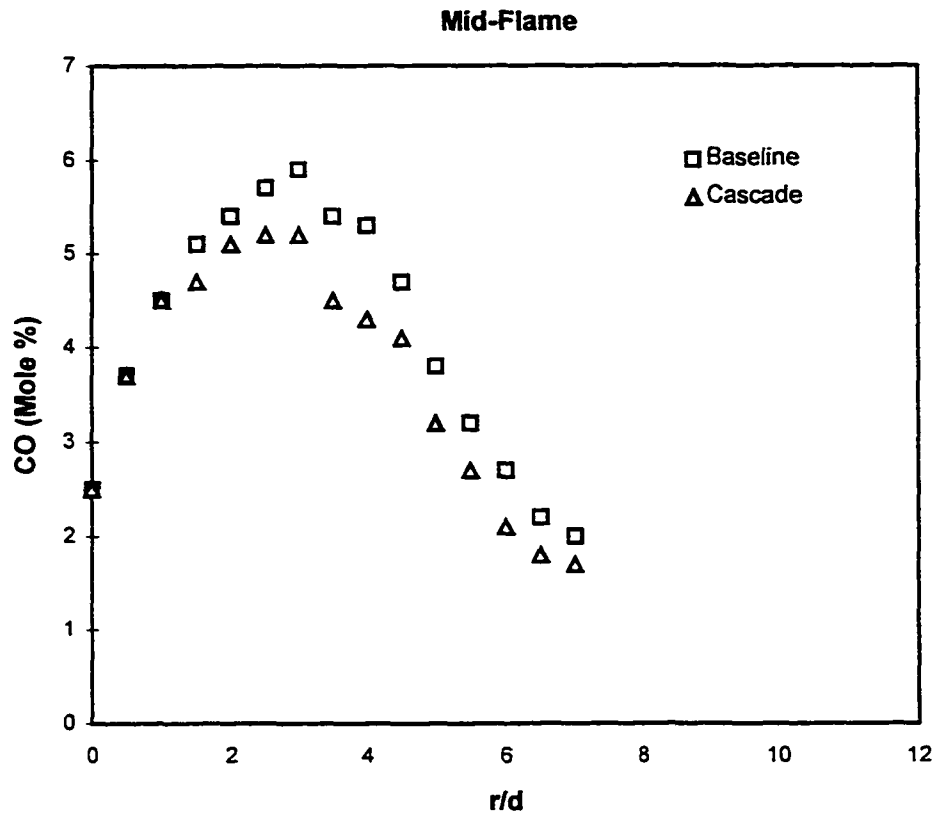


**Fig. 4.10b: Radial concentration profiles of CO for the baseline and cascaded flames in the mid-flame region ( $x/d=100$ ) at  $Re=5100$ .**

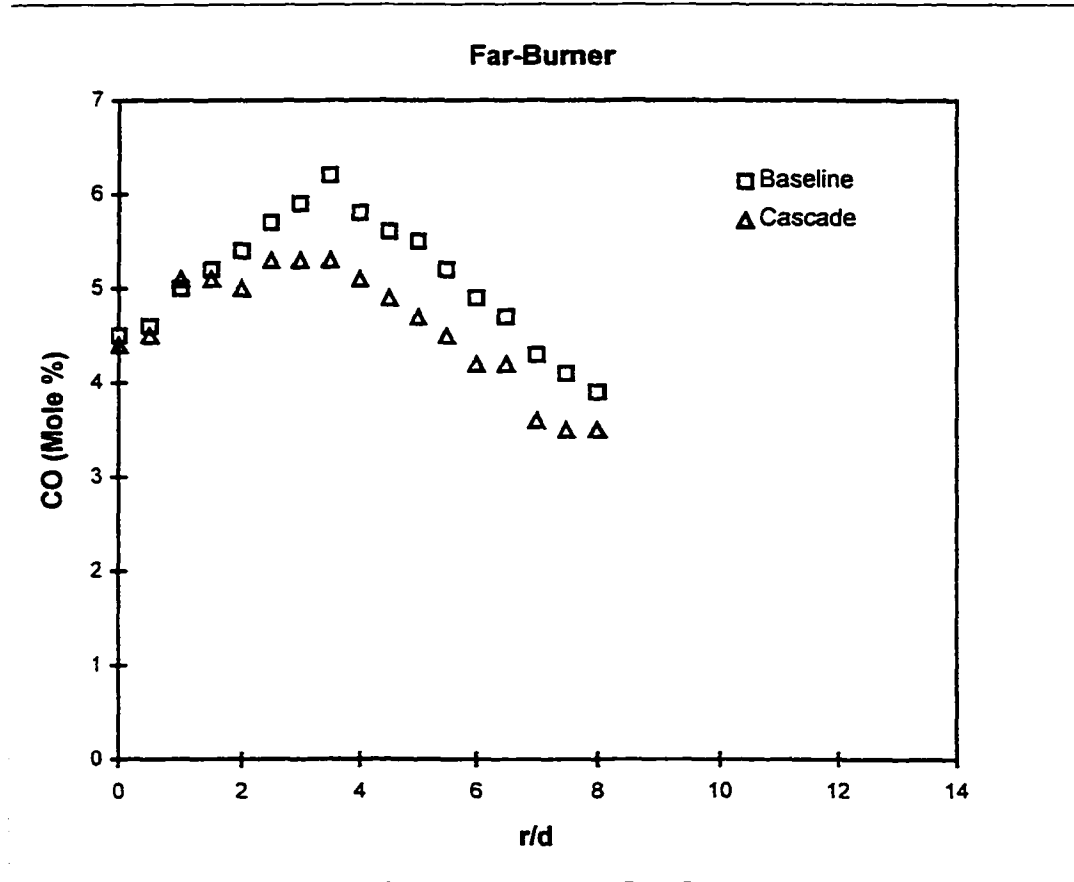


**Fig. 4.10c: Radial concentration profiles of CO for the baseline and cascaded flames in the far-burner region ( $x/d=180$ ) at  $Re=5100$ .**

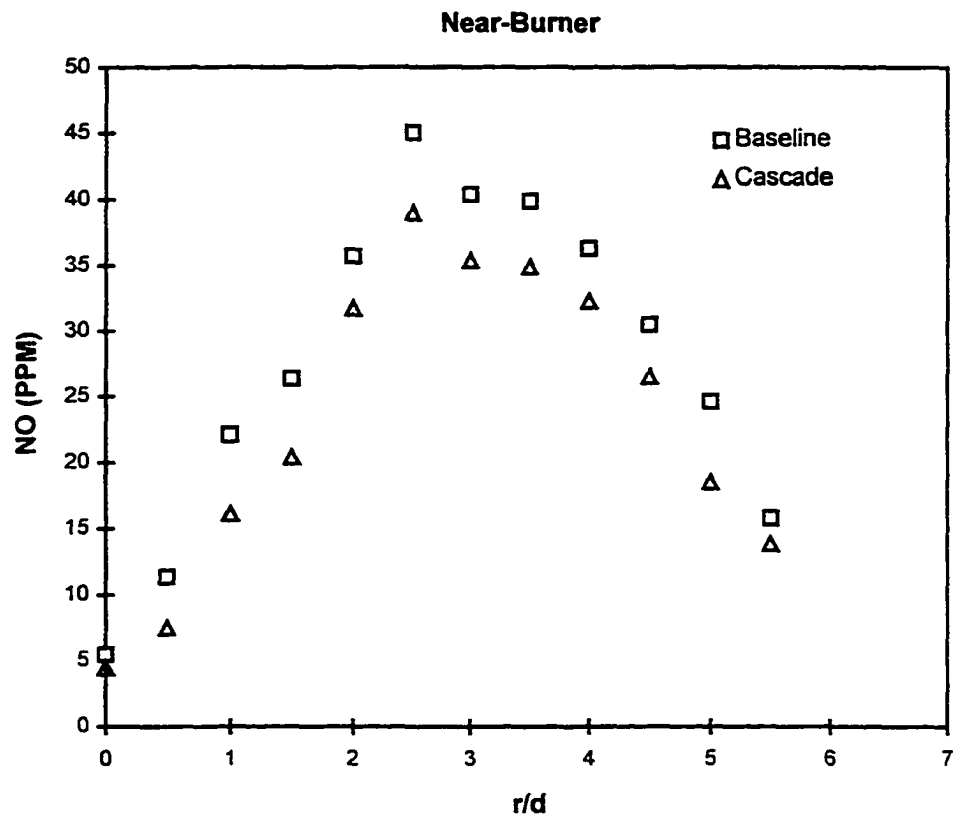


**Fig. 4.11a: Radial concentration profiles of NO for the baseline and cascaded flames in the near-burner region ( $x/d=20$ ) at  $Re=5100$ .**

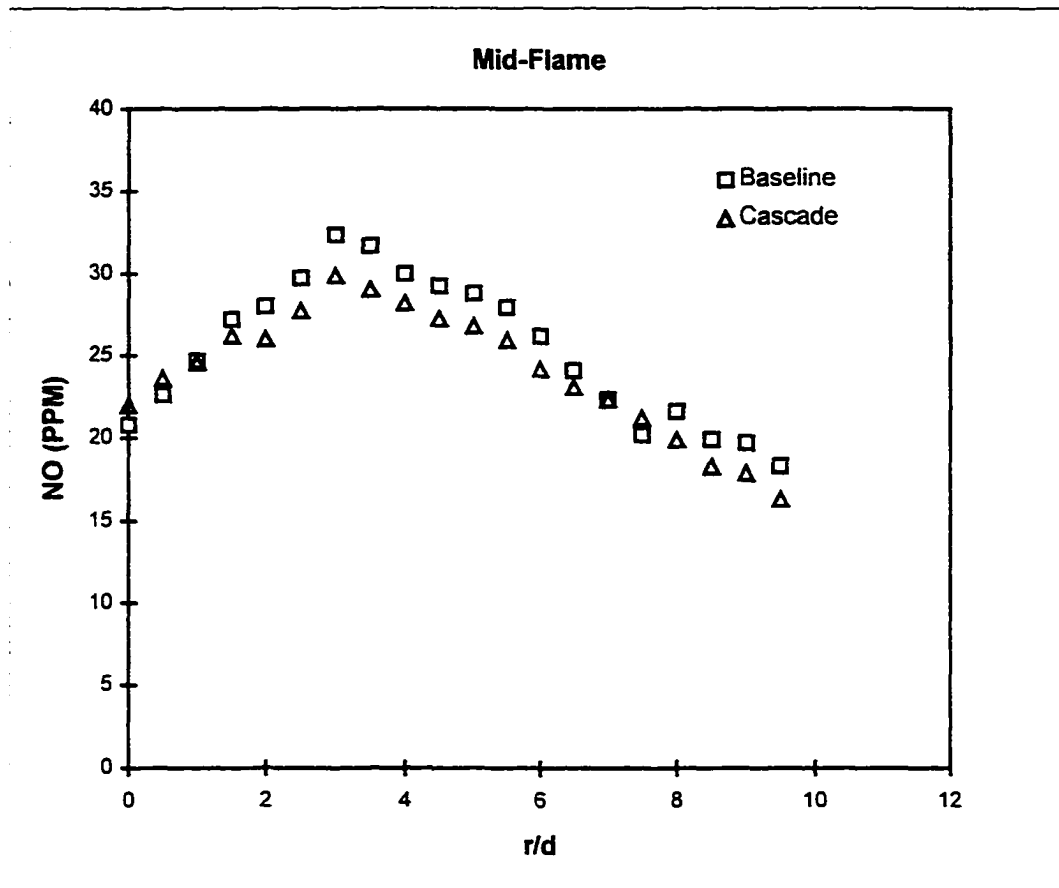


**Fig. 4.11b: Radial concentration profiles of NO for the baseline and cascaded flames in the mid-flame region ( $x/d=100$ ) at  $Re=5100$ .**

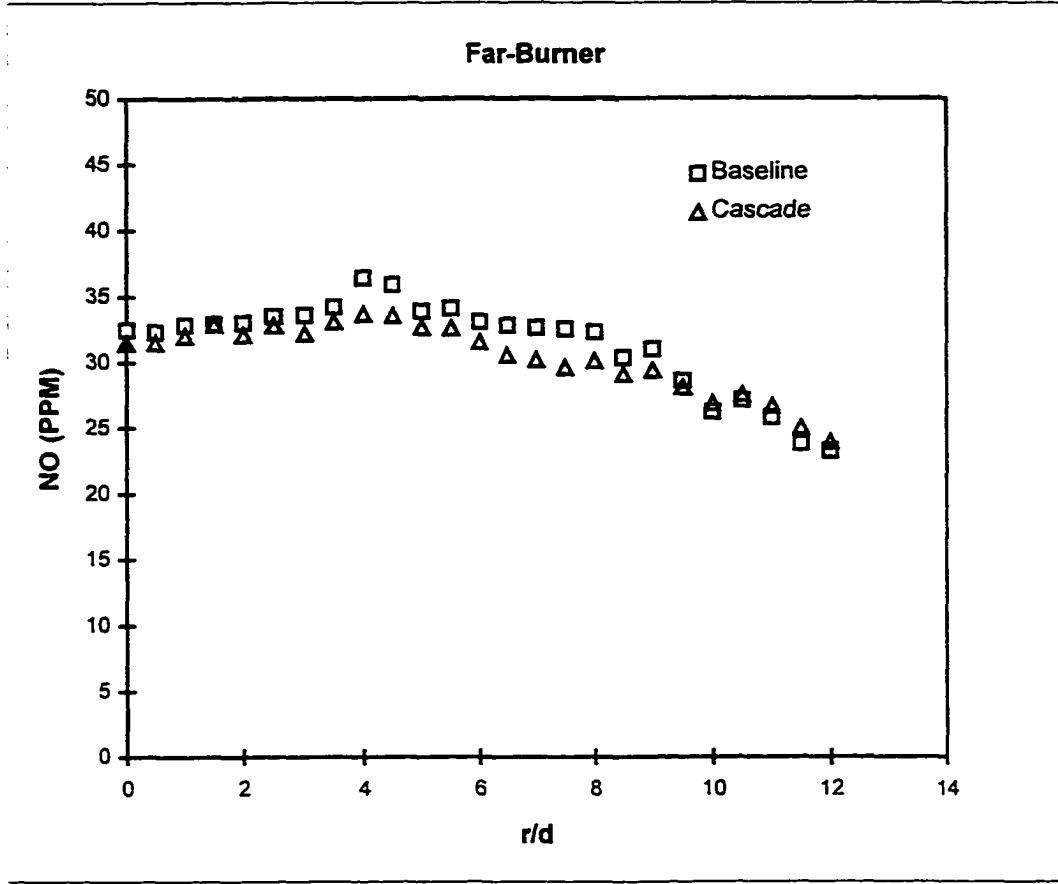


**Fig. 4.11c: Radial concentration profiles of NO for the baseline and cascaded flames in the far-burner region ( $x/d=180$ ) at  $Re=5100$ .**

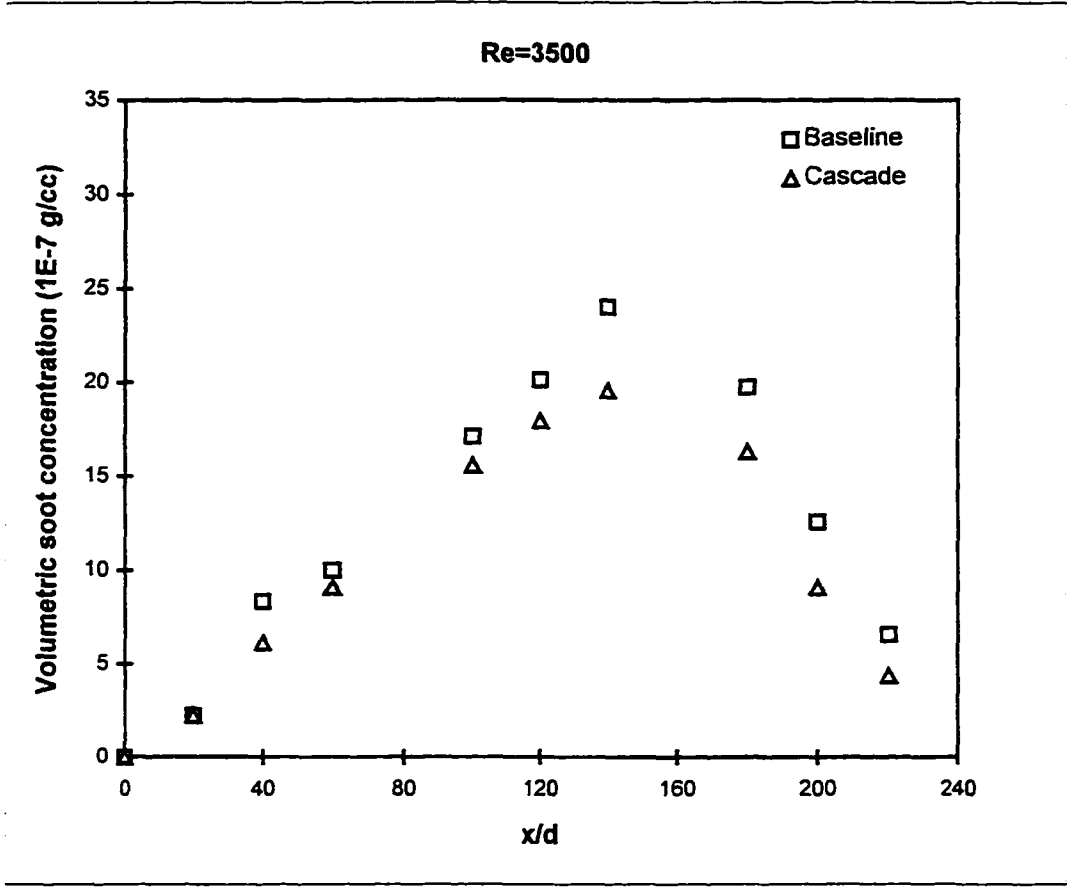


**Fig. 4.12a: Axial volumetric soot concentration profiles for the baseline and cascaded flames at Re=3500.**

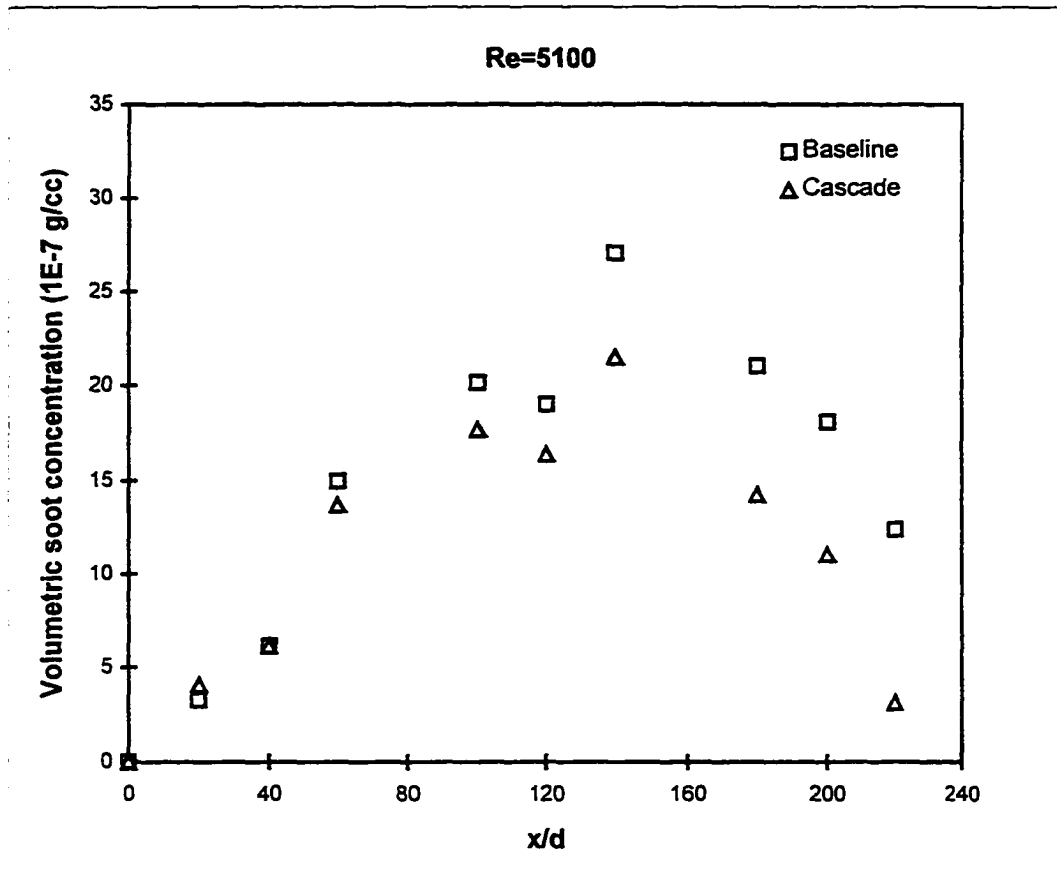


**Fig. 4.12b: Axial volumetric soot concentration profiles for the baseline and cascaded flames at Re=5100.**

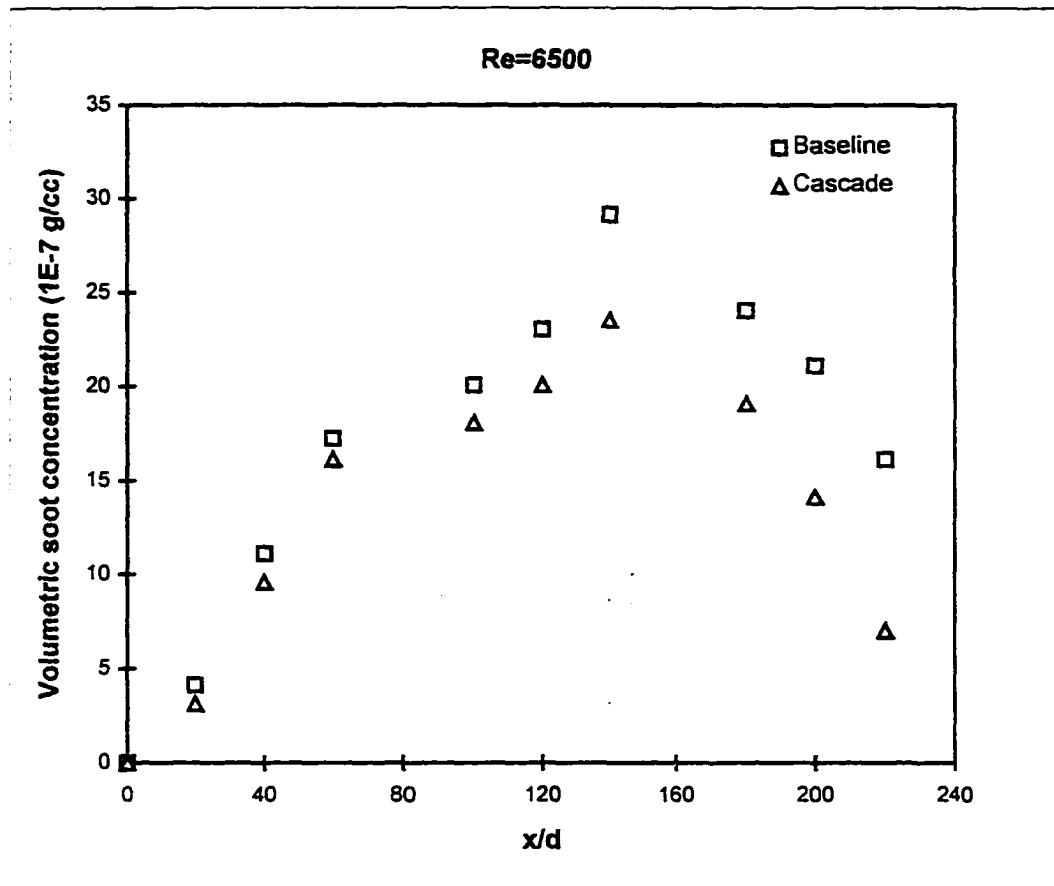


**Fig. 4.12c: Axial volumetric soot concentration profiles for the baseline and cascaded flames at Re=6500.**

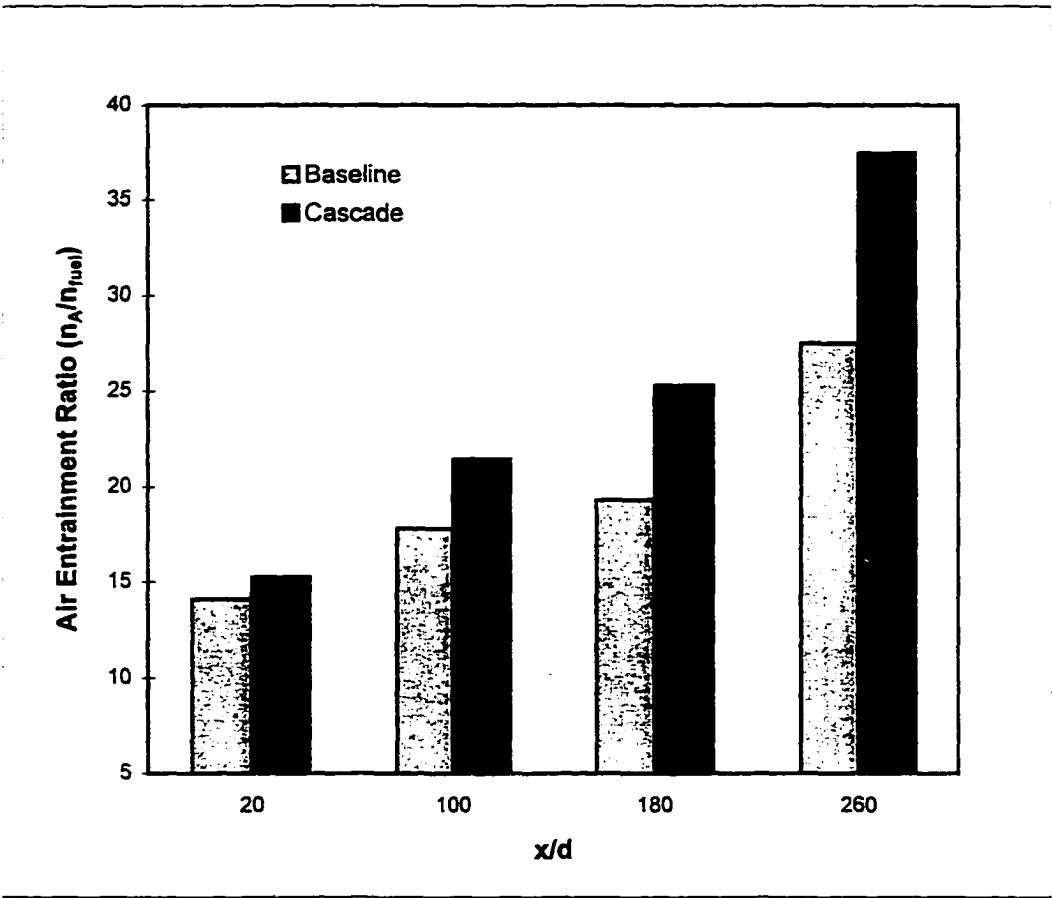


**Fig. 4.13: Secondary air entrainment ratio in the baseline and cascaded cold jets at different axial locations for  $Re=5100$ .**

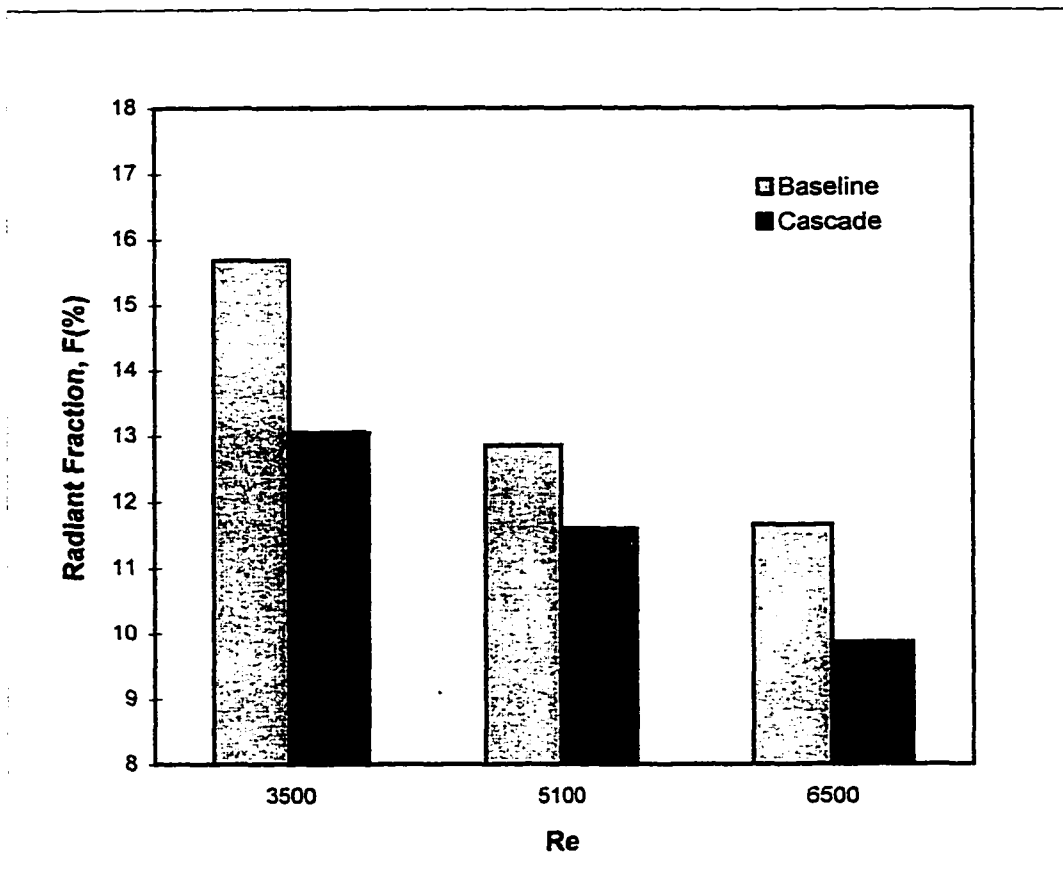


**Fig. 4.14: Radiant fraction for the baseline and cascaded flames at three Reynolds numbers.**

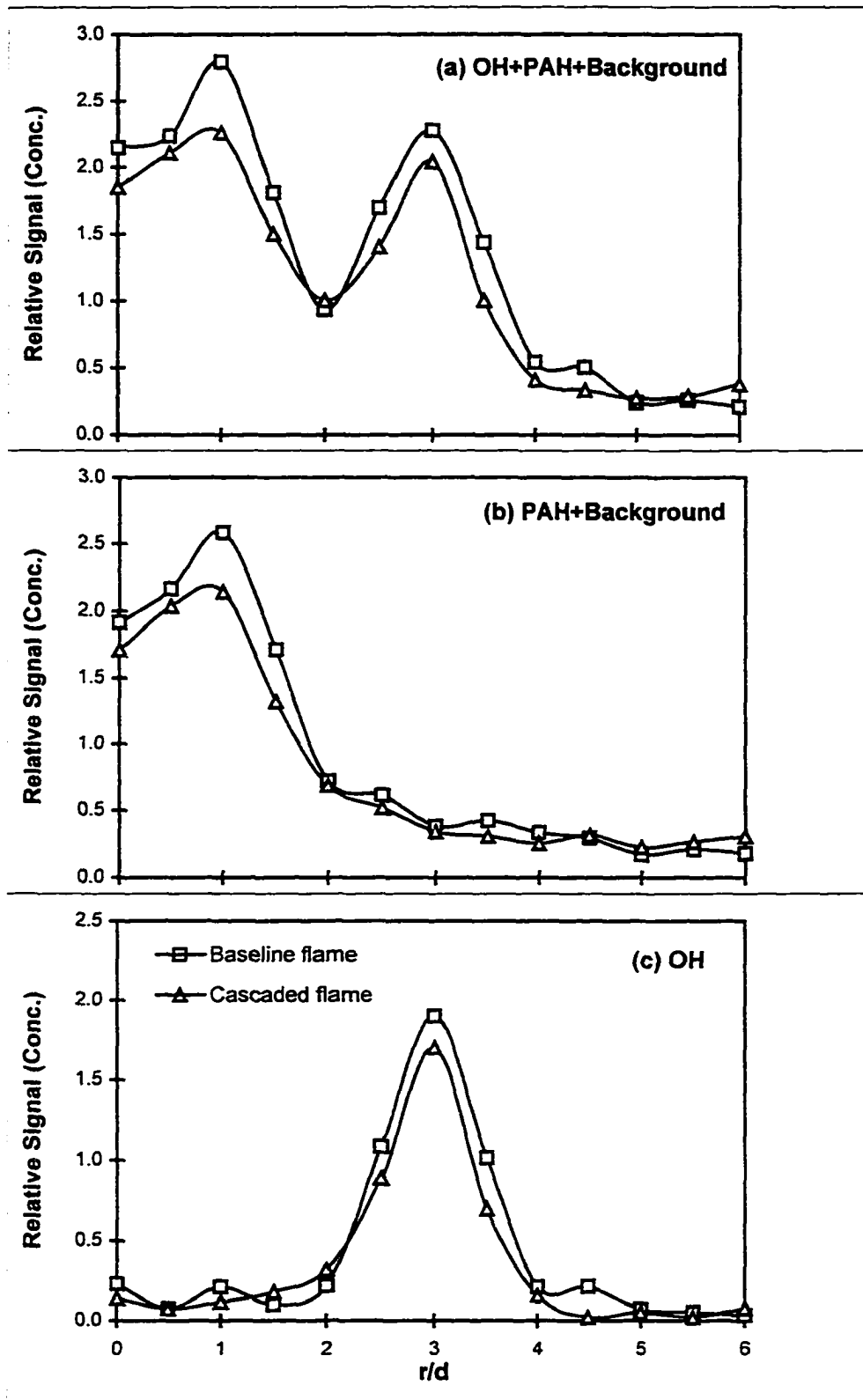


**Fig. 4.15: Relative LIF signal (concentration) profiles at  $x/d=20$  for the baseline and cascaded flames at  $Re=5100$ . Top (a): on resonance (OH+PAH+Background), middle (b): off resonance (PAH+Background), bottom (c): net (OH).**

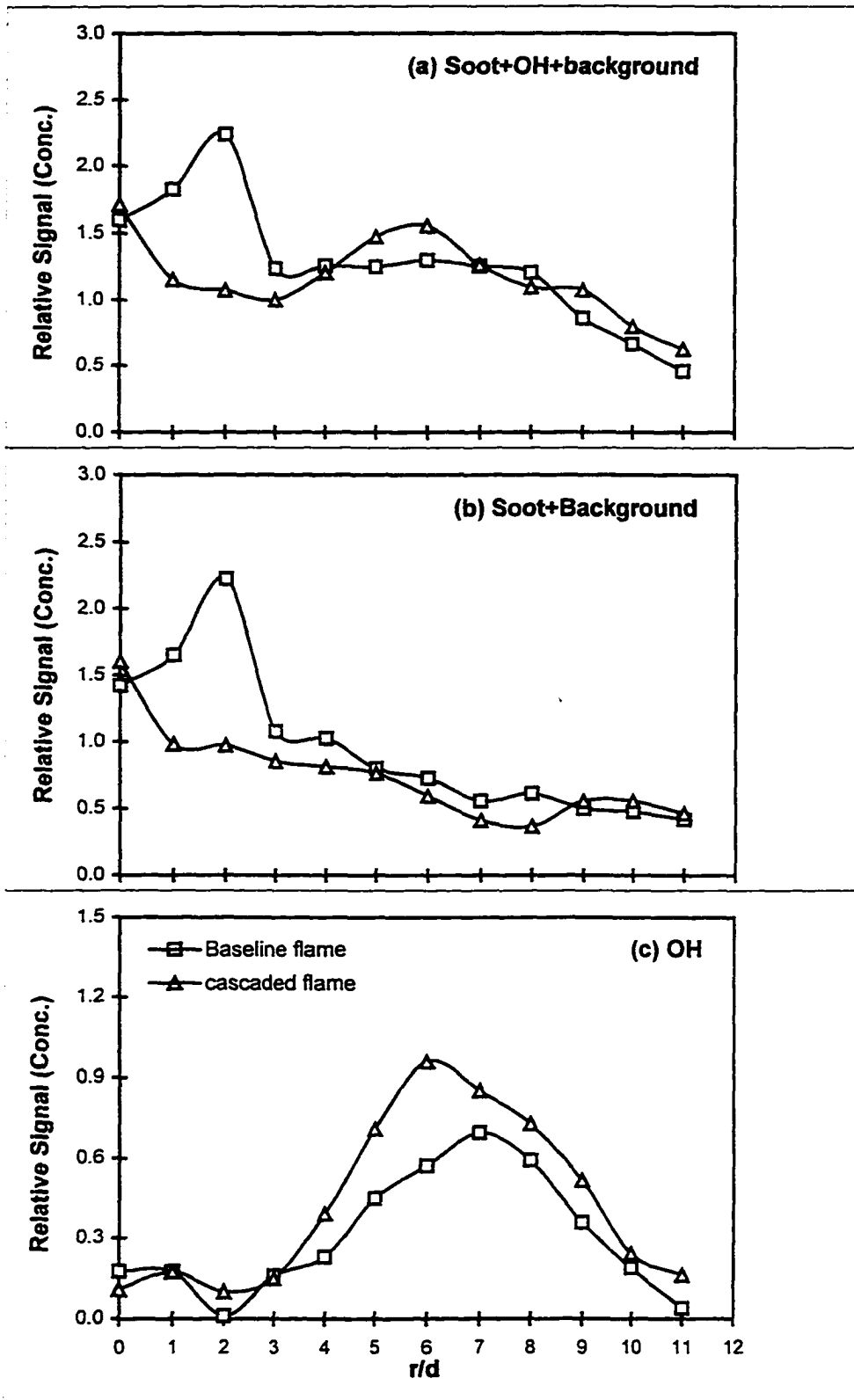


Fig. 4.16: Relative LIF signal (concentration) profiles at  $x/d=100$  for the baseline and cascaded flames at  $Re=5100$ . Top (a): on resonance (OH+Soot+Background) middle (b): off resonance (Soot+Background), bottom (c): net (OH).

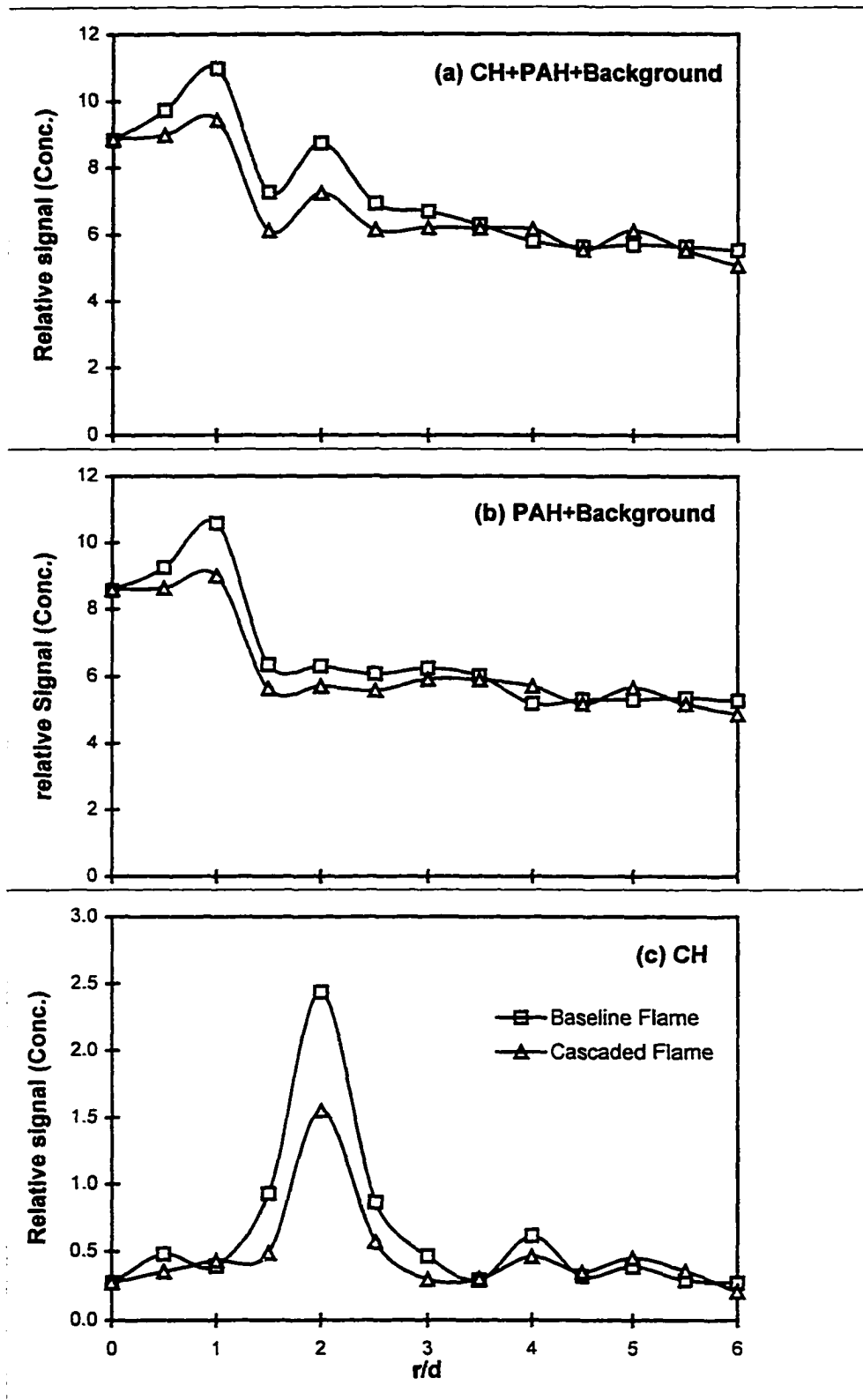


Fig. 4.17: Relative LIF signal (concentration) profiles at  $x/d=20$  for the baseline and cascaded flames at  $Re=5100$ . Top(a):on resonance (CH+PAH+Background) middle (b): off resonance (PAH+Background), bottom (c): net (CH).

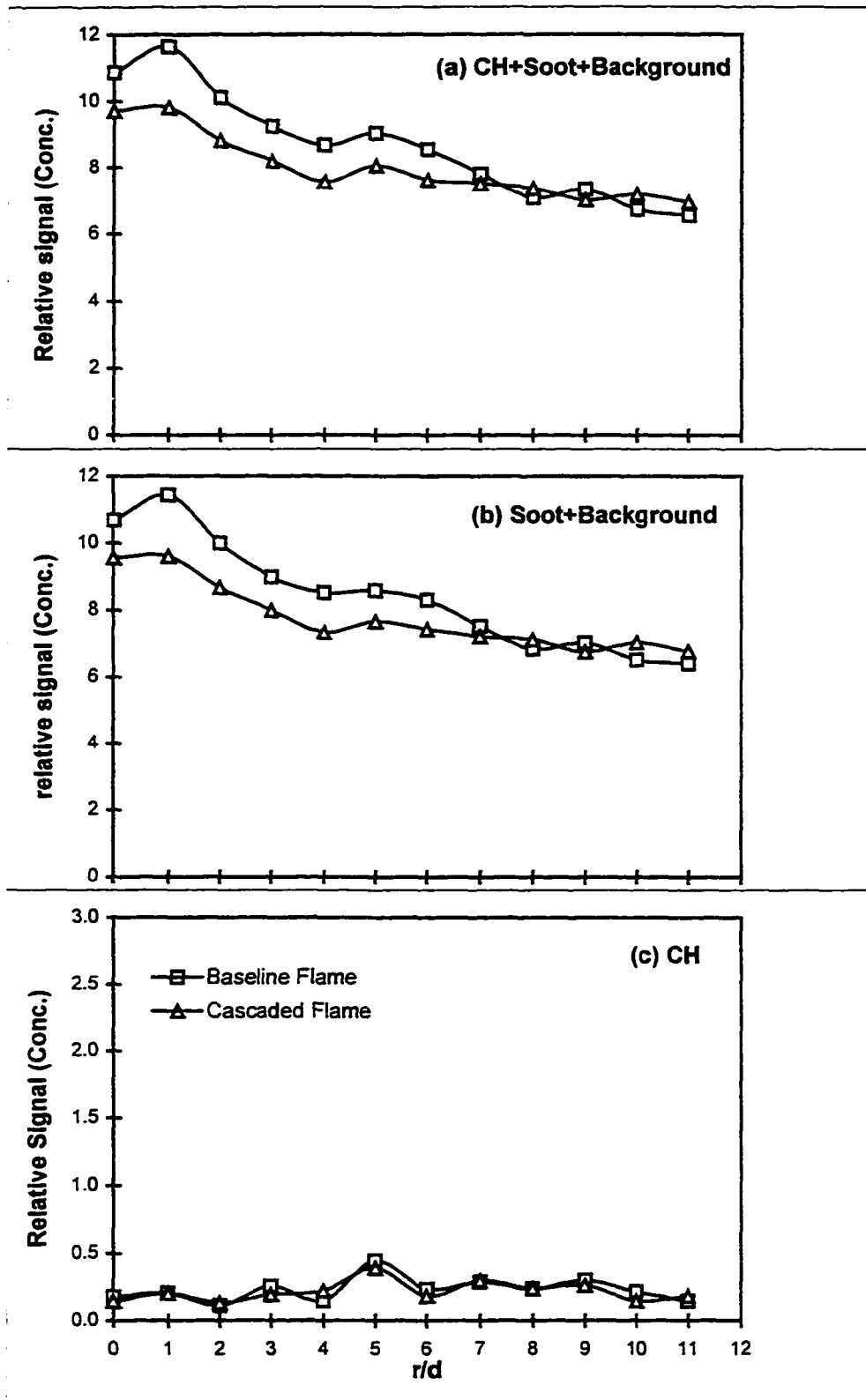


Fig. 4.18: Relative LIF signal (concentration) profiles at  $x/d=100$  for the baseline and cascaded flames at  $Re=5100$ . Top (a): on resonance (OH+Soot+Background), middle (b): off resonance (Soot+Background), bottom (c): net (CH).

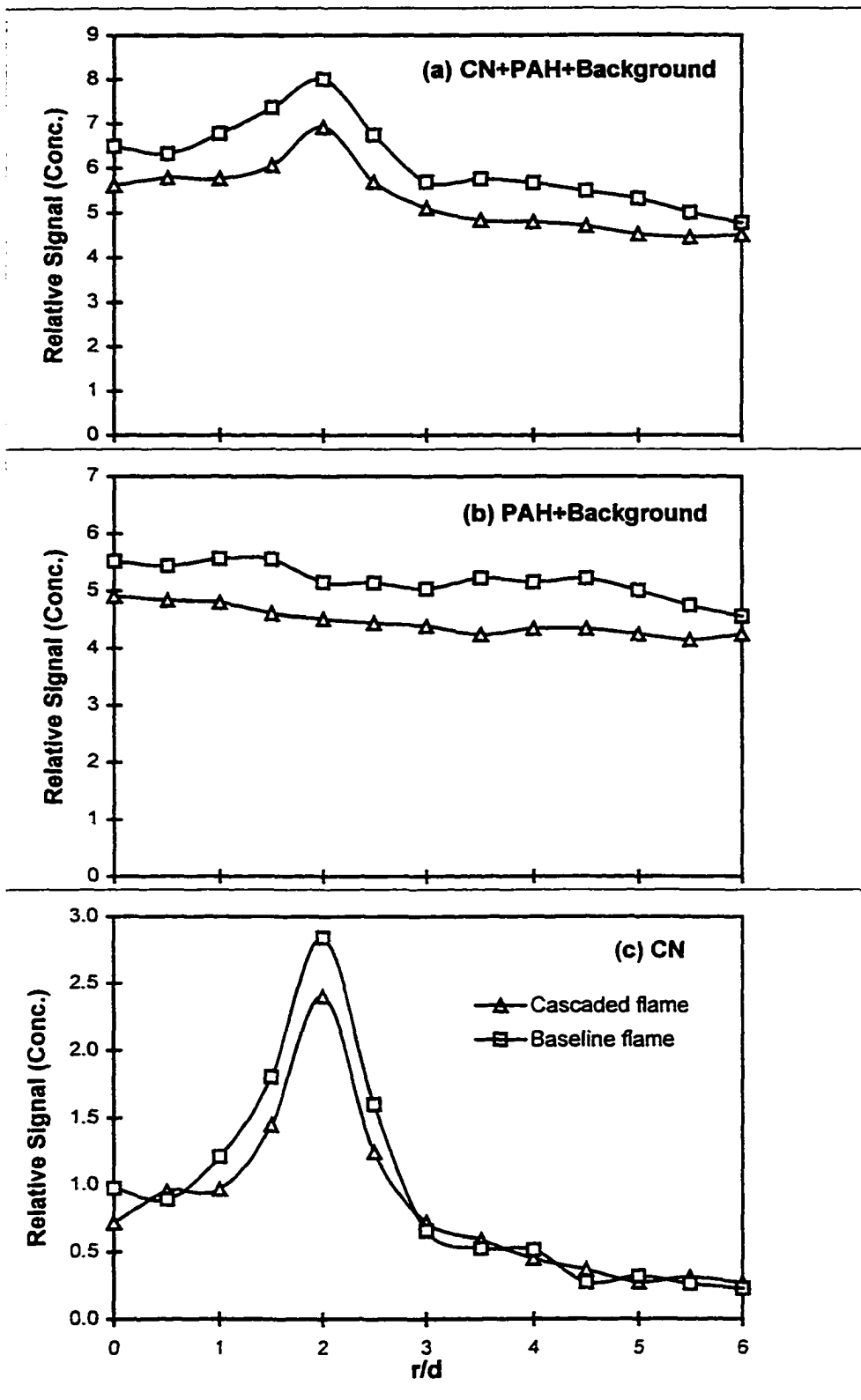


Fig. 4.19: Relative LIF signal (concentration) profiles at  $x/d=20$  for the baseline and cascaded flames at  $Re=5100$ . Top(a): on resonance (CN+PAH+Background) middle (b): off resonance (PAH+Background), bottom (c): net (CN).

# CHAPTER V

## NUMERICAL ANALYSIS

In this chapter, the baseline and cascaded gas jet propane diffusion flames, studied experimentally in this research, are numerically analyzed. The numerical computations were conducted using the *CFDRC-ACE+* (advanced computational environment) software package\*, version 5.0, 1998, in which CFD-GEOM (Interactive Geometric Modeling and Grid Generation software) and CFD-VIEW (3-D Computer Graphics and Animation Software) are incorporated. CFD-POST, a post processing utility program for CFD-ACE+ was also employed in computing CO and NO emissions. The details and results of the numerical modeling are presented in the following sections.

### 5.1 Physical Model

As mentioned in the earlier chapters, experiments were conducted in a steel combustion chamber. A circular opening covered with three layers of fine-mesh screens in the base plate allowed the insertion of a vertically mounted fuel burner. This opening also allowed uniform natural convection of air into the chamber. The top of the chamber was connected to the atmosphere through an exhaust duct. Commercial propane (95%  $C_3H_8$ , 3%  $C_4H_{10}$  and the rest  $C_3$ -hydrocarbons) was used as

---

\* From CFD Research Corporation, Huntsville, Alabama.

the fuel. The baseline flame was generated with a burner made of a stainless-steel circular tube of 2 mm internal diameter. The ambient pressure of the laboratory was maintained slightly above the atmospheric pressure to insure a positive draft inside the combustion chamber.

The cascaded flame is the baseline propane flame with the cascade of venturis installed around it. The cascade consisted of four identical venturis arranged at a certain spacing configuration (Table 5.1).

## 5.2 Numerical Model

The computational domain encompassed half of the flame jet (assuming axisymmetric flow conditions), extended to 64 cm in the axial direction and 14 cm in the radial direction (Fig. 5.1a). A total number of 11160 cells (248×45) were generated with increasing spacing in the radial and axial directions; this provided adequate resolution where gradients were large, near the centerline, and saved CPU time where gradients were small, near the edges (Fig.5.1b). All important factors such as a right-handed grid, smooth transition from small to large cells, and grid orthogonality were taken into account in the grid generation process, and they did have a beneficial effect on the convergence of the solution. Moreover, the computational results were checked for grid independence; it was found that increasing the total number of cells to 15840 (288×55), i.e., reducing the grid size by one third of its current configuration, produced only a change of 2-3% in temperature for the baseline case.

The venturis were modeled as two-dimensional axisymmetric convergent nozzles around the jet. Four identical nozzles of the dimensions and spacing provided in Table (5.1) were used to form the cascade (Fig. 5.1a). With the cascade being added to the jet, the geometric complexity of the problem increased; which required multi-domain structured grid systems to be connected and matched on the boundaries. The CFD-GEOM module (Interactive Geometric Modeling and Grid Generation Software) in the CFD-ACE+ package was used for geometric modeling and grid generation purposes.

### 5.2.1 Governing Equations

The code CFD-ACE+ employs a conservative finite-volume methodology and accordingly all the governing equations are expressed in conservative form in which tensor notation is generally employed. The basic governing equations are for the conservation of mass, momentum and energy:

*Continuity equation:*

$$\frac{\partial \rho}{\partial t} + \frac{\partial}{\partial x_j} (\rho u_j) = 0 \quad \dots\dots\dots (5.1)$$

where  $u_j$  is the  $j^{\text{th}}$  Cartesian component of velocity and  $\rho$  is the fluid density.

*Momentum equations:*

$$\frac{\partial}{\partial t} (\rho u_j) + \frac{\partial}{\partial x_i} (\rho u_i u_j) = -\frac{\partial p}{\partial x_j} + \frac{\partial \tau_{ij}}{\partial x_i} + \rho f_j \quad (j=1, 2, 3) \dots\dots\dots (5.2)$$

where  $p$  is the static pressure,  $\tau_{ij}$  is the viscous stress tensor and  $f_j$  is the body force.

For Newtonian fluids  $\tau_{ij}$  can be expressed as:

$$\tau_{ij} = \mu \left( \frac{\partial u_i}{\partial x_j} + \frac{\partial u_j}{\partial x_i} \right) - \frac{2\mu}{3} \left[ \frac{\partial u_k}{\partial x_k} \right] \delta_{ij} \quad \dots\dots\dots (5.3)$$

where  $\mu$  is the fluid dynamic viscosity and  $\delta_{ij}$  is the Kronecker delta.

*Energy Equation:*

The equation for the conservation of energy can take several forms. The static enthalpy form of the energy equation can be expressed as:

$$\frac{\partial}{\partial t}(\rho h) + \frac{\partial}{\partial x_j}(\rho u_j h) = -\frac{\partial q_j}{\partial x_j} + \frac{\partial p}{\partial t} + u_j \frac{\partial p}{\partial x_j} + \tau_{ij} \frac{\partial u_i}{\partial x_j} - \frac{\partial}{\partial x_j}(J_{mj} h_m) \quad \dots\dots (5.4)$$

where  $J_{mj}$  is the total (concentration-driven + temperature-driven) diffusive mass flux for species  $m$ ,  $h_m$  represents the enthalpy for species  $m$ , and  $q_j$  is the  $j$ -component of the heat flux.  $J_{mj}$ ,  $h_m$  and  $h$  are given as:

$$J_{mj} = -\rho D \frac{\partial Y_m}{\partial X_j} \quad \dots\dots\dots (5.5)$$

$$h_m = \int_{T_0}^T C_{p_m}(T) dT + h_{f_m}^\circ \quad \dots\dots\dots (5.6)$$

$$h = \sum_{m=1}^n Y_m h_m \quad \dots\dots\dots (5.7)$$

Where  $D$  is the diffusion coefficient,  $C_p$  is the constant-pressure specific heat, and  $h_f^\circ$  is the enthalpy of formation at standard conditions ( $P_0=1 \text{ atm}$ ,  $T_0=298 \text{ K}$ ).

The Fourier's law is employed for the heat flux:

$$q_j = -K \frac{\partial T}{\partial x_j} \quad \dots\dots\dots (5.8)$$

where  $K$  is the thermal conductivity.

*Mixture Fractions:*

$$\frac{\partial}{\partial t}(\rho f_k) + \frac{\partial}{\partial x_j}(\rho u_j f_k) = \frac{\partial}{\partial x_j} \left( D \frac{\partial f_k}{\partial x_j} \right) \dots\dots\dots (5.9)$$

where D is the diffusion coefficient,  $f_k$  is the mixture fraction for the  $k^{\text{th}}$  mixture.

The transport properties for a gas mixture are calculated as follow (Kanury, 1992):

$$\mu_{\text{mix}} = \frac{\sum_{i=1}^n X_i \mu_i}{\sum_{j=1}^n X_j \phi_{ij}} \dots\dots\dots (5.10)$$

$$K_{\text{mix}} = \frac{\sum_{i=1}^n X_i K_i}{\sum_{j=1}^n X_j \phi_{ij}} \dots\dots\dots (5.11)$$

$$D_{i-\text{mix}} = \frac{1 - X_i}{\sum_{\substack{j=1 \\ j \neq i}}^n \frac{X_j}{D_{ij}}} \dots\dots\dots (5.12)$$

where  $X_i$  is the mole fraction of species  $i$ ,  $n$  is the total number of species in the mixture,  $D_{ij}$  is the binary diffusion coefficient of species  $i$  and  $j$ .  $\phi_{ij}$  is given as follows:

$$\phi_{ij} = \frac{1}{\sqrt{8}} \left[ 1 + \frac{M_i}{M_j} \right]^{-1/2} \left[ 1 + \left( \frac{\mu_i}{\mu_j} \right)^{1/2} \left( \frac{M_j}{M_i} \right)^{1/4} \right]^2 \dots\dots\dots (5.13)$$

### 5.2.2 Solution Methodology and Algorithm

All governing equations can be expressed in a general form as:

$$\frac{\partial}{\partial t}(\rho \phi) + \frac{\partial}{\partial x_j}(\rho u_j \phi) = \frac{\partial}{\partial x_j} \left( \Gamma \frac{\partial \phi}{\partial x_j} \right) + S_\phi \dots\dots\dots (5.14)$$

where  $S_p$  is the source term,  $\Gamma$  is the transport coefficient and  $\phi$  is the dependent variable.

A cell-centered control volume approach is used, in which the discretized equations or the finite difference equations (FDE) are formulated by evaluating and integrating fluxes across the faces of control volumes (Fig. 5.2) in order to satisfy the above conservation equation. The first order upwind scheme was used for evaluating convective fluxes over a control volume. The result is that each dependent variable ( $\phi$ ) is solved at the center (P) of each control volume in terms of its neighboring values as follow:

$$a_p \phi_P = a_w \phi_W + a_e \phi_E + a_s \phi_S + a_n \phi_N + a_{sw} \phi_{sw} + a_{se} \phi_{se} + a_{nw} \phi_{nw} + a_{ne} \phi_{ne} + S \quad \dots\dots\dots (5.15)$$

where P, W, E, N, S, H, L represent the locations at which the variable is computed (Fig. 5.2. is 2-D case) and  $a_p, a_w,$  etc. are the link coefficients. The above equation is known as the finite difference equation (FDE). This FDE, in general, is nonlinear since the link coefficients themselves are functions of  $\phi_p, \phi_w,$  etc. When the FDE is formulated for each computational cell, it results in a set of coupled nonlinear algebraic equations. Therefore, an iterative solution scheme is employed; in which the assembled equations for each dependent variable are solved sequentially and repeatedly with the goal of improving the solution at each iteration. The non-linear and coupled nature of the equations makes it necessary to under-relax the iteration to iteration changes in order to obtain convergence of the solution.

Since no governing PDE for pressure is presented, pressure-based methods utilize the continuity equation for pressure. In CFD-ACE+ the SIMPLEC scheme, proposed by Van Doormal and Raithby (1984), has been used. SIMPLEC stands for “Semi-Implicit Method for Pressure-Linked Equation Consistent”, in which an equation for pressure correction is derived from the continuity equation. The overall solution procedure for the SIMPLEC algorithm is shown in Fig. 5.3a. Note that NITER (the number of iterations) and C\_ITER (the number of continuity iterations) are parameters to be specified by the user. The number of iterations to be performed is dictated by the overall residual reduction obtained. At each iteration the program will calculate a residual for each variable which is the sum of the absolute value of the residual of that variable at each control cell. In general, it is desirable to obtain a five order of magnitude reduction in the residual before declaring that convergence has been obtained. This occurred after about 12000 iterations, where the residual of each solved quantity was less than  $10^{-5}$ . The steps involved for assembling and solving the equation set for a particular dependent variable are shown in Fig. 5.3b.

### 5.2.3 Reaction Model

The reaction model used by CFD-ACE+ was the instantaneous chemistry model in which the reactants are assumed to react completely upon contact. The reaction rate is infinitely rapid and one reaction step is assumed. Two reactants, which are commonly referred to as “fuel” and “oxidizer”, are involved. A surface “flame sheet” separates the two reactants. The products are  $\text{CO}_2$ ,  $\text{H}_2\text{O}$ ,  $\text{CO}$ ,  $\text{NO}$ , and  $\text{OH}$ .

The mass fractions for this model are computed by first using Eq. 5.16 to obtain the composition that would occur without the reaction. The “unreacted” composition, denoted by the superscript “u”, is given by

$$(Y_i)^u = \sum_{k=1}^K \xi_{ik} f_k \dots\dots\dots (5.16)$$

where  $\xi_{ik}$  is the mass fraction of the  $i^{\text{th}}$  species in the  $k^{\text{th}}$  mixture,  $Y_i$  is the mass fraction of the  $i^{\text{th}}$  species and  $f_k$  is the mixture fraction of the  $k^{\text{th}}$  mixture. The change in composition due to the instantaneous reaction is then added to the unreacted mass fractions, as described below.

A stoichiometrically correct reaction step needs to be specified. The mass of species  $i$  produced per unit mass of fuel consumed is

$$r_i = -\frac{v_i M_i}{v_f M_f} \dots\dots\dots (5.17)$$

where  $v$  is the stoichiometric coefficient of the species in the overall reaction; positive for product species and negative for fuel and oxidizer. The instantaneous reaction mechanism consumes either all the fuel or all the oxidizer, whichever is limiting. The amount of fuel consumed is

$$\Delta Y_f = \min\left(\frac{(Y_f)^u}{-r_f}, \frac{(Y_{ox})^u}{-r_{ox}}\right) \dots\dots\dots (5.18)$$

The change in each species due to the reaction is proportional to the change in fuel, with the proportionality constant given by Eq. 5.17. The mass fraction of each species is then given by

$$Y_i = (Y_i)^u + r_i \Delta Y_f \dots\dots\dots (5.19)$$

The right-hand side of the above equation is only a function of the K mixture fractions. Therefore, K-1 transport equations must be solved for the mixture fractions. These equations have no source terms due to chemical reactions.

#### **5.2.4 Assumptions and Boundary Conditions**

The following is a summary of the approximations and assumptions that have been made to simplify the numerical analysis:

1. Laminar, steady, and axisymmetric 2- dimensional flow
2. Newtonian fluid and ideal gas behavior
3. Uniform inlet velocity profiles
4. One-step, surface-sheet and instantaneous reaction
5. Soot-free diffusion flames
6. Negligible radiation losses from the flame

The geometry, coordinate system, and boundary conditions of the computational model are shown in Fig. 5.1a. The boundary conditions are provided from the physics of the problem. Due to the symmetry around the x-axis, only one half of the flame is modeled. The experimental measurements indicated that the maximum value of half of the flame width, determined from the temperature profiles at  $x = 64$  cm for the baseline case, is 7 cm. Therefore, both the centerline and the boundary at radius ( $y$ ) = 14 cm are specified as symmetry lines in both the baseline and cascaded cases. The fuel inlet velocity is 11 m/s; based on the jet-exit diameter and Reynolds number (Table 5.1). The coflow air velocity convected into the chamber through the fine-

mesh screens is 0.25 m/s, as measured by a hot wire anemometer. The venturis are simulated as thin-wall solid boundaries; by default this provides the no-slip condition ( $U=0, V=0$ ) on both sides. A similar thin-wall boundary condition is also assigned for the tube-burner wall. The exit boundary is assigned a constant pressure (atmospheric) value.

### 5.3 Carbon Monoxide and Nitric Oxide Post Processing

This option is provided by CFD-POST (a post processing utility program for CFD-ACE+ package) for the prediction of CO and NO mass fractions when the concentrations of instantaneous or equilibrium products have been predicted by CFD-ACE+. The CO and NO fields are solved by calculating the CO and NO source terms for each cell and using the convective and diffusive fields as determined by CFD-ACE+. The solution assumes that the upwind scheme was used in CFD-ACE+. It also assumes that CO and NO post processing have a negligible effect on the heat release and the overall flow field.

#### 5.3.1 Carbon Monoxide Post Processing

The Warnatz (1984) CO oxidation reaction is given by



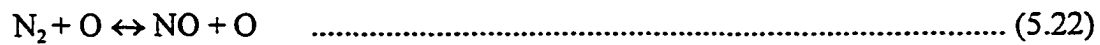
From this, the destruction of CO can be expressed as:

$$\frac{d[\text{CO}]}{dt} = -K_1[\text{OH}]_e \left\{ 1 + \frac{[\text{CO}]_e}{[\text{CO}_2]_e} \right\} ([\text{CO}] - [\text{CO}]_e) \quad \dots\dots\dots (5.21)$$

where the reaction rate  $K_1$  is determined from:  $K_1 = AT^a e^{-E/RT}$  with  $A=3.5e3$ ,  $a=1.5$ , and  $E/RT=373$ . The instantaneous or equilibrium values of  $CO_2$ ,  $CO$  and  $OH$  should have been calculated and available by CFD-ACE+.

### 5.3.2 Nitric Oxide Post Processing

The concentration of  $NO$  was predicted using the thermal- $NO$  (Zeldovich) mechanism, which consists of the following three reactions:



These reactions can be solved using either simplified, simplified reversible or extended Zeldovich methods of CFD-POST. The extended method was used in this study. The production of  $NO$  by the extended method can be expressed as:

$$\frac{d[NO]}{dt} = 2k_1[N_2][O] \left\{ \frac{1 - [NO]^2 / K[N_2][O_2]}{1 + k_{-1}[NO] / (k_2[O_2] + k_3[OH])} \right\} \quad \dots\dots\dots (5.25)$$

where

$$K = \left( \frac{k_1}{k_{-1}} \right) \left( \frac{k_2}{k_{-2}} \right)$$

and  $k_1$ ,  $k_2$ ,  $k_3$ ,  $k_{-1}$ ,  $k_{-2}$  and  $k_{-3}$  are forward and reverse reaction rate constants for the three reactions above. Since the concentration of  $NO$  appears in the right hand side of the above equation for  $NO$  production, the  $NO$  source term is determined by an iterative process. All the species concentrations appearing in the above equation ( $O_2$ ,  $N_2$ ,  $O$  and

OH) must be available from the reaction model used in CFD-ACE+. The reactions rates are those of Miller and Bowman (1989) and are shown in Table 5.2.

## 5.4 Results and Discussion

In this section, the numerical results generated from the CFD-ACE+ model are presented and discussed. These include profiles of: temperature, CO<sub>2</sub>, O<sub>2</sub>, CO, NO, OH and equivalence ratio ( $\phi$ ), for both the cascaded and baseline flames. The results were obtained at a burner-exit Reynolds number 5100 and in the three regions; near-burner, mid-flame and far-burner, which corresponds to the three axial locations  $x/d$  20, 100 and 180, respectively. The concentrations of CO and NO were obtained by further processing through CFD-POST, a post processing CFD-ACE+ utility program. The concentration of NO was predicted using the thermal-NO mechanism. In addition, the corresponding experimental data available from the experimental program of this project were imported for comparison purposes.

### 5.4.1 Flame Temperature Profiles

Figures 5.4 (a, b, c) show the theoretically-predicted radial temperature profiles, for the baseline and cascaded flames, at three axial locations; near burner ( $x/d=20$ ), mid-flame ( $x/d=100$ ) and far-burner ( $x/d=180$ ) regions, respectively. The corresponding experimental data points are added to the same figures for comparison purposes. From the theoretical profiles, the following observations can be made: (i) an off-axis peak exists in all three regions of concern, however, its radial location moves

further outward in the mid-flame and far-burner regions; (ii) the peak temperature of the cascaded flame drops by 9%, 6% and 1% in the near-burner, mid-flame and far-burner locations, respectively; from its baseline values; (iii) the overall average temperature of the cascaded flame decreases by 13%, 19% and 17% in the same three regions of concern, respectively, from its baseline values; (iv) all cascaded profiles are shifted inward towards the fuel-rich side of the flame, the least shift is observed in the near-burner region; (v) the cascaded flame has significantly lower temperatures in the fuel-lean side of the flame, compared to the baseline case. However, it has higher valley temperatures in the fuel-rich side; (vi) the temperature changes, caused by the cascade on the flame show that the venturi-cascade is more influential in the fuel-lean side than in the fuel-rich side; (vii) the cascade effect is the least in the near-burner region, but increases significantly in both mid-flame and far-burner regions.

The observed shift of the temperature profile towards the fuel-rich side of the flame is a direct result of the venturi effect which ejects the co-flow air stream into the core of the combustion zone, thereby leading to better mixing rates of air with the unburned fuel and the consequent shift of the stoichiometric contour towards the center of the flame. This leaning process has two different effects on the fuel-lean and fuel-rich sides of the flame; the temperature of the latter increases while that of the former decreases. The valley temperature increase in the fuel-rich side of the cascaded flame is a result of higher oxygen availability, pushing the mixture towards stoichiometry. On the other hand, the temperature decrease in the lean side is due to the excess air; pushing the mixture far away from stoichiometry. The net effect of the cascade on the flame temperature is determined by the resultant of the two

aforementioned factors.

The theoretical temperature profiles, in all three regions, show that the changes brought by cascading to the fuel-lean side are more significant than those brought to the fuel-rich side. This is reasonable, since the lean side of the flame is closer to the venturis and therefore should be the most affected. This explains the theoretical predicted decrease in overall and peak temperatures by the effect of cascading. The enhanced effect of cascading in the downstream regions was observed and explained earlier, along with the experimental results in chapter 4.

The agreement between the experimentally-measured and theoretically-predicted temperatures is fairly good in the near burner region. However, it becomes poorer in the mid-flame and far-burner regions. The most likely reasons are the soot heterogeneous combustion processes and the radiation effects that play an important role in such a sooty-propane diffusion flame, and particularly in the mid-flame and far-burner regions. These mechanisms and processes are not taken into account by the combustion model used in CFD-ACE+. Moreover, the radiation interactions between the flame and the cascade (radiation blockage by venturis) were also not included in the numerical model.

The good agreement in the near burner region can be explained by the stoichiometric homogenous (soot free) gas-phase reactions taking place in this region, which are basic assumptions incorporated in the reaction model used. However, the discrepancies between theoretical predictions and experimental measurements still exist in this region, but are relatively small. These discrepancies are due to the inherent limitations of the model through several assumptions and simplifications that

were made in the chemical-reaction model including: single step reaction, instantaneous chemistry (i.e., the reactants react completely upon contact), infinitely rapid reaction rate, a surface (flame sheet) approximation, constant specific heats of the species of concern, and many other assumptions to simplify the reaction model.

#### 5.4.2 Carbon Dioxide Concentration Profiles

Figures 5.5 (a, b, c) show the theoretically-predicted radial concentration profiles of CO<sub>2</sub> in the near-burner, mid-flame and far-burner regions, respectively, the same conditions pertaining to the earlier predicted temperature profiles. The corresponding experimental data are also added to the same figure for comparison purposes. From the theoretical profiles the following can be observed: (i) the off-axis peak exists in the three regions of concern; (ii) the peak CO<sub>2</sub> concentrations for the baseline flame are at  $r/d$  2.82, 5.56 and 7.84 in the near-burner, mid-flame and far-burner regions, respectively. The corresponding CO<sub>2</sub> peaks in the cascaded flame are at  $r/d$  2.82, 4.84 and 6.3; (iii) The previously mentioned peak CO<sub>2</sub> radial positions coincide well with those of temperature at the same conditions; (iv) The cascaded CO<sub>2</sub> profiles are shifted inward, like the earlier temperature profiles; the least shift occurs in the near-burner region while the most occurs in the far-burner region; (v) Even though the peak CO<sub>2</sub> values match well with peak temperatures, the CO<sub>2</sub> profiles appear to be sharper and narrower than those of temperature; (vi) The predicted CO<sub>2</sub> valley concentrations are much lower than the temperature-based expectations; CO<sub>2</sub> decreases sharply from its peak value to approach zero in the early fuel-rich region,

whereas the corresponding temperature values still fairly high; (vii) The average CO<sub>2</sub> concentration in the cascaded flame decreases by 35%, 37% and 32% from its baseline values, in the three axial locations of concern, respectively; this corresponds to 13%, 19% and 17% average decrease in theoretical-predicted temperatures at same conditions; (viii) In all three regions, the cascaded flame has higher CO<sub>2</sub> concentrations in the fuel-rich side of the flame compared to the baseline case. However, it has lower CO<sub>2</sub> concentrations in the fuel-lean side. Same behavior has been noticed for temperature profiles.

The existence of off-axis peaks, their radial locations, the inward shift of the profiles, the CO<sub>2</sub> increase in the fuel rich side and decrease in the fuel-lean side, the overall decrease of CO<sub>2</sub> in the cascaded flame; all follow the temperature profiles and similar explanations apply. This is reasonable, since CO<sub>2</sub> is a direct combustion product which depends primarily on temperature and stoichiometry of the flame. However, the sharp-narrow appearance with very low valley CO<sub>2</sub> concentrations does not keep pace with the corresponding temperature trends. The most probable reason is the chemistry-reaction model that has been employed by CFD-ACE+, which assumes instantaneous, infinitely rapid and surface-sheet reaction upon contact of the reactants, thereby not allowing enough time for CO<sub>2</sub> to diffuse towards the fuel-lean and fuel-rich sides of the flame, and therefore leading to the observed narrow and sharp CO<sub>2</sub> profiles.

The comparison between the theoretically-predicted and experimental-measured data shows a good agreement in the near-burner region. However, the agreement is poor in the mid-flame and far-burner regions, a similar discrepancy has been observed

and explained for the temperature measurements before. The theoretical profiles are sharper and narrower than the experimental profiles; CO<sub>2</sub> concentration has been apparently underestimated by the theoretical model in the far fuel-rich and fuel-lean zones. This observation, combined with the original disagreement between the sharpness of predicted CO<sub>2</sub> and temperature profiles, is a strong indication of the drawback in the instantaneous chemistry model that has been mentioned and explained in the previous paragraph. The predicted peak CO<sub>2</sub> concentrations are higher than the experimental measurements i.e., CO<sub>2</sub> peaks are overestimated by the model, this might be also due to the same reason; the instantaneous nature of the model.

### 5.4.3 Oxygen Concentration Profiles

Figures 5.6 (a, b, c) show the predicted O<sub>2</sub> radial concentration profiles in the near-burner, mid-flame and far-burner regions, respectively. From the theoretical predicted profiles the following can be observed: (i) the O<sub>2</sub> concentration starts with a zero value at the central axis and remains zero in the fuel-rich side until it reaches the stoichiometric contour ( $\phi=1$ ), then starts to build up in the radial outward direction until it attains its atmospheric value (~21%) near the outside boundary of the flame; (ii) O<sub>2</sub> profiles spread outward in the radial direction and become wider in the mid-flame and far-burner locations; (iii) O<sub>2</sub> in the baseline flame starts to build up at  $r/d$  2.82, 5.66 and 7.06 in the near-burner, mid-flame and far-burner, respectively, whereas, the corresponding build up radial positions for the cascaded flame are  $r/d$

2.21, 4.14 and 5.56; (iv)  $O_2$  profiles in the cascaded flame build up faster and consequently attain the ambient value earlier than the baseline ones; (v)  $O_2$  concentration in the cascaded flame increases by an average of 7%, 26% and 44% compared to its baseline values, in the near-burner, mid-flame and far-burner axial locations, respectively; (vi)  $O_2$  profiles in the cascaded flame are shifted inward, similar to what has been observed in the earlier temperature and  $CO_2$  profiles.

The zero  $O_2$  concentration observed in the fuel-rich region is consistent with the absence of  $CO_2$  values observed earlier in the same region.  $O_2$  has been entirely consumed at the stoichiometric contour; which is what has been assumed by the flame sheet approximation made in the reaction model employed by CFD-ACE+. The outward spread of the profile in the mid-flame and far-burner regions is a result of the jet growth and greater quantities of air entrained into to the gas jet flame as it proceeds downstream. The faster build-up rate in the cascaded flame compared to the baseline case is a clear indication of the higher rates of mixing with air provided by the cascade of venturis. The average increase of  $O_2$  in the cascaded flame compared to the baseline case is the direct cause of the temperature drop observed and explained earlier. The inward shift of the profiles has been noticed for earlier temperature and  $CO_2$  profiles too, and therefore the same aforementioned explanation applies.

The comparison of the theoretical profiles with the experimental measurements shows a good agreement in the near-burner region. However, the agreement is poorer in the mid-flame and far-burner regions. Similar results were obtained and discussed for temperature and  $CO_2$  profiles, and hence the previously presented explanations apply here too. The experimental profiles, in all three regions of concern, show

clearly the presence of  $O_2$  in the flame core. However, the theoretical results do not indicate any penetration of  $O_2$  into the fuel rich region of the flame. The most likely reason behind this discrepancy is the instantaneous nature of the reaction-chemistry model which consumes all  $O_2$  at the flame sheet and does not allow enough time for  $O_2$  to penetrate further into the flame core.

#### 5.4.4 Carbon Monoxide Concentration Profiles

Figures 5.7 (a, b, c) show the theoretically-predicted CO concentration profiles in the near-burner, mid-flame and far-burner axial locations, respectively. The corresponding experimental data are added to the same figures for comparison purposes. The predicted CO concentrations were calculated by post processing the results obtained from the CFD-ACE+ instantaneous chemistry model, through CFD-POST (a post processing utility program for CFD-ACE+), which assumes that all the carbon in the fuel contribute to CO production, and then CO is oxidized by a finite-rate reaction (Warnatz; 1984).

From the theoretical results, the following observations can be made: (i) an off-axis hump structure exists in the three regions of concern. However, the profiles become wider and flatter in the mid-flame and far-burner regions; (ii) the cascaded flame profiles are shifted inward towards the core of the flame; (iii) the baseline flame peak CO concentrations occur at  $r/d$  2.21, 4.14 and 5.56 in the near-burner, mid-flame and far-burner locations, respectively. However the corresponding radial positions in the cascaded flame are  $r/d$  1.64, 3.47 and 4.84; (iv) comparing these

locations with temperature peaks and equivalence ratio profiles, all CO peaks are located in the fuel-rich side of the flame; inward of the stoichiometric contour; (v) CO concentration in the cascaded flame decreases by an average of 8%, 17% and 15% in the near-burner, mid-flame and far-burner regions, respectively, from its baseline values.

The wider and flatter profiles observed in the downstream regions and the inward shift of the profiles were noticed earlier in the temperature results, and similar explanations apply. The peak CO existence in the fuel-rich side of the flame is expected, since CO is formed in the fuel-rich region as an intermediate product of combustion due to the fuel pyrolysis. The decrease in CO observed in the cascaded flame can be a result of the larger dilution effects provided by cascading and the consequent leaning of the flame.

Comparing the theoretical results with the experimental data, the following can be observed: (i) CO concentrations predicted by the model is overestimated by a factor of 2.5 to 3; the theoretical predicted CO peaks are around 16 mole%, whereas, the experimental ones range from 4.9%-6.2 % (mole); (ii) the experimental CO peaks are shifted more towards the flame core than in the theoretical profiles. However, the experimental results do not clearly show a difference in the shift between the cascaded and baseline cases; (iii) In spite of the highly-overestimated CO concentrations predicted by the model in both baseline and cascaded flames, the effect of the cascade predicted by the model relative to the baseline case is still good. The 8%, 17% and 15% average drop in CO predicted in the near-burner, mid-flame and far-burner regions, respectively, due to the effect of cascade, correspond to 5%, 11%

and 10% average drop in measured CO at same conditions; (iv) in both theoretical and experimental results; the least effect of cascading is in the near-burner region, however, the highest influence occurs in the mid-flame and far burner regions.

The overestimated CO levels predicted by the numerical model seems to be strange and need to be carefully analyzed. In CFD-POST theoretical model, CO is predicted in a two-step sequence; the first of which is the production of CO from the consumption of the fuel (as predicted by CFD-ACE+), in other words, all the carbon in the fuel is assumed to contribute to CO production, with the second step being the oxidization or destruction of CO by a finite rate reaction from Warnatz (1984), as was explained earlier in CO post processing theory (section 5.3.2).

The increased levels of CO is a clear indication of incomplete combustion that might be due to either shortage of oxygen or insufficiently short residence time or both together. Figures 5.6(a,b,c) of O<sub>2</sub> profiles have already indicated a dramatic shortage of oxygen all over the pyrolyzing fuel-rich side of the flame. This was due to the instantaneous-sheet reaction model explained earlier in the O<sub>2</sub> discussion. Therefore, the lack of oxygen in such a region where fuel pyrolysis and CO formation are taking place, might be the direct cause for the overestimated CO values observed in the theoretical results

The kinetics of CO formation and destruction have been the focuses of many studies ( Fenimore, 1963; Caretto, 1973; Dryer and Glassman, 1973). They concluded that CO formation step is fast; on the other hand, CO destruction (or conversion to CO<sub>2</sub>) is a slow process. Based on this argument, the insufficient short residence time available due to the high Reynolds number (5100) used may not allow the CO slow

destruction to keep pace with CO fast production, thereby leading to the overestimated CO levels that have been predicted by the theoretical model. Therefore, this factor, combined with the shortage of oxygen just mentioned in the previous paragraph, is a strong cause for the observed discrepancy.

#### 5.4.5 Nitric Oxide Concentration Profiles

Figures 5.8 (a, b, c) show the radial concentration profiles of predicted thermal-NO for the baseline and cascaded flames in the near-burner, mid-flame and far-burner axial locations, respectively. Thermal-NO concentrations were calculated using CFD-POST post processing utility program of CFD-ACE+. Appropriate reactions in the detailed kinetics model were turned on to evaluate the influence of the thermal mechanism on NO production using the extended Zeldovich mechanism.

From the theoretical thermal-NO profiles, the following observations can be made: (i) thermal-NO profiles follow the trends of temperature profiles, and peak concentrations coincide well with peak temperatures; (ii) the peak thermal-NO concentrations for the baseline flame are: 11 ppm, 20 ppm and 39 ppm in the near-burner, mid-flame and far-burner locations, respectively. However, the corresponding peaks for the cascaded flame are: 1 ppm, 7 ppm and 14 ppm; (iii) thermal-NO concentrations for the cascaded flame decrease by an average of 89%, 70% and 70% in the near-burner, mid-flame and far-burner regions, respectively, compared to the baseline case. However, the corresponding decrease in predicted temperatures are 13%, 19% and 17%.

Since NO concentrations have been predicted by the thermal-NO mechanism, it is quite expected to follow the temperature profiles and consequently have same peak radial locations and trends. However, the influence of the cascade on thermal-NO is much stronger than its earlier predicted influence on temperature. This can be explained by examining the equation for NO production by extended Zeldovich mechanism (Eq. 5.25), from which, the rate of NO production is seen to be not only a function of the forward and reverse reaction rate constants ( $k_1, k_2, k_3, k_{-1}, k_{-2}, k_{-3}$ ), which are in turn strong functions of temperature ( $k=AT^\beta e^{-E/RT}$ ), but also a function of concentrations of  $O_2, N_2, O$  and  $OH$ . In other words, temperature has a strong influence on thermal-NO, through the exponential dependence, and the concentrations of  $O_2, N_2, O$  and  $OH$  can also play an important role.

The comparison between the theoretical and experimental results reveals the following: (i) NO measured concentrations are much higher, in general, than those predicted by the thermal-NO mechanism; (ii) for the baseline flame, measured NO concentrations are 8, 2 and 2 factors of those predicted by thermal mechanism in the same three regions of concern, respectively. The corresponding measured NO values in the cascaded flame are 58, 6 and 4 factors of the thermal predicted ones; (iii) NO measured concentrations in the cascaded flame decrease by an average of 16%, 5% and 3% in the near-burner, mid-flame and far-burner regions, respectively, from its baseline values. However, the corresponding values predicted by thermal-NO are 89%, 70% and 70%, respectively, at same the conditions; (iv) the experimental peak NO concentrations do not coincide with those predicted by the thermal-NO

mechanism (at the stoichiometric contour); however, the experimental peaks are quite shifted toward the fuel-rich side of the flame.

The high discrepancy between the experimentally measured NO concentrations and those theoretically-predicted by thermal-NO, shows clearly that thermal-NO mechanism is not the only or even the primary route for NO production in this propane diffusion flame; it represents, 12.5%, 50% and 50% of the total measured NO for the baseline flame in the three regions of concern, respectively. Moreover, the influence of thermal-NO decreases even more with cascading to represent only 1.7%, 17% and 25% of the total measured NO at the same conditions. In other words, cascading suppresses the influence of thermal-NO to 14%, 33% and 50% of the baseline values.

The location of experimental NO peaks in the fuel-rich zone of the flame; inward from the stoichiometric contour ( $\phi=1$ ), is another indication of the presence of another route for NO production other than thermal-NO, and most likely Prompt-NO Fenimore mechanism, which forms in the fuel-rich region and becomes dominant in a temperature range of less or equal to 1800 K (Turns, 1996), within which our measured temperatures lie.

The low predicted thermal-NO contribution to the total NO production, the peaks and abundance of measured NO in the fuel-rich regions and the measured range of temperatures in favor of prompt-NO, all together offer a strong support to our earlier explanations of the experimental results, in chapter 4, concerning the reduction of NO by cascading and its discrepancy with temperature. Our early assumption that prompt-

NO mechanism is most likely taking part in NO production and the consequent analysis and explanations made there appear reasonable.

The amount of NO formed by prompt-NO is, in general, small. However, the fast kinetic reactions involved in prompt-NO mechanism, make it possible for prompt-NO to contribute significantly to the total NO production, particularly at lower temperatures and higher Reynolds numbers. In fact, a similar result was found earlier when its name was coined; when Fenimore (1970) discovered that some NO was rapidly produced in the flame zone of laminar premixed flames long before there would be time to form NO by thermal-NO mechanism, and he gave this rapidly formed NO the appellation *prompt-NO*. In conclusion, both thermal-NO and prompt-NO mechanisms should have played an important coupled role in NO production in our propane diffusion flame and the consequent cascading effect on it.

#### 5.4.6 Hydroxyl Radical Concentration Profiles

Figures 5.9 (a, b, c) show the radial concentration profiles of the instantaneous predicted OH radical, for the baseline and cascaded flames, in the near-burner, mid-flame and far-burner regions, respectively. The measured by LIF technique relative concentrations are added to the same figures for comparison. From the theoretical results, the following can be observed: (i) peak OH concentrations for the baseline flame occur at  $r/d$  2.82, 5.56 and 7.84 in the three regions of concern, respectively. The corresponding peak locations for the cascaded flame are  $r/d$  2.82, 4.84 and 6.3; (ii) the OH radical exists over a narrow region around the stoichiometric contour of

the flame, whereas, the earlier temperature profiles were much broader and wider; (iii) the predicted OH concentrations of the cascaded flame decrease by an average of 79%, 49% and 45% in the near-burner, mid-flame and far-burner regions, respectively, from the baseline case. This corresponds to 13%, 19% and 17% average predicted drop in temperature; (iv) OH concentration profiles of the cascaded flames are shifted inward, compared to the baseline case, and particularly in the mid-flame and far-burner regions.

Peak OH locations coincide well with peak temperatures observed earlier. Moreover, OH profiles have the same general trend of temperature profiles, except that the former ones are narrower. This is quite understood, since OH radical needs a high temperature environment to survive, like that exists in the stoichiometric areas. However, the predicted drop in OH by cascading is apparently higher than what can be expected from the corresponding predicted drop in temperature. This can be explained by the fact that cascading not only brings changes to temperature, but also affects the whole stoichiometry of the flame; the inward shift of the profiles by cascading leads to a decrease in the stoichiometric contour area, the source land of OH, and the consequent decrease of OH.

Furthermore, the hydroxyl radical plays an important role in the flame combustion chemistry, its decrease in the cascaded flame compared to the baseline case, could explain the earlier predicted drop in both thermal-NO and CO<sub>2</sub> concentrations in that flame. Recalling the thermal-NO production reaction ( $N + OH \leftrightarrow NO + H$ ), and the

CO oxidation reaction ( $\text{CO} + \text{OH} \leftrightarrow \text{CO}_2 + \text{H}$ ), it is quite clear that any decrease in OH should result in a decrease in both thermal-NO and  $\text{CO}_2$  concentrations.

The comparison of the theoretical predicted OH profiles with the experimental LIF results reveals the following: (i) relative agreement exists in the near-burner region; in terms of peak OH radial locations, width of profiles and the overall trend. However, the agreement is poor in the mid-flame region; (ii) in spite of the general agreement observed in the near-burner region, the effect of cascade is overestimated by the CFD-ACE+ model; 79% predicted average drop in OH concentrations by the effect of cascading, corresponds to 18% average decrease in OH LIF measurements; (iii) in the mid-flame region, the effect of cascading is apparently different, 49% average predicted drop in OH concentrations by cascading, corresponds to 40% average increase in OH LIF measurements; (iv) considerable quantities of OH are predicted in the far-burner region. However, no LIF signal was detected in that particular region.

Theoretical OH concentrations have been predicted using the instantaneous chemistry model. On the other hand, the experimental measurements have been obtained by Laser Induced Fluorescence (LIF); a sensitive, non-intrusive and instantaneous technique. Therefore, a reasonable basis for comparison exists. However, the agreement is apparently poor in the downstream regions of the flame. The most probable reason for this discrepancy is the soot heterogeneous combustion processes taking place in the downstream regions, particularly in the sooty propane diffusion flame, which is not taken into consideration in the CFD-ACE+ numerical

model. The soot has a considerable influence upon OH by one or all of the following:

(i) It is the main source of radiation losses from the flame which affects the flame temperature and consequently OH; (ii) soot oxidation, taking place in the downstream regions of the flame, is primarily due to the reaction between soot and OH radical (Puri et al., 1994; Smyth, et al., 1994; Villasenor et al., 1992), thereby consuming considerable quantities of OH; (iii) soot oxidation will also affect the heat release rate and the consequent changes in temperature and OH.

Therefore, the observed increase of LIF-measured OH by cascading, in the mid-flame region, can be attributed to the higher rates of soot oxidation and the consequent lower soot loading provided by the cascade, which had quite evidence from the soot concentration measurements (chapter 4). Higher soot oxidation and lower soot loading in the cascaded flame result in higher rates of heat release and lower radiation losses, thereby leading to higher temperatures and the consequent increase of OH.

Another factor that might have played a role in this discrepancy, and was not taken into account in the current numerical model, is the radiation interaction between the flame and the cascade of venturis or in other words; radiation blockage by venturis, which results in a considerable increase in the flame temperature and decrease in the quenching rates and consequently might have led to higher OH. On the other hand, the higher soot oxidation in the cascaded flame should consume more OH and consequently can lead to a decrease in OH.

In conclusion, the higher measured OH that has been observed in the cascaded flame compared to the baseline case, which could not be predicted by the model, is

the net or resultant effect of many factors interacting with each other in a complicated manner; higher heat release rates, lower soot loading, higher temperatures and lower quenching rates in the cascaded flame, working together on one hand, to enhance OH, and higher consumption of OH due to higher soot oxidation; working on the other hand, to suppress OH.

It should be noticed that the radiation blockage mentioned earlier and the consequent increase in flame temperature and decrease in quenching rates can play a role, not only in the mid-flame region, but also in the near-burner one. This factor might also contribute to the discrepancy in the influence of cascade in the near-burner region. In the far-burner region, no LIF measurements could be obtained; the high interference of soot with the LIF signal, in addition to the presence of soot wings and flickering, made it very difficult to recover any LIF signal in that particular region.

#### **5.4.7 Equivalence Ratio Profiles**

Figures 5.10 (a, b, c) show the radial profiles of the predicted local equivalence ratio ( $\phi$ ) for the baseline and cascaded flames, in the near-burner, mid-flame and far burner regions, respectively. The baseline flame radial locations corresponding to  $\phi=1$  are;  $r/d$  2.85, 5.7 and 7.62 in the near-burner, mid-flame and far-burner regions, respectively. The corresponding radial locations in the cascaded flame are;  $r/d$  2.5, 4.53 and 5.95, respectively, at same conditions. These radial locations represent the positions of the stoichiometric contour of the flame, where the fuel and oxidizer exist

at chemically correct proportions. Therefore, peak temperatures were observed at or almost close to these locations.

The equivalence ratio profiles are shifted towards the fuel rich side of the flame by the effect of the cascade, similar effect was observed in earlier temperature, CO<sub>2</sub>, and CO predicted profiles, and same explanations apply. However, the changes brought by the cascade on equivalence ratios determine the stoichiometry of the flame, and therefore, could be the drive for all other changes including temperature, CO<sub>2</sub>, O<sub>2</sub>, NO and OH.

Moreover, these equivalence ratio profiles were extremely useful in the analysis of results presented in the discussion section. They served as a guide for the locations of the stoichiometric contour, fuel-rich region, fuel-lean region as well as flame boundaries.

#### **5.4.8 Axial and Radial Velocity Profiles**

Figures 5.11 (a, b, c) show the radial profiles of the axial velocity component ( $U$ ) for the baseline and cascaded flames in the near-burner ( $x/d=20$ ), mid-flame ( $x/d=100$ ) and far-burner ( $x/d=180$ ) regions, respectively. In the cascaded flame, the radial planes correspond to the locations just above venturis 1, 2, and 3 (Fig. 5.1c). From these profiles the following observations can be made: (i) the centerline velocities for the baseline flame are 12, 9 and 5 m/s in the near-burner, mid-flame and far-burner regions, respectively. The corresponding velocities for the cascaded flame are 12, 9 and 5.4 m/s; (ii) the cascaded flame has higher velocities and wider profiles

than the baseline flame; (iii) the effect of the cascade is small in both the near-burner and fuel-rich regions of the flame. However, the highest effect is observed in the downstream and fuel-lean regions, i.e., the cascade becomes more influential away from the burner-rim in both radial and axial directions.

In general, for a circular jet, the centerline velocity decreases and the jet becomes wider as the jet grows downstream due to the viscous shear and more air entrained. The higher velocities and wider profiles, observed for the cascaded flame compared to the baseline flame, are indications of the rapid and faster growth of the gas jet flame in the presence of the cascade. This is due to the effect of the cascade which inducts more of the co-flow air stream into the combustion zone, thereby leading to higher rates of mixing between the fuel and air and the consequent rapid growth of the jet.

The higher effect of the cascade in the fuel-lean side regions, away from the centerline, can be explained by the fact that those regions are closer to the venturis and consequently are expected to be the most affected. Also, the larger effect of the cascade in the downstream regions, and particularly in the far-burner axial location, can be attributed to the cumulative influence of more venturis while proceeding downstream.

The higher central axial velocity component in the far-burner region of the cascaded flame and the consequent smaller residence time, compared to the baseline case, can account for the increase in flame length that has been visually observed with the venturi-cascade.

Figures 5.12 (a, b, c) show the transverse profiles of the radial velocity component ( $V$ ) for the baseline and cascaded flames in the near-burner ( $x/d=20$ ), mid-flame

( $x/d=100$ ) and far-burner ( $x/d=180$ ) regions, respectively. As before, these locations correspond to the planes just above venturis 1, 2, and 3. The general trend of these profiles is that the radial velocity is zero at the center line, then it increases to attain a peak value in the fuel-rich region, beyond which it starts decreasing until it reaches a minimum (negative) value close to the stoichiometric contour, then it starts increasing again in the fuel-lean side of the flame to attain an asymptotic value near the flame edge. In addition, the following observations can be made: (i) The peak radial velocities in the fuel-rich side of the reaction zone are 0.062 m/s, 0.036 m/s and 0.026 m/s, for the baseline flame, in the near-burner, mid-flame and far-burner regions, respectively. The corresponding peak velocities for the cascaded flame are almost the same; (ii) The minimum radial velocities are -0.082 m/s, -0.017 m/s and -0.003 m/s, for the baseline flame, in the near-burner, mid-flame and far-burner regions, respectively. The corresponding minimum velocities for the cascaded flame are -0.06 m/s, -0.004 m/s and 0.006 m/s; (iii) the minimum radial velocities of the cascaded flame are shifted inward, towards the centerline of the flame, by  $r/d$  of 1 in both the near-burner and mid-flame regions, and by  $r/d$  of 1.5 in the far-burner region; (iv) both the baseline and cascaded flames almost have equal radial velocities in the fuel-rich region. However, the cascaded flame has substantially higher velocities in the fuel-lean side of the flame (outside of the stoichiometric contour). This result is enhanced further in the downstream regions.

The positive velocities observed close to centerline imply an outward velocity direction due to jet momentum. On the other hand, the negative velocities noticed farther from the centerline indicate an inward velocity direction. These positive and

negative velocities are necessary to satisfy the conservation of mass. The decrease in the absolute magnitudes of the radial velocities with the downstream distance, the inward shift of the minimum values and the highest effect of the cascade observed in both fuel-lean and downstream regions, were explained in the earlier discussions.

The higher positive radial velocities observed with the cascade, in the fuel-lean side (close to the venturis), suggests an increase in the outward flow due to the venturi-cascade. This observation appeared to be surprising at first since higher inward velocities were initially expected by the effect of the venturis. However, the axial locations at which these profiles were obtained are just above the exits of the venturis (see Fig. 5.1c). At these locations, the fluid is ejected with higher velocities due to the smaller flow area. Moreover, the slight outward concave profile of the venturi at the exit imparts an outward radial component. Nevertheless, the expected higher inward velocities by the venturis indeed exists, but inside of each venturi. Therefore, the flow inside the venturis was also investigated next.

Figures 5.13 (a, b, c) show the radial profiles of the axial velocity component ( $U$ ) for the baseline and cascaded flames at  $x/d=80$ ,  $x/d=160$  and  $x/d=240$  axial locations, respectively. These locations correspond to the planes at the mid-level inside venturis number 2, 3 and 4, respectively (see Fig. 5.1c). These profiles have almost the same trends observed in Figs. 5.11, and the same explanations are offered.

Figures 5.14 (a, b, c) present the transverse profiles of the radial velocity component ( $V$ ) at the same conditions of Figs. 5.13; at the mid-level inside venturis 1, 2 and 3, respectively. A dramatic increase in the inward radial velocities compared to the outward velocities are observed due the effect of the veturi-cascade in the three

regions of concern. The negative radial velocities with the cascade indicate clearly the generation of an inward flow (towards the centerline of the jet) by the venturis, thereby leading to the higher rates of mixing and its consequent impact on the combustion process. This result can also be seen from the total velocity vector field provided in Fig. 5.17.

Figures 5.15 (a, b, c) and Figs. 5.16 (a, b, c) show the radial profiles of the axial and radial velocity components (U and V) for the baseline and cascaded flames at  $x/d=40$ ,  $x/d=120$  and  $x/d=200$  axial locations, respectively (see Fig. 5.1c). These radial planes correspond to the mid-spacings between venturis 1 and 2, 2 and 3 and 3 and 4, respectively. The trends of these profiles are almost similar to those of Figs. 5.11 and 5.12 which were obtained just above the throats of the venturis. However, the increase of the outward velocities (V) due to the cascade, seen in Figs 5.16 is less than that in Figs. 5.12. The similarity of the profiles is reasonable because both locations are in the space between the venturis. Since the locations corresponding to Figs. 5.16 are farther from the throat the effect is expected to be less than that observed in Figs 5.12.

To provide a detailed understanding of the flow inside venturis, venturi number 3 was selected for further examination (see Fig. 5.1a). The intermediate location of that venturi in the cascade was the reason for its selection.

Figures 5.18 (a, b, c, d, e, f, g, h) and 5.19 (a, b, c, d, e, f, g, h) provide the radial velocity profiles of the axial and radial velocity components (U and V), respectively, on transverse planes at the following axial locations of venturi number 3: At the base; Just above the base; half the distance between mid-level and base; mid-level; half

distance between the mid-level and throat; just below throat; at the throat. These locations are shown in Fig. 5.1d.

From Figs. 5.18 (a, b, c, d, e, f, g, h), it is noticed that the effect of the venturi on the axial velocity component ( $U$ ) exhibits the same trend throughout the entire venturi. The axial velocity component ( $V$ ) increases due to the venturi at all locations, for the reasons explained earlier. Furthermore, with the increase in the distance above the base, the influence of venturi becomes stronger. This can be attributed to the gradual reduction of area in that direction.

Figures 5.19 (a, b, c, d, e, f, g, h) of  $V$  velocity component throughout the venturi reveal that until  $10d$  above the base (i.e., approximately in the first quarter of the venturi), the flow still has an outward radial component (positive value if  $V$ ), particularly in the fuel lean regions. However, the flow appears to turn inward (negative value of  $V$ ) after  $10d$  from the base. This result is supported qualitatively by the static pressure measurements along the interior surface of the venturi in appendix 7. Above that plane, the inward radial velocity increases until it reaches a maximum (negative) value at the mid-level of the venturi. Then the inward radial velocity begins to decrease towards the throat to reach a minimum value at  $5d$  below the throat of the venturi.

Higher inward velocities indicate larger air infusion and consequently higher rates of mixing of fuel with air. Therefore, the venturis are effective in enhancing the rates of mixing over the region from  $10d$  to  $30d$  above the base of the venturi. These observations are also clear from the total velocity vector field plot in Fig. 5.20.

In Summary, at these locations, the venturis appear to increase the flame velocity in both the axial and inward radial directions. The increase in the inward radial velocity component substantiates the higher rates of mixing with air. This change in fluid dynamics allows more oxygen penetration into the core of the flame, and the consequent inward shift of the thermal and concentration profiles that have been noticed earlier.

**TABLE 5.1**  
**Conditions Used in the Computations**

Fuel	Propane (95%+)
Jet diameter	2 mm
Jet exit Reynolds number	5100
Jet exit velocity	11 m/s
Convected air velocity	0.25 m/s
Venturi throat diameter, D	70 mm
Venturi height, H	70 mm
Venturi inlet diameter, DI	140 mm
Venturi locations*	x/d=0, 80, 160, 240
Axial locations*	near-burner (x/d=20) mid-flame (x/d=100) far-burner (x/d=180)
Ambient temperature	295 K
Ambient pressure	100 kPa

\* See Fig. 5.1a

**TABLE 5.2**  
**Extended Zeldovich Reaction Rate Constants**  
( $k = AT^\beta e^{-E/RT}$ )

Constant	A	$\beta$	E/R
$k_1$	3.7E9	0.3	0.0
$k_2$	6.40E6	1.0	3160
$k_3$	3.80E10	0.0	0.0

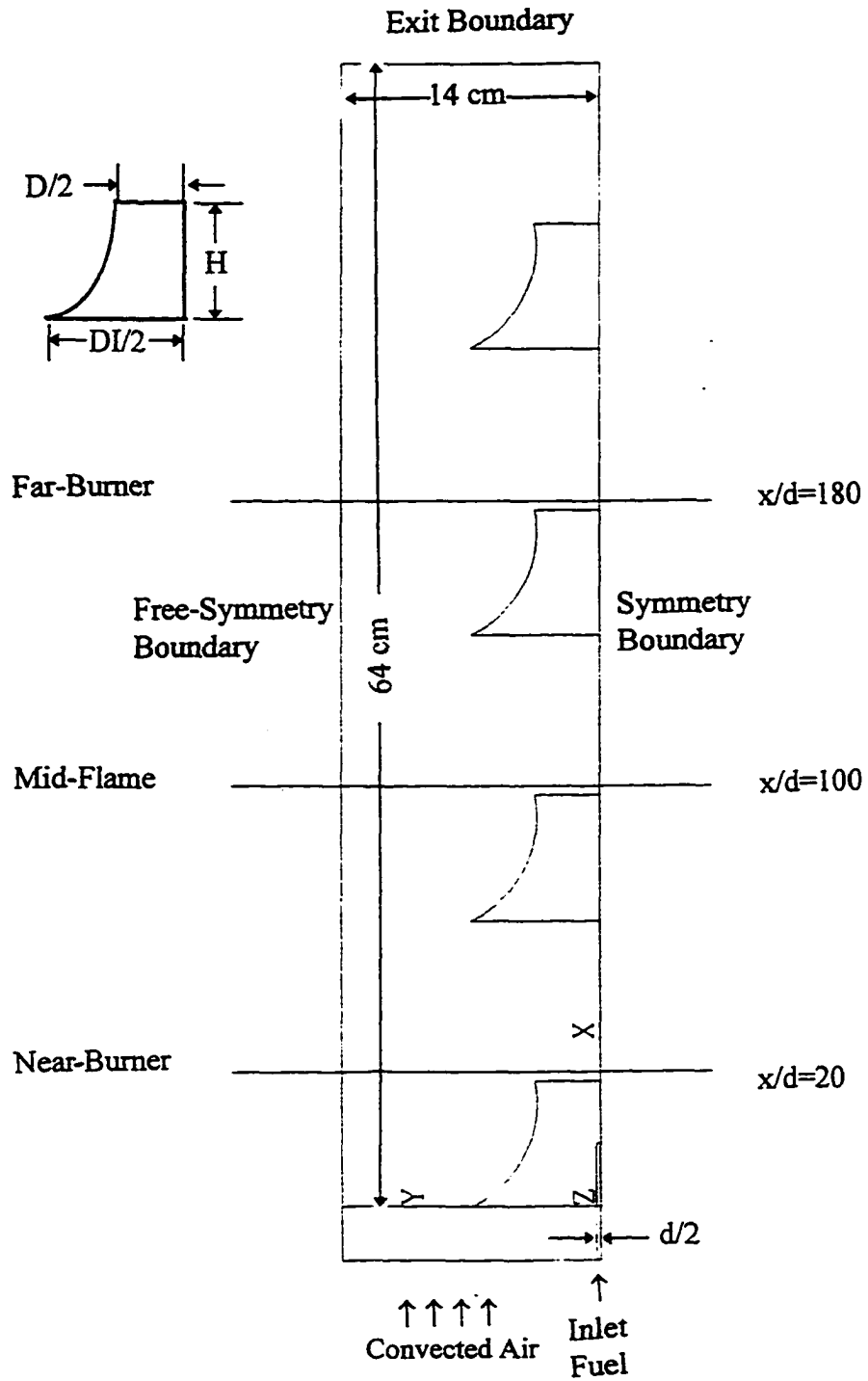
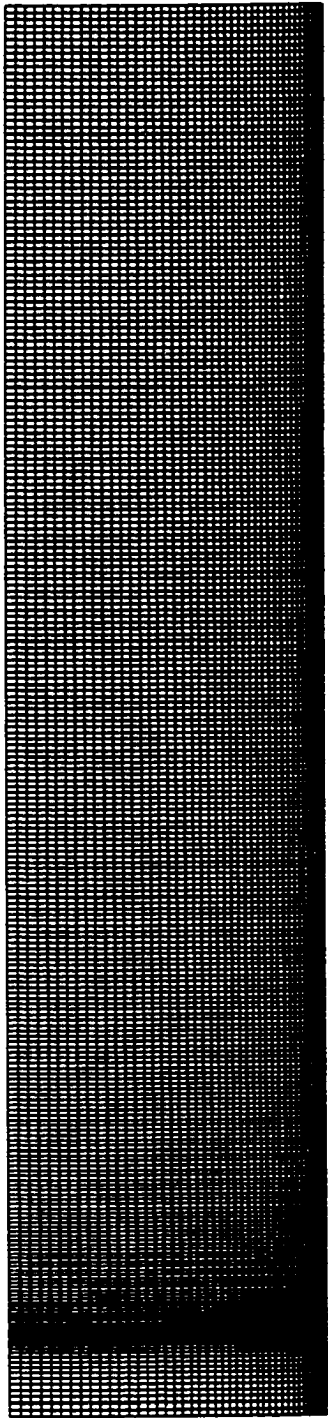
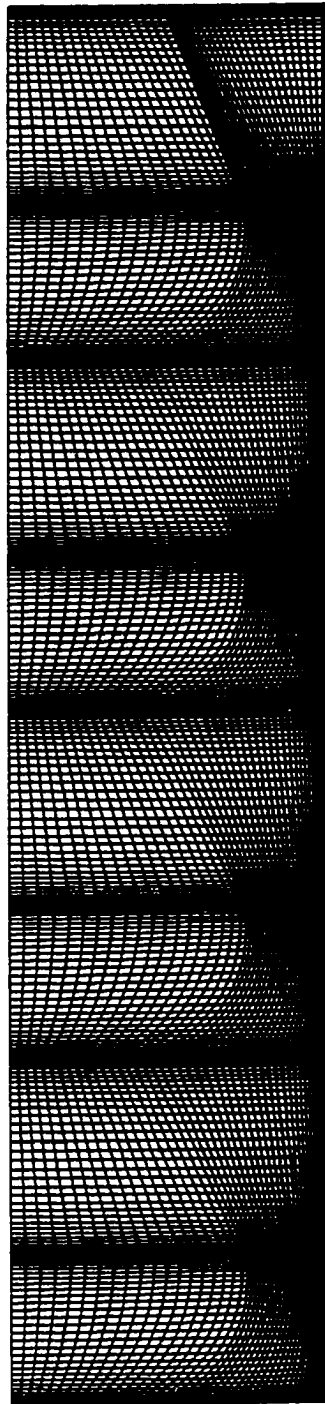


**Fig. 5.1a: Geometry and boundary conditions**



**Baseline**



**Cascaded**

**Fig. 5.1b: Non-uniform grid used for flow computations**

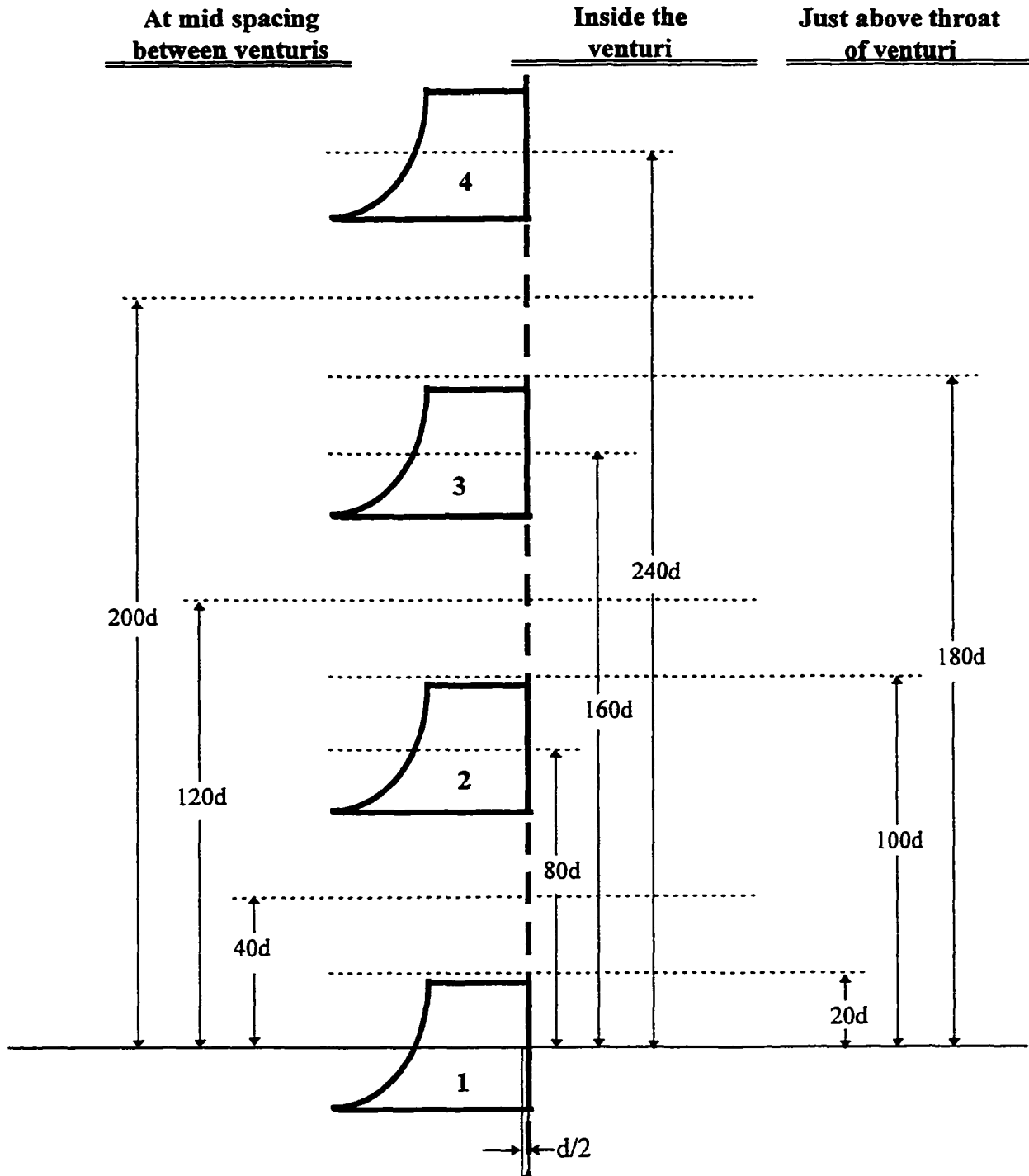


**Fig 5.1c: Locations of velocity computations with respect to the venturis**

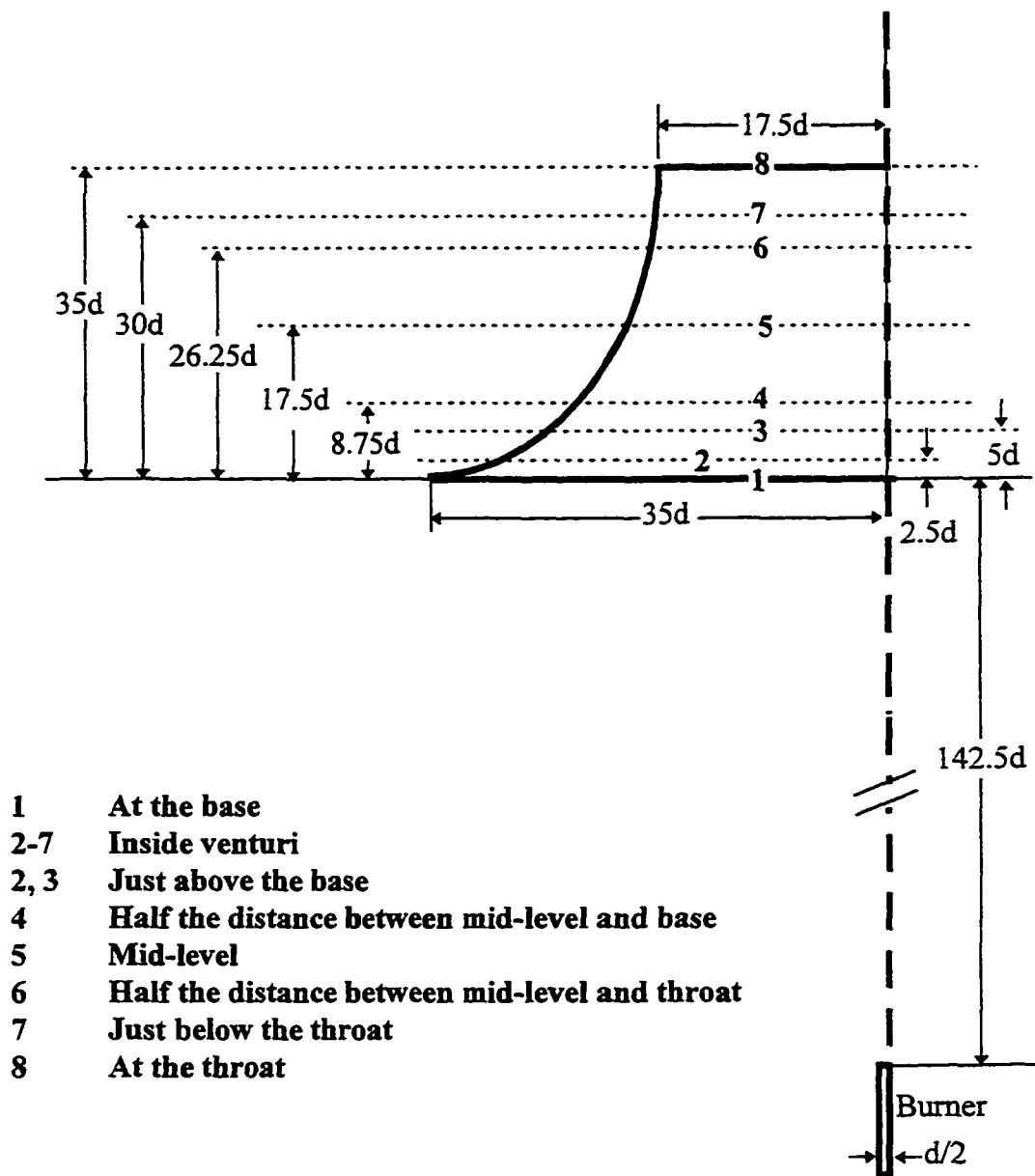
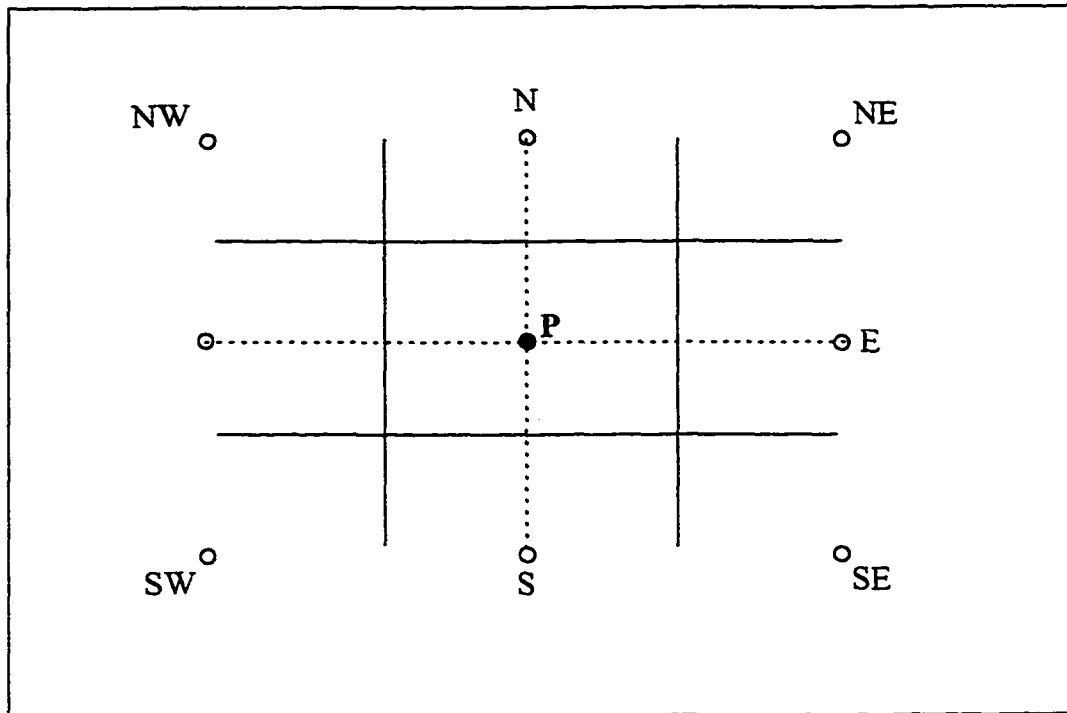
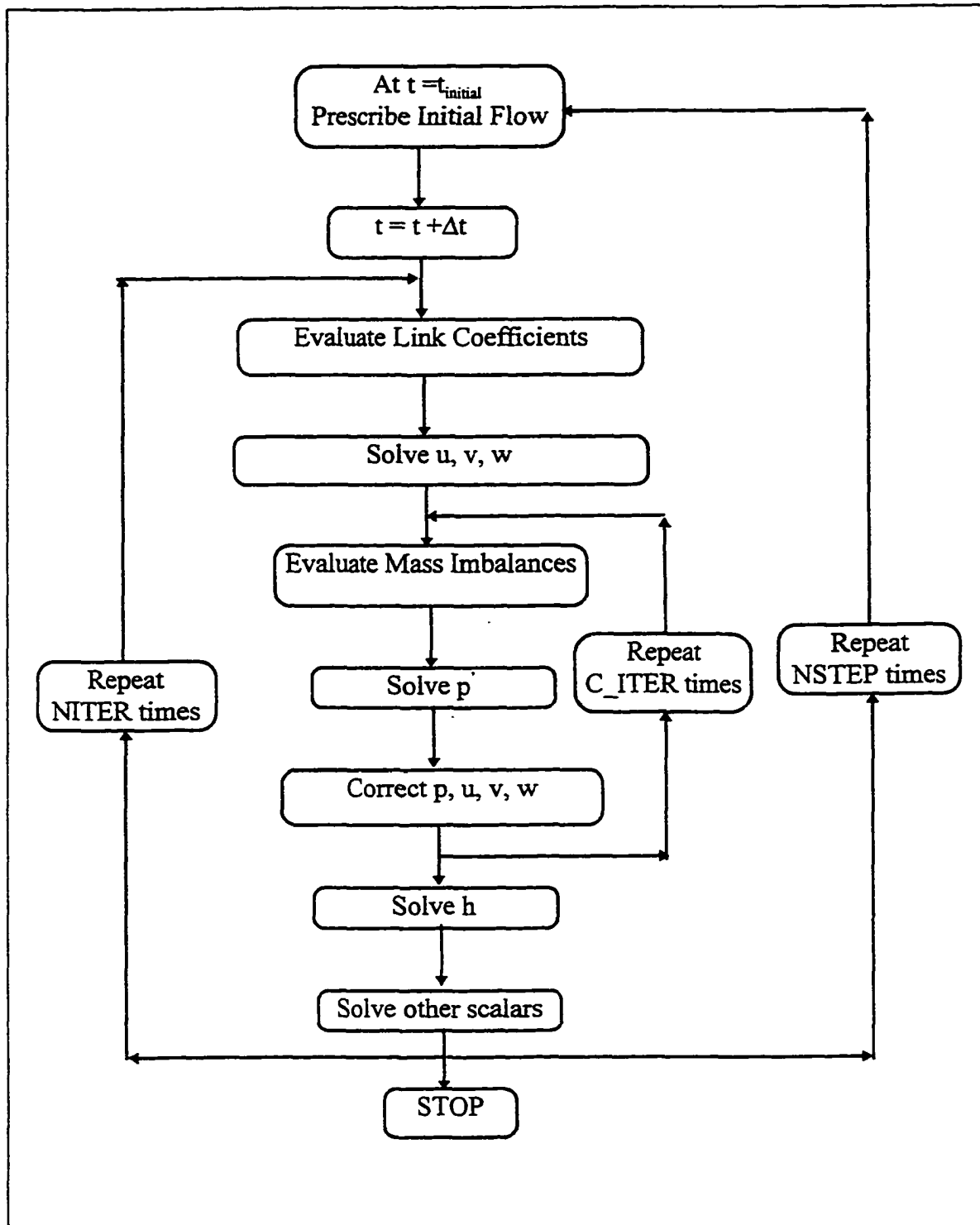


Fig. 5.1d: Locations of velocity computations for venturi number 3



**Fig. 5.2: 2-D discretization of convection and diffusion terms**



**Fig. 5.3a: Solution flowchart for SIMPLEC algorithm**

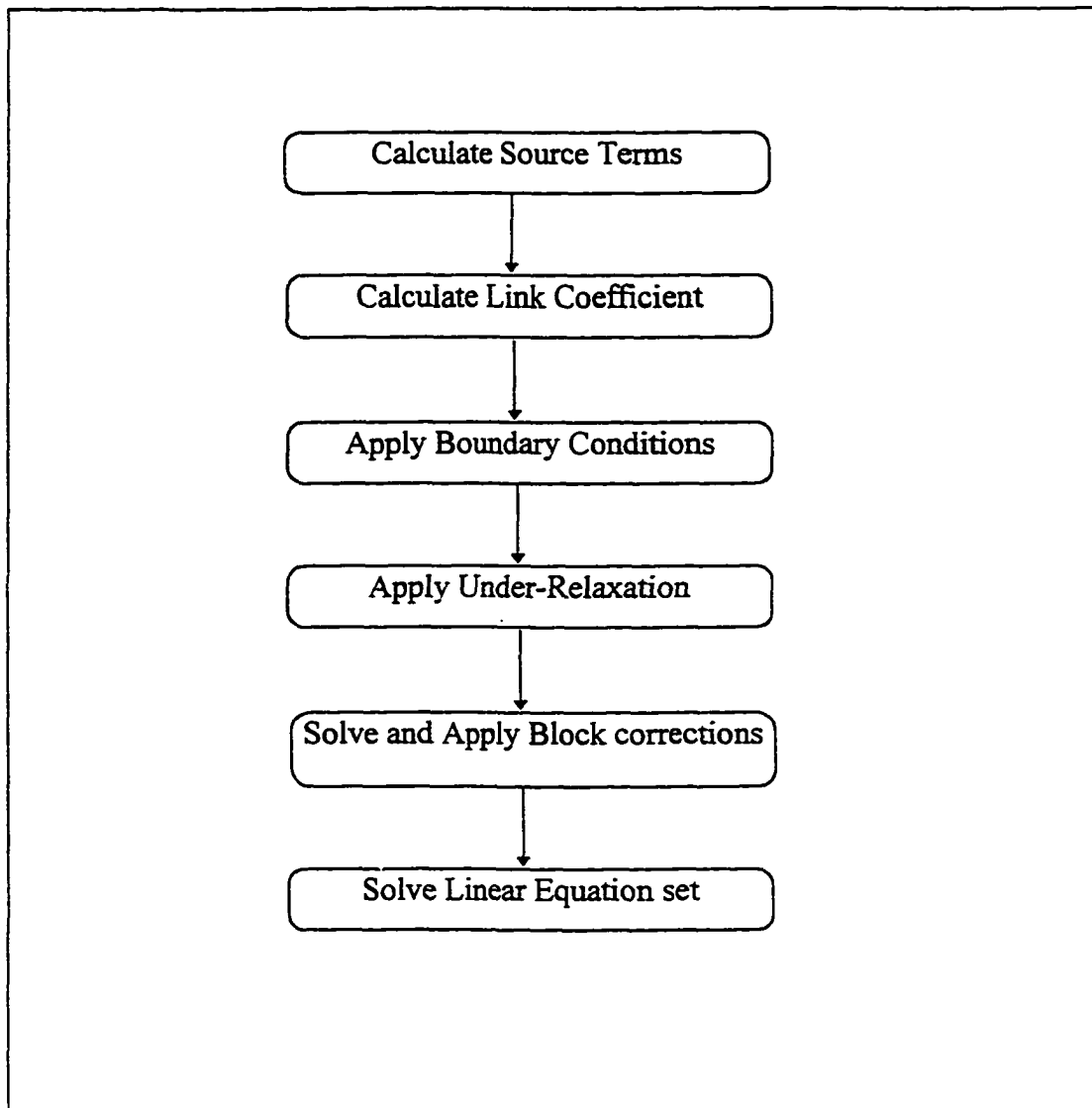


**Fig. 5.3b: Solution procedure for a Single dependent variable**

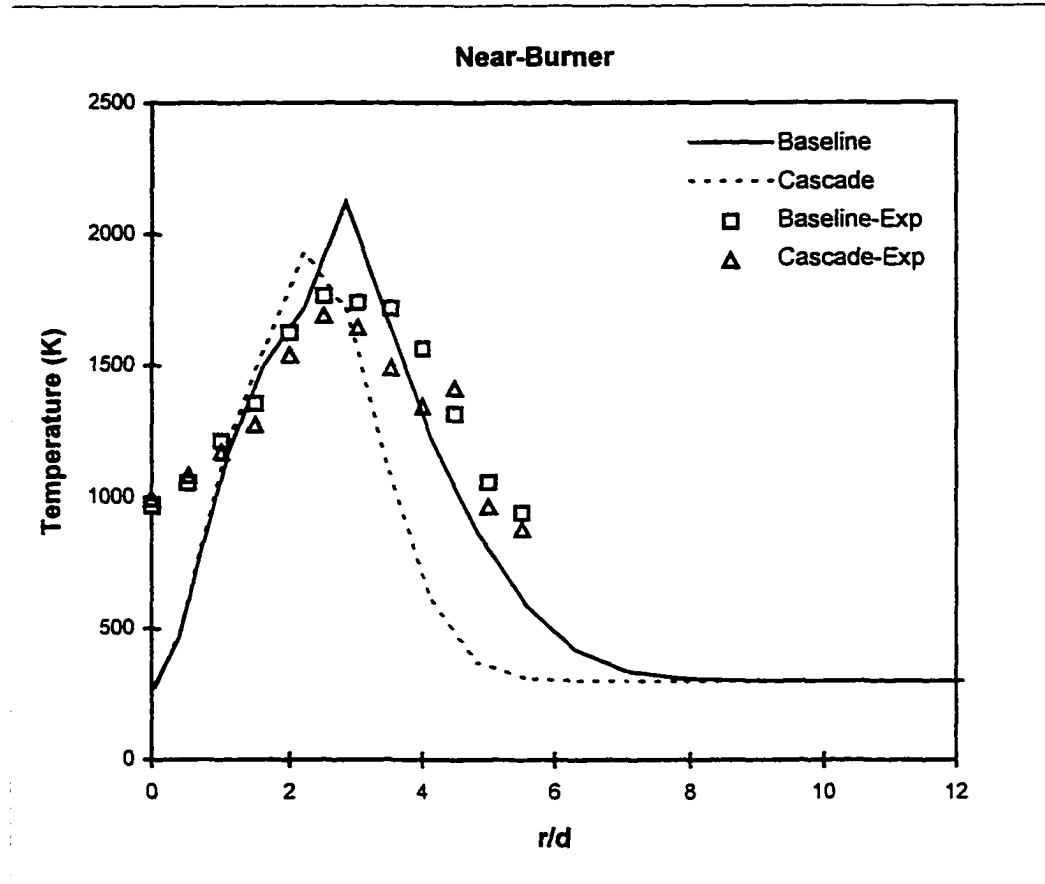


**Fig. 5.4a: Radial temperature profiles for the baseline and cascaded flames in the near-burner region ( $x/d=20$ ). Experimental data are shown for comparison.**

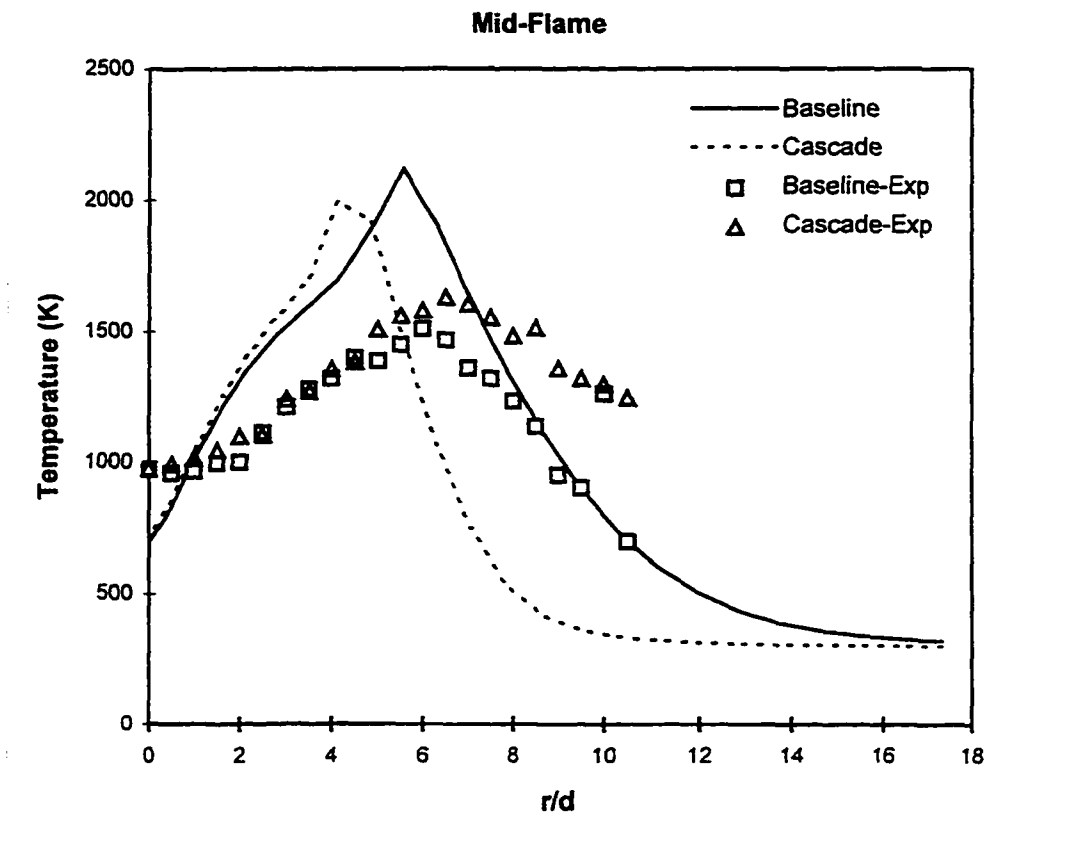


**Fig. 5.4b: Radial temperature profiles for the baseline and cascaded flames in the mid-flame region ( $x/d=100$ ). Experimental data are shown for comparison.**

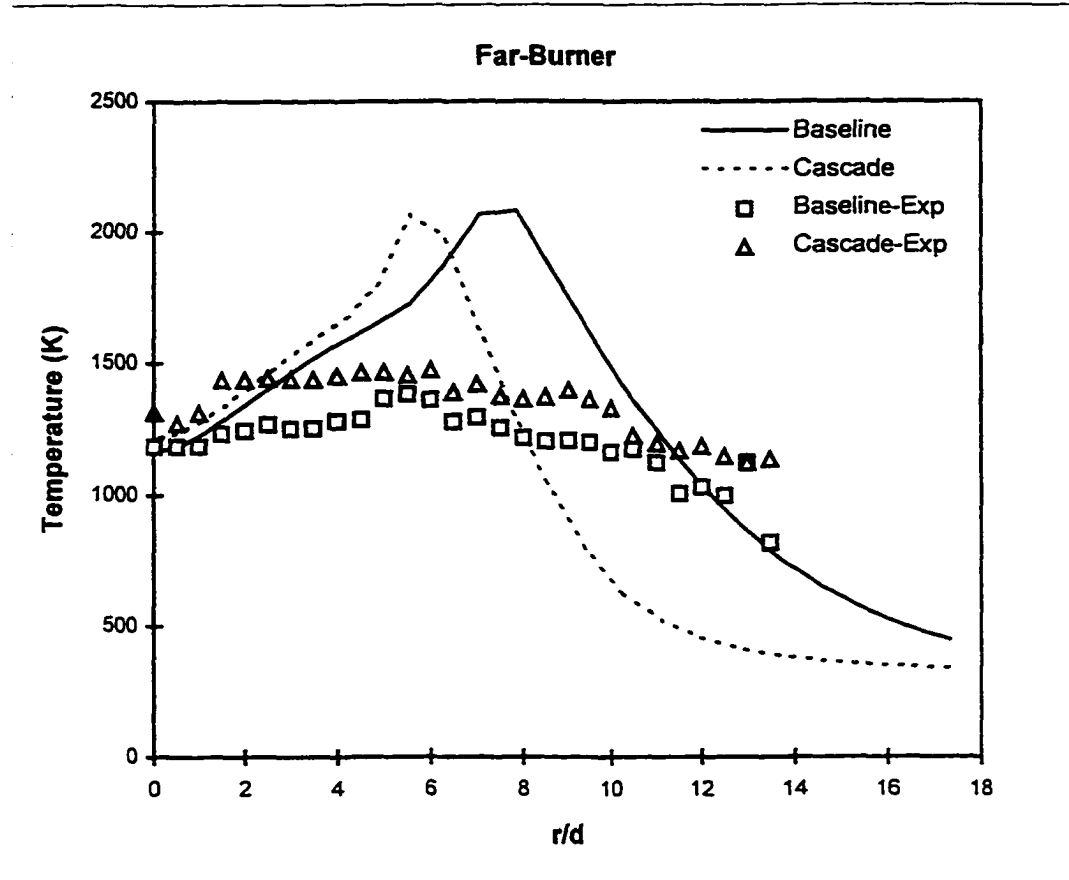


**Fig. 5.4c: Radial temperature profiles for the baseline and cascaded flames in the far-burner region ( $x/d=180$ ). Experimental data are shown for comparison.**

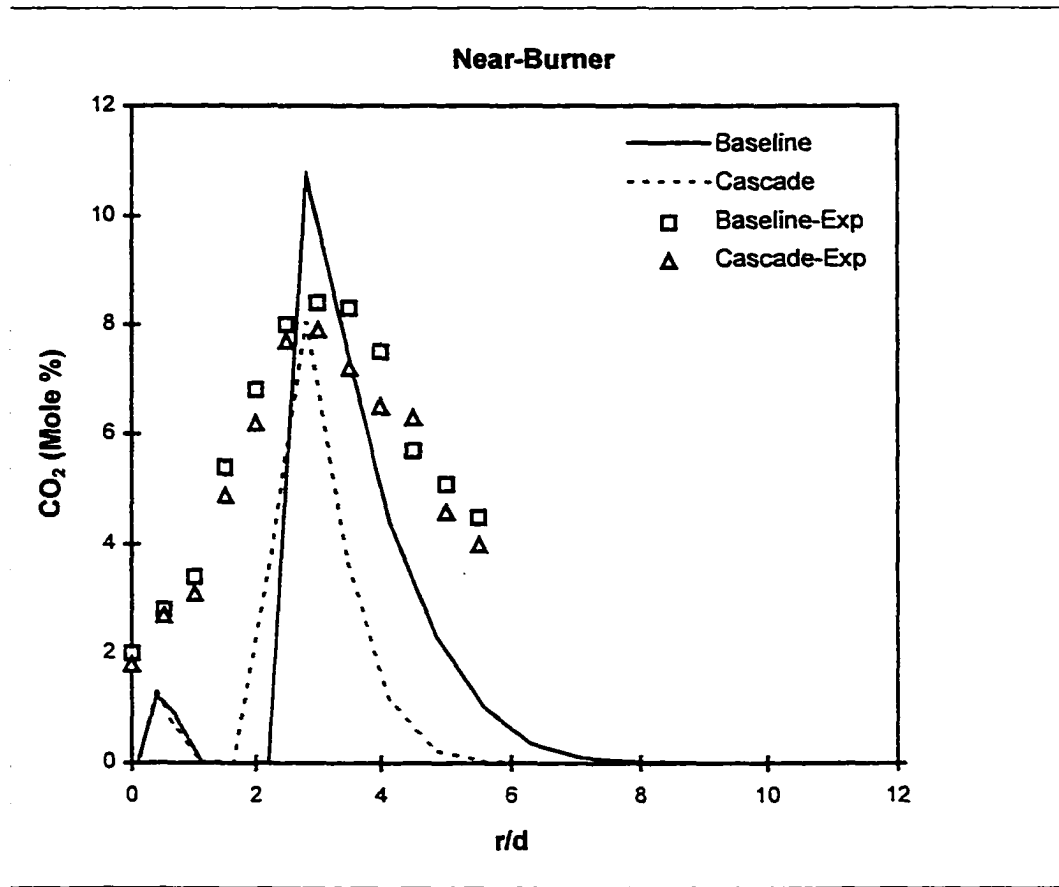


**Fig. 5.5a: Radial concentration profiles of CO<sub>2</sub> for the baseline and cascaded flames in the near-burner region ( $x/d=20$ ). Experimental data are shown for comparison.**

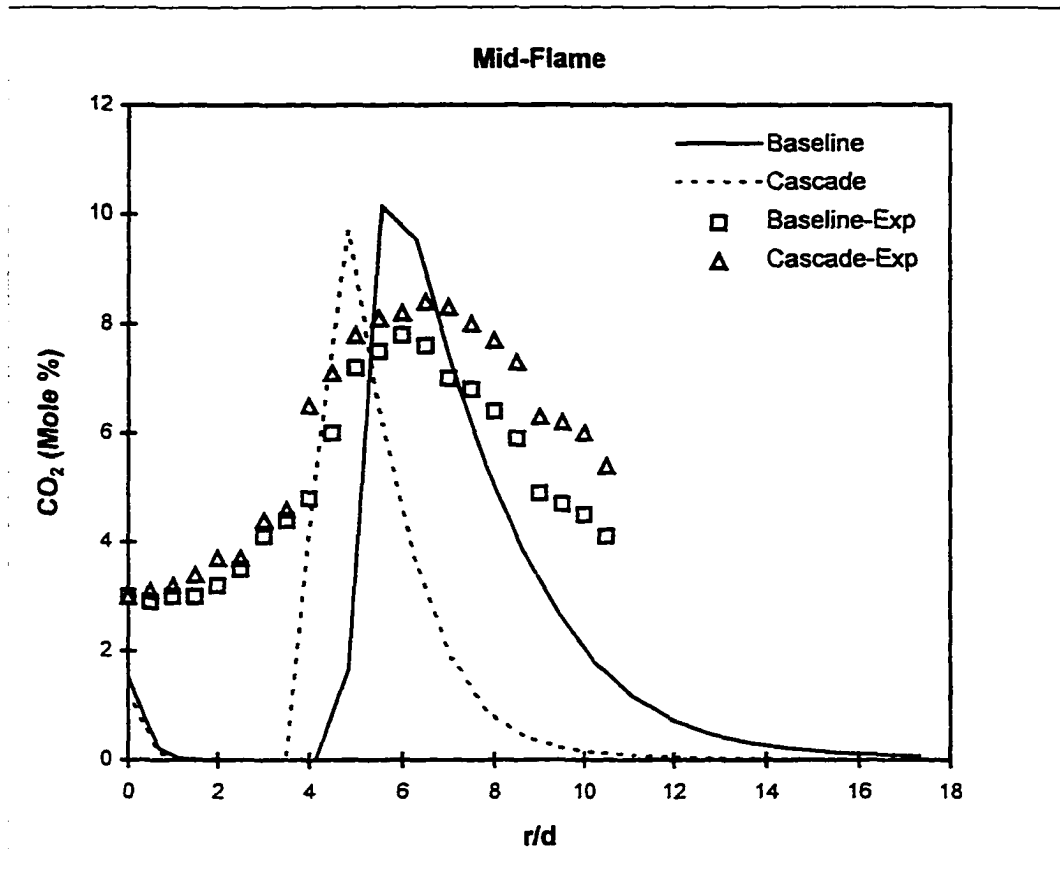


**Fig. 5.5b: Radial concentration profiles of CO<sub>2</sub> for the baseline and cascade flames in the mid-flame region ( $x/d=100$ ). Experimental data are shown for comparison.**

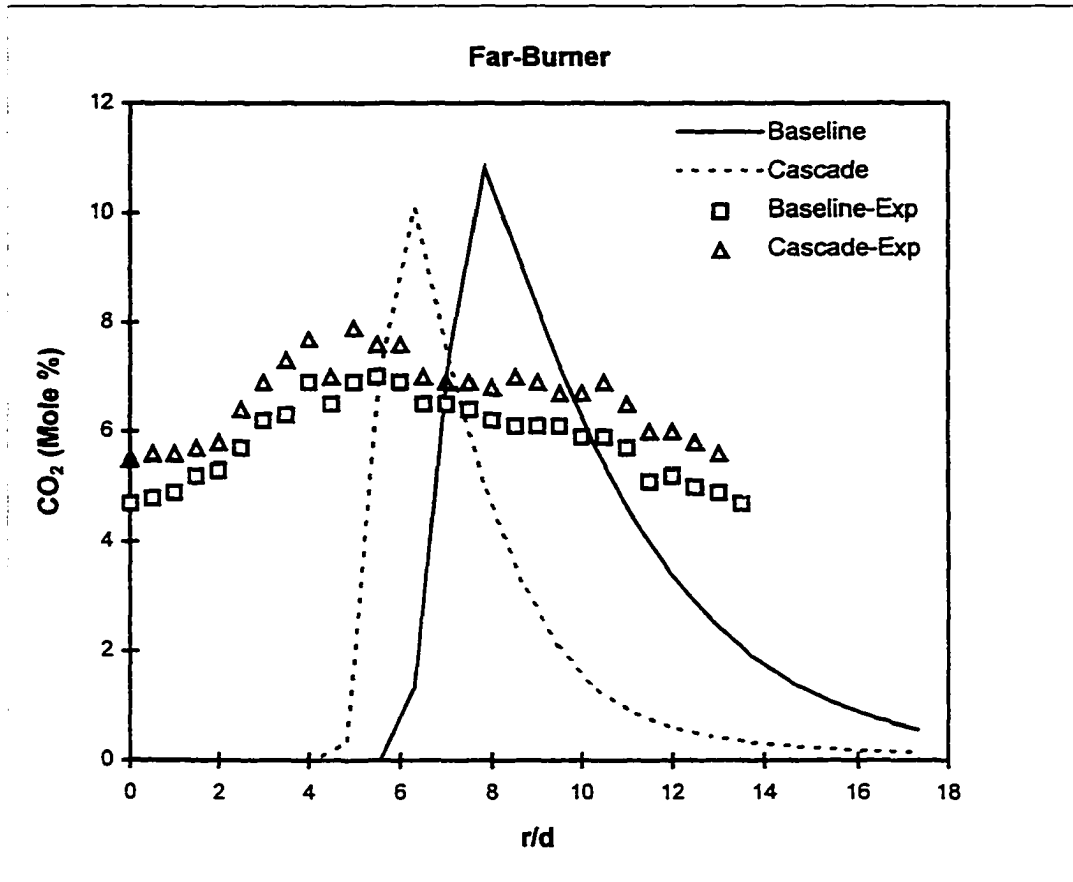


**Fig. 5.5c: Radial concentration profiles of CO<sub>2</sub> for the baseline and cascaded flames in the far-burner region ( $x/d=180$ ). Experimental data are shown for comparison.**

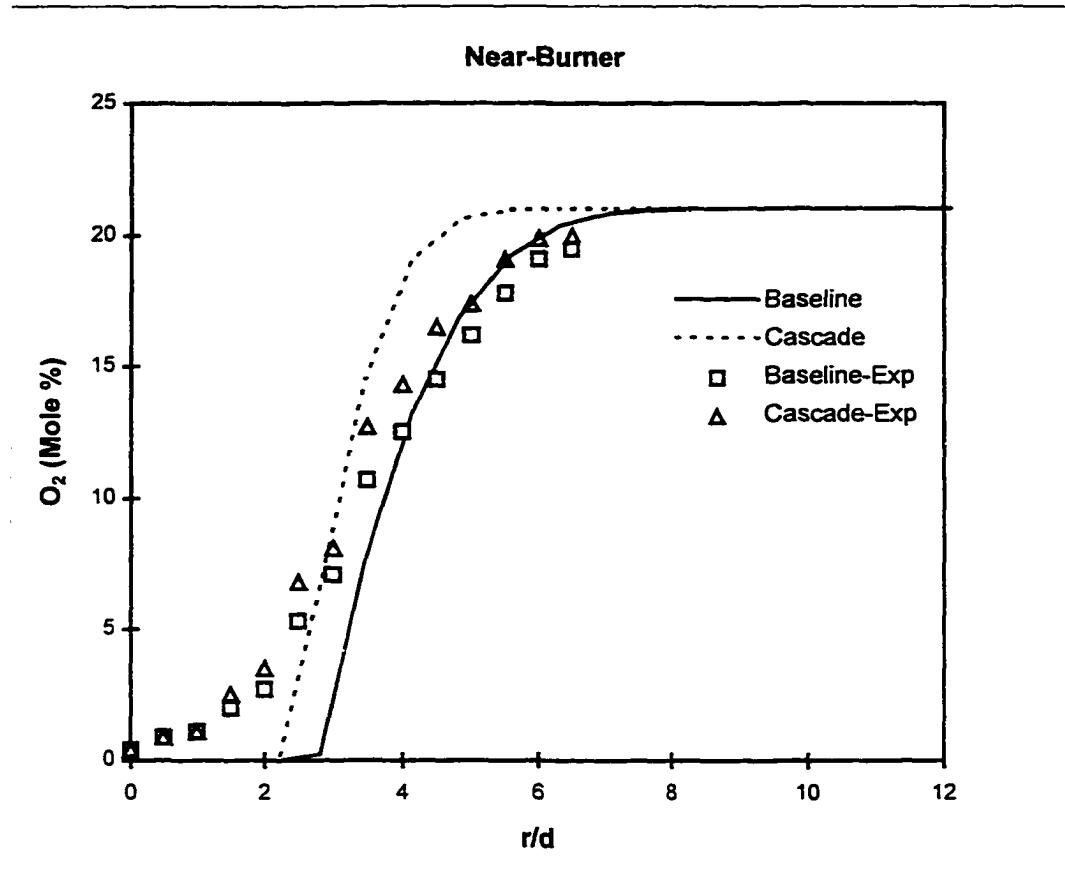


**Fig. 5.6a: Radial concentration profiles of  $O_2$  for the baseline and cascaded flames in the near-burner region ( $x/d=20$ ). Experimental data are shown for comparison.**

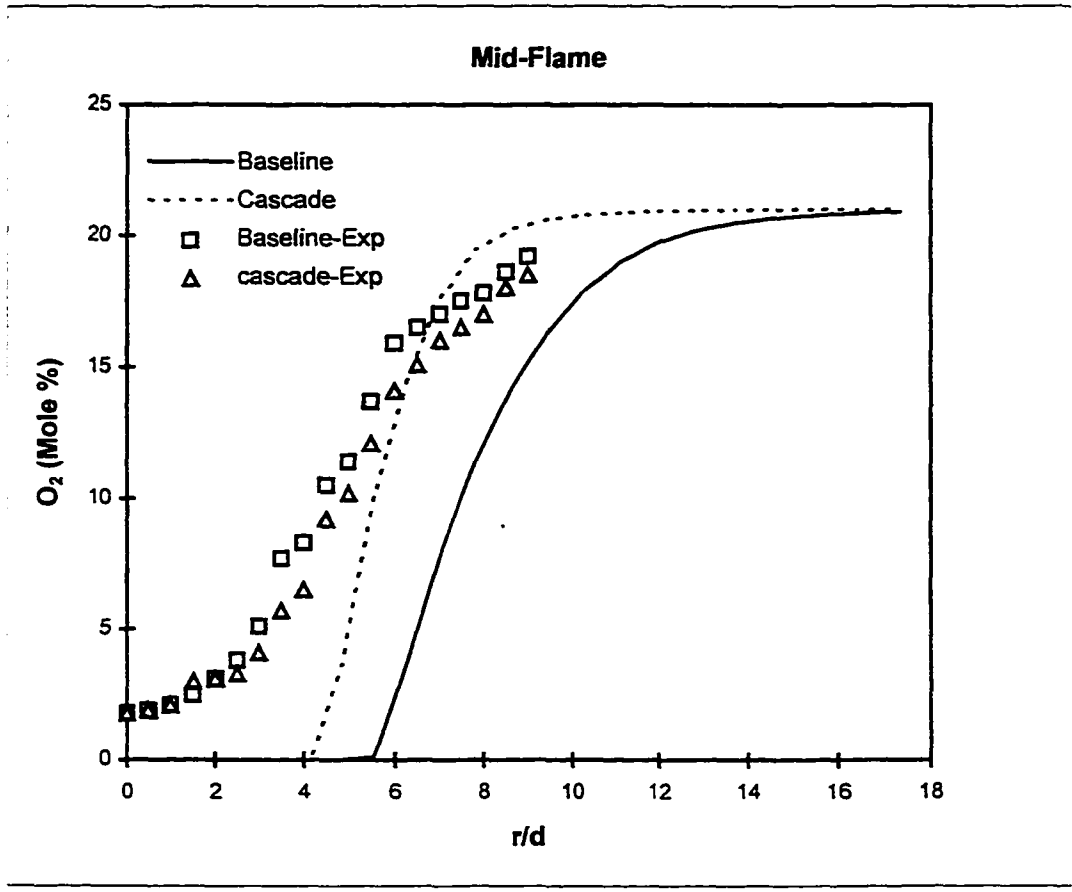


**Fig. 5.6b: Radial concentration profiles of O<sub>2</sub> for the baseline and cascaded flames in the mid-flame region (x/d=100). Experimental data are shown for comparison.**

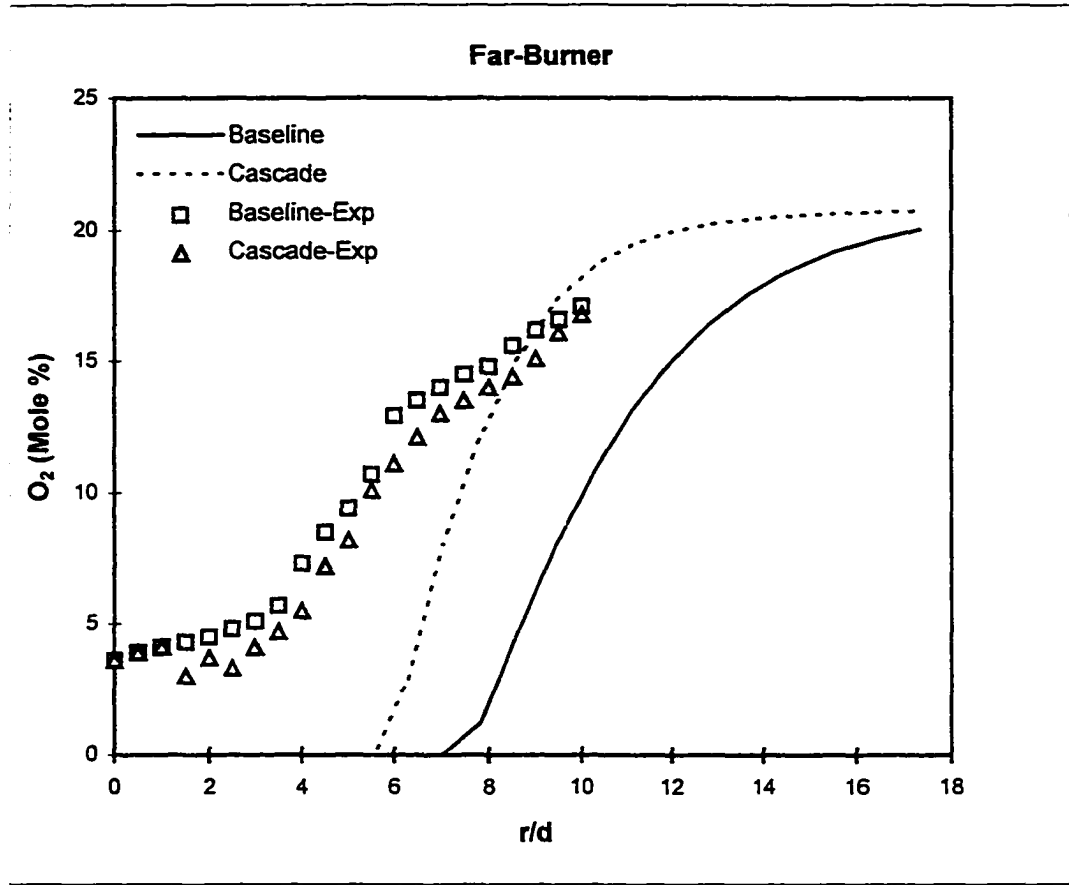


**Fig. 5.6c: Radial concentration profiles of O<sub>2</sub> for the baseline and cascaded flames in the far-burner region (x/d=180). Experimental data are shown for comparison.**

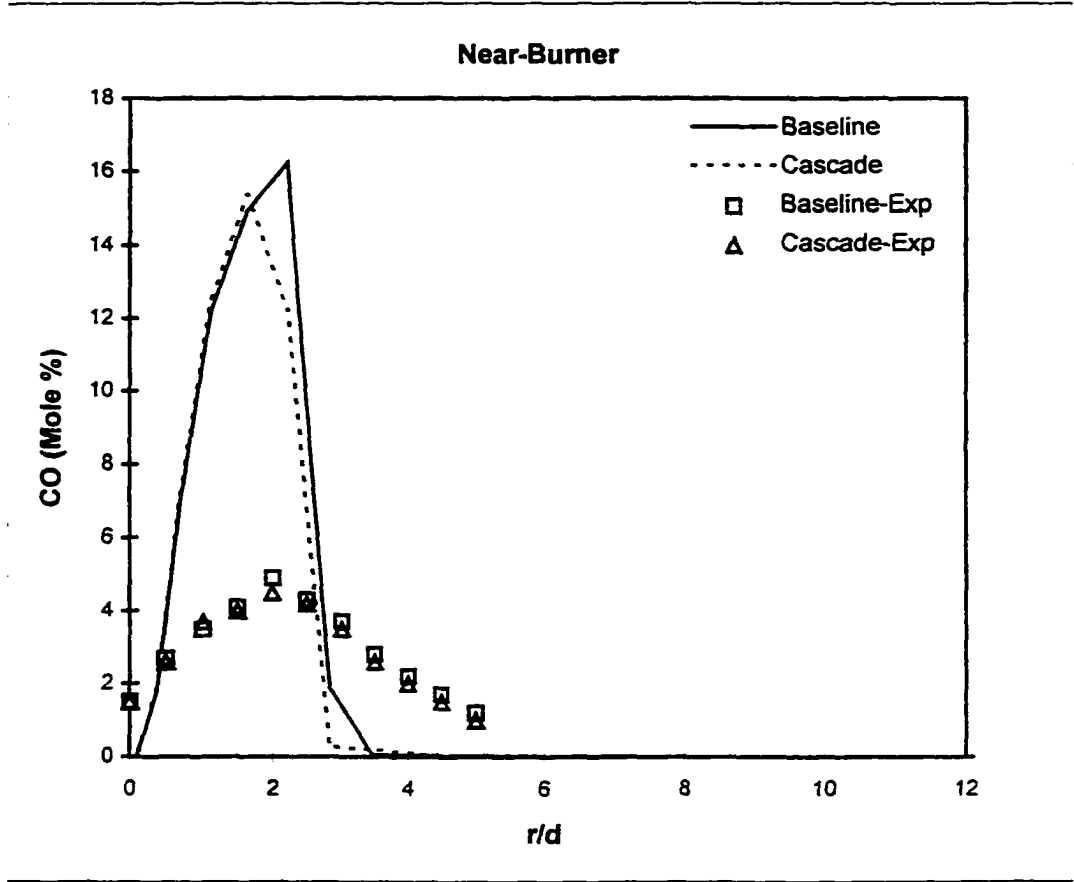


**Fig. 5.7a: Radial concentration profiles of CO for the baseline and cascaded flames in the near-burner region ( $x/d=20$ ). Experimental data are shown for comparison.**

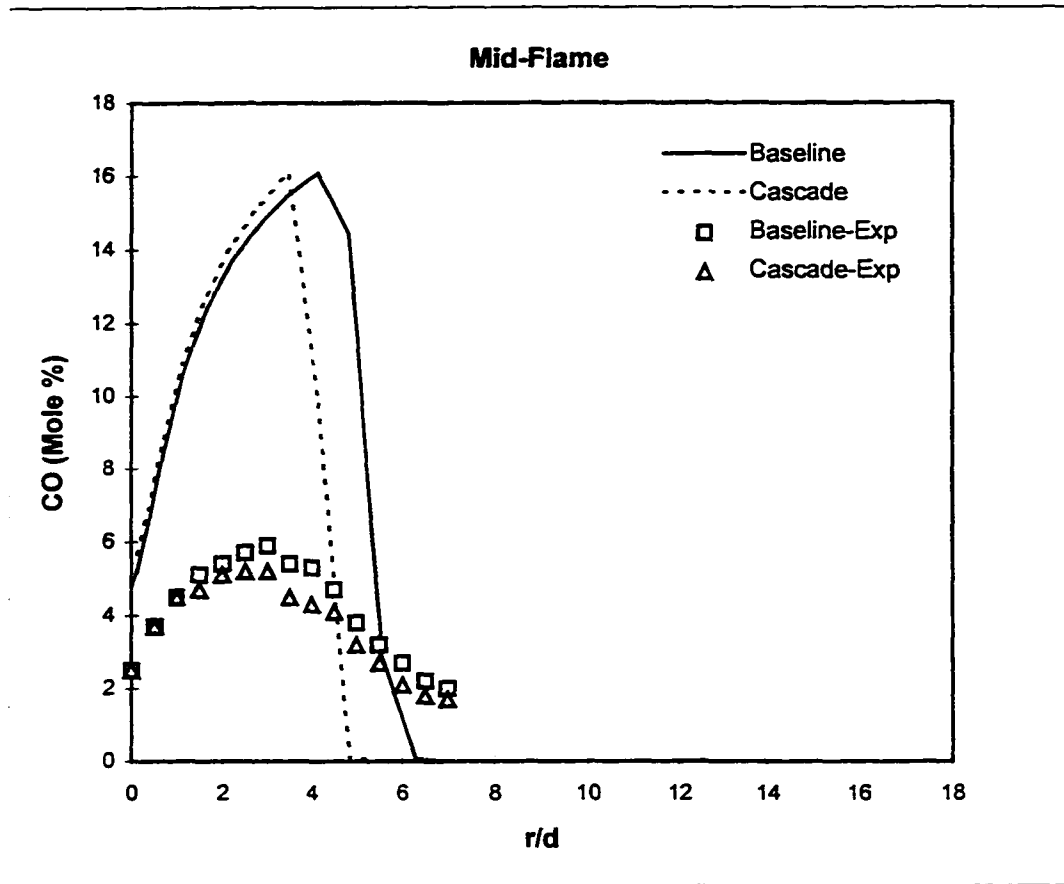


**Fig. 5.7b: Radial concentration profiles of CO for the baseline and cascaded flames in the mid-flame region ( $x/d=100$ ). Experimental data are shown for comparison.**

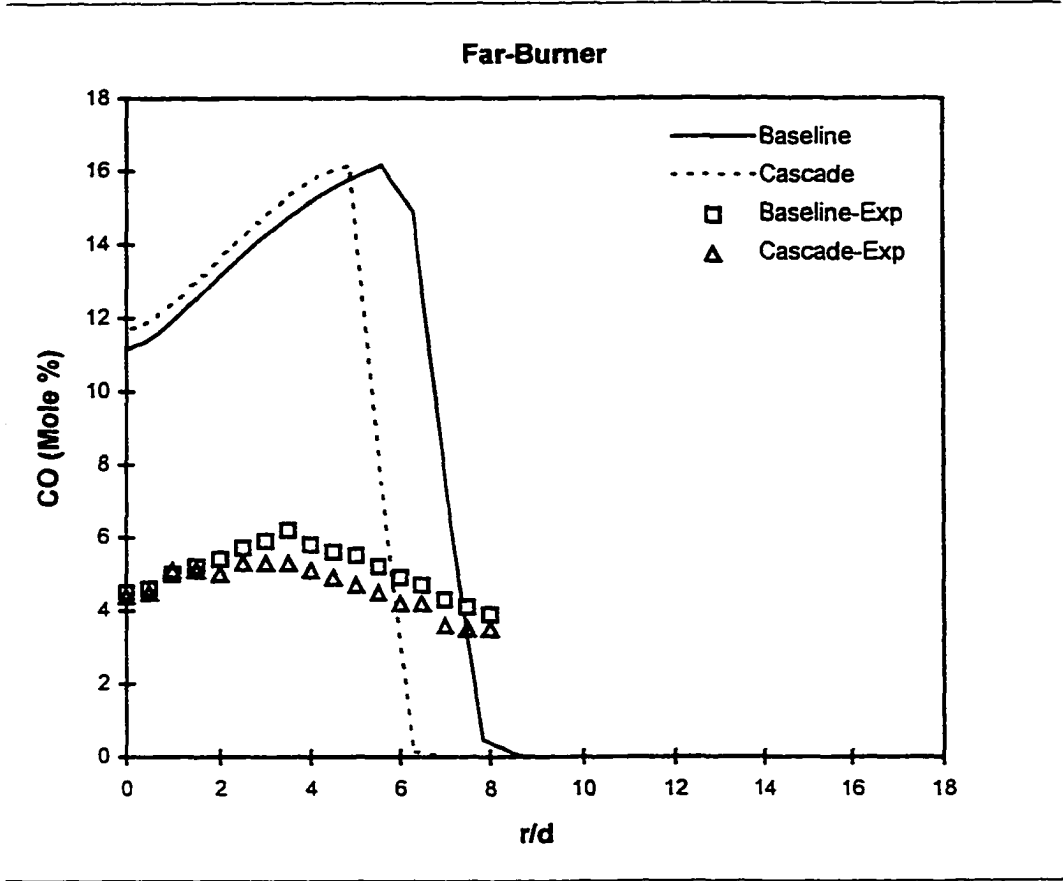


**Fig. 5.7c: Radial concentration profiles of CO for the baseline and cascaded flames in the far-burner region ( $x/d=180$ ). Experimental data are shown for comparison.**

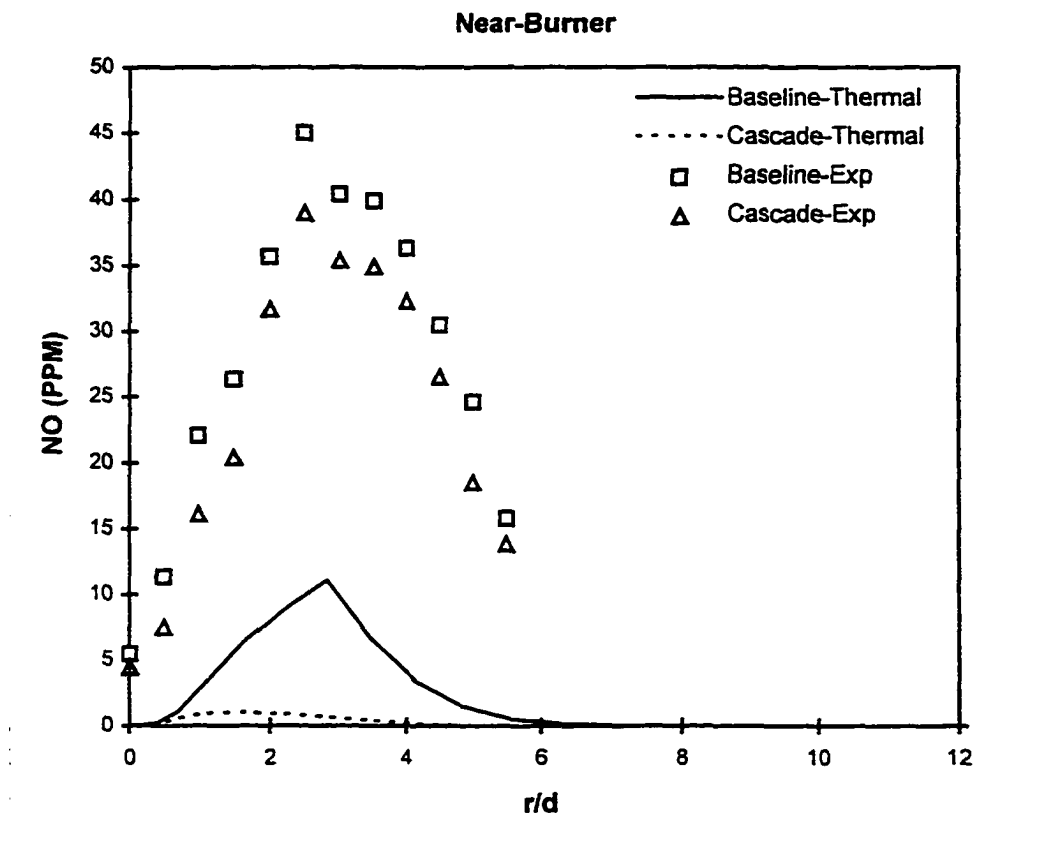


**Fig. 5.8a: Radial concentration profiles of thermal-NO for the baseline and cascaded flames in the near-burner region ( $x/d=20$ ). Experimental data are shown for comparison.**

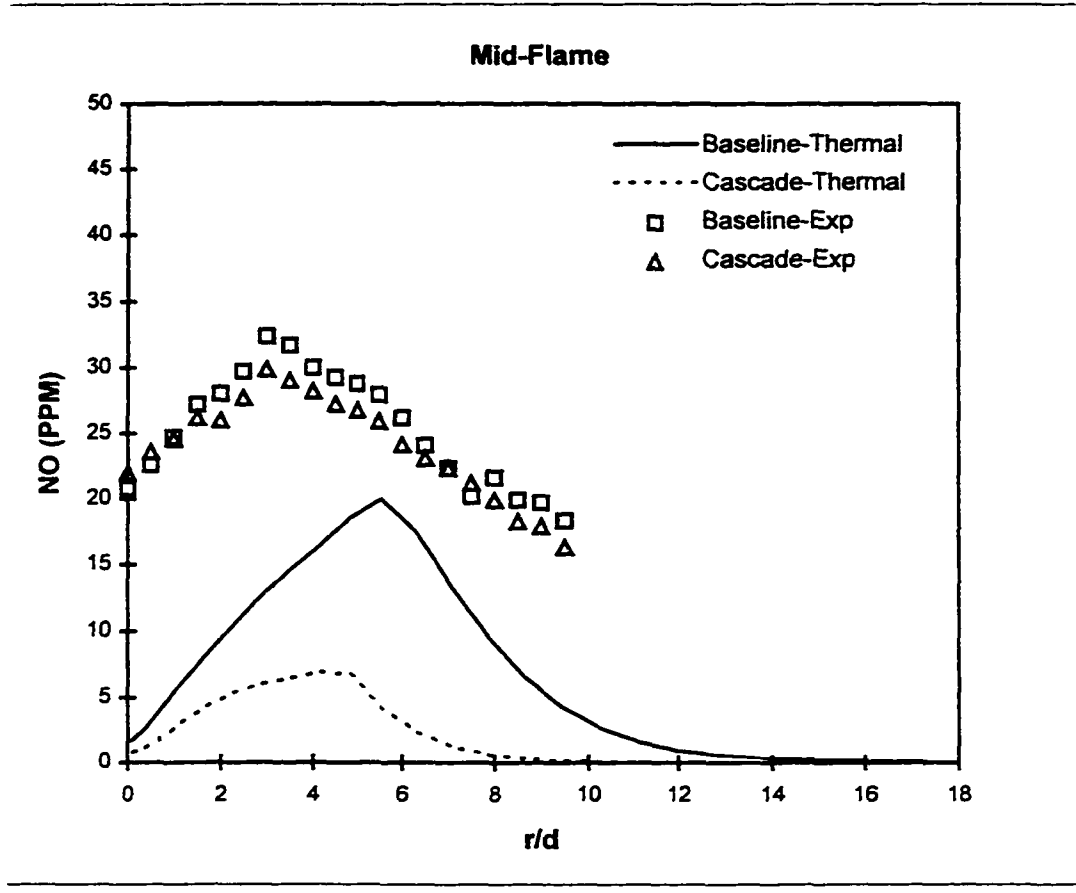


**Fig. 5.8b: Radial concentration profiles of thermal-NO for the baseline and cascaded flames in the mid-flame region ( $x/d=100$ ). Experimental data are shown for comparison.**

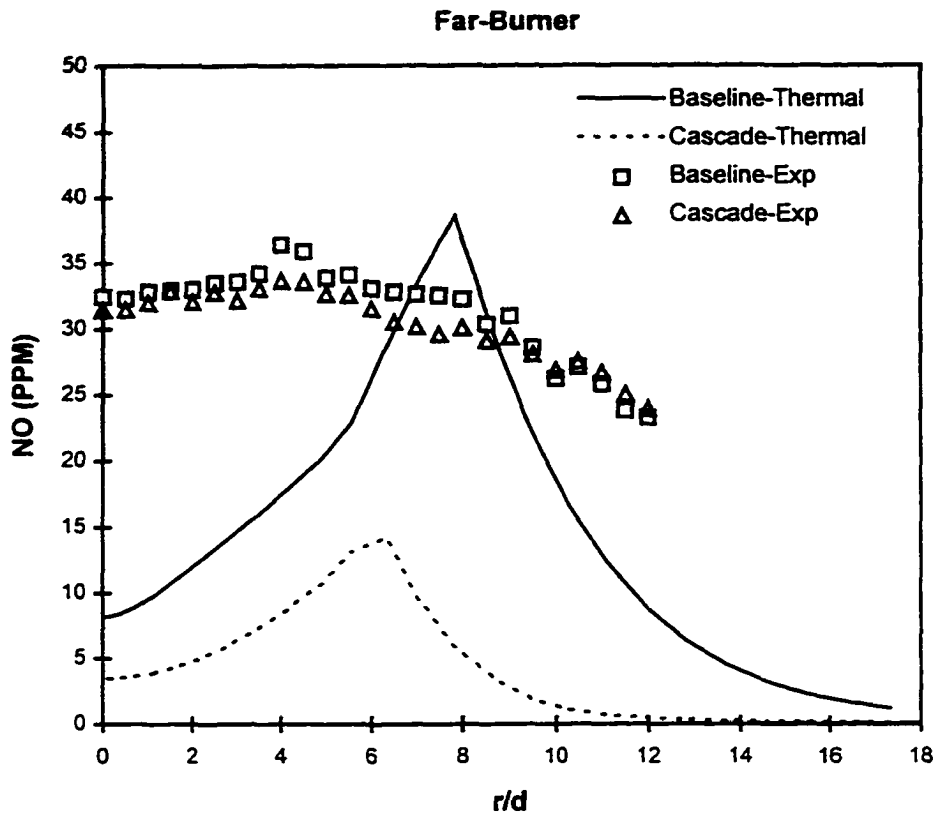


**Fig. 5.8c: Radial concentration profiles of thermal-NO for the baseline and cascaded flames in the far-burner region ( $x/d=180$ ). Experimental data are shown for comparison.**

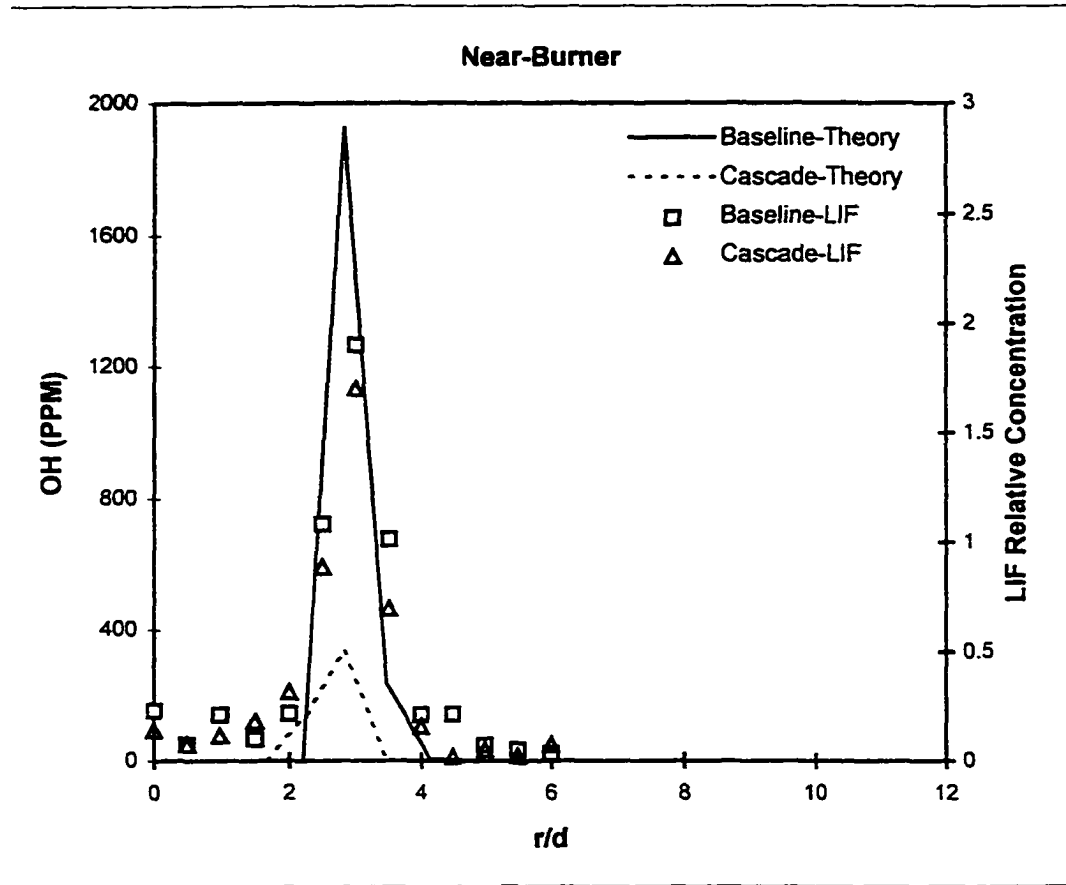


**Fig. 5.9a: Radial concentration profiles of OH radical for the baseline and cascaded flames in the near-burner region ( $x/d=20$ ). Experimental LIF data are shown for comparison.**

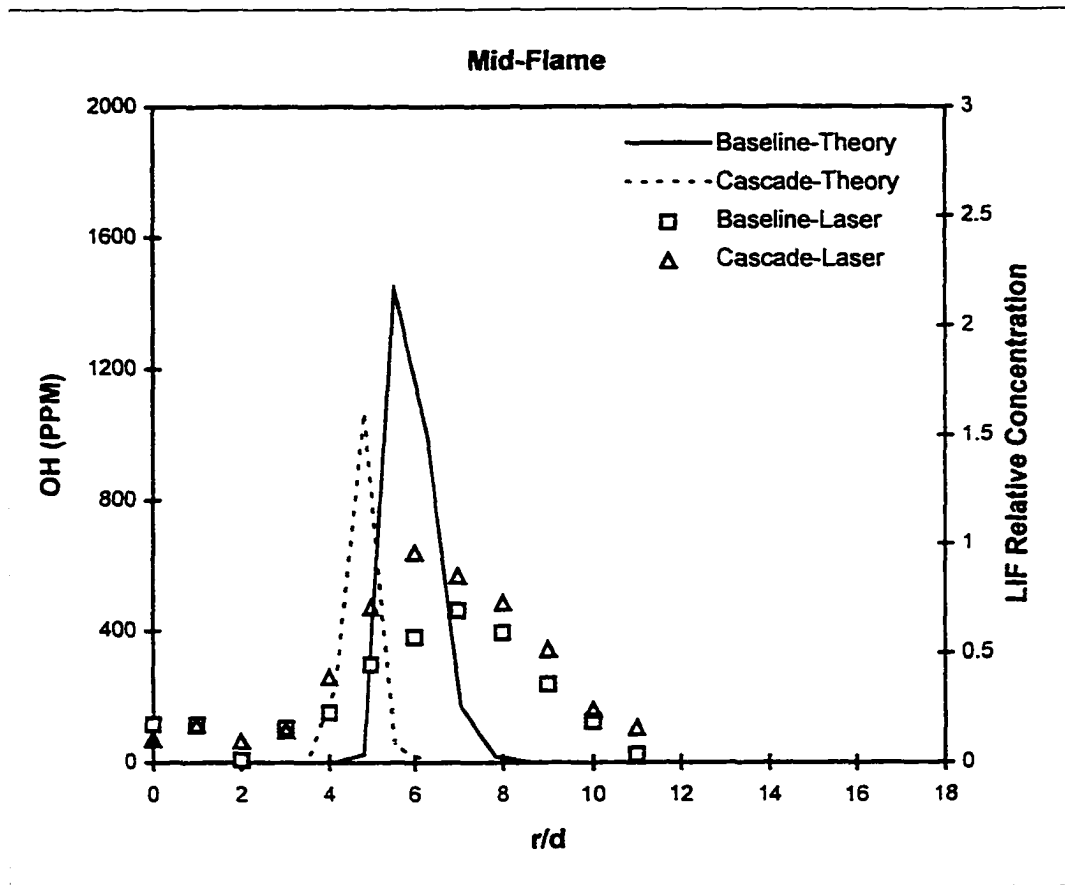


**Fig. 5.9b: Radial concentration profiles of OH radical for the baseline and cascaded flames in the mid-flame region ( $x/d=100$ ). Experimental LIF data are shown for comparison.**

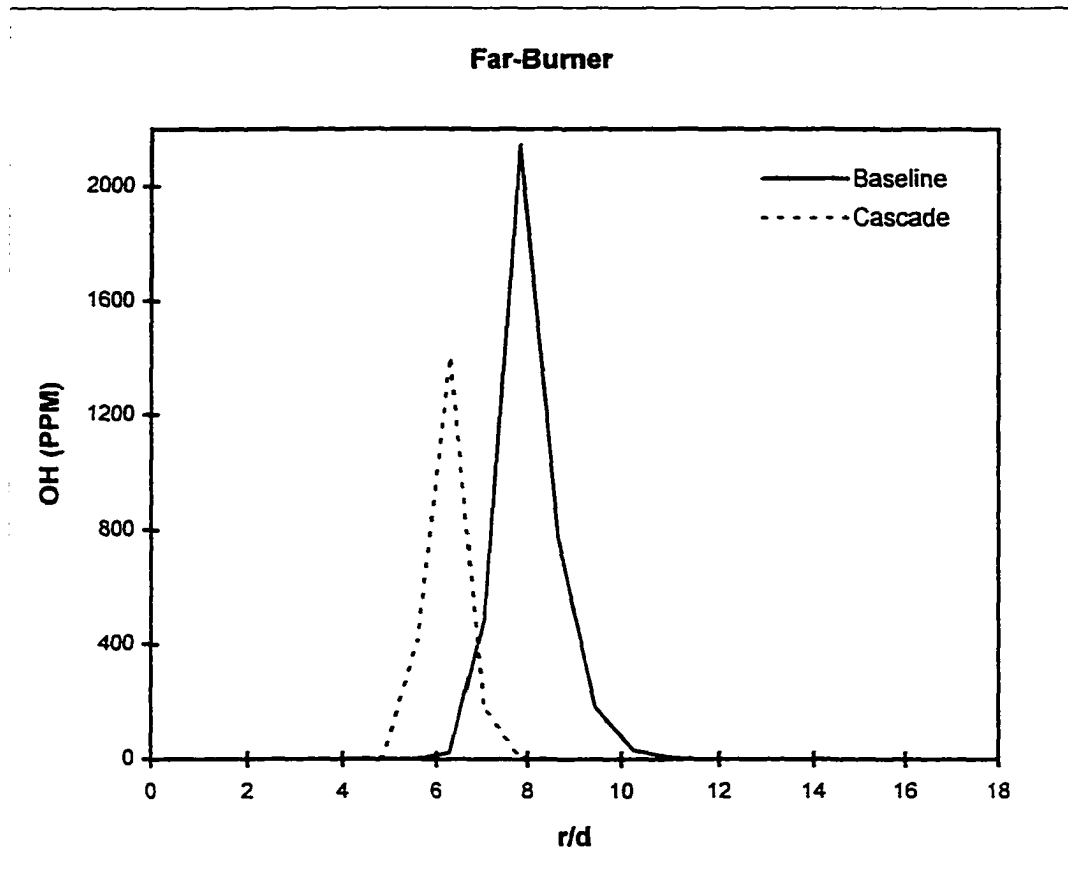


**Fig. 5.9c: Radial concentration profiles of OH radical for the baseline and cascaded flames in the far-burner region ( $x/d=180$ ).**

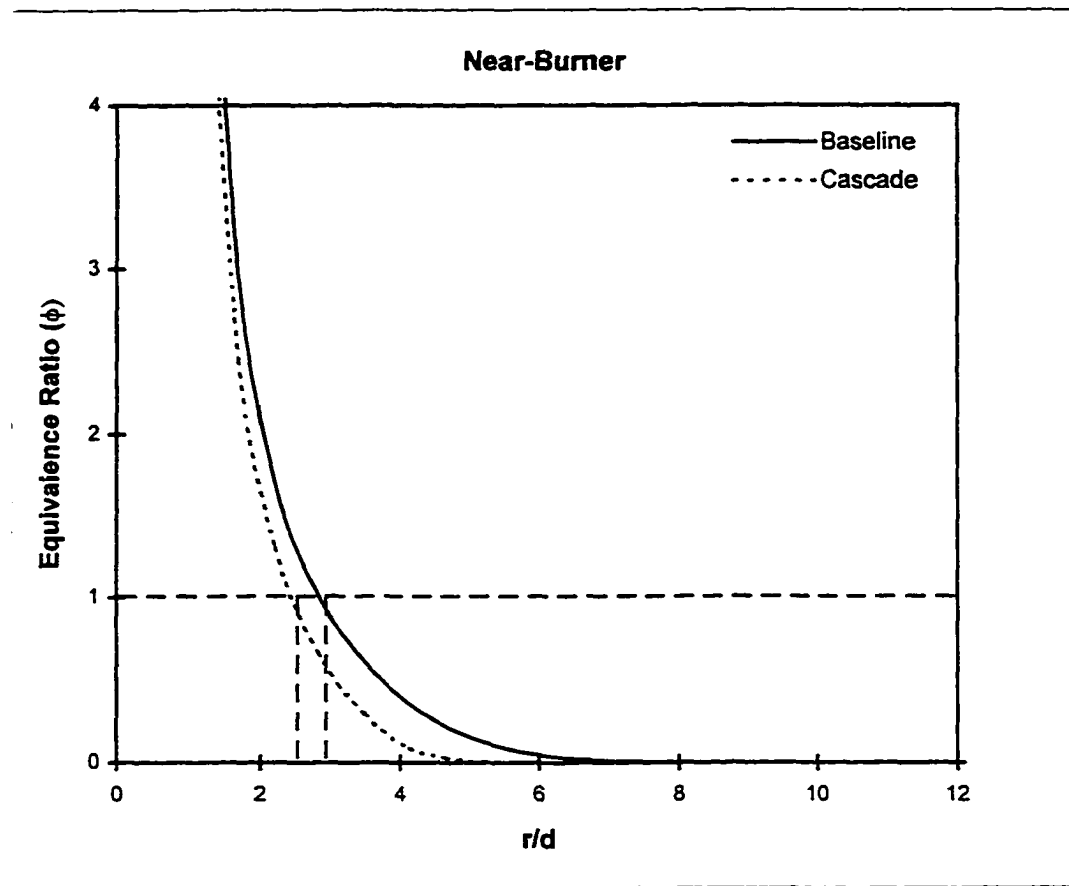


**Fig. 5.10a: Radial profiles of equivalence ratio ( $\phi$ ) for the baseline and cascaded flames in the near-burner region ( $x/d=20$ ).**

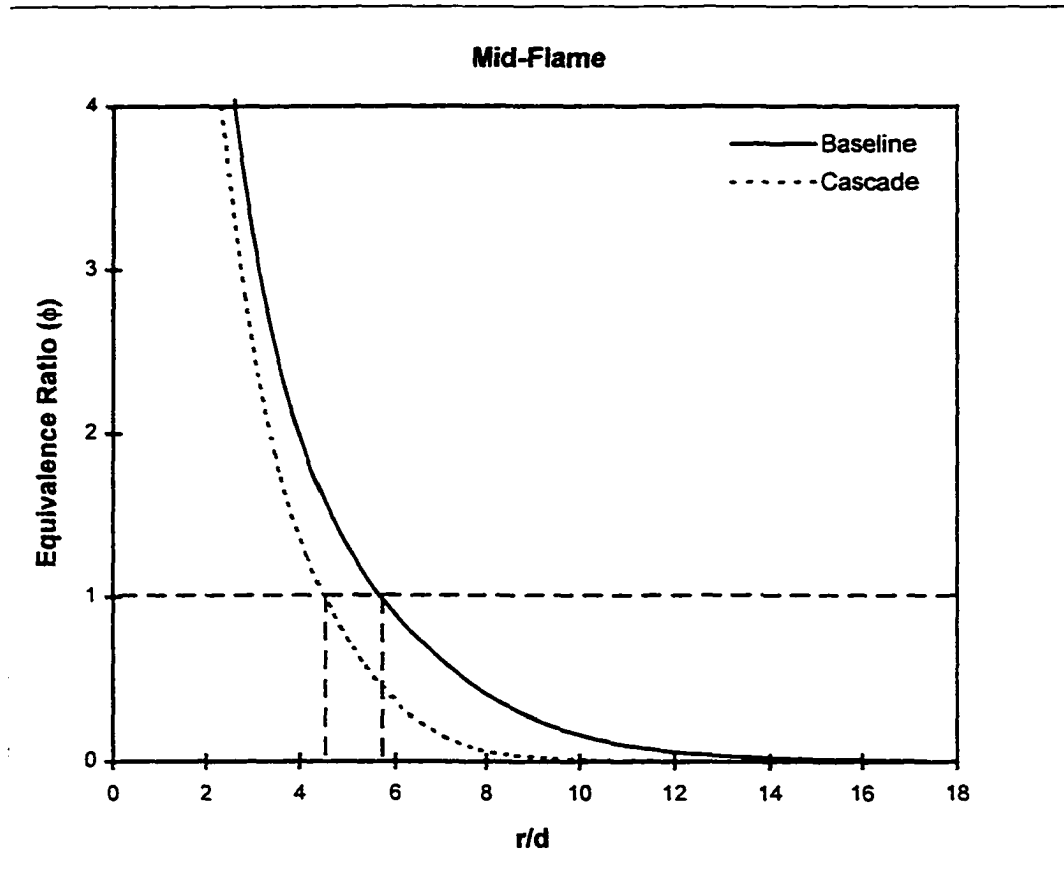


**Fig. 5.10b: Radial profiles of equivalence ratio ( $\phi$ ) for the baseline and cascaded flames in the mid-flame region ( $x/d=100$ ).**

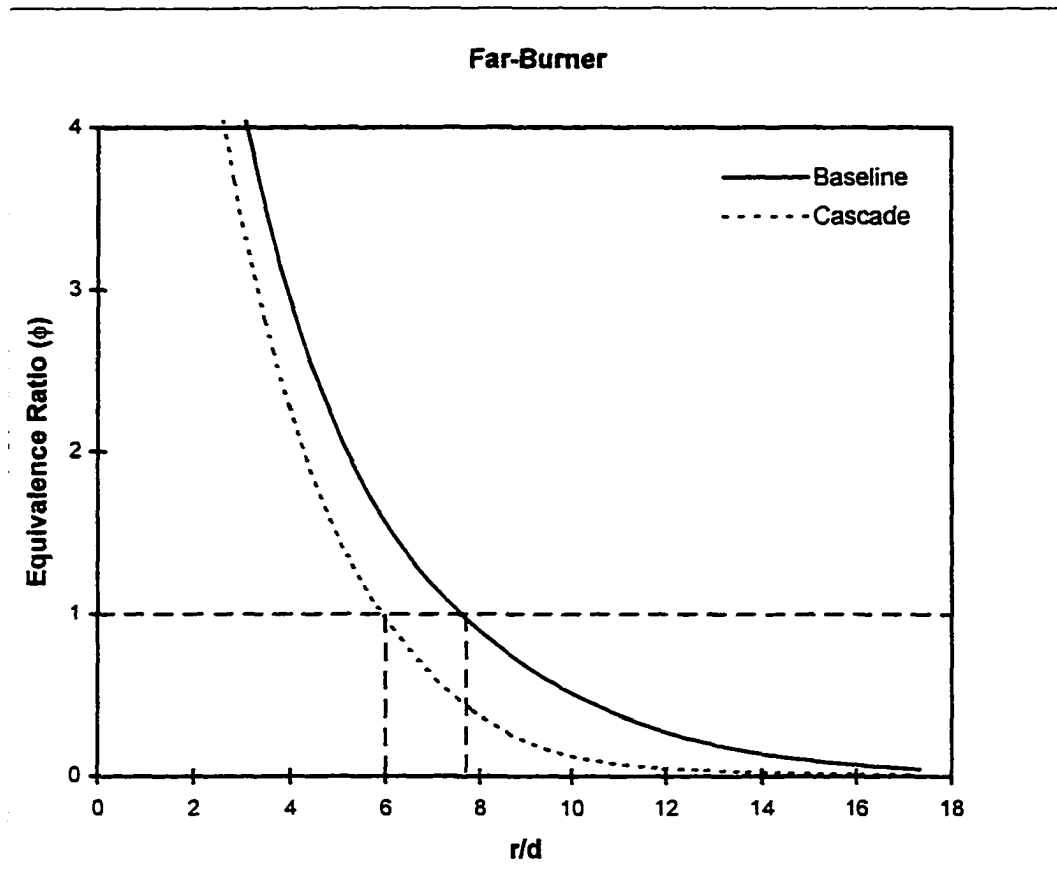


**Fig. 5.10c: Radial profiles of equivalence ratio ( $\phi$ ) for the baseline and cascaded flames in the far-burner region ( $x/d=180$ ).**

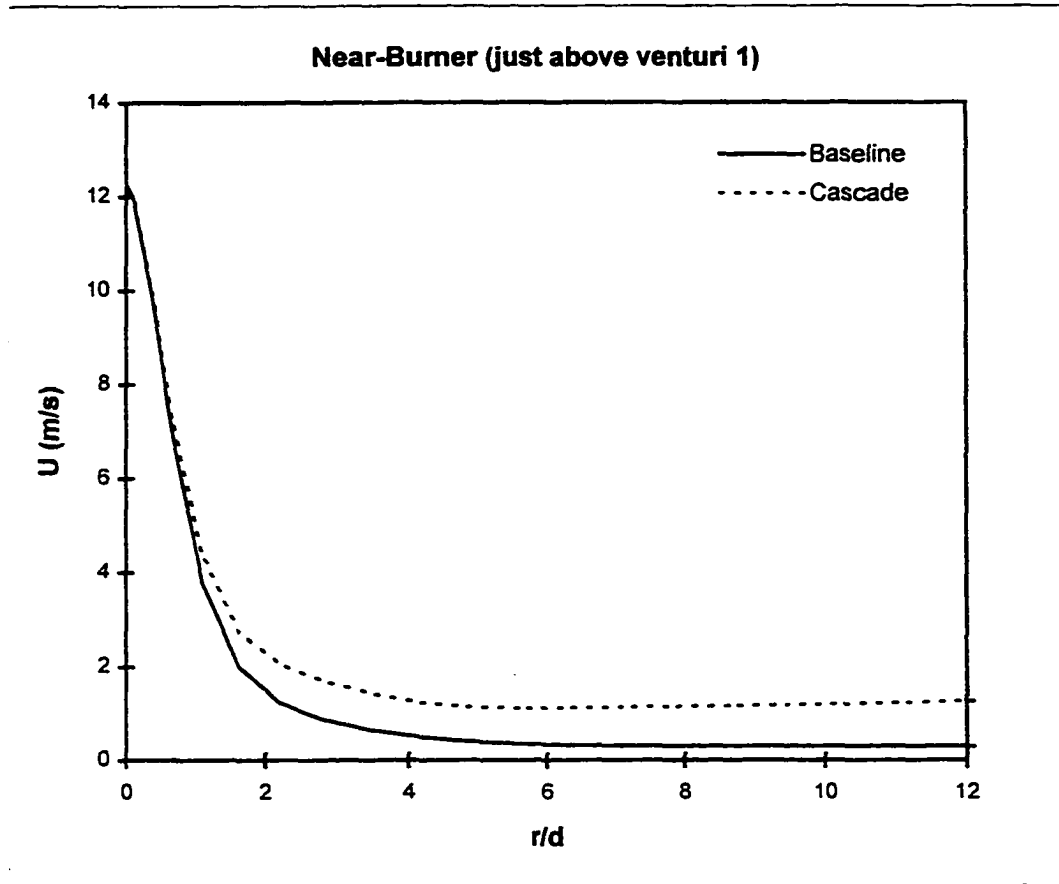


**Fig. 5.11a: Radial profiles of axial velocity (U) for the baseline and cascaded flames in the near-burner region ( $x/d=20$ ).**

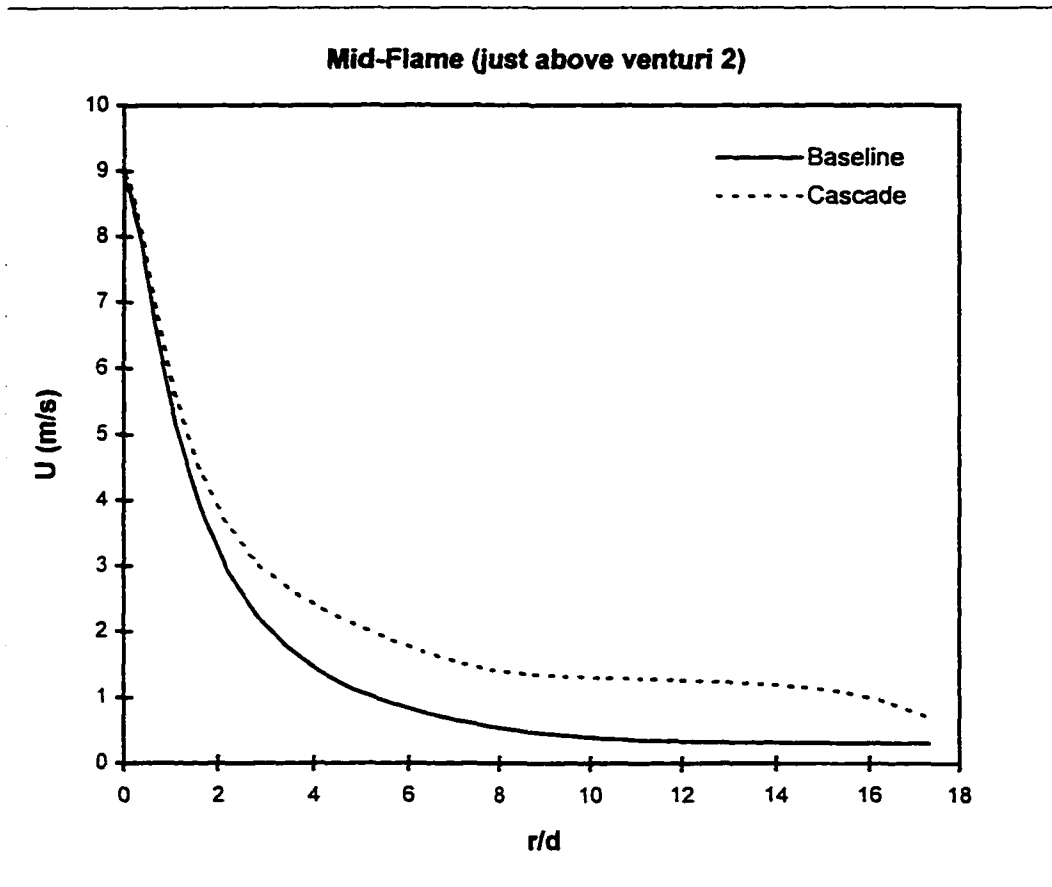


**Fig. 5.11b: Radial profiles of axial velocity ( $U$ ) for the baseline and cascaded flames in the mid-flame region ( $x/d=100$ ).**

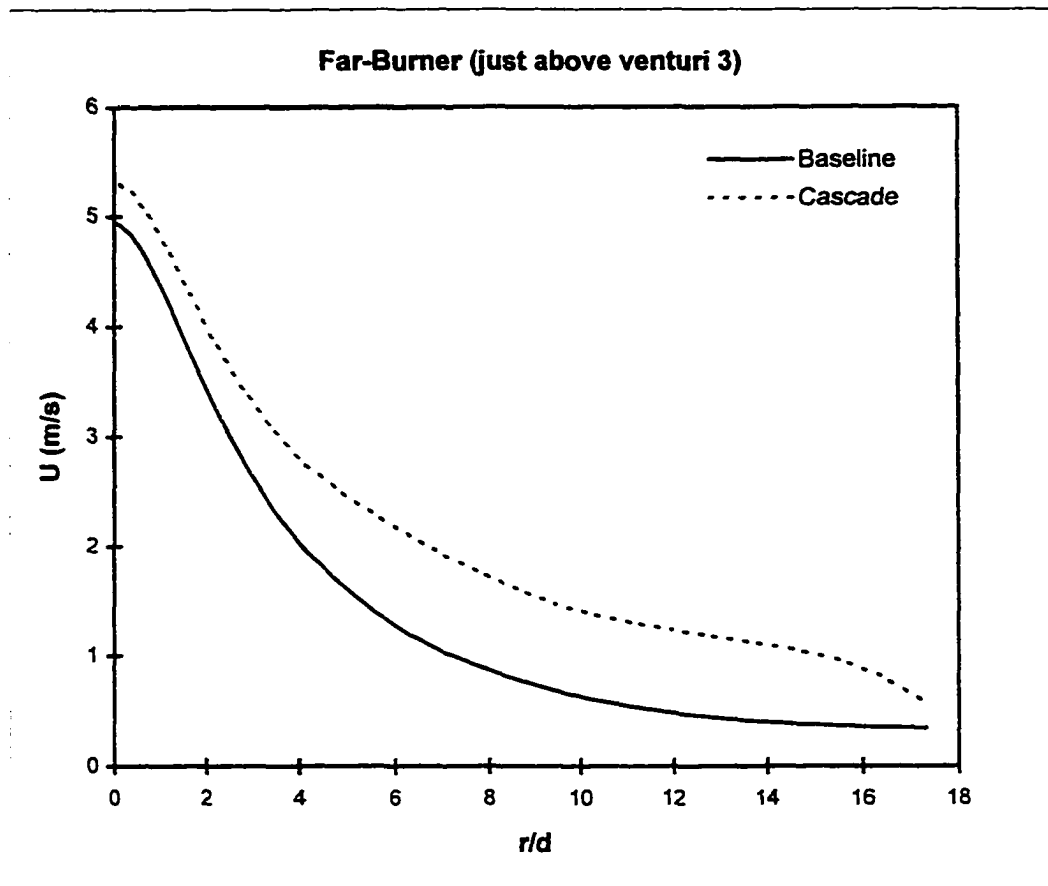


**Fig. 5.11c: Radial profiles of axial velocity ( $U$ ) for the baseline and cascaded flames in the far-burner region ( $x/d=180$ ).**

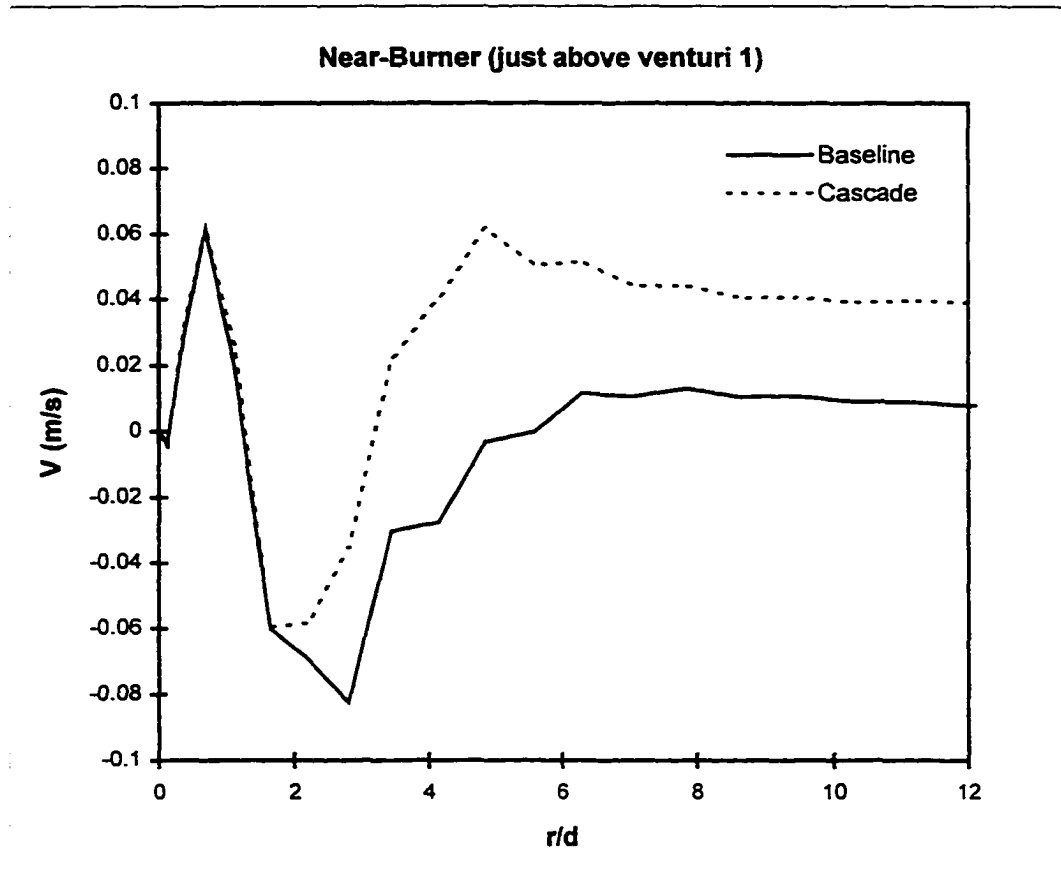


**Fig. 5.12a: Radial profiles of radial velocity ( $V$ ) for the baseline and cascaded flames in the near-burner region ( $x/d=20$ ).**

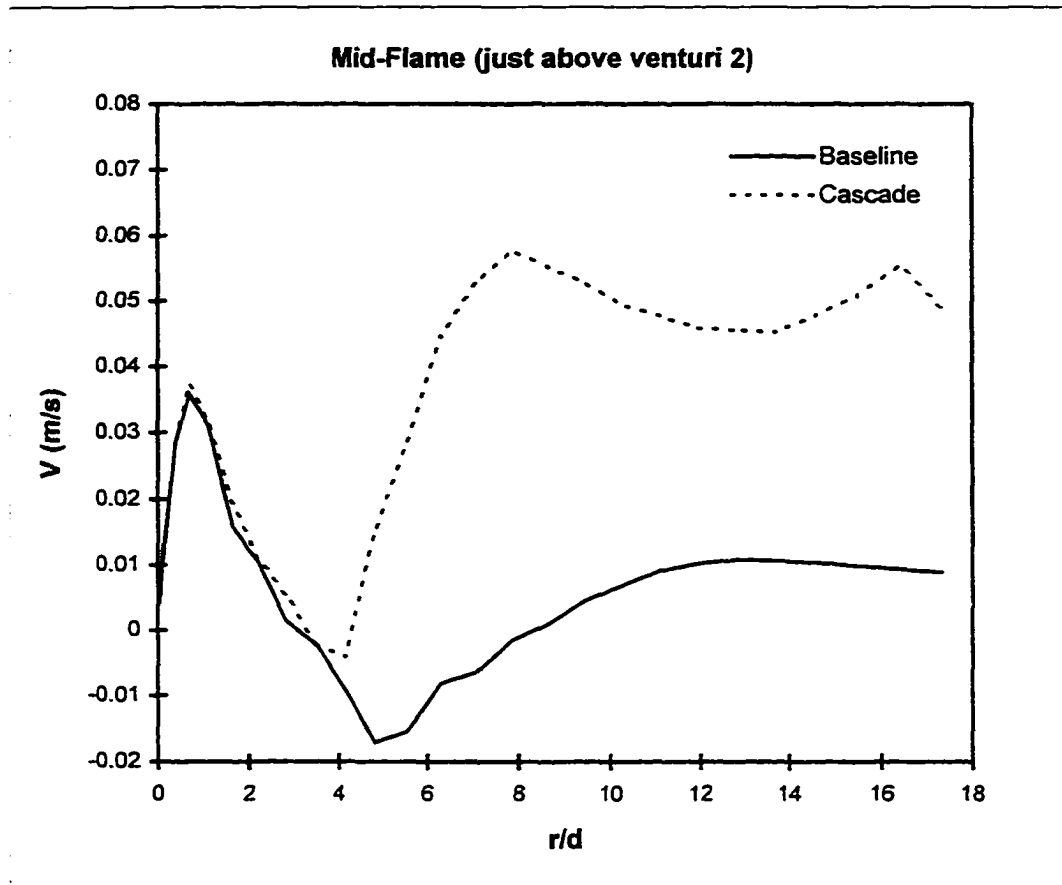


**Fig. 5.12b: Radial profiles of radial velocity ( $V$ ) for the baseline and cascaded flames in the mid-flame region ( $x/d=100$ ).**

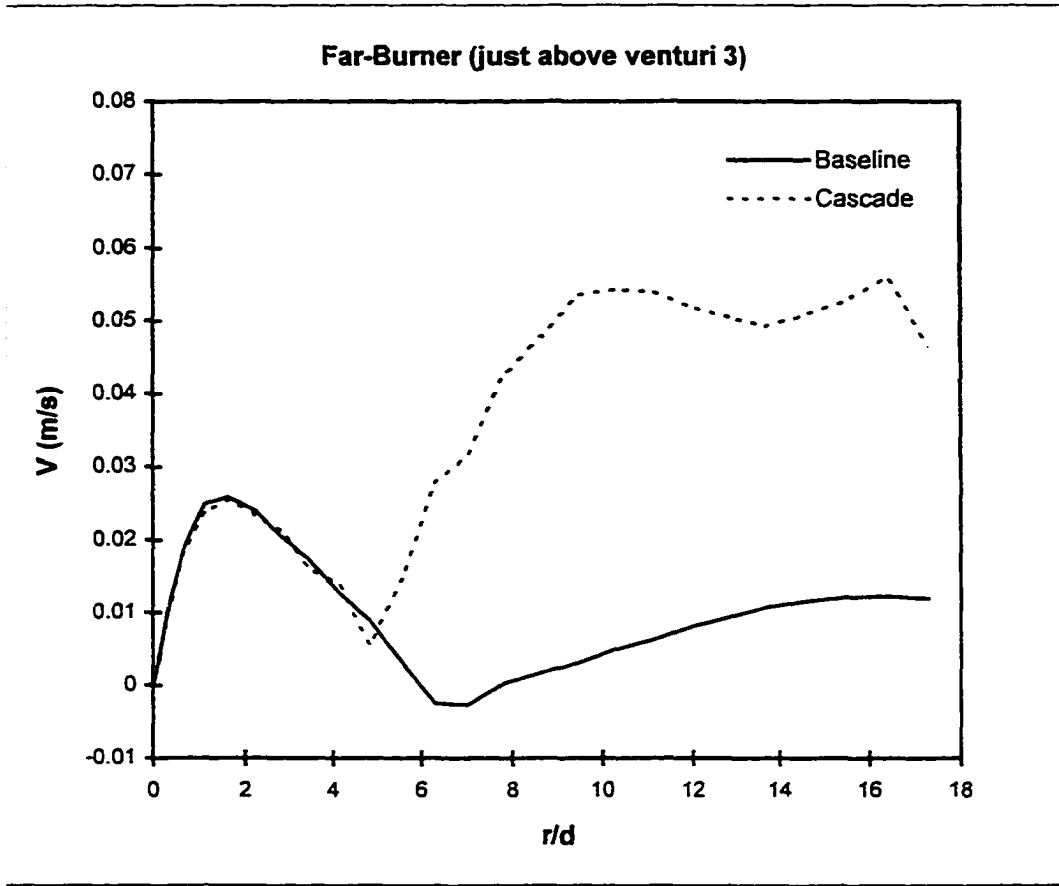


**Fig. 5.12c: Radial profiles of radial velocity ( $V$ ) for the baseline and cascaded flames in the far-burner region ( $x/d=180$ ).**

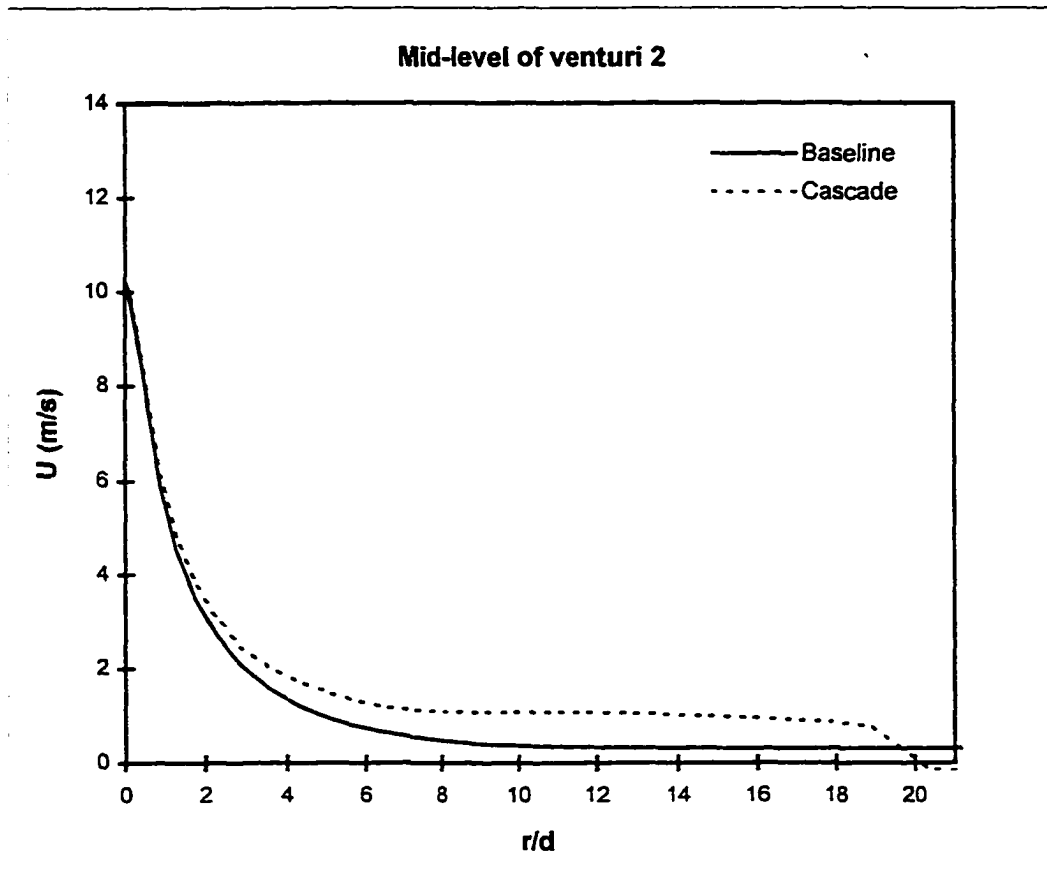


**Fig. 5.13a: Radial profiles of axial velocity (U) for the baseline and cascaded flames at  $x/d=80$  (see Fig. 5.1c).**

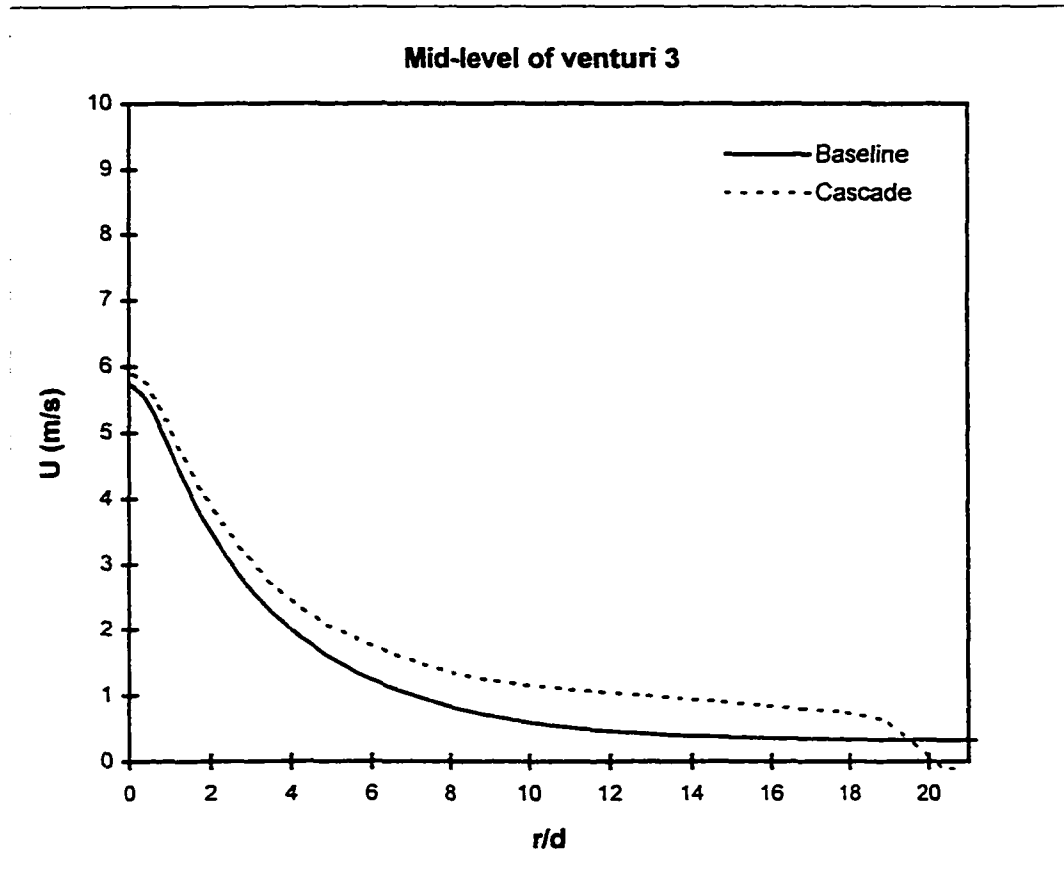


**Fig. 5.13b: Radial profiles of axial velocity ( $U$ ) for the baseline and cascaded flames at  $x/d=160$  (see Fig. 5.1c).**

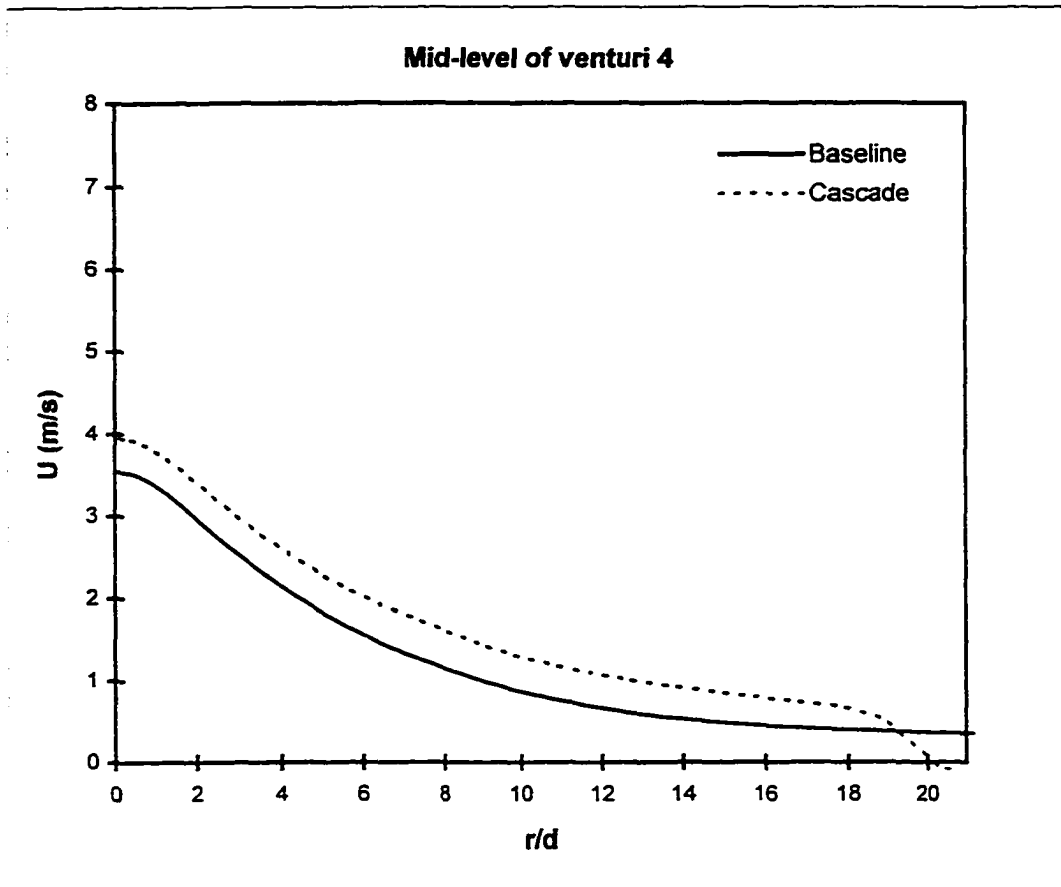


**Fig. 5.13c: Radial profiles of axial velocity ( $U$ ) for the baseline and cascaded flames at  $x/d=240$  (see Fig. 5.1c).**

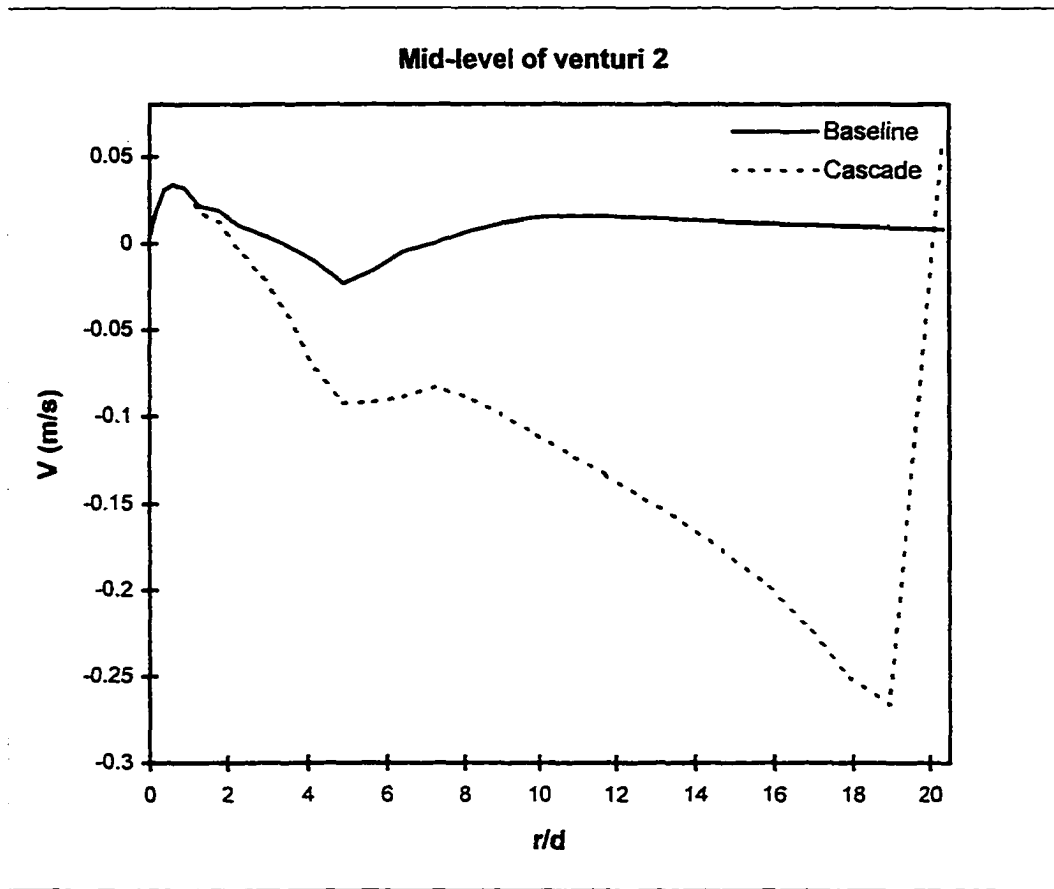


**Fig. 5.14a: Radial profiles of radial velocity (V) for the baseline and cascaded flames at  $x/d=80$  (see Fig. 5.1c).**

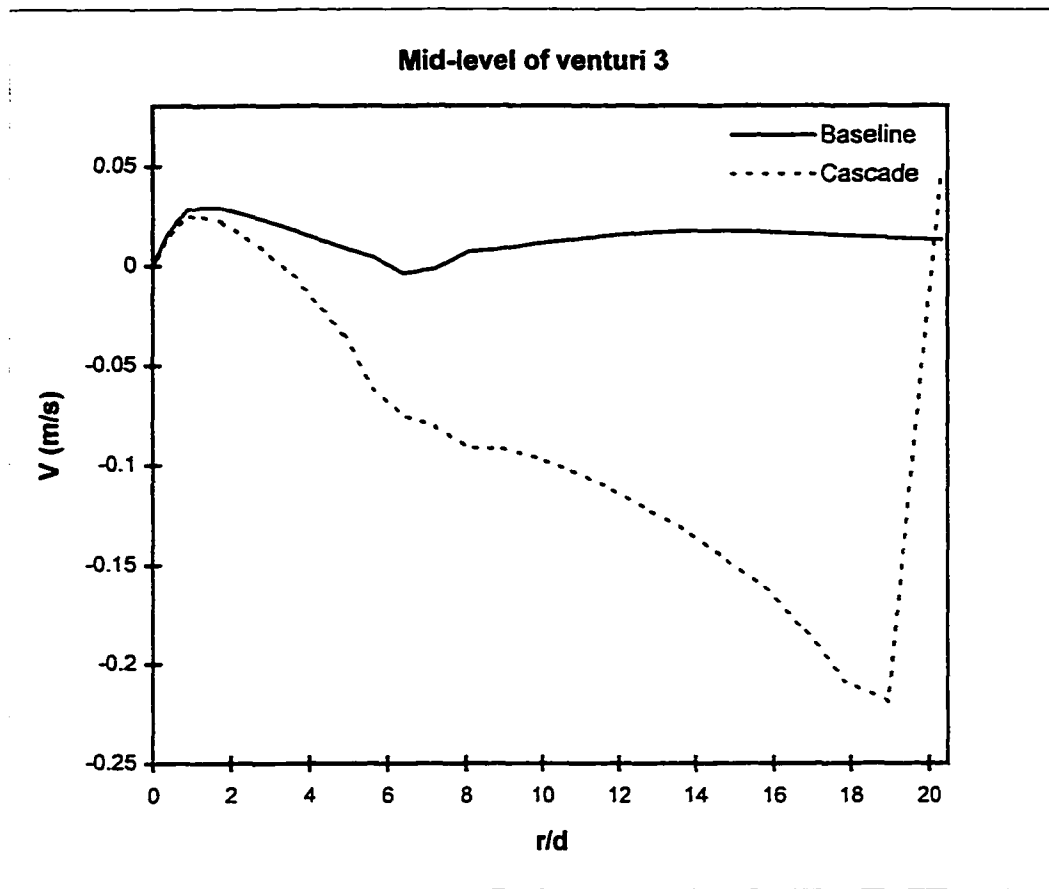


**Fig. 5.14b: Radial profiles of radial velocity (V) for the baseline and cascaded flames at  $x/d=160$  (see Fig. 5.1c).**

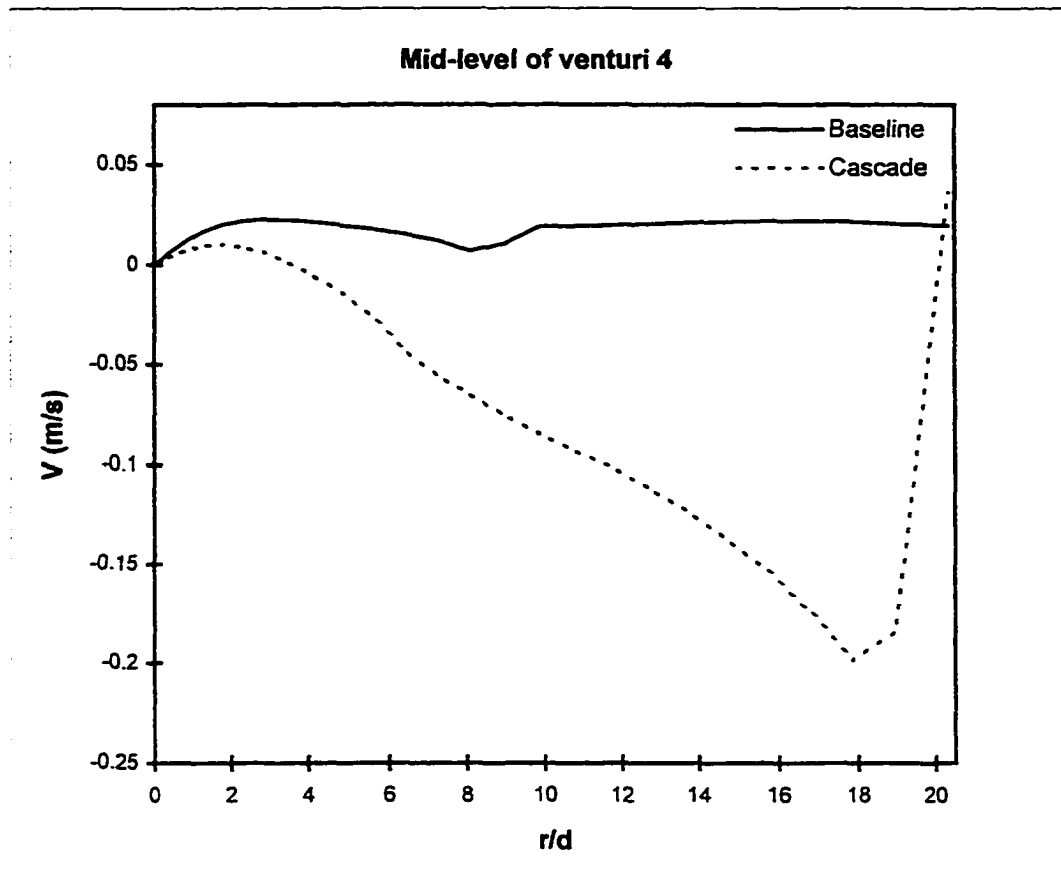


**Fig. 5.14c: Radial profiles of radial velocity ( $V$ ) for the baseline and cascaded flames at  $x/d=240$  (see Fig. 5.1c).**

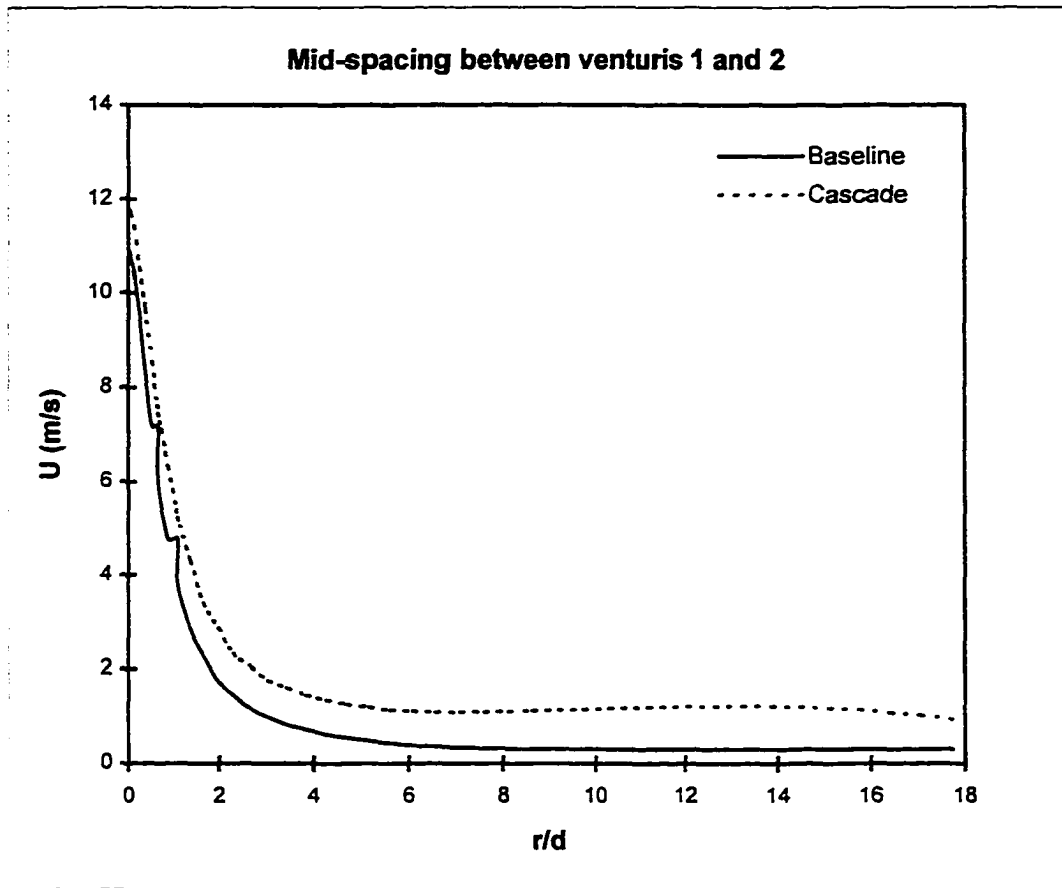


**Fig. 5.15a: Radial profiles of axial velocity (U) for the baseline and cascaded flames at  $x/d=40$  (see Fig. 5.1c).**

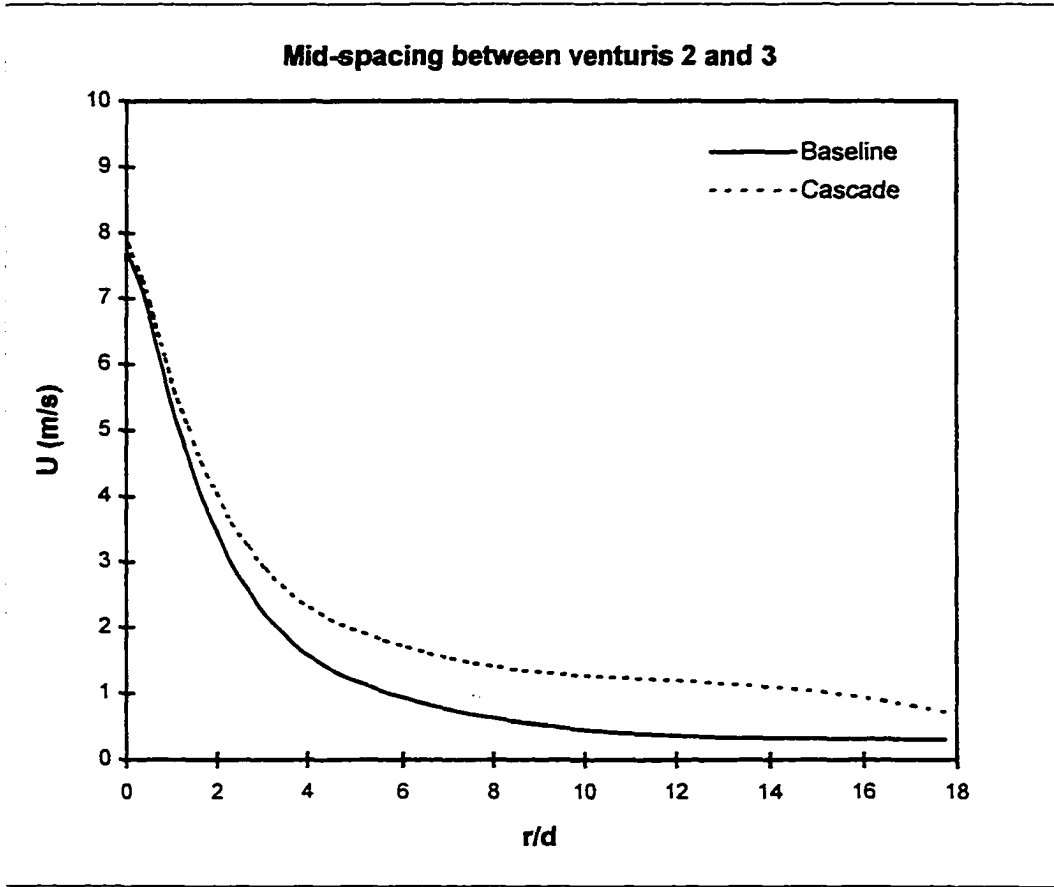


**Fig. 5.15b: Radial profiles of axial velocity (U) for the baseline and cascaded flames at  $x/d=120$  (see Fig. 5.1c).**

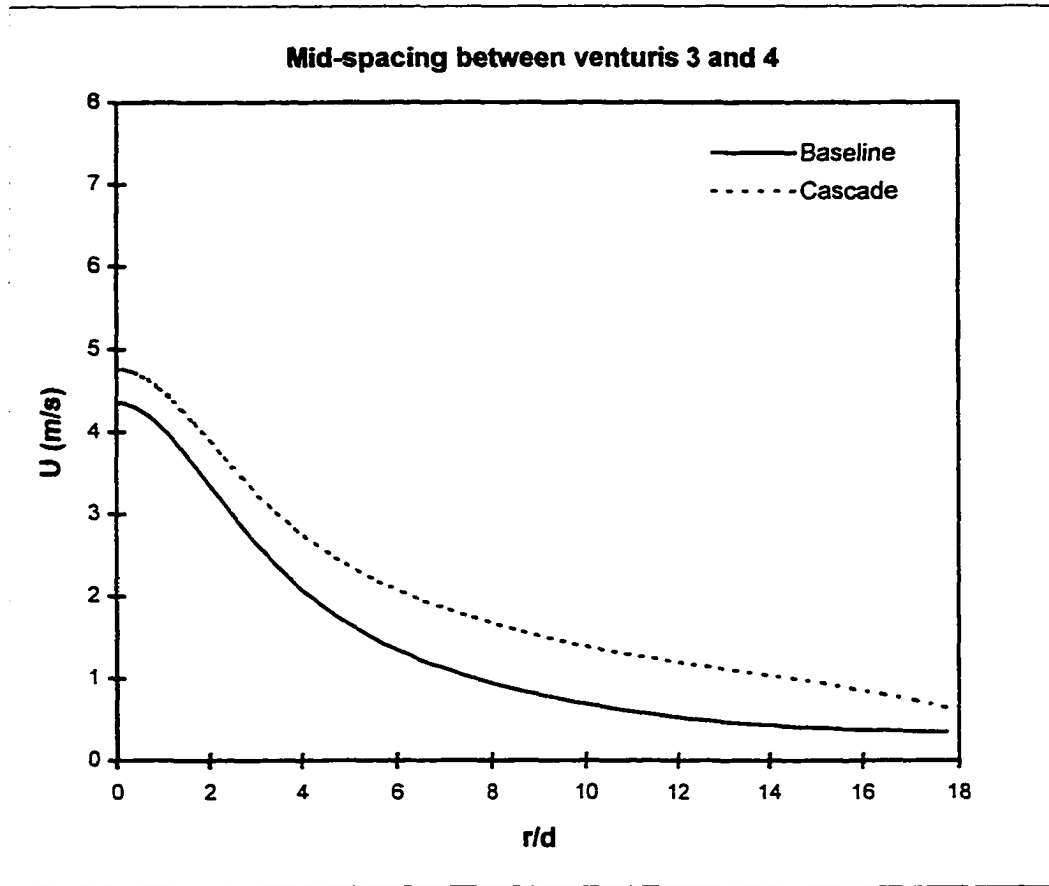


**Fig. 5.15c: Radial profiles of axial velocity (U) for the baseline and cascaded flames at  $x/d=200$  (see Fig. 5.1c).**

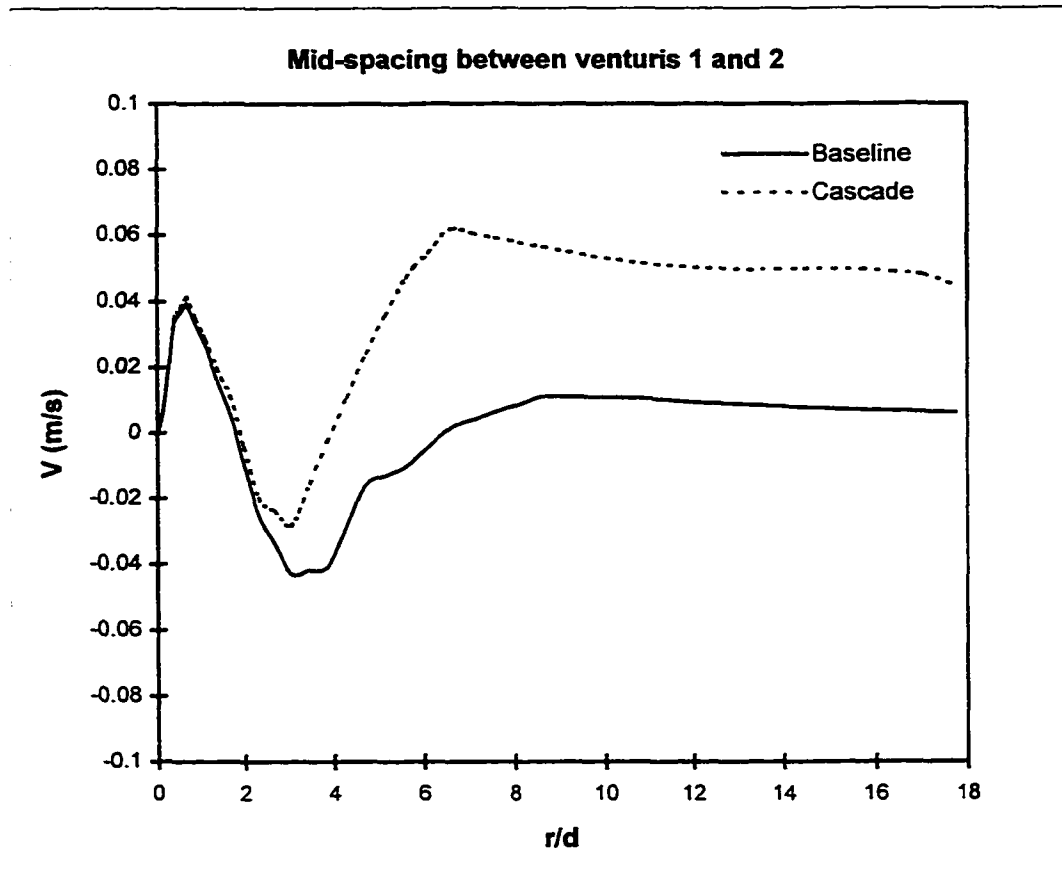


**Fig. 5.16a: Radial profiles of radial velocity ( $V$ ) for the baseline and cascaded flames at  $x/d=40$  (see Fig. 5.1c).**

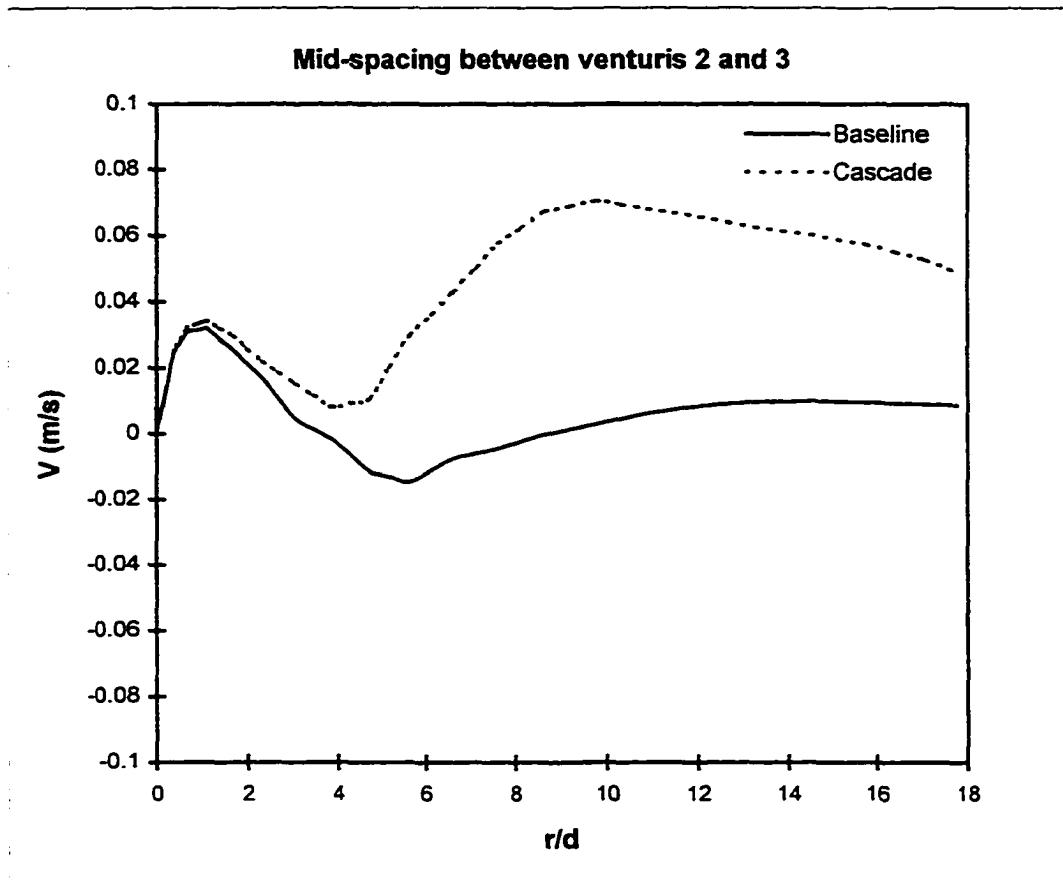


**Fig. 5.16b: Radial profiles of radial velocity ( $V$ ) for the baseline and cascaded flames at  $x/d=120$  (see Fig. 5.1c).**

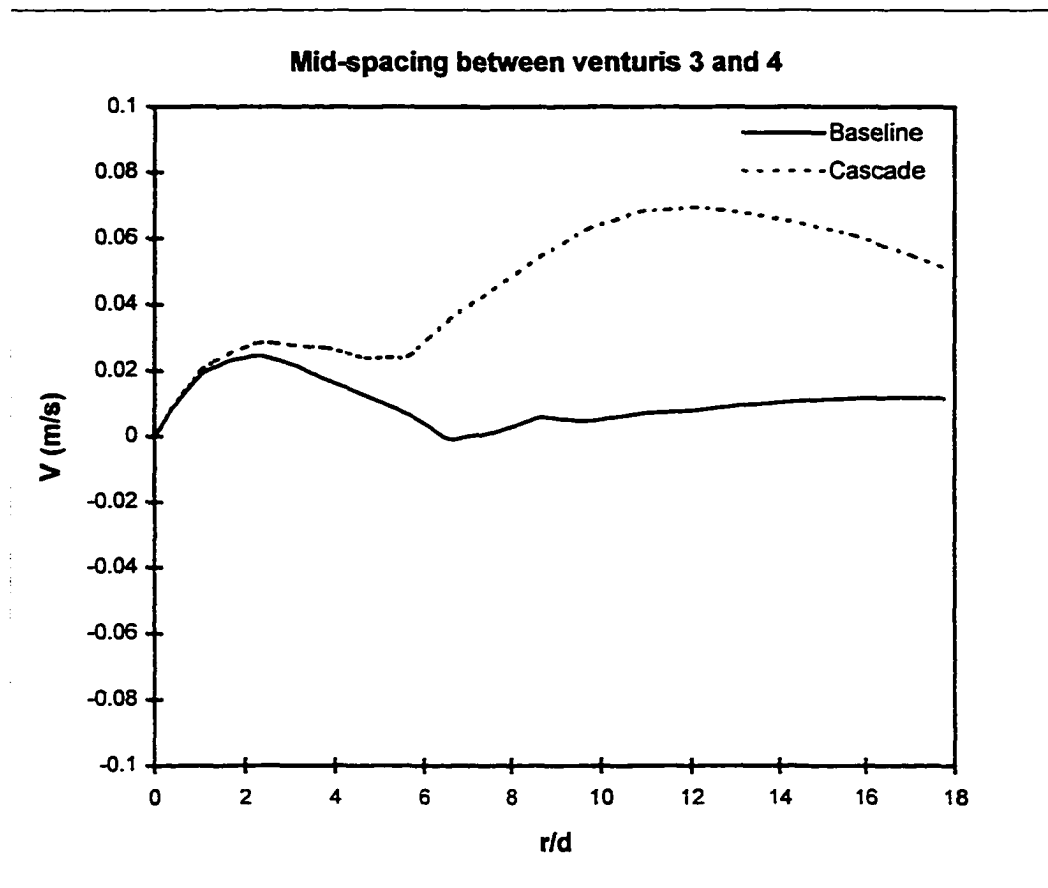
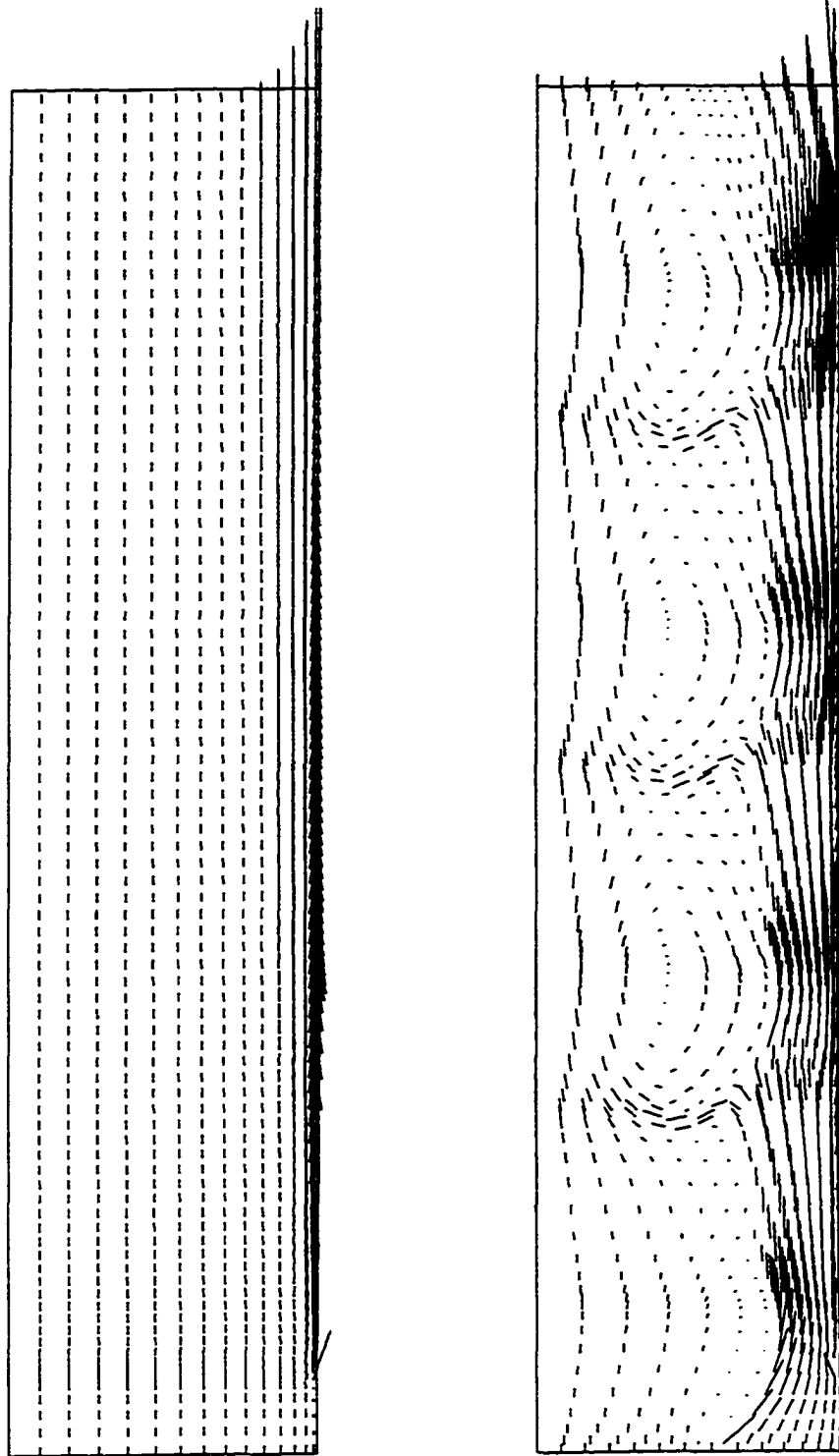


**Fig. 5.16c: Radial profiles of radial velocity (V) for the baseline and cascaded flames at  $x/d=200$  (see Fig. 5.1c).**



**(a) Baseline**

**(b) Cascaded**

**Fig. 5.17 (a, b): Total velocity vector field in the baseline and cascaded flames.**

At the base of venturi 3

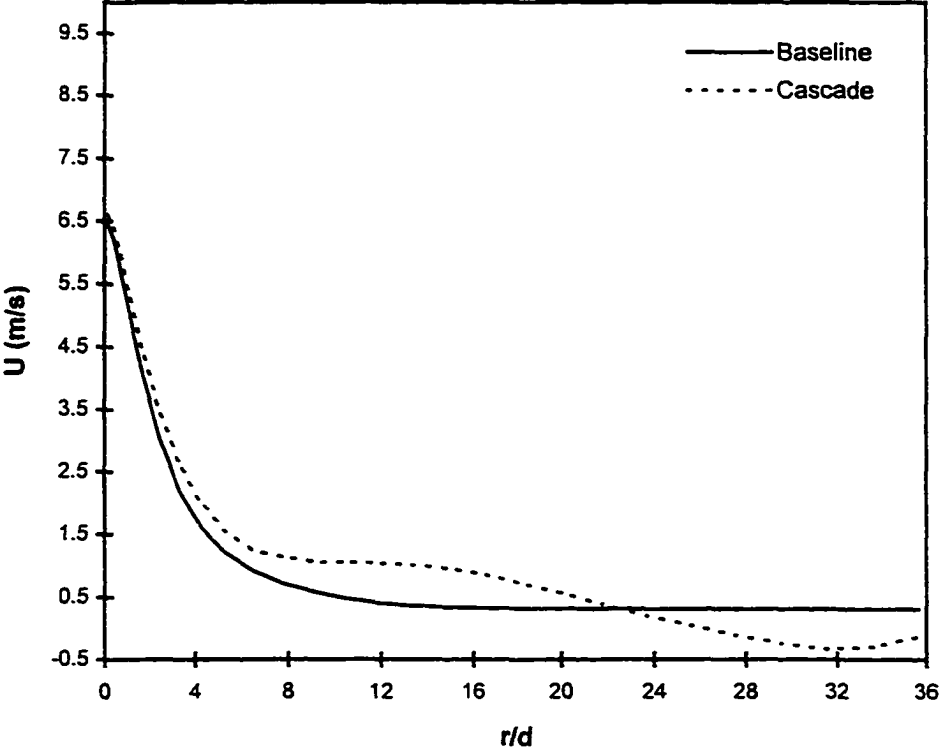
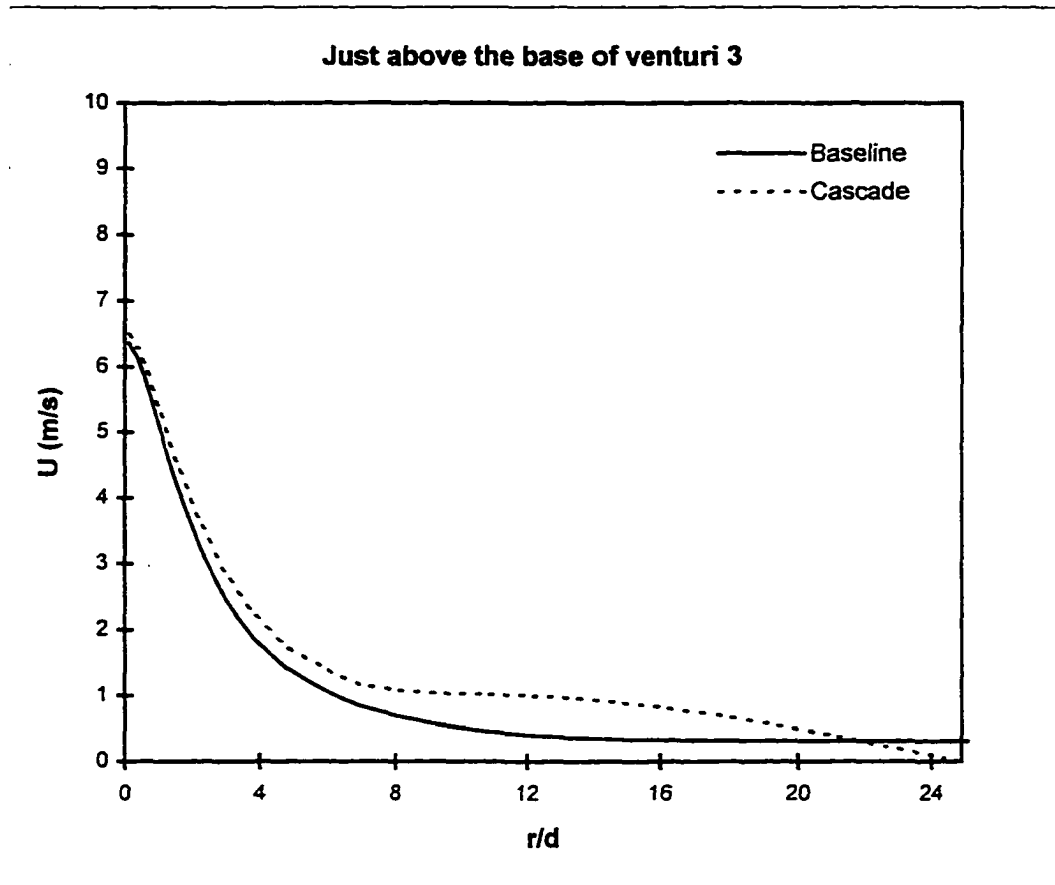
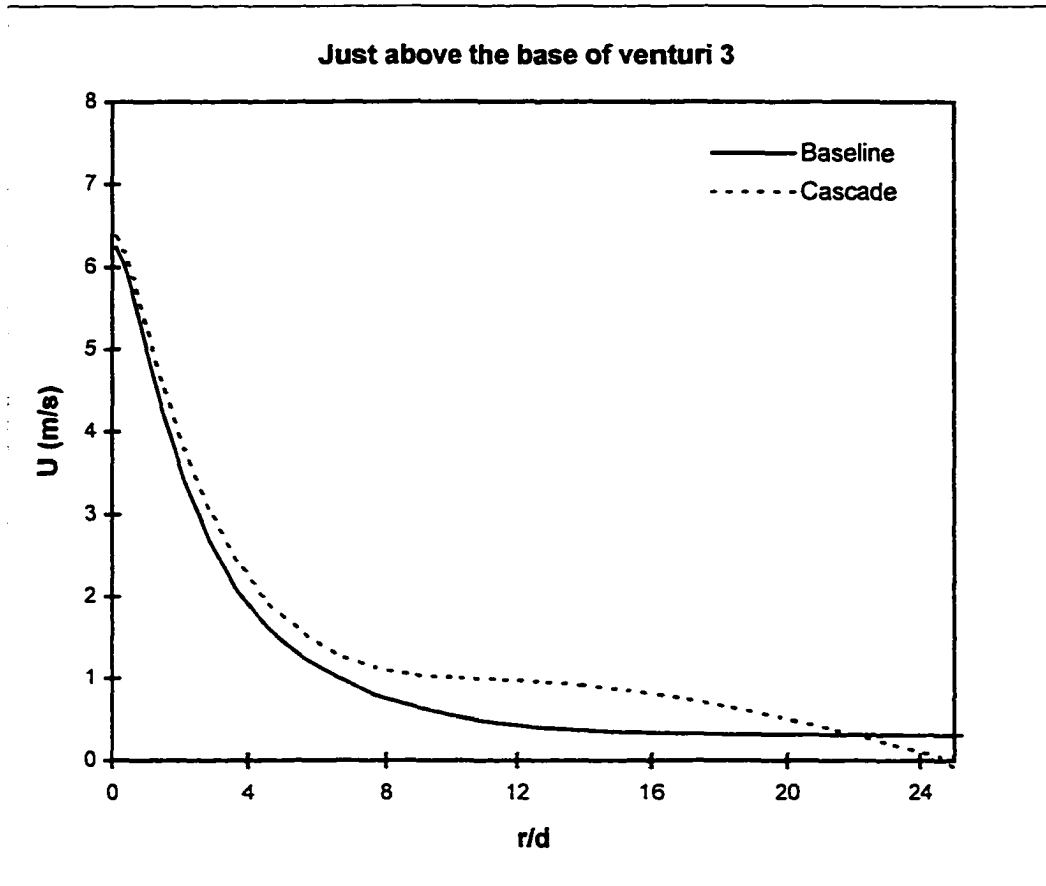


Fig. 5.18a: Radial profiles of axial velocity (U) for the baseline and cascaded flames at  $x/d=142.5$  (see Fig. 5.1d).



**Fig. 5.18b: Radial profiles of axial velocity (U) for the baseline and cascaded flames at 2.5d above base of venturi 3 (see Fig. 5.1d).**



**Fig. 5.18c: Radial profiles of axial velocity (U) for the baseline and cascaded flames at 5d above base of venturi 3 (see Fig. 5.1d).**

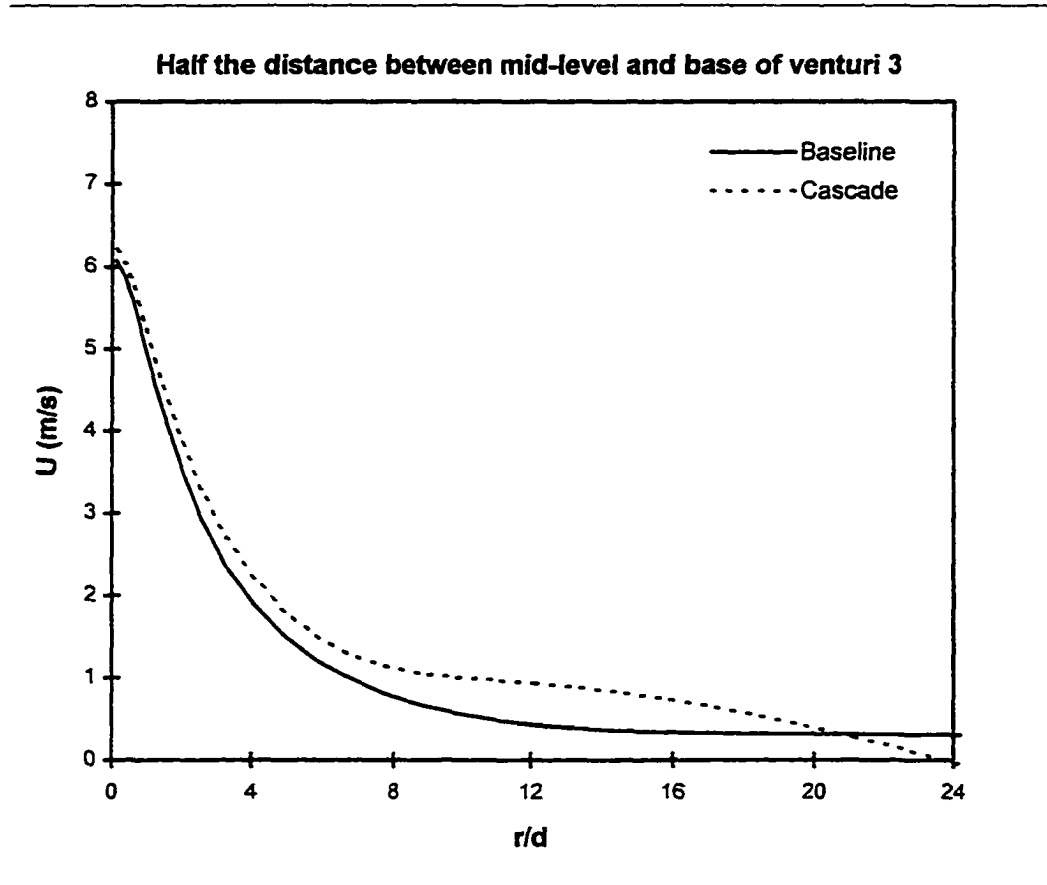


**Fig. 5.18d: Radial profiles of axial velocity ( $U$ ) for the baseline and cascaded flames at  $8.75d$  above base of venturi 3 (see Fig. 5.1d).**

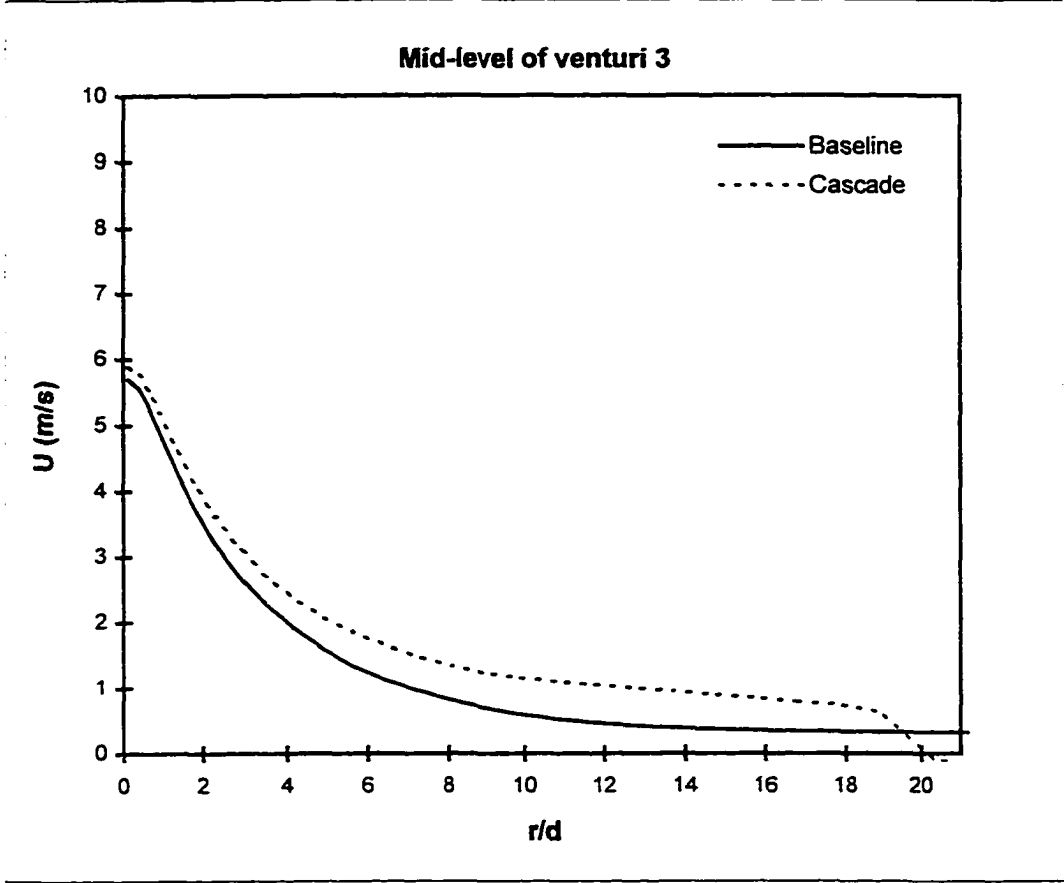


**Fig. 5.18e: Radial profiles of axial velocity (U) for the baseline and cascaded flames at 17.5d above base of venturi 3 (see Fig. 5.1d).**

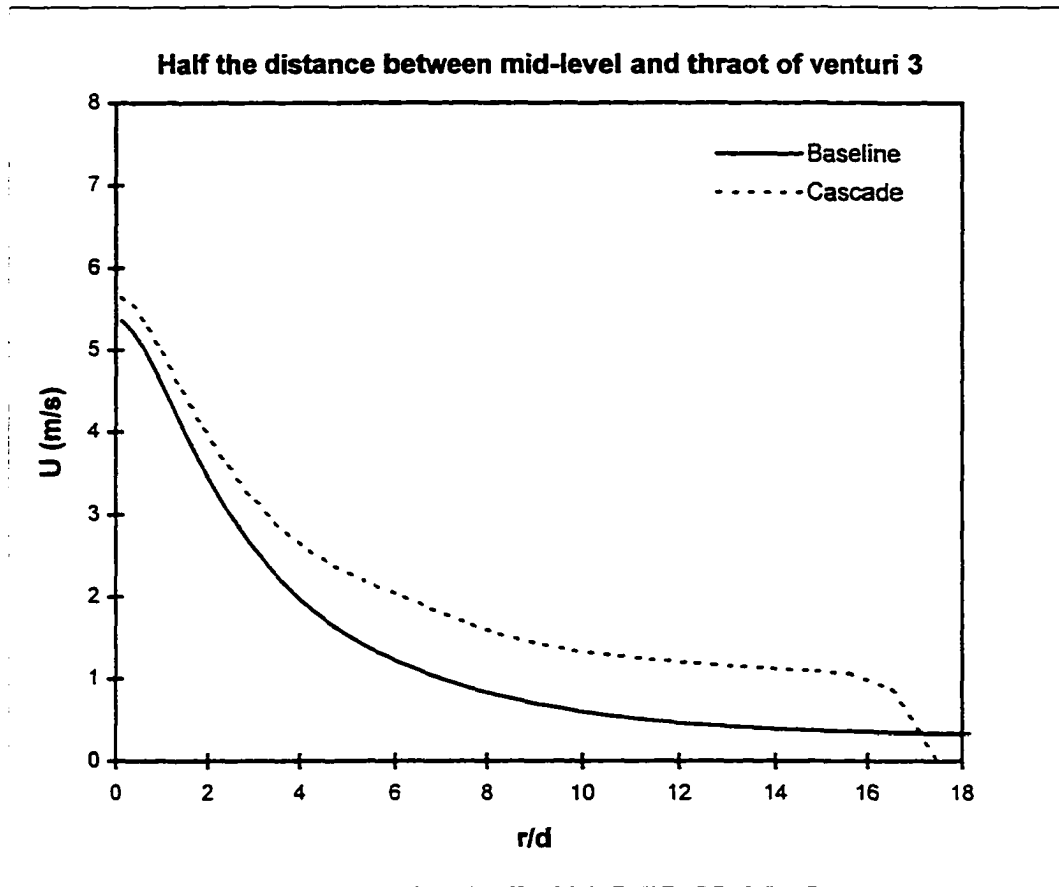


**Fig. 5.18f: Radial profiles of axial velocity ( $U$ ) for the baseline and cascaded flames at  $26.25d$  above base of venturi 3 (see Fig. 5.1d).**

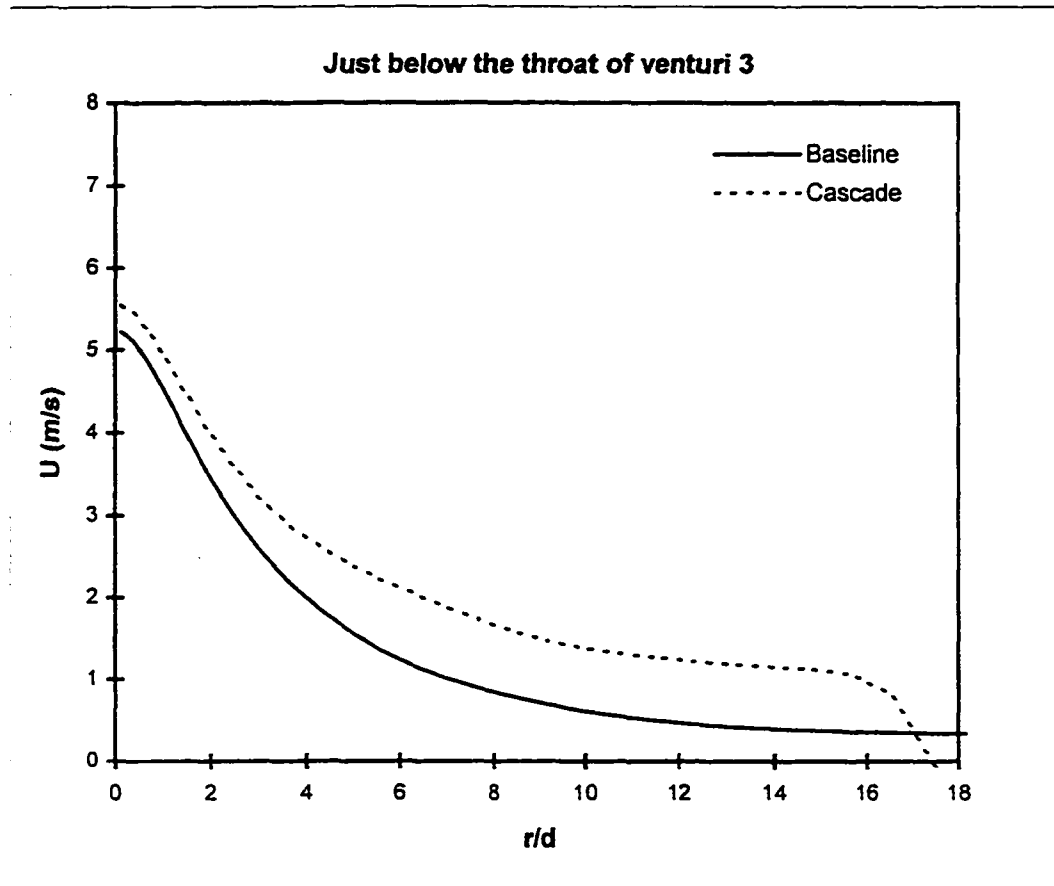


**Fig. 5.18g: Radial profiles of axial velocity (U) for the baseline and cascaded flames at 30d above base of venturi 3 (see Fig. 5.1d).**

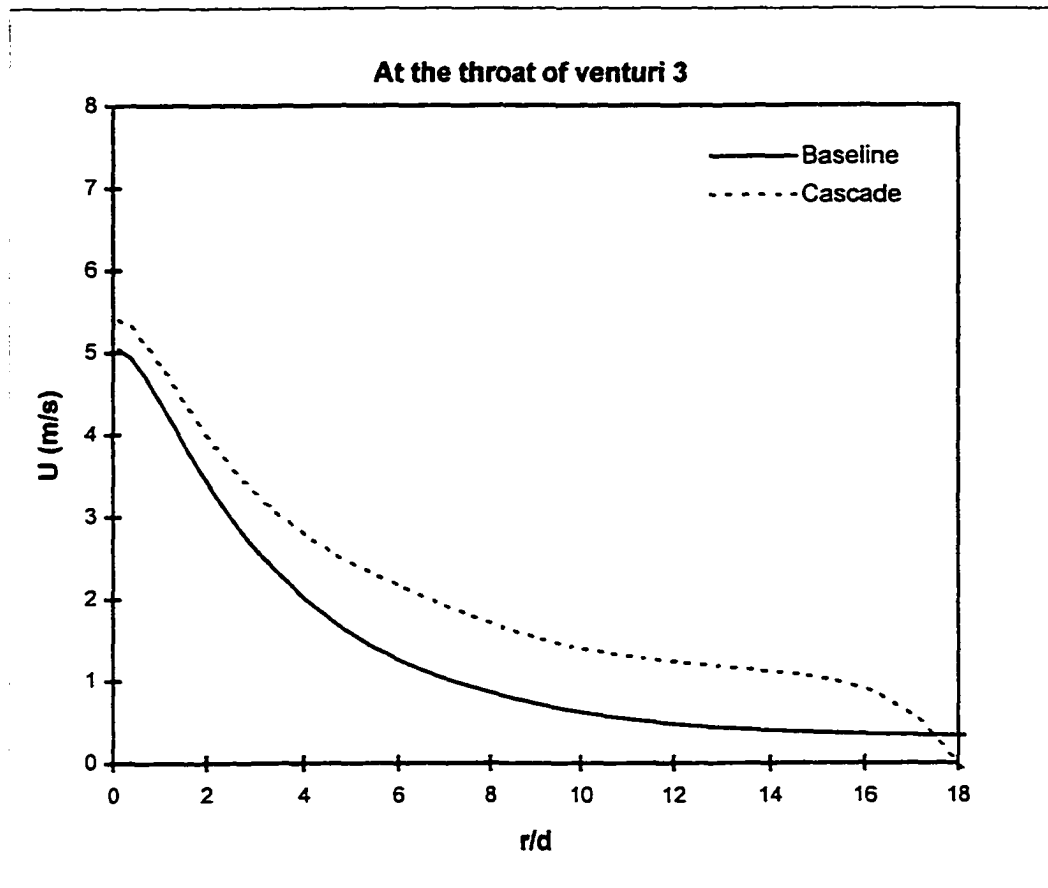


**Fig. 5.18h: Radial profiles of axial velocity ( $U$ ) for the baseline and cascaded flames at  $35d$  above base of venturi 3 (see Fig. 5.1d).**

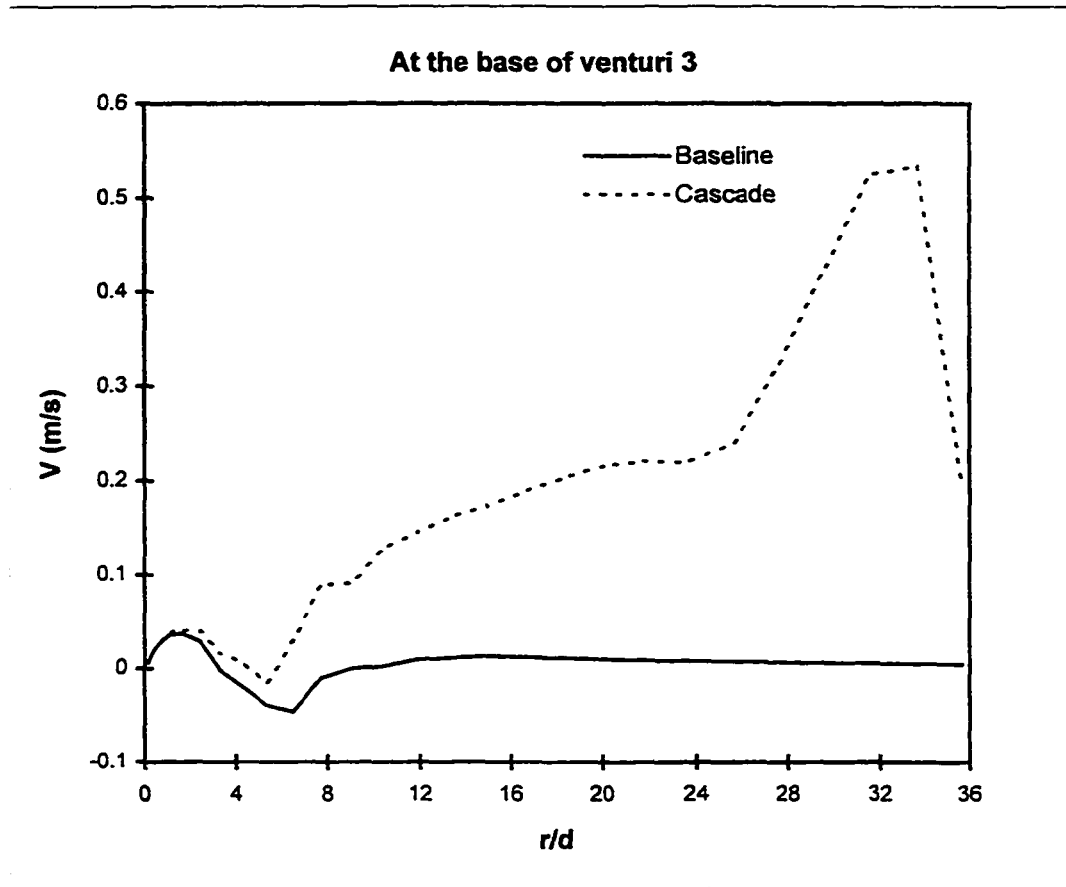


**Fig. 5.19a: Radial profiles of radial velocity ( $V$ ) for the baseline and cascaded flames at  $x/d=142.5$  (see Fig. 5.1d).**

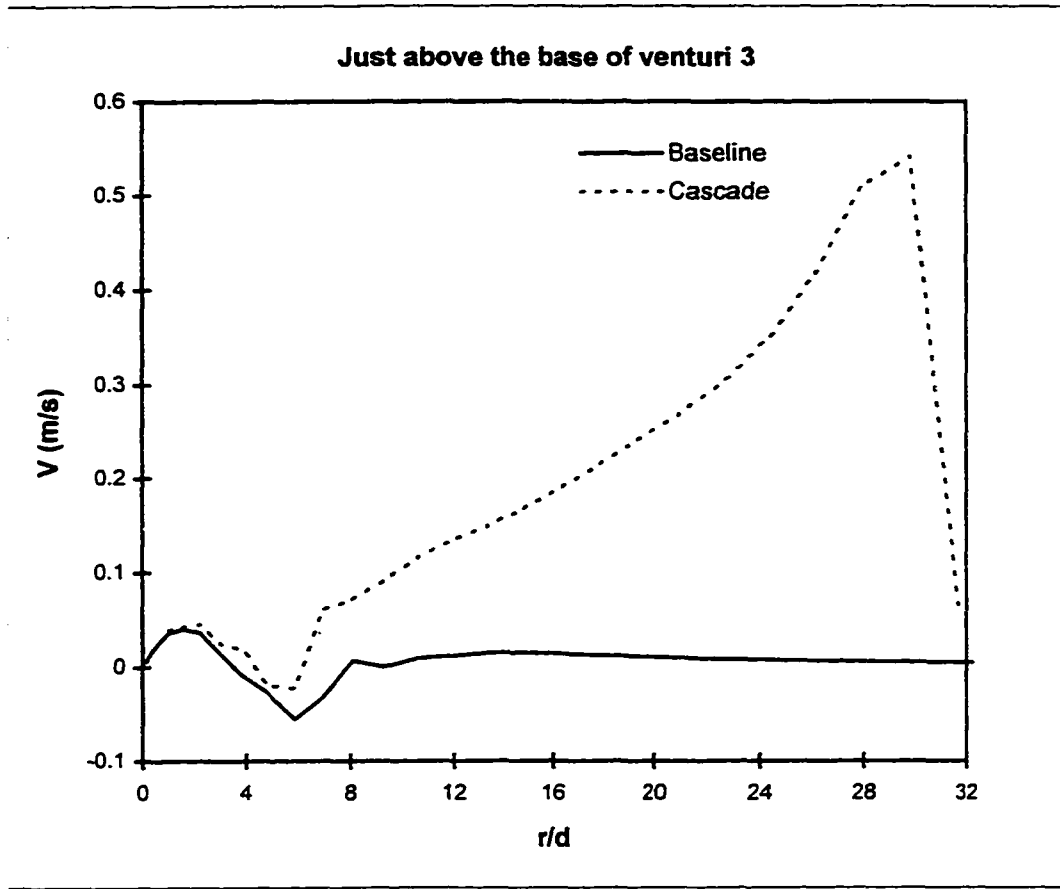


**Fig. 5.19b: Radial profiles of radial velocity ( $V$ ) for the baseline and cascaded flames at  $2.5d$  above base of venturi 3 (see Fig. 5.1d).**

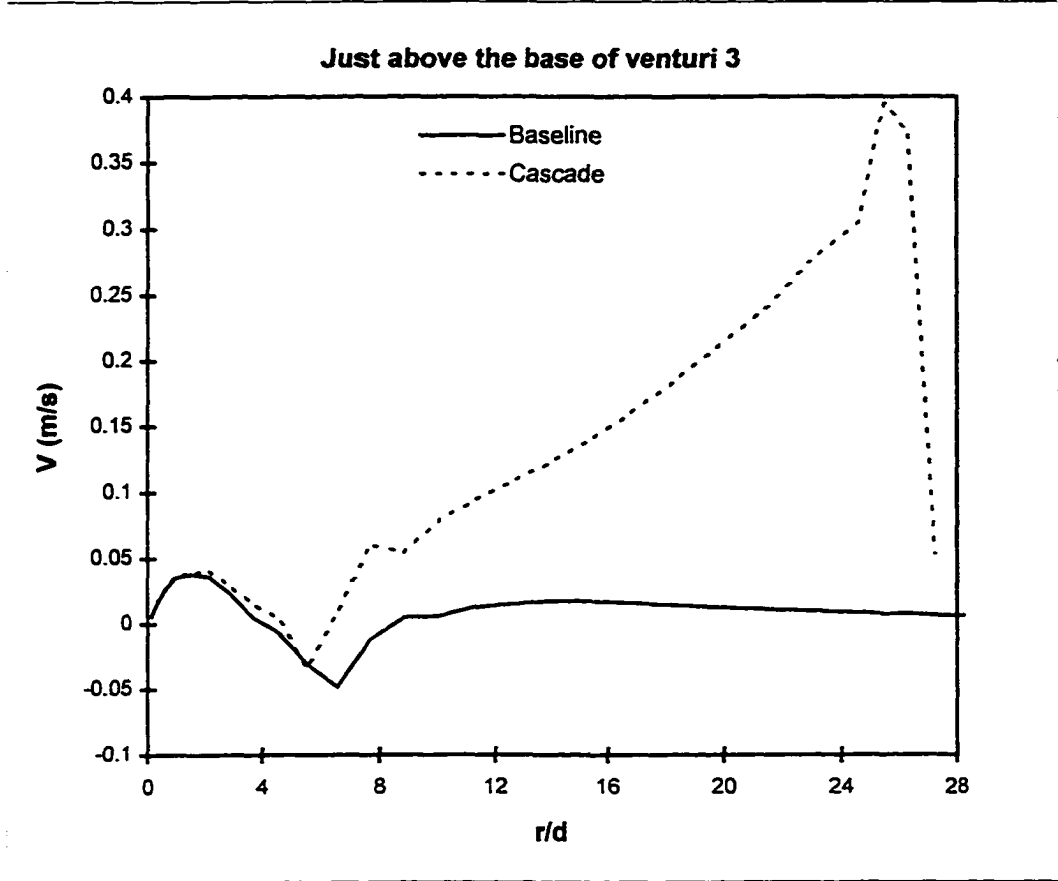


**Fig. 5.19c: Radial profiles of radial velocity ( $V$ ) for the baseline and cascaded flames at 5d above base of venturi 3 (see Fig. 5.1d).**

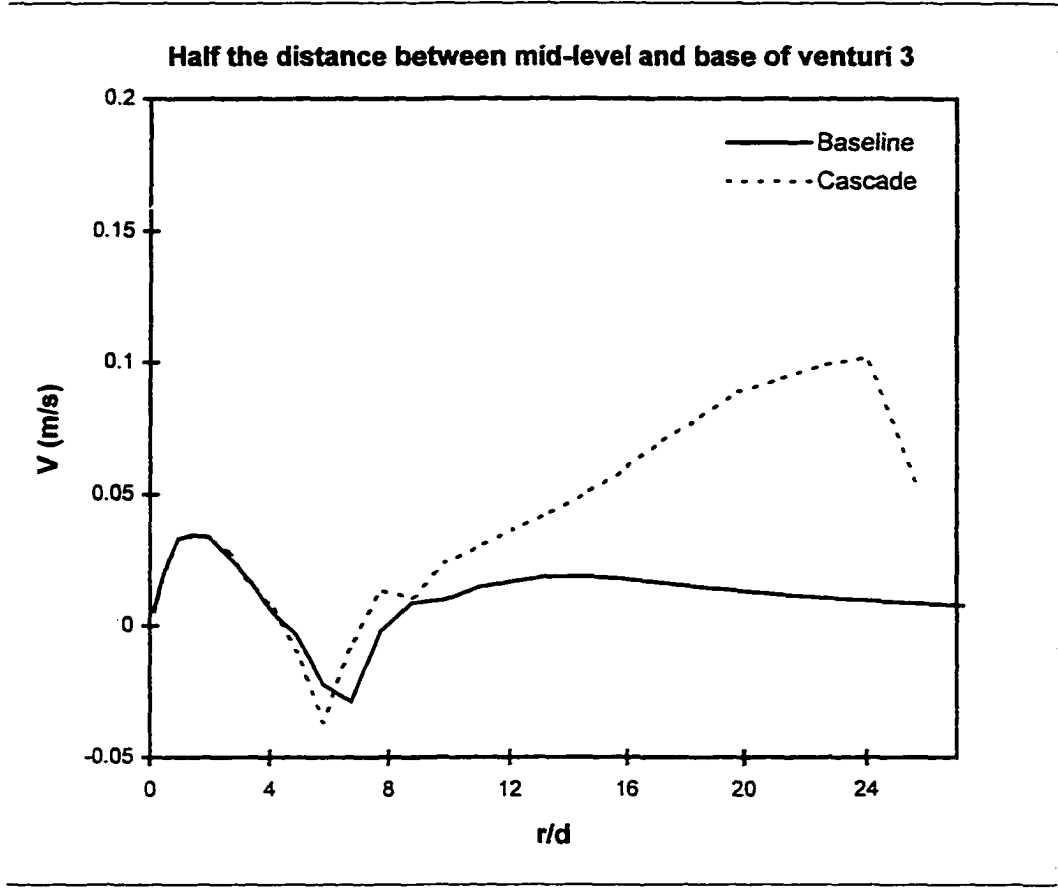


**Fig. 5.19d: Radial profiles of radial velocity ( $V$ ) for the baseline and cascaded flames at  $8.75d$  above base of venturi 3 (see Fig. 5.1d).**

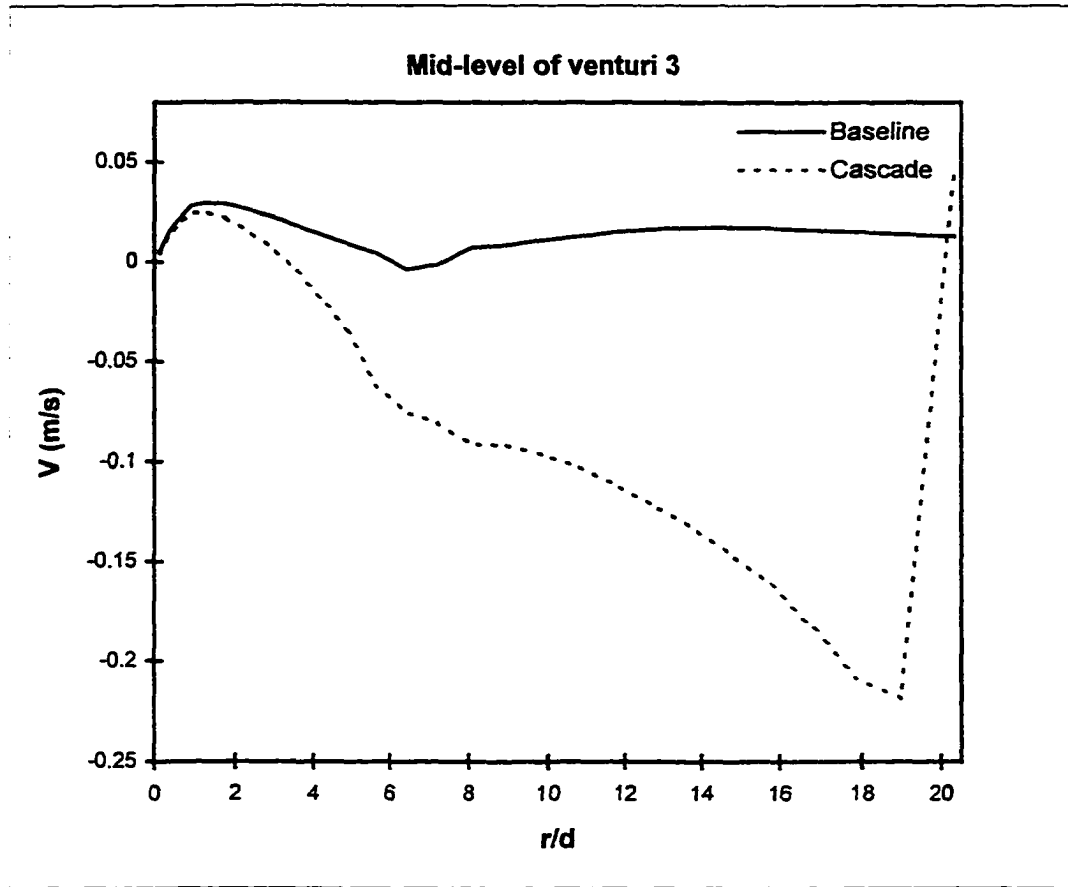


**Fig. 5.19e: Radial profiles of radial velocity (V) for the baseline and cascaded flames at 17.5d above base of venturi 3 (see Fig. 5.1d).**

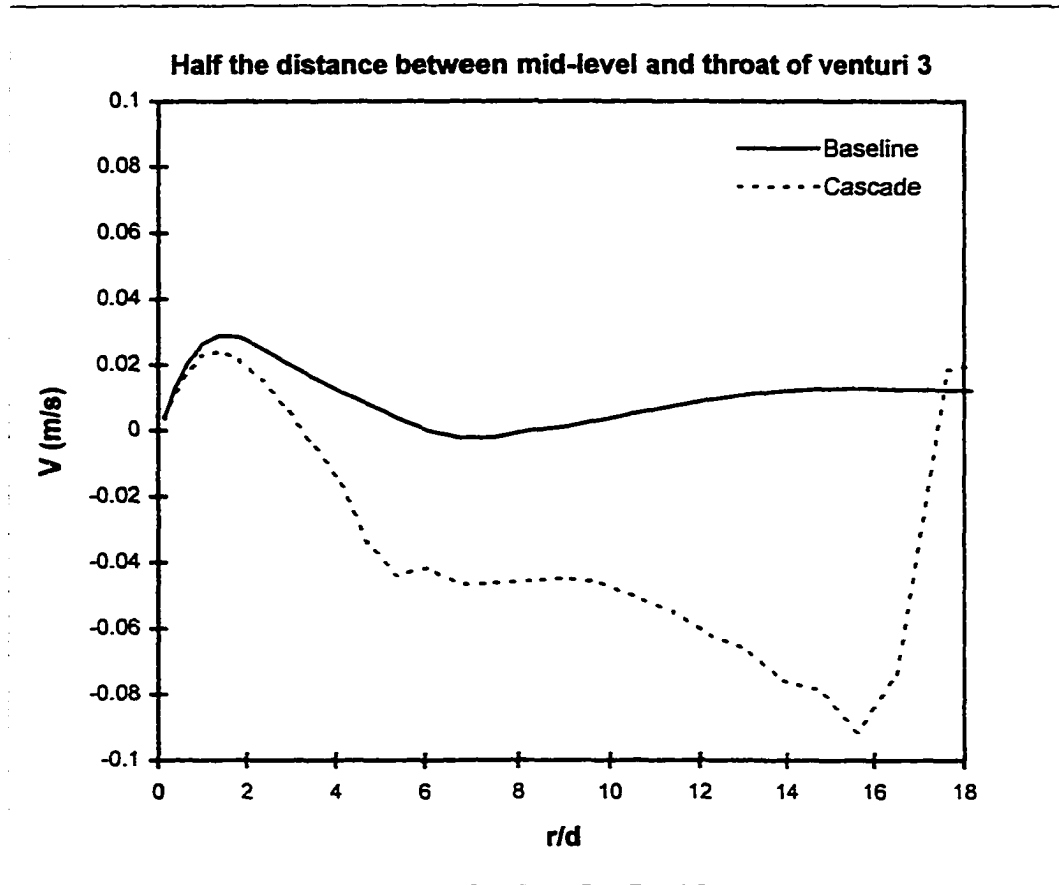


**Fig. 5.19f: Radial profiles of radial velocity (V) for the baseline and cascaded flames at 26.25d above base of venturi 3 (see Fig. 5.1d).**

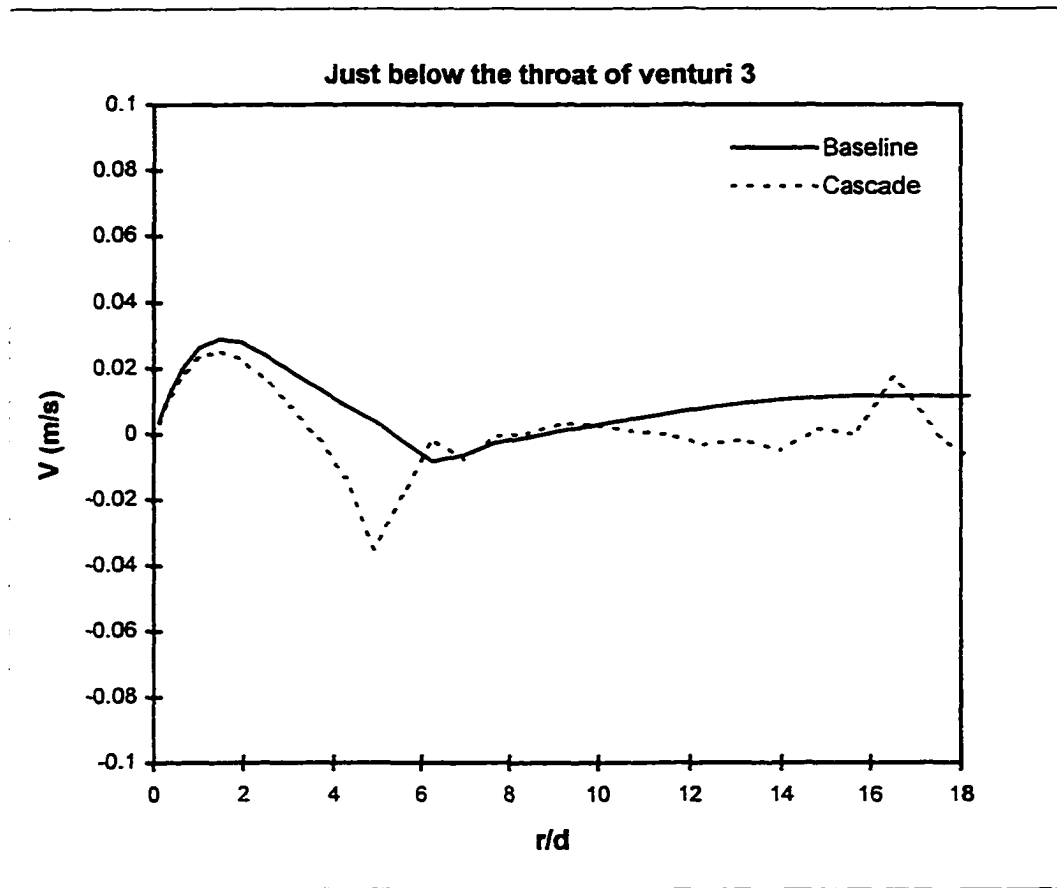


**Fig. 5.19g: Radial profiles of radial velocity ( $V$ ) for the baseline and cascaded flames at  $30d$  above base of venturi 3 (see Fig. 5.1d).**

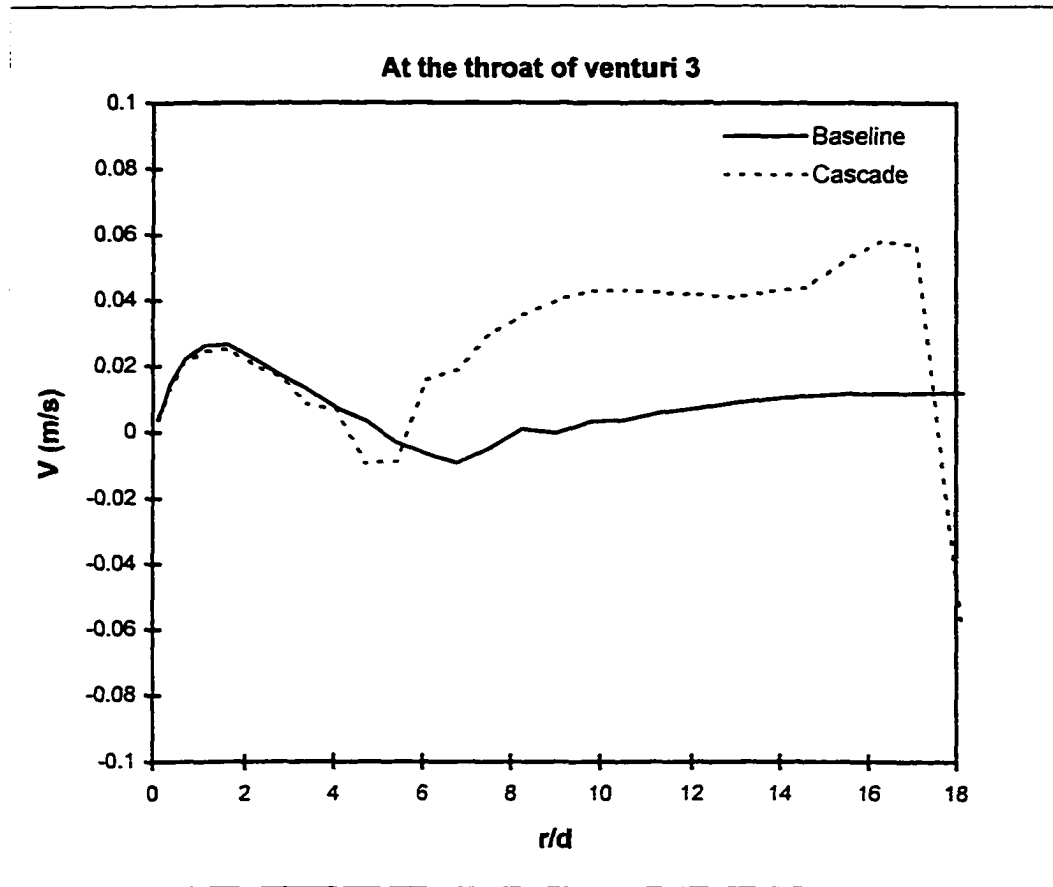
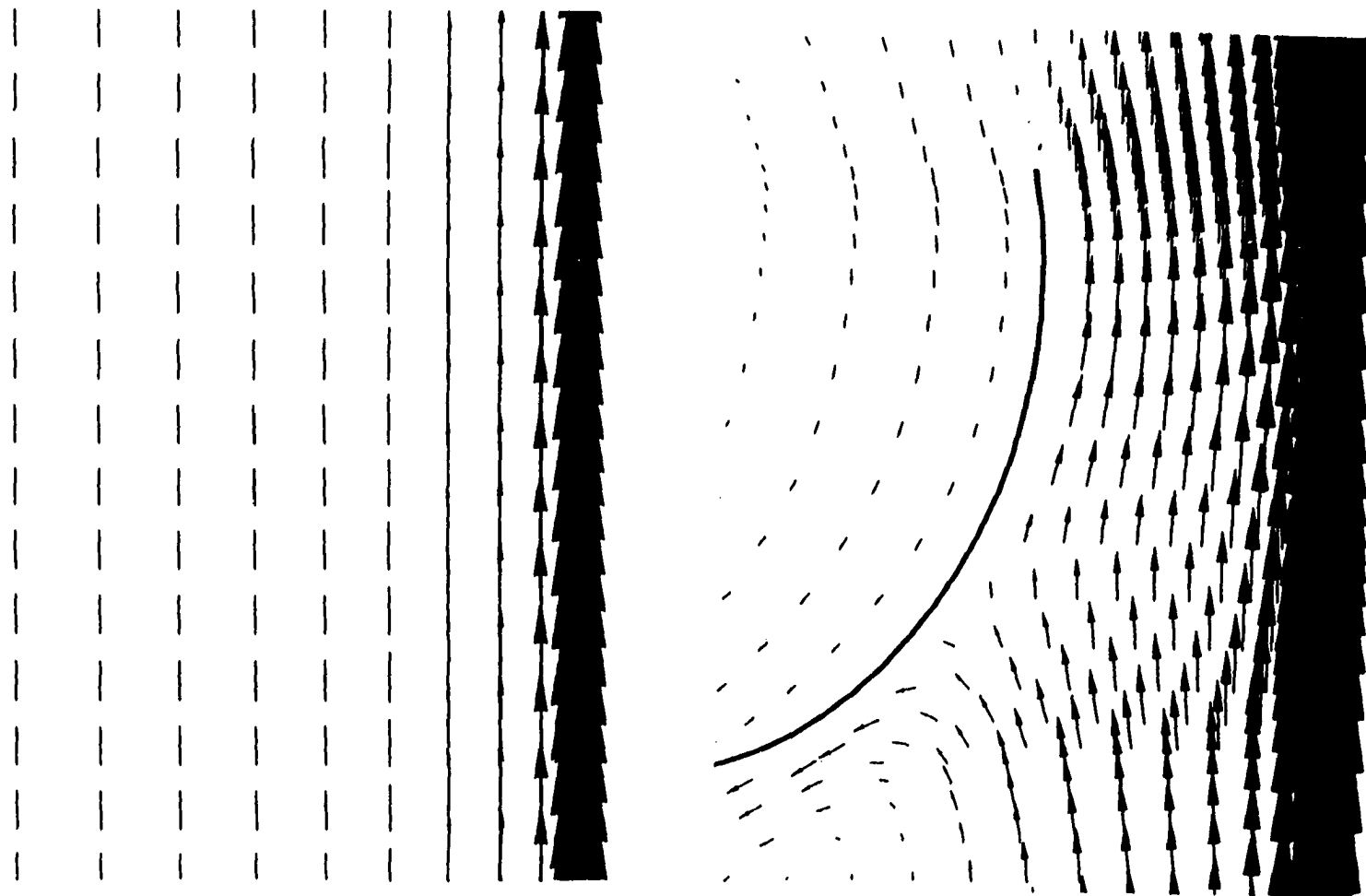


**Fig. 5.19h: Radial profiles of radial velocity ( $V$ ) for the baseline and cascaded flames at  $35d$  above base of venturi 3 (see Fig. 5.1d).**



**(a) Baseline**

**(b) Cascaded**

**Fig. 5.20 (a, b): Total velocity vector field for venturi 3 in the baseline and cascaded flames.**

# CHAPTER VI

## CONCLUSIONS AND RECOMMENDATIONS

This chapter summarizes the overall conclusions that have been drawn in this study. In addition, it provides some recommendations for future research work regarding venturi-cascading.

### 6.1 Conclusions

The present experimental and numerical study of enveloping a propane jet diffusion flame with a cascade of venturis has shown the following:

- ◆ Venturi-cascading is a feasible method for controlling the pollutant emissions of a burning gas jet, if used at proper conditions.
- ◆ The ratio of venturi diameter to burner diameter, burner-exit Reynolds number and venturi spacing distribution, all affect the flame characteristics. The strongest influence is of the venturi/burner diameter ratio, while the weakest effect is of the spacing distribution.
- ◆ The optimal value of venturi throat/burner-exit diameter ratio ( $D/d$ ) is  $32 \pm 3$ , which corresponds to an approximate clearance of  $5 \pm 2$  mm between the venturi throat and the burning jet width at the mid-flame height.
- ◆ The optimal arrangement was the equal spacing, in which the venturis were distributed at equal intervals over the whole length of the flame.

- ◆ The highest influence of venturi-cascading was observed for the flame in transition from the attached to the lifted condition ( $Re=5100$ ); in other words, the transitional flame was more susceptible than the attached/lifted flames to the air infusion.
- ◆ The venturi-cascaded flame at its optimal conditions, compared to the baseline case, results in the following:
  - Flame length increases.
  - Combustion efficiency, in terms of temperature and  $CO_2$ , increases.
  - CO and NO emission indices decrease.
  - Average volumetric soot concentration decreases.
  - Radiative heat loss factor decreases.
- ◆ The simultaneous reduction of NO and CO in addition to soot are the main favorable outcomes of venturi-cascading.
- ◆ The increase in flame length and decrease in radiation losses (blockage of radiation by venturis) are the main disadvantages of venturi-cascading for some applications.
- ◆ The different combustion mechanisms in the near-burner and downstream regions, indicated by the temperature and composition profiles, account for the effects of the venturi-cascade in those regions.
- ◆ The changes due to venturi-cascading, including NO and CO reductions, are the resultant of the following factors:
  - Lower formation rates of soot precursors (PAH)

- Higher oxidation rates of soot in the downstream regions
  - Better oxidation of pyrolysis fragments of fuel (CN and CH radicals)
  - Lower radiation losses
- ◆ The reduction of soot in the downstream regions caused by the venturi-cascade is primarily due to the effect of OH radicals than a consequence of temperature changes.
- ◆ The predictions of the numerical model show a good agreement with the experimental measurements in the near-burner region. However, the agreement is poor in the downstream regions.
- ◆ The region from 10d to 30d, above the base of the venturi, accounts for the enhanced rates of mixing by venturis.
- ◆ Both LIF and numerical results reveal that prompt-NO mechanism plays a significant role besides thermal-NO mechanism in the current flame configuration.

## 6.2 Recommendations

The following recommendations are proposed for further research:

- ◆ Studying the effect of venturi-cascading on premixed flames.
- ◆ Introducing swirl into the combustion chamber along with venturi-cascading. This might lead to an enhanced performance of the burner.
- ◆ Using a cascade of high temperature-resistance glass (Pyrex) venturis. This might help in overcoming radiation shielding by venturis, and possibly extending the suitability of venturi-cascading to a wider range of applications.

## REFERENCES

- Allen M. G. and Hanson R. K. (1986). Digital Imaging of Species Concentrations Fields in Spray Flames. *Twenty-First Symposium (International) on Combustion*, Combustion Institute, Pittsburgh, pp. 1755-1762.
- Axelbaum, R. L. and Law, C. K. (1990). Soot Formation and Inert Additives in Diffusion Flames. *Twenty-Third Symposium (International) on Combustion*, Combustion Institute, Pittsburgh, PA, pp. 1517-1523.
- Bernal, L. and Sarohia, V. (1983). Entrainment and Mixing in Thrust Augmenting Ejectors. *AIAA Paper 83-0172*.
- Bonczyk, P. A. and Shirley, J. A. (1979). Measurement of CH and CN Concentration in Flames by Laser Induced Saturated Fluorescence. *Combustion and Flame*, Vol. 34, pp. 253-264.
- Bowman, Craig T. (1992). Control of Combustion-Generated Nitrogen Oxide Emissions: Technology Driven By Regulations. *Twenty-Fourth Symposium (International) on Combustion*, Combustion Institute, Pittsburgh, pp. 859-878.
- Calcote, H. F. (1981). Mechanisms of Soot Nucleation in Flames - a Critical Review. *Combustion and Flame*, Vol. 42, pp. 215-228.
- Caretto L. S. (1973). Modeling Pollutant Formation in Combustion. *Fourteenth Symposium (International) on Combustion*, Combustion Institute, Pittsburgh, PA, pp. 803-817.
- CFD Research Corporation (1998). CFD-ACE<sup>+</sup> Theory Manual, Version 5.

- Chen, R. H., and Driscoll, J. F. (1988). The Rule of the Recirculation Vortex in Improving Fuel-Air Mixing within Swirling Flames. *Twenty-Second Symposium (International) on Combustion*, Combustion Institute, Pittsburgh, pp. 531-440.
- Chen, Y. C. and Mansour, M. S. (1997). Simultaneous Raleigh Scattering and Laser-Induced CH Fluorescence for Reaction Zone Imaging in High Speed Premixed Hydrocarbon Flames. *Applied Physics*, Vol. 64, pp. 599-605.
- Daily, J. W. (1997). Laser-Induced Fluorescence Spectroscopy in Flames. *Progress in Energy and Combustion Science*, Vol. 23, pp. 133-199.
- De Soete, G. G. (1975). Overall Reaction Rates of NO and N<sub>2</sub> Formation from Fuel Nitrogen. *Fifteenth Symposium in Combustion*, Combustion Institute, Pittsburgh, pp. 1094-1102.
- Dryer, F. L. and Glassman, I. (1973). High Temperature Oxidation of CO and CH<sub>4</sub>. *Fourteenth Symposium (International) on Combustion*, Combustion Institute, Pittsburgh, PA, pp. 987-1003.
- Eckbreth, A. C. (1996). Laser Diagnostics for Combustion Temperature and Species. 2<sup>nd</sup> Edition, *Abacus Press*, UK.
- Fenimore, C. P. and Jones G. W. (1963). The Dcomposition of Ethylene and Ethane in Premixed Hydrocarbon-Oxygen-Hydrogen Flames. *Ninth Symposium (International) on Combustion*, Combustion Institute, Pittsburgh, PA, pp. 597-606.
- Fenimore, C. P. (1970). Formation of Nitric Oxide in Premixed Hydrocarbon Flames. *Thirteenth Symposium (International) on Combustion*, Combustion Institute, Pittsburgh, PA, pp. 373-380.

- Glassman, I. (1987). Combustion, Second Edition, *Academic Press*, Orlando.
- Glassman, I. (1988). Soot Formation in Combustion Processes. *Twenty-Second Symposium (International) on Combustion*, Combustion Institute, Pittsburgh, pp. 295-311.
- Gollahalli, S. R. (1994). Research on Combustion Processes Relevant to Burners in HVAC Systems. *Final Report, GRI-94/0420*, Gas Research Institute, Illinois, Chicago.
- Gollahalli, S. R. and Wright, E. A. (1996). Emission Control from Cascade Burners. *International Joint Power Generation Conference and Exposition*, Houston, Texas. ASME FACT Vol.21, pp. 325-331.
- Gollahalli, S. R., Khanna, T., and Prabhu, N. (1992). Diffusion Flames of Gas Jets Issued From Circular and Elliptic Nozzles. *Combustion Science and Technology*, Vol. 86, pp. 267-288.
- Gollahalli, S. R., Rasmussen, M. L., and Moussavi, S. J. (1980). Combustion of Drops and Sprays of No. 2 Diesel Oil and Its Emulsions with Water. *Eighteenth Symposium (International) on Combustion*, Combustion Institute, Pittsburgh, PA, pp. 349-360.
- Gupta, A. K. and Lilley, D. G. (1985). Flow field Modeling and Diagnostics. Abacus Press, Kent, UK.
- Gutmark, E., Shadow, K. C. and Wilson, K. J. (1991). Subsonic and Supersonic Combustion Using Noncircular Injectors. *Journal of Propulsion*, Vol. 7, No. 2, pp. 240-249.

- Hicks, Y. R., Locke, R. J., Anderson, R. C. and Ockunzzi, K. A. (1995). Planar Imaging of Hydroxyl in a High Temperature, High Pressure Combustion Facility. *NASA Technical Memorandum 107074*, Lewis Energy Center, Ohio.
- Ho, C. M. and Gutmark, E. (1987). Vortex Induction and Mass Entrainment in a Small Aspect Ratio Elliptic Jet. *Journal of Fluid Mechanics*, Vol. 179, pp. 383-405.
- Huadiquert, A., Cessou, A., Stepowski, D. and Coppalle, A. (1997). OH and Soot Concentration Measurements in a High-Temperature Laminar Diffusion Flame. *Combustion and Flame*, Vol. 11, pp. 338-349
- Kamal, A. (1995). Turbulent Diffusion Gas Jet Flames From Circular and Elliptic Nozzles. *Ph.D. Thesis*. School of Aerospace and Mechanical Engineering, The University of Oklahoma, Norman, OK.
- Kamal, A. and Gollahalli, S. R. (1993). Effects of Noncircular Fuel Nozzle on the Pollutant Emission Characteristics of Natural Gas Burner for Residential Furnaces. *Combustion, Modeling, Cofiring and NOx Control, ASME. FACT*. Vol.17, pp. 41-50.
- Kanury, M. A. (1992). Introduction to Combustion Phenomena. *Gordon and Breach Science Publishers*. USA.
- Laufer, G. (1996). Introduction to Optics and Lasers in Engineering. *Cambridge University Press*, NY.
- Lund, T. S. (1991). Viscous-Inviscid analysis of Dual Jet Ejectors. *Journal of Propulsion*, Vol. 7, No. 1, pp. 99-107.

- Lund, T. S., Tavella, D. A., and Roberts, L. (1986). Thrust Augmentor Inlet Optimization. *Journal of Propulsion*, Vol. 2, No. 3, pp. 253-258.
- Luque, J. and Crosley, D. R. (1996). Absolute CH Concentrations in Low Pressure Flames Measured with Laser-Induced Fluorescence. *Applied Physics*, Vol. 63, pp. 91-98.
- Miller, J. A. and Bowman, C. T. (1989). Mechanisms and Modeling of Nitrogen Chemistry in Combustion. *Progress in Energy and Combustion*, Vol. 15, pp. 287-338.
- Miller, P. and Seel, M. W. (1991). The Application of High Pressure Ejectors to Reaction Control Systems. *Aeronautical Journal*, November Issue, pp. 297-312.
- Mokhov, A. V., Levinsky, H. B., Van der Meij, C. E., and Jacobs, R. A. (1995). Analysis of Laser-Induced Fluorescence Carbon Monoxide in Turbulent Nonpremixed Flames. *Applied Optics*. Vol. 34, No. 30, pp. 7074-7082.
- Nana, F. N. (1998). Pressure Drop through Venturis. A report submitted for AME Undergraduate Research Studies.
- Neoh, K. J., Howard, J. B. and Sarofim, A. F. (1984). Effect of Oxidation on The Physical Structure of Soot. *Twentieth Symposium (International) on Combustion*, Combustion Institute, Pittsburgh, pp. 951-957.
- Norton, T. S. and Smyth, K. C. (1991). Laser Induced Fluorescence of CH in a Laminar CH<sub>4</sub>/Air Diffusion Flames: Implication for Diagnostic Measurements and Analysis of Chemical Rates.. *Combustion Science and Technology*, Vol. 76, pp.1-20.

- Norton, T. S., Smyth, K. C., Miller, J. H. and Smooke, M. D. (1993). Comparison of Experimental and Computed Species Concentration and Temperature Profiles in Laminar Two Dimensional Methane/Air Diffusion Flames. *Combustion Science and Technology*, Vol. 90, pp.1-34.
- Papanikolaou, N. and Wierzba, I. (1996). Effect of Burner Geometry on the Blowout Limits of Jet Diffusion Flames in a Co-Flowing Air Stream. *Journal of Energy Resources Technology*, Vol. 118, pp. 134-139.
- Papanikolaou, N., Wierzba, I., and Fergusson, B. (1997). The Structure of Jet Diffusion Flames Issuing into Co-Flowing Air Stream. *Energy Week*, Pennwell publications, Houston, TX, Book V, pp. 222-228.
- Porter, J. L. and Squyers, R. A. (1981). A Summary/Overview of Ejector Augmentor Theory and Performance. *ATC Report R-91100/9CR-47A*, Vought Corp., Dayton, OH.
- Pourkashanian, M. P., Missaghi, M. and Yap, T. L. (1993). Reduction of NO<sub>x</sub> Emissions Using CFD as a Design Tool. *FACT-Vol.17, ASME*.
- Presz, W. M., Morin, B. L. and Gousy, R. G. (1988). Forced Mixer Lobes in Ejector Designs. *Journal of Propulsion Power*, Vol. 4. No. 4, pp. 350-355.
- Puri, R., Moser, M., Santro, R. J. and Smyth, K. C. (1992). Laser-Induced Fluorescence Measurements of OH Concentrations in the Oxidation Region of Laminar, Hydrocarbon Diffusion Flames. *Twenty-Fourth Symposium (International) on Combustion*, Combustion Institute, Pittsburgh, pp. 1015-1022 .

- Puri, R., Santro, R. J. and Smyth, K. C. (1994). The Oxidation of Soot and Carbon Monoxide in Hydrocarbon Diffusion Flames. *Combustion and Flame*, Vol. 97, pp. 125-144.
- Qubbaj, Ala R. (1998). Optimization and Structure of Gas Jet Diffusion Flames in Cascade Burners. *International Technical Conference on Coal Utilization and Fuel System*, March 9-13, Clearwater, Florida.
- Qubbaj, Ala R. and Gollahalli, S. R. (1997). Emission Control of Diffusion Flames. *ASME/AIAA Symposium XVII*, February 22, Tulsa, Oklahoma.
- Qubbaj, Ala R. and Gollahalli, S. R. (1998). Optimization of Venturi-Cascade Enveloped Burners. *Energy Sources Technology Conference and Exhibition*, February 2-4, Houston, Texas, USA.
- Shadow, K. C., Gutmark, E., Koshigoe, S., and Wilson, K. J. (1989). Combustion Related Shear-Flow Dynamics in Elliptic Supersonic Jets. *AIAA Journal*, Vol. 27, No. 10, pp. 1347-1353.
- Smith, O. I. and Chandler, D. W. (1986). An Experimental Study of Probe Distortions to the Structure of One-Dimensional Flames. *Combustion and Flame*, Vol. 63, pp. 19-29.
- Smyth, K. C. and Tjossem, P. J. (1990). Concentration Measurements of OH and Equilibrium Analysis in a Laminar Methane-Air Diffusion Flame. *Combustion and Flame*, Vol. 79, pp. 366-380.
- Smyth, K. C., Norton, T. S., Miller, J. M. and Smooke, M. D. (1994). Radical Concentrations in Diffusion Flames. Soot Formation in Combustion. Ed. H. Bockhorn, Springer-Verlag, New York, pp. 113-133.

- Steffensive, R. J., Angnew, J. T. and Olsen, R. A. (1966). Tables for Adiabatic Gas Temperature and Equilibrium Composition of Six Hydrocarbons. Engineering Bulletin of Purdue University, Engineering Extension Series, No. 122.
- Tangirala, V., Chen, R. H., and Driscoll, J. F. (1987). Effect of Heat Release and Swirl on the Recirculation within Swirl-Stabilization Flames. *Combustion Science and Technology*, Vol. 51, pp. 75-95.
- Tavella, D. A. and Roberts, L. (1987). Simple Viscous-Inviscid Aerodynamic Analysis of Two-Dimensional Augmentors. *Journal of Propulsion*, Vol. 3, No. 5, pp. 467-471.
- Turns, S. R. (1996). An Introduction to Combustion: Concepts and Applications. McGraw-Hill Inc., NY.
- Turns, S. R., Myhr, F. H., Bandaru, R. V., and Mound, E. R. (1993). Oxides of Nitrogen Emissions from Turbulent Jet Flames: Part II- Fuel Dilution and Partial Premixing Effects. *Combustion and Flame*, Vol. 93, pp. 255-269.
- Van doormaal, J. P. and Dryer, F. L. (1984). Enhancements of the SIMPLE Methods for Predicting Incompressible Fluid Flows. *Numerical Heat Transfer*, Vol. 7, pp. 147-163.
- Villasenor, R. and Kennedy, I. M. (1992). Soot Formation and Oxidation in Laminar Diffusion Flames. *Twenty-Fourth Symposium (International) on Combustion*, The Combustion Institute, Pittsburgh, pp. 1023-1030.
- Warnatz, J. (1984). Rate Coefficients in the C/H/O System. *Combustion Chemistry*, W. C. Gardiner, Jr., Editor, Springer-Verlag, New York, pp. 197-360.

- Weastblom, U., Alonso, F. F., Mahon, C. R., Smith, G. P., Jeffries, J. B., and Crosley, D. R. (1994). Laser-Induced Fluorescence Diagnostics of a Propane/Air Flame with a Manganese Fuel Additive. *Combustion and Flame*, Vol. 99, pp. 261-268.
- Yagi, S. and Iino, H. (1960). Radiation from Soot Particles in Luminous Flames. *Eighth Symposium (International) on Combustion*, Combustion Institute, Pittsburgh, PA, pp. 288-293.

## **APPENDICES**

# APPENDIX 1

## Energy Balance Equation for Thermocouple

The heat transfer losses from the thermocouple bead may significantly affect the measured flame temperature and lead to lower values. Heat transfer could occur by one of the following:

1. conduction through the wires
2. convection between the flame and the bead
3. radiation between the bead and the surroundings

The energy balance equation for thermocouple bead is as follows: (Kamal, 1995)

$$hA_b(T_g - T_b) = \frac{K_w A_w (T_b - T_r)}{L} + \sigma \epsilon A_b (T_b^4 - T_g^4)$$

where

$$A_b = \text{Surface area of the bead} = \pi(\text{bead radius})^2 = \pi(3 \times 10^{-4})^2 = 28.3 \times 10^{-8} \text{ m}^2$$

$$A_w = \text{Cross sectional thermocouple wires} = \pi(\text{wire diameter})^2 / 4 = 1.3 \times 10^{-8} \text{ m}^2$$

$h$  = Convective heat transfer coefficient between the thermocouple bead and surrounding gases:

$$h = \frac{Nu \times K}{\text{Bead diameter}} = 0.8 \times Re^{0.25} \times K_o \times \left(\frac{T_b}{T_o}\right)^{0.94} \text{ W / m}^2 - K$$

where

$$K_o = \text{Thermal conductivity of air at } T_o = 0.0241 \text{ W/m-K}$$

$$T_o = \text{Reference temperature} = 273 \text{ K}$$

$Re$  = Reynolds number based on bead diameter

$K_w$  = Thermal conductivity of the thermocouple wire = 73 W/m-K ( Type R :  
Platinum-13% Platinum-Rhodium)

$L$  = Length of the thermocouple wire = 1.021 m

$T_b$  = Thermocouple bead temperature (measured temperature)

$T_g$  = Surrounding gas temperature (actual flame temperature)

$T_r$  = Cold junction temperature = 298 K

$\sigma$  = Stefan Boltzmann Constant =  $5.67 \times 10^{-8}$  W/m<sup>2</sup>K<sup>4</sup>

$\varepsilon$  = Emissivity

For a  $T_b=1276$  K,  $T_g$  was calculated as 1373 K.

## APPENDIX 2

### Derivation of Equations

#### Volumetric Soot Concentration ( $w$ )

The volumetric soot concentration of soot is calculated using the method described by Yagi and Lino (1960). The spectral emissivity of a soot particle can be expressed as

$$\varepsilon_{\lambda} = 1 - e^{\left(\frac{-4.14wt}{\lambda}\right)} \dots\dots\dots (A2.1a)$$

where

$t$  = flame thickness

$w$  = volumetric soot fraction (ml/ml)

$\lambda$  = wavelength of the laser source

According to Kirchoff's law, emissivity can be assumed equal to absorptivity (i.e.,  $\alpha = \varepsilon$ ). Therefore,

$$\alpha = 1 - e^{\left(\frac{-4.14wt}{\lambda}\right)} \dots\dots\dots (A2.1b)$$

Recalling that:

$$\alpha = \frac{I_i - I_e}{I_i}$$

where

$I_i$  = Intensity of the incident laser beam

$I_e$  = Intensity of the emitted laser beam

And assuming that the soot material density is 2g/cc (Kamal, 1995), the soot concentration can be expressed as:

$$w_{\text{soot}}(\text{g / cc}) = -2 \ln\left(\frac{I_e}{I_i}\right) \times \frac{\lambda}{4.14t} \dots\dots\dots (A2.2)$$

### Air Entrainment

These were cold jet experiments in which nitrogen was used instead of propane.

The jet exit Reynolds number was corrected to account for the changes in density and viscosity. If  $X_{O_2}$  is the mole fraction of  $O_2$  in the jet,  $n_{O_2}$ ,  $n_{N_2}$ ,  $n_A$  and  $n_{\text{fuel}}$  is the number of moles of  $O_2$ ,  $N_2$ , air and fuel respectively, then:

$$X_{O_2} = n_{O_2} / (4.76 n_{O_2} + n_{N_2})$$

Substituting  $n_{\text{fuel}}$  instead of  $n_{N_2}$  and solving for  $n_{O_2}$ , get:

$$n_{O_2} = X_{O_2} * n_{\text{fuel}} / (1 - 4.76 X_{O_2})$$

Then,

$$n_A = 4.76 n_{O_2} = 4.76 * X_{O_2} * n_{\text{fuel}} / (1 - 4.76 X_{O_2})$$

$$\rightarrow \boxed{n_A / n_{\text{fuel}} = 4.76 * X_{O_2} * n_{\text{fuel}} / (1 - 4.76 X_{O_2})} \dots\dots\dots (A2.3)$$

## Radiant Fraction of Heat Release (F)

The radiant fraction or radiative heat release factor is defined as the ratio of radiative heat transfer from the flame to the total heat input rate based on the fuel flow rate and the heating value of the fuel:

$$\boxed{\text{Radiant Fraction} = F = \frac{Q_{\text{radiated}}}{Q_{\text{total}}}} \dots\dots\dots (A2.4)$$

where

$$Q_{\text{radiated}} = \text{Radiant heat transfer rate from the flame to the surrounding} \\ = 4\pi d^2 \times S \times R^*$$

$$Q_{\text{total}} = \text{Total heat input rate} = m_f \times \text{LHV}$$

where

$$m_f = \text{Mass flow rate of the fuel} = \rho_{\text{fuel}} \times Q_{\text{fuel}}$$

LHV = Lower heating value of the fuel

$d$  = Distance between the radiometer and the flame

$S$  = Radiometer sensitivity ( W/m<sup>2</sup>-mV)

$R^*$  = Corrected reading of the radiometer (mV) =  $R - R_B$

$R$  = Direct reading of the radiometer (mV)

$R_B$  = Background radiation when the flame is extinguished (mV)

## APPENDIX 3

### Sample Calculations

#### Emission Indices

From experiment at  $Re = 5100$  for the baseline propane flame, the readings from exhaust gas analyzers are:

$CO_2$  : 3.65 %

$CO$  : 80 PPM

$NO$ : 14.98 PPM

The properties of the species of interest are:

$n = 3$  ( $n$  is number of carbon atoms in  $C_3H_8$ )

$M_f = 44$

$M_{CO} = 28$

$M_{NO} = 30$

Using Eq. 4.1

$$\Rightarrow EI_{CO} = 4.2 \text{ g/Kg of Fuel}$$

$$\Rightarrow EI_{NO} = 8.4 \text{ g/Kg of Fuel}$$

#### Volumetric Soot Concentration (w)

From experiment at  $Re=5100$  and  $x/d = 100$  for the baseline (no venturi) propane flame:

$$I_i = 3.88 \text{ mW}$$

$$I_e = 2.65 \text{ mW}$$

$$t = 0.019 \text{ m}$$

$$\lambda = 633 \text{ nm}$$

Using Eq. A2.2

$$\Rightarrow w = -2 \times \ln\left(\frac{2.65}{3.88}\right) \times \frac{633 \times 10^{-9}}{0.019} = 6.13 \times 10^{-7} \text{ g / cc}$$

### **Air-Entrainment**

The air-entrainment ratio was calculated using Eq. A2.3 for nitrogen cold jet experiments. The whole radial plane was traversed for oxygen concentration, and the oxygen profiles were obtained. From which, the weighted area average oxygen concentration ( $\bar{X}_{O_2}$ ) was determined and converted into air-entrainment ratio as follow:

For the baseline flame at  $Re = 5100$  and  $x/d = 100$ :

$$\bar{X}_{O_2} = 19.89 \%$$

Using Eq. A2.3:

$$\Rightarrow \frac{n_A}{n_f} = \frac{4.76 \times 0.1989}{(1 - 4.76 \times 0.1989)} = 17.8$$

### **Radiant Fraction of Heat Release (F)**

$$F = \frac{Q_{\text{radiated}}}{Q_{\text{total}}}$$

where

$$Q_{\text{radiated}} = 4\pi d^2 \times S \times R'$$

$$Q_{\text{total}} = m_F \times \text{LHV}$$

$$m_F = \rho_{\text{fuel}} \times Q_{\text{fuel}}$$

$$\text{LHV for Propane} = 46357 \text{ kJ/kg}$$

$$d = l$$

$$S \text{ for Radiometer} = 23.81 \text{ W/m}^2\text{-mV}$$

$$R^* = R - R_b$$

For the baseline flame at  $Re = 5100$

$$l = 0.46 \text{ m}$$

$$R = 6.20 \text{ mV}$$

$$R_b = 0.05 \text{ mV}$$

$$R^* = 6.15 \text{ mV}$$

$$Q_{\text{total}} = \frac{(1.87 \times 2097 \times 10^{-6} \times 46357 \times 10^3)}{60} = 3030 \text{ Watt}$$

$$Q_{\text{Radiated}} = 4\pi \times (0.46)^2 \times 23.81 \times 6.15 = 389.4 \text{ Watt}$$

$$\Rightarrow F = \frac{389.4}{3030} \times 100\% = 17.8\%$$

## APPENDIX 4

### Estimation of Uncertainties

The uncertainties related to measurements is due to two types of errors: *Precision (Random) error* and *Bias (Fixed) error*. Random error can be estimated statistically, whereas, biased error is dependent on the instrument and the measurement technique. The overall uncertainty can be calculated as:

$$\omega = \sqrt{(P_{\bar{x}}^2 + B^2)}$$

where

B = Biased error

$P_{\bar{x}}$  = Precision error of mean =  $t_{\alpha/2} \cdot S_{\bar{x}}$

$$S_{\bar{x}} = \frac{S_x}{\sqrt{n}} = \frac{\sqrt{\left(\sum (x_i - \bar{x})^2\right)}}{\sqrt{n(n-1)}}$$

$t_{\alpha/2} = 2.262$  (for  $\nu = 9$  or  $n=10$ )

where  $\nu$  = degree of freedom =  $n-1$

In this present study, all instruments were calibrated prior to the experiment and least count errors were neglected. Hence, the bias errors may be assumed approximately to be zero. Some experiments were repeated 10 to 12 times and the uncertainties were calculated using the *Student's t- test* at 95% confidence interval.

From experiment at  $Re = 5100$  for the baseline flame :

<b>Observations</b>	<b>CO2 (Mole %)</b>
1	3.65
2	3.85
3	3.95
4	3.35
5	3.05
6	3.75
7	4.15
8	3.85
9	3.45
10	3.15
<b>Mean</b>	<b>3.62</b>
<b>St. dev.</b>	<b>0.359</b>
<b><math>P_x</math></b>	<b>0.257</b>
<b><math>P_x</math> (% of mean)</b>	<b>7.1 %</b>

→ uncertainty in  $CO_2$  (w) =  $\pm 7.1$  % of mean

# APPENDIX 5

## Details of the Laser Diagnostic System

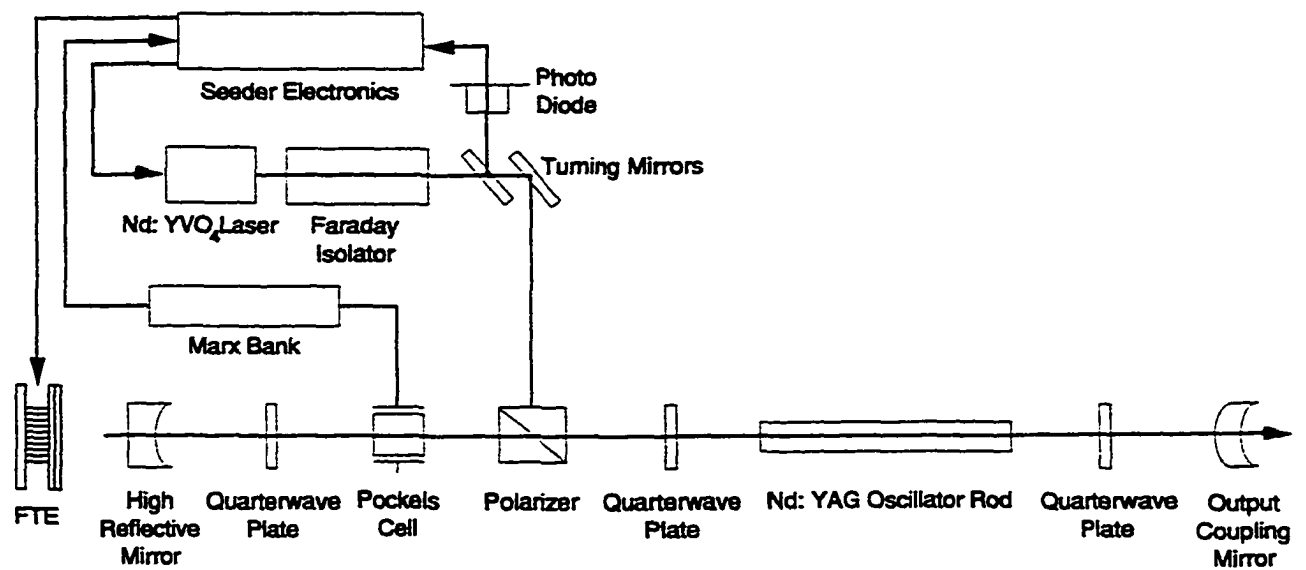
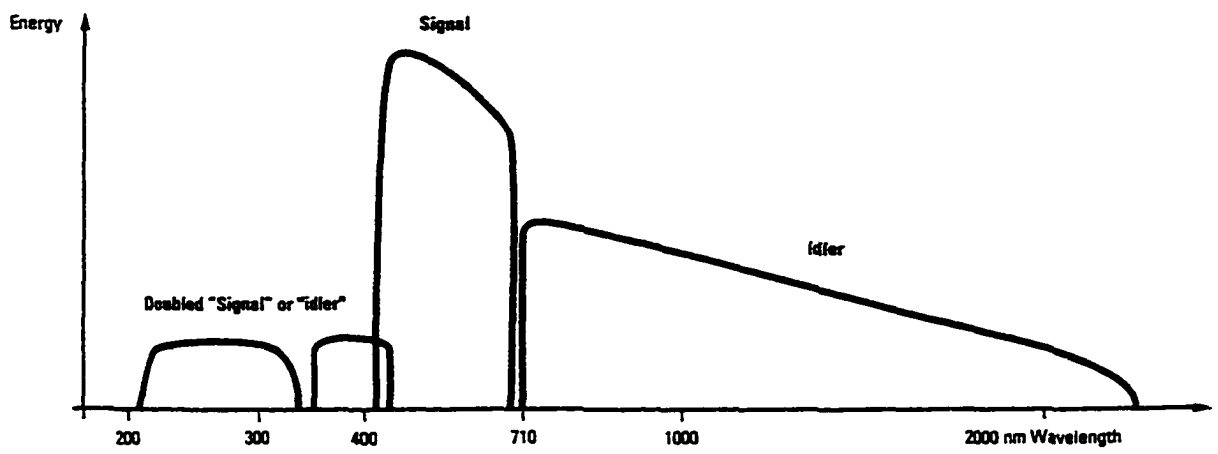


Fig. A5.1 : Injection seeder and GCR host laser





**Fig. A5.3: Typical tuning performance of MOPO-FDO**

## APPENDIX 6

### Gas Jet Ejectors: Principle and Applications

A thrust augmenting ejector consists of one or more high momentum primary jets that are issued into the confines of an aerodynamic shroud (see Fig. A6.1). As the jet evolves, it entrains some of the ambient fluid contained within the ejector, thereby inducing a secondary stream to flow in through the ejector inlet. As the secondary flow is accelerated around the leading edges of the ejector shroud, it lowers the surface pressure in these regions. The resulting leading edge suction create aerodynamic forces that have a large component in the direction of the primary nozzle throat. These forces augment the force produced by the primary jet.

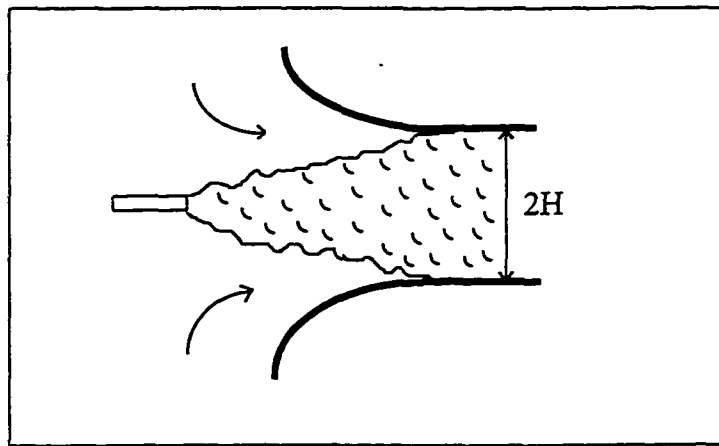


**Fig. A6.1: Thrust augmenting ejector**

An important application of thrust augmenting ejectors is found in vertical and short takeoff/landing of aircrafts, where there is a need for a large source of powered lift. Another application of gas ejectors, is the mixer-ejector concept developed by Presz et al. (1988); which was effective in reducing the noise from aircraft engines.

Lund et al. (1986) developed a computational model, using the viscous-inviscid interaction methodology, to optimize the inlet shape and primary-nozzle location for a two dimensional thrust augmenting ejector (Fig. A6.2). The surface pressure distribution predicted by the model was compared with the experimental measurements taken by Bernal et al. (1983) as shown in Fig. A6.3. The agreement was seen to be good.

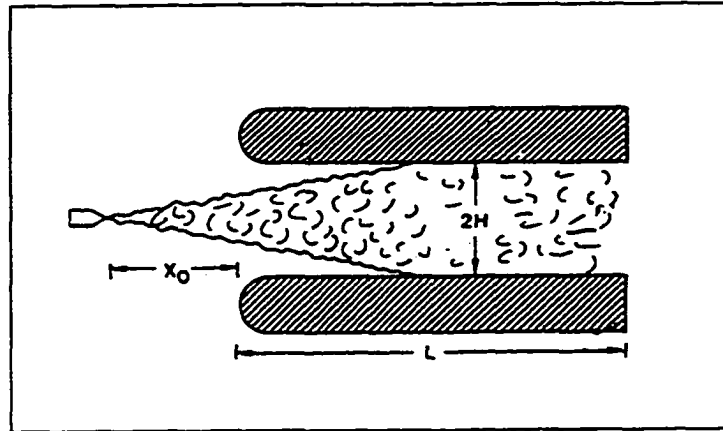


**Fig A6.2: Test configuration (Lund et al., 1986)**

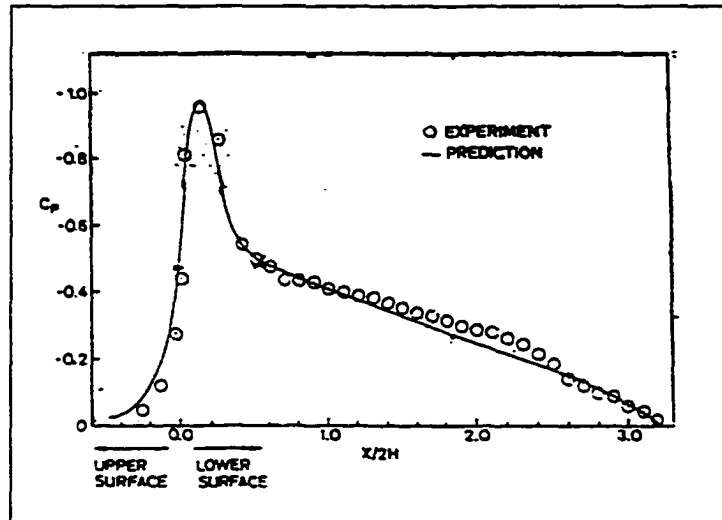


**Fig. A6.3: Comparison of surface pressure distribution (Lund et al., 1986)**

Furthermore, in the above mentioned study a constrained optimization analysis of the two-dimensional thrust augmentor inlet design for the shroud was conducted. Figure A6.4 shows a perturbed configuration in which the jet nozzle is free to move along the plane of symmetry, and a section of the inlet lip is allowed to rotate. The geometric design variables were the jet nozzle location, the length of the inlet section rotated, the jet primary thrust (or Reynolds number) and the rotation angle.

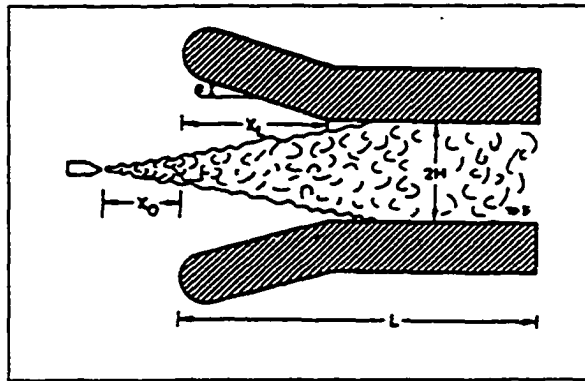


**Fig. A6.4: Optimization parameters:  $X_0$ ,  $X_L$  and  $\theta$ ,  $L/2H=3.28$   
(Lund et al., 1986)**

In the same study, a quasi-Newton optimization routine was coupled with the developed code to systematically search through the design parameters. Results showed that the optimal design shapes are strong functions of Reynolds number. At low Reynolds numbers the optimal nozzle position was located up to one channel width ahead of the shroud, while the inlet is slightly expanded. As Reynolds number was increased the nozzle moved roughly up to the entrance plane of the shroud. The inlet lips rotate through the horizontal and then toward the jet as the Reynolds number was increased. The length of the inlet lip which was rotated was seen to increase with Reynolds number.

Tavella et al. (1987) predicted theoretically thrust augmentation as a function of the primary nozzle position (see Fig. A6.5) . The augmentation showed a maximum for a location of the primary nozzle near the inlet plane. Similar behavior was observed experimentally by Porter et al. (1981).

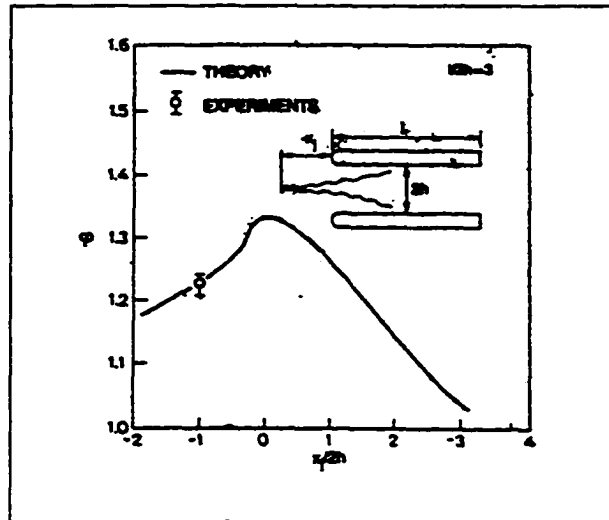


**Fig. A6.5: Effect of primary nozzle position on thrust augmentation (Tavella et al., 1987)**

Choi, Y. H. and Soh, W. Y. (1990) conducted a computational analysis of the flow field of a two dimensional ejector nozzle for NASA Lewis Research center. They found out that there is an optimum nozzle ejector area ratio for the optimum pumping of the secondary flow. At high area ratios, a free stream flow passes directly through the mixing duct without giving a adequate pumping. At low area ratios, the jet boundaries blocks the incoming flow.

Lund, T. S. (1991) developed a viscous-inviscid interaction method to predict the performance of a two-dimensional incompressible flow ejector that use two primary jets (see Fig. A6.6). The flow field was subdivided into a viscous region that contains the turbulent jets and an inviscid region that contains the ambient fluid drawn into the device, the inviscid flow was modeled with a higher order panel method, and an integral method was used for description of the viscous part. The viscous and inviscid solutions were matched together in an iterative process that simulates the interaction between the jets and the ambient fluid. The results of this study showed that the dual jet configuration consistently yields better performance over the identical single jet configuration.

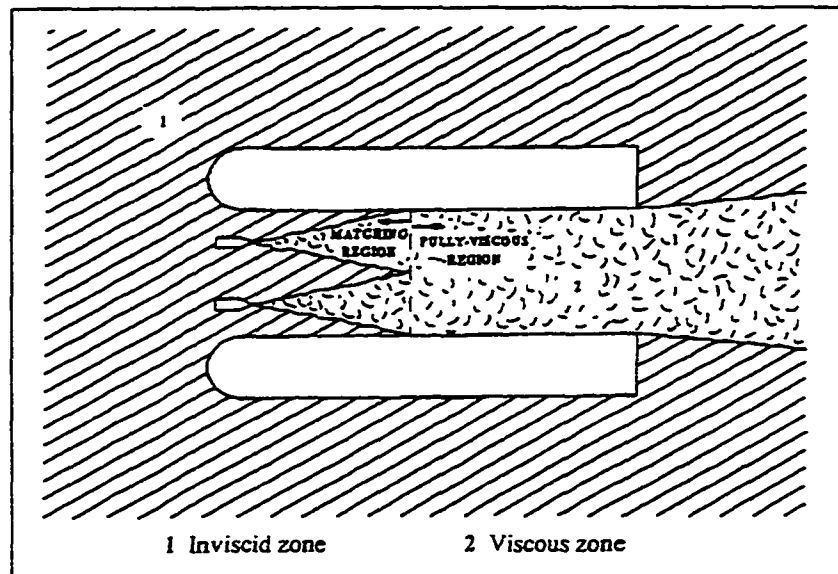


**Fig. A6.6: Dual jet ejectors and the viscous-inviscid approach (Lund, 1991)**

The aforementioned conclusion had been observed earlier by Porter et al. (1981), who found out experimentally that the ejector performance is increased significantly when more than one primary jet is used.

Miller et al. (1991) used a high pressure ejector diffuser with injection occurring at the throat plane (see Fig. A6.7). He found out that a diffuser enhances the performance by reducing the static pressure in the mixing region, which therefore increases the secondary flow rates. However, this configuration led to choking at high ejector pressure ratios.

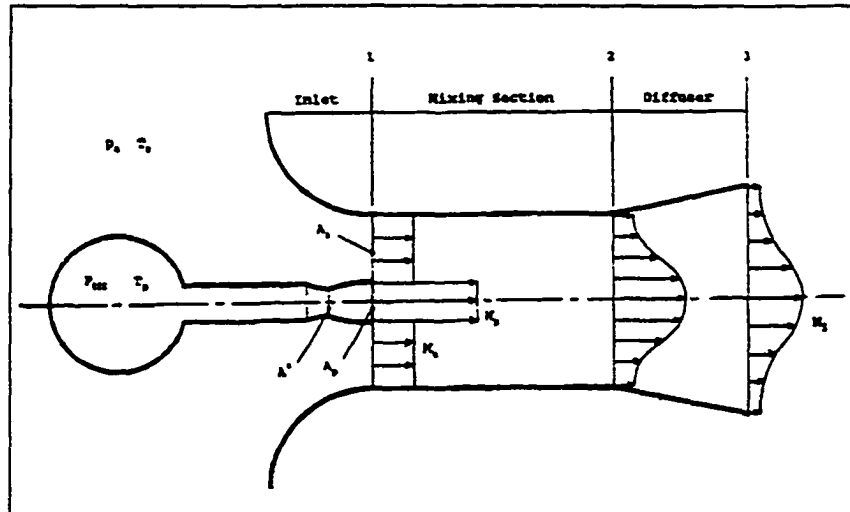


**Fig. A6.7: Ejector schematic (Miller et al., 1991)**

## APPENDIX 7

### Static Pressure Drop Through Venturis

The pressure drop along the interior surface of the venturi was measured by Nana (1998). An electronic Barocel manometer was used for that purpose. The static pressure was recorded for the axial locations 5d, 11d, 17d, 23d, and 29 above the base of the venturi. Figure A7.1 shows the pressure drop through a single venturi for a nitrogen cold jet at Reynolds number of 5100, the same venturi was positioned at three locations corresponding to venturi 1, 2 and 3 (see Fig. 5.1c). Figure A7.2 gives the pressure drop at the same conditions of Fig. A7.1, but the pressure along each venturi was measured in the presence of the other venturis (i.e., in the cascade case). Figure A7.3 provide the pressure drop through venturi 1, 2 and 3 (see Fig. 5.1c), in the presence of the cascade, for the propane flame at Reynolds number 3500.

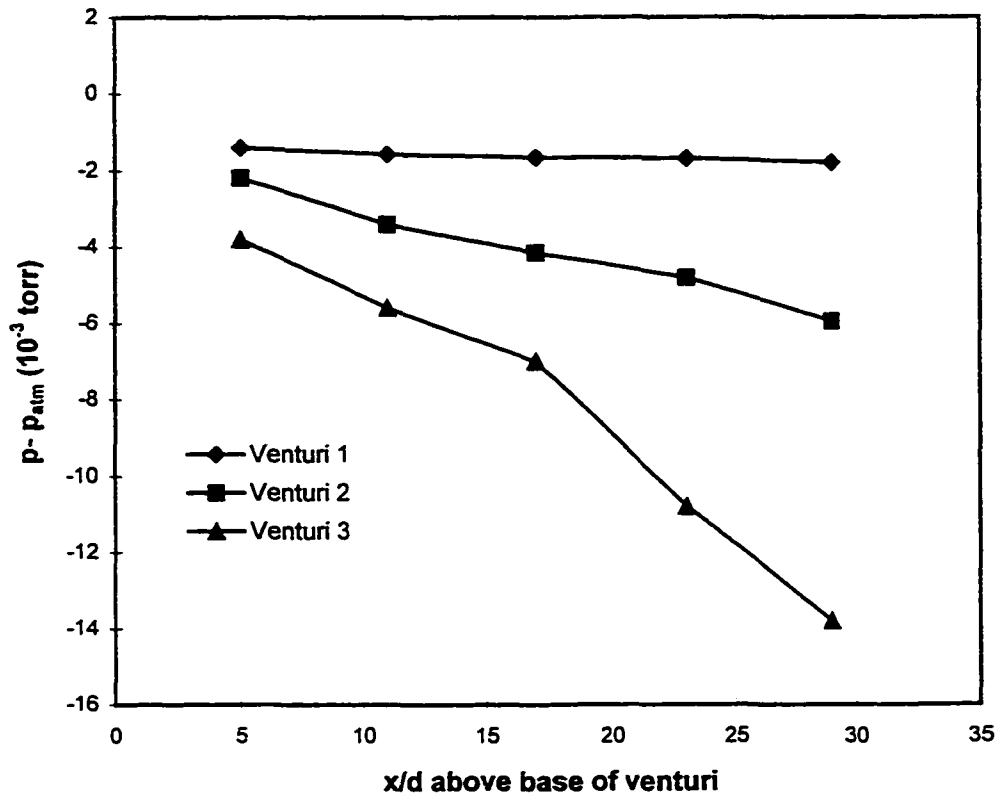


**Fig. A7.1: Static pressure drop along a single venturi positioned at the three locations: 1, 2 and 3 (Fig. 5.1c) for a nitrogen cold jet at Re=5100**

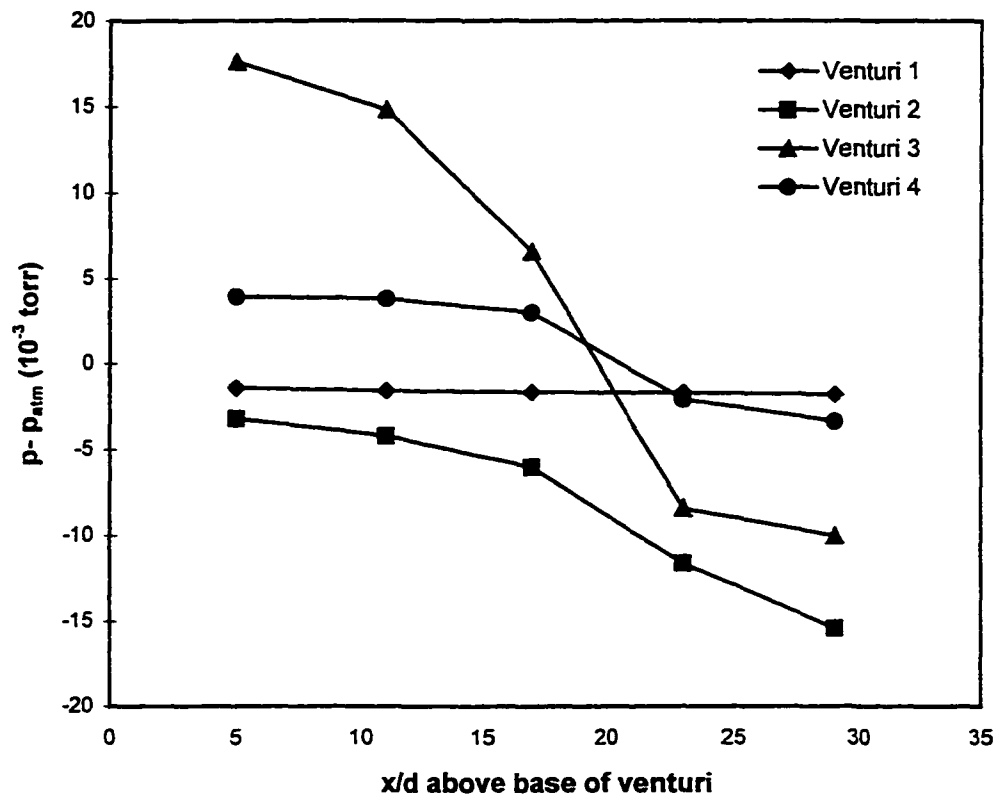


**Fig. A7.2: Static pressure drop along venturi 1, 2, 3 and 4 in the cascade (Fig. 5.1c) for a nitrogen cold jet at Re=5100**

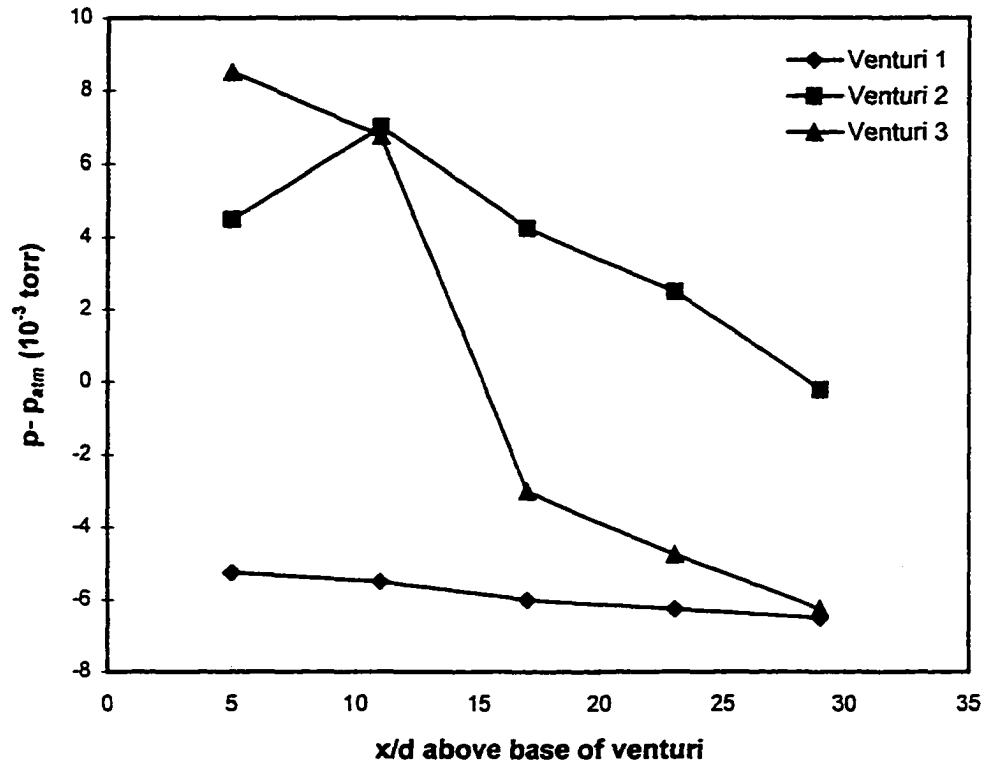
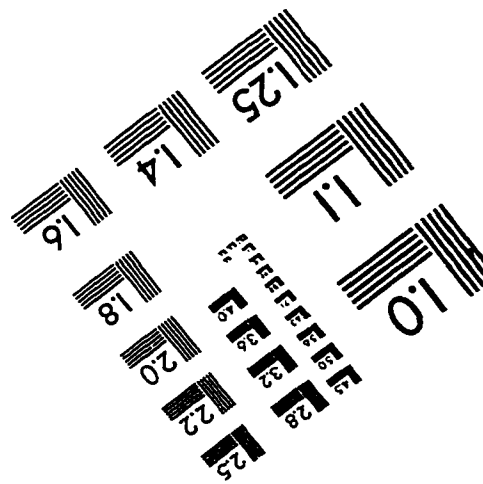
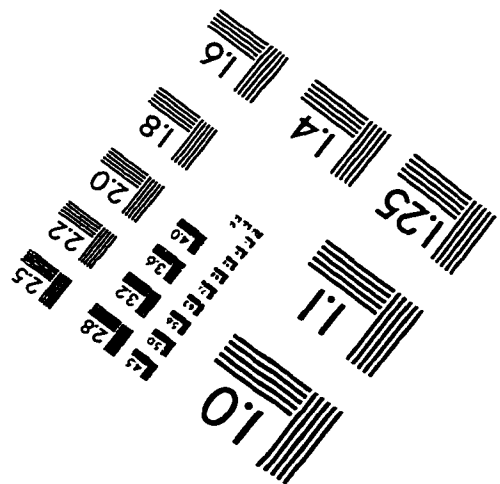
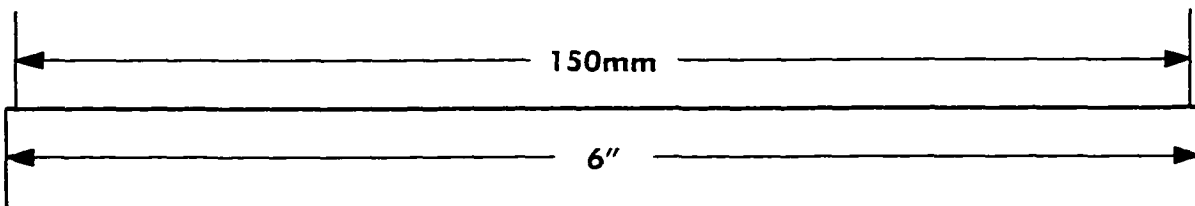
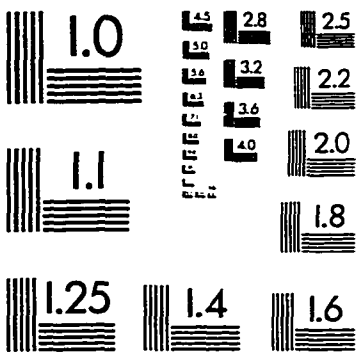
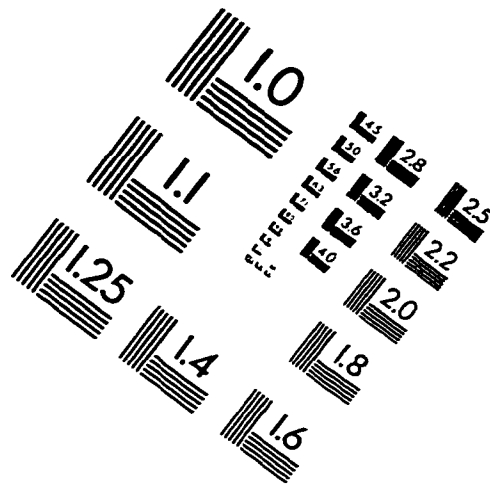
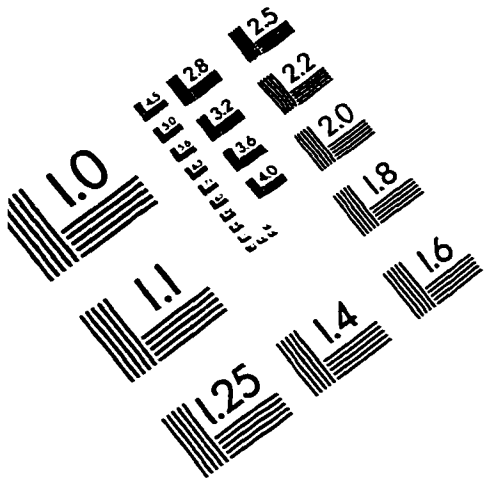


**Fig. A7.3: Static pressure drop along venturi 1, 2 and 3 in the cascade (Fig. 5.1c) for the propane flame at  $Re=3500$**

# IMAGE EVALUATION TEST TARGET (QA-3)



APPLIED IMAGE, Inc  
1653 East Main Street  
Rochester, NY 14609 USA  
Phone: 716/482-0300  
Fax: 716/288-5989

© 1993, Applied Image, Inc., All Rights Reserved